On some eigenvalue problems for elastic instabilities in tension

submitted by

Xiang Liu

for the degree of PhD

of the

College of Science and Engineering

University of Glasgow

February 2013

Abstract

It is well known that buckling instabilities occur when elastic solids are subject to compressive stresses. However, this does not preclude the occurrence of instabilities in systems subject to global tensile loads. Such tensile instabilities may be caused by certain discontinuities (geometrical or material) which re-distribute the stresses applied on its boundary, generating local compressive stresses inside the solid. This research deals with the tensile instabilities in elastic solids by using linear bifurcation analysis, which leads to eigenvalue problems. Then the links between mechanics and mathematics in these tensile instabilities/eigen-systems are demonstrated by using a combination of both numerical and asymptotic analyses. Three main problems have been investigated: a hybrid energy method on edge-buckling, the tensile wrinkling of a stretched bi-annular plate, and the tensile instabilities developed in a radially stretched thick cylindrical tube.

We start by recording a coordinate-free derivation for Föppl–von Kármán equations and the corresponding bifurcation equations (both weak forms and strong forms with their boundary conditions) based on minimum energy principle. This set of equations is applicable to anisotropic elastic thin plates in any planar geometries, which is then specialised for the bifurcation problem of isotropic elastic plates, and a further case under in-plane loading.

In the first main problem, we propose a hybrid energy method which provides an accurate and computationally efficient algorithm for the instability analysis of a class of edge-buckling problems. This algorithm is based on the existing simplest asymptotic approximations and an energy principle (weak form for bifurcation). Fairly accurate and robust approximations can be achieved for both the critical buckling load and mode number even though the simplest asymptotic ansatz is employed. We also explore a number of additional mathematical features that have an intrinsic interest in the context of multi-parameter eigenvalue problems.

Then we consider the wrinkling instabilities of a stretched bi-annular plate, which consists of two fully bonded concentric annuli with different mechanical properties. The effects of the mechanical and geometrical parameters on critical wrinkling are studied, using both numerical and asymptotic techniques. It is found that the critical external buckling loading, the wrinkle numbers and the wrinkled-shape can behave completely differently compared with the single-annular case. The influence of discontinuities (the interface between these two annuli) on localised instabilities is also illustrated thoroughly. Finally, a WKB analysis is conducted

which provides accurate approximations.

In the third problem, we consider the bifurcation of an infinite thick cylindrical tube made of St. Venant–Kirchhoff elastic material, subject to radial tensile loading on both inner and outer walls. In particular, linear Lamé solutions in plane-strain are taken for the pre-bifurcation state, and the bifurcation equations are obtained by using Biot's incremental bifurcation theory. The bifurcation of this plane-strain problem is completely different from the corresponding plane-stress case. Numerical investigations reveal two main bifurcation modes: a long-wave local deformation around the central hole of the domain, or a material wrinkling-type instability along the same boundary. Strictly speaking, the latter scenario is related to the violation of the Shapiro-Lopatinskij condition in an appropriate traction boundary-value problem. It is further shown that the main features of this material instability mode can be found by using a singular-perturbation strategy.

Acknowledgements

Dedicated to my parents,

Xiyun and Bingkun.

Contents

Chapter 1

Basic concepts and research context

1.1 Introduction

In this first chapter we present the background for the work included in the Thesis and introduce some of its main themes. The motivation for the mathematical investigations reported in the later chapters comes from wrinkling phenomena. In Solid Mechanics *wrinkling* is commonly understood as a particular form of buckling characterised by a short-wavelength deformation pattern. It is typically encountered in thin sheets and is present in a range of overwhelmingly familiar situations; a number of such examples are included in Figure 1-1.

Figure 1-1: Everyday wrinkling.

The mechanical behaviour of thin elastic plates or shells is intimately dictated by the geometrical separation of scales that allows bending deformations more easily than in-plane shearing or stretching. Most of the interesting fine-scale patterns observed on these structures in response to imposed far-field loading originate in their differential bending/stretching properties.

Wrinkling, just like traditional buckling instabilities, requires the presence of compressive stresses. However, this does not preclude the occurrence of wrinkles in systems subject to global tensile loads. Indeed, geometrical discontinuities in an elastic solid are known to re-distribute the stresses applied on its boundary, thus leading to unexpected regions of compressive stresses inside the solid. A classical example is the famous Kirsch Problem (see pp.75-77 in [117]) concerning the distribution of stresses in a thin elastic plate with a hole at its centre, and subjected to pulling forces on two opposite edges. Figure 1-2 gives a graphical representation of the (linear) classical solution. If the plate is sufficiently thin, when the magnitude of the far-
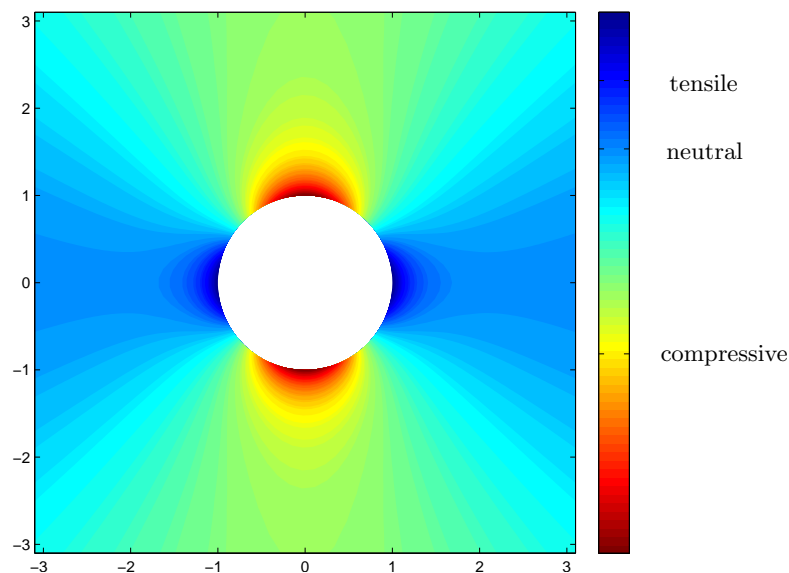
Figure 1-2: Elastic stress concentration around a hole in a rectangular plate subjected to uniform tensile forces on the horizontal sides and traction-free on the other two boundaries. 'Red' identifies regions of compressive (negative) azimuthal stresses, 'dark blue' is used for large tensile (positive) stresses, and the areas shown in 'pale blue' are only modestly affected by the presence of the hole.

field tractions exceeds a critical threshold the originally flat plate deforms out-of-plane, resulting in (possibly) unwanted effects. Interestingly, until recently such phenomena have received only sporadic attention in the literature. Most investigations have dealt with either purely numerical or experimental aspects (e.g., [18, 61, 111, 113]). Mansfield [85] seems to have been the first to examine elastic wrinkling of an annular plate uniformly stretched along the inner rim and traction-free on the other boundary. Other interest in similar situations came from modelling deep-drawing processes [115], and involved plastic effects [25, 109, 128, 129, 130].

In the two-dimensional approximation theories of Linear Elasticity there have been numerous studies that extended the Kirsch Problem to different hole geometries and loading

conditions. Most of them are focused exclusively on the calculation of certain stress intensity factors and ignore any instability phenomena. An extensive collection of results along this line can be found in the classic text by Savin [108] (also, reference [87] contains some chapters with more recent material).

Recent interest in wrinkling of thin films or membranes comes from biomedical applications [21] and biologically-inspired problems [22, 23]. Relevant questions in these areas involve the dependence of the length and the number of wrinkles on the intensity of the applied load or some geometrical characteristics. Of particular interest are also various scaling laws involving the thickness of the films [23]. Given the unwieldy nature of the nonlinear equations usually employed for describing the post-wrinkling regime (i.e., far from the onset of the instability), most authors have resorted to ad-hoc arguments, numerical simulations and curve-fitting results.

The route we take is quite different, in the sense that we regard wrinkling as an eigenvalue problem and confine our attention to the linearised effects that describe the incipient stage of wrinkles rather than their evolution far from the critical load values. While this is admittedly more limiting than a nonlinear analysis, it does permit us to explore analytically the wrinkling phenomena in considerably more depth than it would be possible within a nonlinear framework.

The scope of the investigations presented in the Thesis and their relationship to the literature is amplified in §1.4. Our immediate aim is to introduce in some detail the mathematical models used in the next chapters, the formulation theories of the bifurcation equations in solid structures, such as the *Calculus of Variations* and the *Method of Adjacent Equilibrium*. Then, a detailed description of the concept of *neutral stability envelope* is given, which is one of the central themes of this work as it will be recurring in each of the following chapters. Finally, we provide an overview of the Thesis.

1.2   Linear bifurcations and formulation strategies

The physical phenomena investigated in this Thesis fall within the class of *linear bifurcations* and are closely related to the coexistence of different mechanical states for certain critical load values. Notice that in the literature the terms 'stability' and 'bifurcation' are used interchangeably. There are two main strategies in formulating linear bifurcations in static problems. The first one belongs to the province of the *Calculus of Variations* (CV) and entails a study of the second variation of the total energy (its sign or its various coerciveness properties). An extensive discussion can be found in [12, 75, 76]. In this section, we will first outline some fundamental ideas on the CV for conservative systems (the application of CV is on full display in *Chapter 2* where we derive the Föppl–von Kármán plate theory and bifurcation equations). Then we move on to the *Method of Adjacent Equilibrium* (MAE), which can be used alternatively in all problems investigated in this Thesis, and will be particularly demonstrated in the problem discussed in *Chapter 5*. It is important to keep in mind that this is not the only

strategy available for exploring linear bifurcations. Other options include the *energy method*, which will be reviewed in some detail in the next chapter as applied to the class of bifurcations for thin elastic plates, and the *dynamic method* on which we touch only briefly below.

1.2.1 Calculus of Variations

The *Calculus of Variations* (*CV*) is actually based on the extension of the principle of virtual displacements to static elastic bodies with infinite degree of freedom. Here we assume a conservative system (an elastic system under the action of conservative loading), with potential energy $\mathcal{V} = \mathcal{E} + \mathcal{V}_e$ (where $\mathcal{E}$ is the strain energy and $\mathcal{V}_e$ the potential energy of external loads). If we use $\boldsymbol{u}$ to describe the displacement field of the elastic body, we can obtain an expression for the potential energy functional in which only the displacement $\boldsymbol{u}$ (rather than stress) appears. Given an arbitrarily small variation $\varepsilon \boldsymbol{u}_1$ to the displacement $\boldsymbol{u}$ (where $0 < \varepsilon \ll 1$ and $\max_{x \in \Omega} |\boldsymbol{u}_1| = 1$), the change in potential energy $\Delta \mathcal{V}$ can be expanded in terms of Taylor's series as

$$\Delta \mathcal{V} = \delta \mathcal{V}(\boldsymbol{u})[\boldsymbol{u}_1] + \frac{1}{2!}\delta^2 \mathcal{V}(\boldsymbol{u})[\boldsymbol{u}_1, \boldsymbol{u}_1] + \dots ,$$

Then the stationary point of $\mathcal{V}$, when the conservative system is in equilibrium, is given by

$$\delta \mathcal{V}(\boldsymbol{u})[\boldsymbol{u}_1] = 0 . \tag{1.1}$$

We mention in passing that this also leads to the principle of virtual displacement: $\delta \mathcal{E} = -\delta \mathcal{V}_e$. According to some basic arguments in *CV*, we can obtain the governing equations and boundary conditions for the equilibrium in terms of displacement $\boldsymbol{u}$ (for example, the equilibrium equations involving $\boldsymbol{u}$ alone as (3.26) on p.87 in [19]). There is no loss of generality to assume that such equilibrium is governed by a (possibly vector) differential equation for the non-dimensional displacement field $\boldsymbol{u}$,

$$\begin{cases} \mathcal{L}(\boldsymbol{u}; \lambda) = \boldsymbol{0} & \text{in} \quad \Omega , \\ \mathcal{B}(\boldsymbol{u}; \lambda) = \mathcal{B}_* & \text{on} \quad \partial\Omega , \end{cases} \tag{1.2}$$

where $\lambda > 0$ denotes some dimensionless loading parameter, $\mathcal{L}$ and $\mathcal{B}$ represent time-independent nonlinear differential operators, and $\mathcal{B}_*$ is a known constant expression defined on $\partial\Omega$. Here Ω is assumed to be a bounded domain in $\mathbb{R}^2$ or $\mathbb{R}^3$, as this is the prevalent situation in the Thesis. Assume further that a certain particular solution $\mathring{\boldsymbol{u}}$, the *basic state*, is available by solving the system (1.2) with a given λ: it may be known explicitly in closed form or it may be available only numerically.

When $\delta \mathcal{V} = 0$, the sign of $\Delta \mathcal{V}$ now depends on that of $\delta^2 \mathcal{V}$. The local minimum of the potential energy ('stability') requires that the second derivative must be nonnegative: $\delta^2 \mathcal{V} \geq 0$. More specifically, as the loading parameter λ in (1.2) is sufficiently small, the second variation

is positive definite. As λ increases, $\delta^2 \mathcal{V}$ might go from positive to zero, when the system loses stability. The loss of stability is defined by the critical state which is caused by the smallest loading parameter λ_C for which $\delta^2 \mathcal{V}$ is no longer positive definite for at least one variation $\boldsymbol{u}_1$ (denoted by $\delta \boldsymbol{u}_1$). In order to find the minimum external loading λ_C and corresponding bifurcation mode $\boldsymbol{u}_{1C}$, we take the variation of the second variation of the energy functional, namely,

$$\delta \left\{ \delta^2 \mathcal{V}(\lambda_C, \boldsymbol{u}_{1C}) \right\} [\delta \boldsymbol{u}_1] = 0 \,. \tag{1.3}$$

Similarly, we can get the governing equations together with the boundary conditions for such a critical (bifurcation) state by using the CV arguments on the above equation.

1.2.2 Method of Adjacent Equilibrium

Indeed, the governing equations obtained by CV can alternatively be pursued by applying the *Method of Adjacent Equilibrium* (MAE) procedure on the equilibrium equation (1.2).

MAE has its origins in Euler's analyses of compressed elastic rods. Its gist lies in the fact that under certain conditions the equilibrium solutions of (nonlinear) elastic systems are not unique, that is, under given boundary conditions and prescribed loads these systems can have more than one equilibrium configuration (e.g., a compressed rod could be straight or buckled).

Assuming that we already have governing equations (1.2) for the basic state, which is allowed to be inhomogeneous, this does not play any role in the following discussion.

The next step is to *postulate* the existence of an adjacent (i.e., as close as one pleases to the original) equilibrium state under constant load. This will be characterised by a displacement $\varepsilon \boldsymbol{u}_1$ ($0 < \varepsilon \ll 1$ and $\max_{x \in \Omega} |\boldsymbol{u}_1| = 1$) with reference to the basic state, so it is expected that $\boldsymbol{u} = \mathring{\boldsymbol{u}} + \varepsilon \boldsymbol{u}_1$ will satisfy the same equilibrium equations (1.2). Owing to the infinitesimal nature of this secondary state, we can write

$$\mathcal{L}(\mathring{\boldsymbol{u}} + \varepsilon \boldsymbol{u}_1; \lambda) = \mathcal{L}(\mathring{\boldsymbol{u}}; \lambda) + \varepsilon \, \mathcal{L}_{\mathrm{lin}}(\boldsymbol{u}_1; \mathring{\boldsymbol{u}}, \lambda) + \mathcal{O}(\varepsilon^2) \,,$$

$$\mathcal{B}(\mathring{\boldsymbol{u}} + \varepsilon \boldsymbol{u}_1; \lambda) = \mathcal{B}(\mathring{\boldsymbol{u}}; \lambda) + \varepsilon \, \mathcal{B}_{\mathrm{lin}}(\boldsymbol{u}_1; \mathring{\boldsymbol{u}}, \lambda) + \mathcal{O}(\varepsilon^2) \,,$$

where the 'lin' label on the right-hand sides of these equations indicates that the corresponding operators are linear in $\boldsymbol{u}_1$, but may depend nonlinearly on the basic state $\mathring{\boldsymbol{u}}$. On subtracting the corresponding differential equations for the two adjacent states, dividing through by ε, and then ignoring the $\mathcal{O}(\varepsilon)-$terms yields

$$\begin{cases} \mathcal{L}_{\mathrm{lin}}(\mathring{\boldsymbol{u}}; \boldsymbol{u}_1, \lambda) = \boldsymbol{0} & \text{in} \quad \Omega \,, \\ \mathcal{B}_{\mathrm{lin}}(\mathring{\boldsymbol{u}}; \boldsymbol{u}_1, \lambda) = \boldsymbol{0} & \text{on} \quad \partial\Omega \,, \end{cases} \tag{1.4}$$

which are actually the same as we would have obtained from (1.3) using the previous CV

strategy. The mathematical justification of the approach of MAE requires the existence of a variational structure for (1.2), as shown earlier in (1.1). Knops and Wilkes (pp.224-228 in [75]) give an informative discussion of the theory behind the validity of MAE. More readable accounts covering similar material can be found in [19] and [79].

These equations lay at the foundation of most bifurcation analyses in elastostatics. Because the boundary conditions in (1.4) are homogeneous and Ω is bounded, the existence of a nontrivial $\boldsymbol{u}_1$ turns out to be possible only for a discrete set of values of λ, the so-called *spectrum* of the linearised problem. For problems that have a variational structure (e.g., (1.1)) the differential system (1.4) is self-adjoint and standard results from Functional Analysis (e.g., [123]) guarantee the existence of such values of λ. It is the lowest positive such critical number which is important in applications.

We mention in passing that alongside λ there are other parameters that appear in equation (1.4) – mechanical constants, aspect ratios, etc. When solving this equation one is usually interested in the locus of λ as a function of one of these parameters, in some two-dimensional plane. The diagram obtained by graphically representing this dependence makes it possible to determine the so-called *neutrally stable* states of the particular configuration under investigation. Since the second variation is not involved in such analyses, strictly speaking the points on these curves identify only the coexistence of at least two potential distinct states. Whether they are stable or unstable in a physical sense is a different matter.

However, large classes of elasticity problems with non-conservative loading must be analysed within a broader framework in which time effects are accounted for right from the outset. Such strategies bring elastic stability closer to the general theory of stability of motion and its applications in other fields such as Fluid Mechanics, for instance.

1.2.3 Dynamic Method

The other general strategy used for analysing linear bifurcations is the *Dynamic Method* that amounts to the study of small oscillations superimposed on the basic state [79, 120]. The first equation in (1.2) is replaced by its dynamic counterpart, that usually can be cast in the form

$$\mathcal{L}(\boldsymbol{u}; \lambda) = \frac{\partial^2 \boldsymbol{u}}{\partial t^2} \, .$$

Following the linearisation procedure outlined above one arrives at

$$\mathcal{L}_{\mathrm{lin}}(\boldsymbol{u}_1; \mathring{\boldsymbol{u}}, \lambda) = \frac{\partial^2 \boldsymbol{u}_1}{\partial t^2} \, .$$

The solution of the last equation is sought in the form $\boldsymbol{u}_1 = \hat{\boldsymbol{u}}\mathrm{e}^{\mathrm{i}\omega t}$, where the arbitrary amplitude $\hat{\boldsymbol{u}}$ depends on the spatial coordinates; ω is a complex-valued constant that needs to be found and plays the same role as λ in (1.4). On substituting this expression into the linearised equation

one finds a "static" problem

$$\overline{\mathcal{L}}_{\text{lin}}(\hat{\boldsymbol{u}}, \omega; \mathring{\boldsymbol{u}}, \lambda) = \boldsymbol{0}\,,$$

with $\overline{\mathcal{L}}_{\text{lin}}$ a time-independent differential operator with real coefficients. The main task is to study the dependence $\omega = \omega(\lambda)$ and identify how the sign of the imaginary part of ω changes as λ is varied. A negative such imaginary part will lead to some disturbances $\boldsymbol{u}_1$ which grow exponentially in time. According to the Lyapunov criterion of stability the values of λ for which this happens will correspond to unstable states. It must be clear that for self-adjoint problems MAE is just a particular case of this method since in that case all ω^2's are real; if the dependence of ω on λ is continuous then the critical values obtained by the static method are recovered by solving the (implicit) equation $\omega(\lambda) = 0$ (e.g., see [79]).
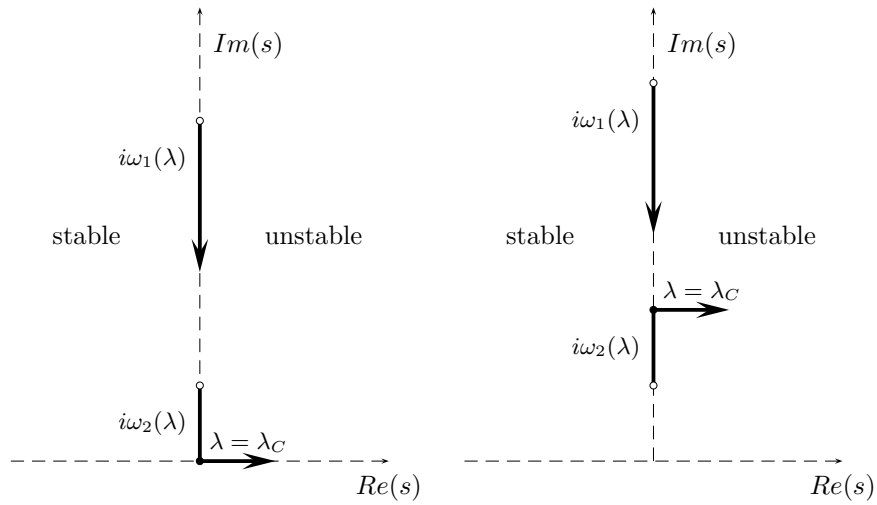
Figure 1-3: Typical behaviour of the characteristic exponents for the *static instability* (left) and the *oscillatory instability* (right). In the former case one of these exponents crosses into the right half-plane via the origin when $\lambda = \lambda_C$ and then remains on the real axis. For the oscillatory instability the crossing takes place at some other location on the imaginary axis.

In discussing the effect of stability by the dynamic method it is customary to use the so-called characteristic exponents $s := i\omega$. With this notation, stability amounts to all of these exponents being in the left-hand plane. As λ is incrementally increased or decreased, the location of these quantities changes. The smallest positive value of λ for which at least one of the characteristic exponents crosses the imaginary axis identifies the critical values of the eigenvalue, λ_C, say. There are many ways in which this can happen, depending on the particular situation investigated. Two important generic situations can be distinguished, as shown in Figure 1-3. On the left one of the characteristic exponents passes through the origin before it enters the right-hand plane and remains purely real for $\lambda \simeq \lambda_C+$. This is the so-called *static instability* that can be captured with the MAE explained above. In the second example on the right, one exponent enters the right half-plane at some point of the imaginary axis (different from the origin O), leading to an *oscillatory instability* or *flutter*. For $\lambda \simeq \lambda_C+$

the behaviour of $\boldsymbol{u}_1$ in the two cases is rather different: in the first situation disturbances grow monotonically in time, while in the second case this increase has an oscillatory nature.

Some authors (e.g., [1]) have used the dynamic method to solve static wrinkling problems, but the extra overhead required by this technique does not justify its use in this Thesis since the same results can be reached more expediently by employing the standard MAE.

1.3   The neutral stability envelope

A central role in all investigations in this work will be played by the concept of the *neutral stability envelope* (NSE). It is difficult to give a general definition since such envelopes are not uniquely defined and they are highly sensitive to the choice of non-dimensional scalings used for the problem at hand. Instead, we prefer to introduce the NSE by looking at two simple elastic stability problems that share some common characteristics with what will appear later in the Thesis; our presentation follows [3, 19, 119] to a certain degree. One of the main simplifying features in both examples is the constant-coefficient nature of the governing differential equations. Here we record the bifurcation equations for isotropic elastic thin plates under in-plane loading

$$D\nabla^4 w - \mathring{\boldsymbol{N}} : (\boldsymbol{\nabla} \otimes \boldsymbol{\nabla} w) = 0 \,, \tag{1.5}$$

whose detailed formulation is contained in *Chapter 2* and finally arrives at (2.40a).

Let us consider a thin elastic plate simply supported on all four edges and subject to uniform compressive in-plane loads acting in the direction of the x-axis. The (linear) basic state is characterised by $\mathring{N}_{11} = N > 0$, $\mathring{N}_{12} = \mathring{N}_{22} = 0$, so that the first equation in (1.5) reduces to

$$D\nabla^4 w - N\frac{\partial^2 w}{\partial x^2} = 0 \,. \tag{1.6}$$

The simply-supported boundary conditions can be expressed as

$$w = \frac{\partial^2 w}{\partial x^2} = 0 \,, \quad \text{on} \quad x = 0, a \,, \tag{1.7a}$$

$$w = \frac{\partial^2 w}{\partial y^2} = 0 \,, \quad \text{on} \quad y = 0, b \,. \tag{1.7b}$$

Motivated by the fact that (1.6) represents a constant-coefficient equation, its solution is sought in the form

$$w(x, y) = C\sin(p_m x)\sin(q_n y) \,, \tag{1.8}$$

that can be seen to satisfy (1.7) *a priori*. Here, $p_m := m\pi/a$ and $q_n := n\pi/b$ depend on the arbitrary positive integers $m, n \in \mathbb{N}$ that must be determined as explained next. On

substituting (1.8) into (1.6) we find immediately that

$$N = \frac{D}{p_m^2} \left(p_m^2 + q_n^2 \right)^2 , \qquad (1.9)$$

i.e., $N \equiv N(m,n)$. No proper eigenvalue problem is solved here because we were able to guess the eigenmodes right from the start, so the boundary conditions play no role after postulating (1.8). This is an exceptional situation that is no longer true in more complicated scenarios. The critical buckling load N_{cr}, say, is identified as the smallest positive value of this expression or, in other words,

$$N_{cr} = \min_{m,n \in \mathbb{N}} N(m,n) \,.$$

Given that the behaviour of (1.9) with n is monotonic increasing, we must obviously set $n = 1$, thus yielding

$$N = \frac{D\pi^2}{b^2} \left(\frac{m}{\eta} + \frac{\eta}{m} \right)^2 \equiv D \left(\frac{\pi}{b} \right)^2 \Phi^2(m;\eta) , \qquad (1.10)$$

where $\eta := a/b$, a geometrical parameter that characterises the slenderness of the plate. Minimising the new value of N with respect to $m \in \mathbb{N}$ will entail carrying out that process on Φ. As a consequence, the critical value of m obtained from solving $\partial\Phi/\partial m = 0$ will depend on η.

If $\eta < 1$ (i.e. the plate is wider than its length), $m/\eta > \eta/m$ and N_{cr} always corresponds to $m = 1$. As the length-to-width ratio η increases, the buckling load will increase and the plate will tend to adopt a neutrally stable configuration for which $m > 1$. By way of example let us examine the inequality

$$N(m,1) \leq N(m-1,1) \,,$$

which expresses the condition under which a plate of aspect ratio η will buckle into m half-sine waves in the loaded direction, rather than $m = 1$. Simple algebra gives

$$\eta^2 \geq m(m-1) \,,$$

and we can immediately see that the plate will experience buckling in two half-sine waves rather than one when $\eta \geq \sqrt{2}$, in three rather than two when $\eta \geq \sqrt{6}$, and so on – see Figure 1-4. A plot like this is particularly useful as it provides an expedient means of identifying the critical load and the corresponding mode number associated with a given aspect ratio η.

The overview given above paints a somewhat distorted picture because it relies heavily on the explicit-form solution (1.8). In general, if the simply-supported boundary conditions are abandoned, one must account for more freedom in the assumed expression of w. An example that anticipates the work in the later chapters is described next. This involves, again, a rectangular elastic plate simply supported on the edges $x = 0, a$, and some other type of constraints (as yet unspecified) on the sides $y = 0, b$. Since (1.7b) still applies, a solution can
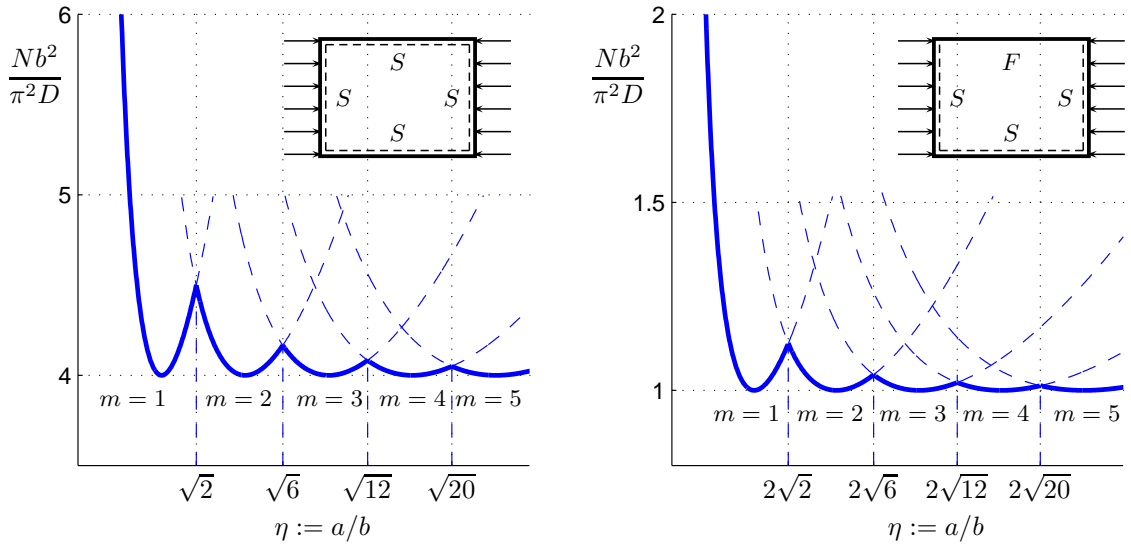
Figure 1-4: The influence of the aspect ratio η on the mode number $m \in \mathbb{N}$ for the bifurcation of rectangular plates with two different sets of boundary conditions. The blue curves are obtained by plotting the curves of $Nb^2/\pi^2 D$ with respect to η for a family values of m, and we note that it is only the solid line that is physically relevant (this is the so called *neutral stability envelope* of the given eigenproblem). The left window shows the the case when all four edges of the plate are simply supported, corresponding to the equation (1.10); the right plot includes the results of (1.13), in the case when the plate is simply supported on the edges $x = 0$, a and $y = 0$, while the other edge, $y = b$, is traction-free.

be sought in the form

$$w(x,y) = W(y)\sin(p_m x)\,, \tag{1.11}$$

where p_m has the same definition as in the previous example and the arbitrary function W accounts for the changes in the boundary conditions.

The result of plugging (1.11) into (1.6) indicates that the amplitude $W \equiv W(y)$ satisfies the *differential equation*

$$\frac{\mathrm{d}^4 W}{\mathrm{d}y^4} - 2p_m^2 \frac{\mathrm{d}^2 W}{\mathrm{d}y^2} + p_m^2\left(p_m^2 - \frac{N}{D}\right)W = 0\,.$$

Its general solution can be expressed as

$$W(y) = C_1 e^{-\alpha y} + C_2 e^{\alpha y} + C_3 \cos(\beta y) + C_4 \sin(\beta y)\,,$$

where

$$\alpha := \left(p_m\sqrt{\frac{N}{D}} + p_m^2\right)^{1/2} \qquad \text{and} \qquad \beta := \left(p_m\sqrt{\frac{N}{D}} - p_m^2\right)^{1/2}\,,$$

and $C_j \in \mathbb{R}$ $(j = 1,2,3,4)$ represent constants that are to be determined by applying the remaining boundary conditions for w. We shall assume, for example, that the side $y = 0$ is

simply-supported so that (1.7b) still holds, and the edge $y = b$ is stress-free, which amounts to

$$\frac{\partial^2 w}{\partial y^2} + \nu \frac{\partial^2 w}{\partial x^2} = \frac{\partial^3 w}{\partial y^3} + (2 - \nu) \frac{\partial^3 w}{\partial x^2 \partial y} \qquad \text{at} \qquad y = b \,. \tag{1.12}$$

Use of (1.11) in (1.7b) gives immediately $C_3 = 0$ and $C_1 = -C_2$, leaving us with $W(y) = A \sinh(\alpha y) + B \sin(\beta y)$ after a suitable relabelling of the constants $(A, B \in \mathbb{R})$. With this information in (1.12), we find the homogeneous system

$$\left[(\alpha^2 - \nu p_m^2) \sinh(\alpha b) \right] A - \left[(\beta^2 + \nu p_m^2) \sin(\beta b) \right] B = 0 \,,$$

$$\left\{ \alpha \left[\alpha^2 - (2 - \nu) p_m^2 \right] \cosh(\alpha b) \right\} A - \left\{ \beta \left[\beta^2 + (2 - \nu) p_m^2 \right] \cos(\beta b) \right\} B = 0 \,,$$

whose non-trivial solvability demands that the determinant of the coefficient matrix vanishes, i.e.

$$(\beta b) \left[(\alpha b)^2 - \nu (p_m b)^2 \right]^2 \tanh(\alpha b) = (\alpha b) \left[(\alpha b)^2 + \nu (p_m b)^2 \right]^2 \tan(\beta b) \,, \tag{1.13}$$

where

$$\alpha b = \left[\left(\frac{m\pi}{\eta} \right)^2 + \frac{m\pi}{\eta} \sqrt{\frac{Nb^2}{D}} \right]^{1/2} \,,$$

$$\beta b = \left[- \left(\frac{m\pi}{\eta} \right)^2 + \frac{m\pi}{\eta} \sqrt{\frac{Nb^2}{D}} \right]^{1/2} \,.$$

Owing to its transcendental nature, the determinantal equation (1.13) must be solved numerically to identify the dependence of N on m for a given η and D. This is then used to identify the critical values of the applied load and the preferred mode number. The comparison of the neutral stability curves (NSE) between two cases in Fig. 1-4 suggests that: even though the NSE's of these two cases are of similar tendency, a free boundary condition reduces the anti-buckling ability (NSE's magnitude) of the plate.

Moreover, if we change the boundary conditions on the edges $x = 0$ and a (along which the compressive loads are applied) into clamped ones, this problem becomes complicated when one is trying to obtain the eigenvalues or eigenmodes. That is because the normal-mode approach, such as (1.8) and (1.11) adopted in the previous two examples, is no longer applicable. Instead, we can solve the partial differential equations directly using some numerical techniques, such as finite different method or finite element method. For example, if we consider the boundary conditions

$$w = \frac{\partial w}{\partial x} = 0 \,, \qquad \text{on} \quad x = 0, a \,, \tag{1.14a}$$

$$w = \frac{\partial^2 w}{\partial y^2} = 0 \,, \qquad \text{on} \quad y = 0, b \,, \tag{1.14b}$$

we can use finite different formulae to discretise the eigen-PDE problem into a generalised eigenvalue problem. Then we can obtain the eigenvalue with smallest magnitude, together with the associated eigenvector. This eigenvalue indicates the critical external force, while the eigenvector approximates the buckling configuration. In the right graph of Fig. 1-5 we record the uni-axially compressed plate with the boundary conditions specified in (1.14), compared with the left plot where all edges are simply supported as discussed earlier. It can be seen from
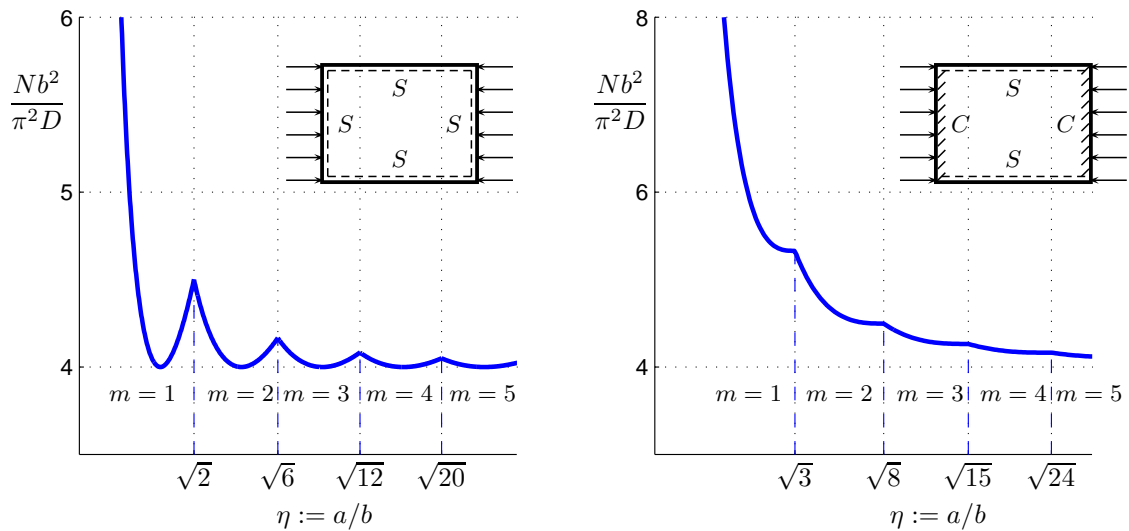
Figure 1-5: Comparison between two types of neutral stability envelopes (NSE) developed by the same rectangular plate subject to two sets of different boundary conditions. The left window records the NSE when all four edges simply supported (the same as the left window in Fig. 1-4); while the right records the NSE for the case when the plate is simply supported on the edges $y = 0$ and b, and the other edges, $x = 0$ and a, are clamped.

Fig. 1-5 that, clamped boundary conditions enhance the resistance capability of buckling for the plate; moreover, clamped supports on the uniaxial compressive loading boundaries will lead to gradually decreasing envelopes (see the right plot of Fig. 1-5) rather than horizontal ones when the same boundaries are simply supported (see the left window in Fig. 1-5).

So far, we have shown the neutral stability envelope (NSE) in terms of the bifurcation of an uni-axially compressed plate under a variety of boundary conditions. To conclude, the NSE is very sensitive to the boundary conditions. In other words, the boundary conditions play a pivotal role on NSE: not only on its amplitude, but also on the way that the response curves intersect with each other, thus, the tendency of the NSE. These findings will repeatedly appear in the bifurcations within more complex geometries in later chapters.

1.4   Literature review

The remainder of this chapter gives a general overview of *partial wrinkling* phenomena in elastic systems by tracing their historical development from the early pioneering works in the first half of the twentieth century through to some of the modern developments that constitute the

object of much research interest nowadays. In the next section we trace a number of relevant contributions using a classical approach that is based on *tension field theories*. That is followed by a more in-depth analysis of the singular perturbation approach initiated by Coman and his associates, while the last part of this section will touch briefly on various numerical strategies that have been used to explore wrinkling for structures in tension, and which are pertinent to the problems targeted in the subsequent parts of the Thesis.

1.4.1 Tension field theories and classical approaches

While the rudiments of classical elastic stability were developed by Euler more than three hundred years ago, and the mathematical study of compressive buckling in elastic plates was already well under way in the late 1800's, the role of tensile and shearing forces on similar instabilities was not recognised until much later. It was the development of the aircraft industry and the need for a more efficient design of wings that motivated the first tension field theories through the works of the German engineer Wagner [125] and some contributions by Eric Reissner [101]. This framework is applicable to wrinkling phenomena understood as a post-buckling equilibrium configuration and load transmission mode in membranes, thin-walled shear panels, elastic shells, and other similar structural components.

Tension field theories were further developed by Stein and Hedgepeth in the mid-1960's [116], who introduced the concept of variable Poisson's ratio that permits "over-contraction" in the direction of the minor principal stress. Their work was confirmed by the experimental results of Mikulas [88] which displayed excellent correlation with the theory, albeit for a limited range of practical configurations. In recent times this approach has also been used by Coman [30] to treat the localised wrinkling of radially stretched membranes with prescribed displacements applied to the outer and inner rims. His results captured a number of both qualitative and quantitative features revealed by the numerical post-buckling analysis performed by Geminard *et al.* in [59] for a related configuration. The original motivation for the study of these latter investigators came from a biomechanical application and was related to the fact that the quantitative analysis of wrinkled patterns produced by living cells crawling on polymer nanomembranes could give an indication of the force applied by the cell cytoskeleton. Biomedical applications and the development of nanoscience are partly responsible for the renewed surge of interest in wrinkling problems in the past decade. Lubarda [83] dealt with an extension of [30] by considering a number of different boundary conditions and/or loading situations.

A general and far-reaching extension of the early tension field theories to problems involving finite elastic deformations was achieved by Pipkin and Steigmann [97] by employing the relaxed-energy approach.

One must bear in mind that, irrespective of the type of kinematics adopted, tension field theories are just approximations whose accuracy cannot be gauged easily. It is interesting to note that recently such theories have been challenged by comparing their predictions to full

finite element simulations. By considering the tension field due to twisting of a central hub in an initially stretched membrane (with small bending stiffness), Iwasa *et al.* [68] showed that there are wrinkled regions of the membrane in which the tension field solution is at variance with the numerical results based on nonlinear bifurcation theory. This is not the first instance when such discrepancies have transpired. An earlier study by Rimrott and Cverko [103] examined the gravity-induced wrinkling in vertical membranes (the so-called "wet blanking problem"), a situation discussed by Mansfield [86] a few years before them by using a special theory of tension field theory valid for nonlinear thin elastic plates. The former authors showed that the introduction of a critical compressive stress perpendicular to wrinkles does lead to results that better match the experimentally observed patterns.

All works cited above have been carried out within the framework of elastostatics, time-dependent effects being ignored completely. This is a sensible approximation for a wide range of situations, although there are circumstances in which the dynamic character of the wrinkling phenomenon or the kinetic properties of the material response cannot realistically be ignored. Such effects have been taken in consideration in a number of recent works. In an interesting paper Vermorel *et al.* [122] looked at the transverse impact of rigid projectiles on a circular rubber membrane by using analytical, numerical, and experimental techniques. They found that on impact of the membrane the projectile gives rise to two axisymmetric waves: the first is a tensile wave propagating at the speed of sound and leaving behind a stretched domain; the second, a transverse wave, propagates on this domain at a lower speed. In the stretched area, due to geometric confinement compressive radial stresses are induced that result in time-dependent circumferential buckling similar to the static situation reported by Coman and Haughton in [47]. The time-evolution of these buckling patterns as well as their wavelength were studied by using numerical simulations and a number of simplifications. Lubarda and Marzani [84] have also dealt with time-dependent phenomena in the wrinkling of a stretched annulus with no bending stiffness, but their interest was in viscoelastic behaviour. Although these authors stated that their interest in the problem was motivated by applications to red blood (erythrocyte) membranes, they used small-strain kinematics and made the assumption that the elastic strains admit an additive decomposition into an elastic and, respectively, a viscoelastic part, which seems rather restrictive. Given the scarcity of the existing results in the literature there is ample scope for extending such viscoelastic analyses to thin plates as well, even though the mathematical models might tend to be rather cumbersome and intractable from an analytical point of view (e.g., see [17]).

1.4.2 Singular-perturbation results

The application of asymptotic methods for describing partial wrinkling phenomena in thin elastic plates in tension has a more recent history. In a number of recent investigations [28, 29, 31, 32, 33, 34, 39, 40, 41, 42, 44, 47], Coman *et al.* have explored several non-trivial features of

the bifurcation equation (to be obtained in *Chapter 2* with the form (1.5)) for the case when the initial pre-buckling stress distribution was inhomogeneous. The work of these investigators was based on the classical normal-mode approach and revolved around a class of eigenvalue problems for a fourth-order linear differential equations with variable coefficients that were cast in the form

$$W'''' + A_3(\rho)W''' + A_2(\rho; \mu, n, \lambda)W'' + A_1(\rho; \mu, n, \lambda)W' + A_0(\rho; \mu, n, \lambda)W = 0, \qquad (1.15)$$

where ρ is the dimensionless independent variable, the prime represents the derivative with respect to ρ, and the coefficients A_j $(j = 0, \dots, 3)$ exhibited dependence on the non-dimensional variables/parameters indicated above. Here $\mu \gg 1$ is directly linked to the small thickness of the plate and the presence of tensile forces in the pre-buckling phase, while λ represents the eigenvalue (some combination of the various loading parameters). As in the simpler examples discussed in §1.3 the amplitude function W for which the equation (1.15) is solved comes from the normal mode solution and $n \in \mathbb{N}$ denotes the mode number which forms part of the unknowns.

Unlike in the two examples already seen in §1.3, a closed-form solution of (1.15) is not available, so new strategies had to be developed in order to obtain useful analytical results. Owing to the asymptotic nature of μ, it turned out that various approximations could be found, hence leading to a number of simple and practical formulae for both the critical load and the mode number as a function of μ.

It is the arbitrary mode number in (1.15) that is largely responsible for compounding the difficulties associated with the presence of variable coefficients. As seen already in the previous sections, to find the physically relevant values of this parameter one has to plot the response curves and identify their envelope (similar to the thick blue lines seen Figures 1-4 and 1-5). Alternatively, this critical value of the mode number is obtained as the global minimum of the curve

$$\lambda \equiv \lambda(n). \qquad (1.16)$$

One of the difficulties here originates in the implicit nature of this relationship. In references [41, 44], the crucial step in capturing this information through analytical means was the observation that $n \sim \mu^\alpha$ as $\mu \gg 1$, where $\alpha = 3/4$ for a whole range of different geometries and/or prebuckling scenarios (see Figure 1-6). The constancy of the exponent $\alpha \in \mathbb{R}$ across a whole range of different problems was linked to the FvK equations used in all of those investigations; the in-plane nature of the initial loading was also deemed to play a significant part. For the case of the elastic instability associated with the stretched and twisted elastic strip discussed in [42] this exponent was equal to $1/2$. It was conjectured that α might have a different value for other types of bifurcation equations, although the problem is still open.

Two distinct asymptotic approaches were used in describing the neutral stability envelope
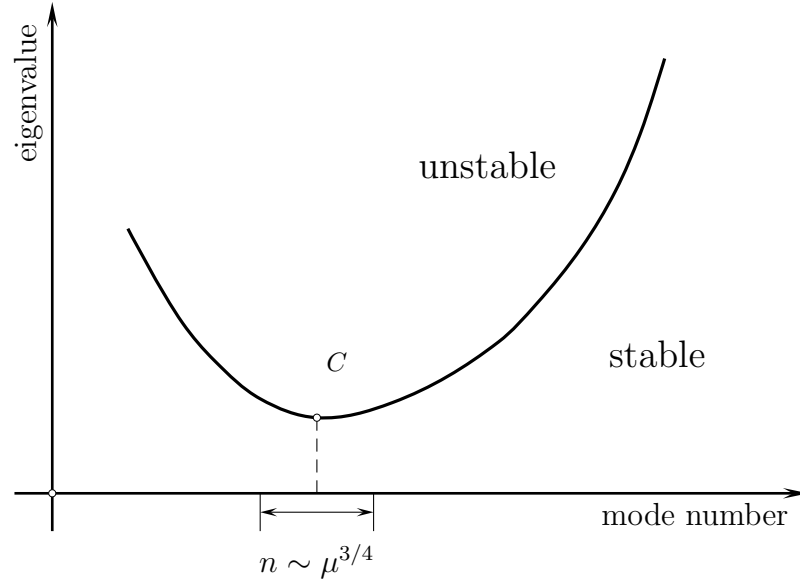
Figure 1-6: Sketch of the neutral stability curves for the buckling problems discussed in [40, 41]. The critical eigenvalue is indicated by 'C', and was found to reside within an $\mathcal{O}(\mu^{3/4})$-layer indicated by the labelled region in this picture.

of (1.15). The original study by Coman and Haughton [47] relied on WKB methods to extract some information about the *general* (not necessarily critical) response curves (1.16) when both $n \gg 1$ and $\mu \gg 1$. A first application of the WKB method using the latter assumption and treating $n \in \mathbb{R}$ as a fixed parameter allowed the reduction of (1.15) to a second-order eigenvalue problem

$$B_2(\rho; \mu, n, \lambda)\overline{W}'' + B_1(\rho; \mu, n, \lambda)\overline{W}' + B_0(\rho; \mu, n, \lambda)\overline{W} = 0 \,, \tag{1.17}$$

where $\overline{W}$ was introduced here to distinguish with W in the original equation (1.15), and the coefficients B_j $(j = 0, 1, 2)$ were obtained from the original equation and had somewhat simpler expressions. Since the order of the differential equation had dropped to two, it was necessary to investigate which of the original four boundary conditions of (1.15) had to be discarded. This was achieved through a second application of the WKB method, this time using $n \gg 1$, in conjunction with the asymptotic simplification of the 4×4 determinantal equation associated with the original problem.

In [41, 43] Coman and Bassom exploited the localised nature of the eigenmodes of (1.17) for large μ and n, by further reducing the already simplified eigenvalue problem to an algebraic equation; that was then solved by perturbation methods involving $n^{-1/3}$ as a small parameter. The outcome was an expression of the form

$$\lambda = a_0 + a_1 n^{-1/3} + a_2 n^{-2/3} + \dots \,, \tag{1.18}$$

for some known coefficients $a_j \in \mathbb{R}$ $(j = 0, 1, \dots)$. This represented an approximation for

the originally implicit dependence (1.16), and was later plotted in order to identify the global minima of those curves. The neutral stability envelope was obtained by substituting these values of the mode number back into (1.18) for different choices of η's.

One of the key ingredients in the strategy outlined above was the presence of a *turning point* (TP) in the reduced equation (1.17), where $\overline{W}'$ changes sign. This was related to the circular boundary separating the regions of compressive and tensile stresses in the membrane ($\mu = 0$), but was not exactly equal to it. As shown in [43] for the azimuthal shearing of a radially stretched membrane, the relationship between these points is akin to a regular perturbation. The tendency of the TP was to migrate towards one of the plate boundaries as $\mu \to \infty$, and it was this particular characteristic that allowed the reduction from the differential equation (1.17) to a simple algebraic relationship. This property of the turning point is typically encountered in similar eigenvalue problems with localised eigenmodes that crop up in the area of hydrodynamic stability (e.g., [53]).

The novel asymptotic arguments that led to (1.17) relied on a characteristic property of the response curves, regarded as $\lambda = \lambda(\eta; n)$. In this formula λ is a function of the aspect ratio η, with n being a secondary parameter. Coman and Haughton [47] discovered that these curves exhibit two distinct types of behaviour. For $n \ll \mu^{1/2}$ the eigenvalues were found to increase with η, while the corresponding buckling load decreased as the mode number was increased. This behaviour is reminiscent of that encountered in membranes, which tend to adopt energy-minimimum configurations with a large number of wrinkles (strictly speaking, an infinite number). However, the presence of bending stiffness inhibits that tendency as one stage is reached when $n = \mathcal{O}(\mu^{1/2})$ and subsequently $n \gg \mu^{1/2}$. It turned out that the energy configurations available within the latter range were the preferred ones, and the corresponding response curves were seen to be very similar to those encountered in the compressive buckling of thin elastic plates. By coupling this observation with the presence of the aforementioned TP facilitated the reduction of (1.15) to two qualitatively different versions of (1.17), although it was only one of them that was relevant to identifying the critical values of the load and the mode number. Figures 1-7 and 1-8 illustrate graphically the feature described above for the annular plate discussed in [47].

While the WKB approach does permit easy access to a number of analytical features of the wrinkling problems studied in [41, 43] like, for instance, the description of the curves (1.16) as $n \to \infty$, the critical neutral stability envelope can only be obtained after some intermediate numerical work (see Figures 3 and 4 in [41]). To circumvent such difficulties, Coman and Bassom proposed a more powerful strategy based on matched asymptotics and the interaction between two boundary layers of thickness $\mathcal{O}(\mu^{-1/2})$ and $\mathcal{O}(\mu^{-1})$, respectively. The larger of the two layers is directly related to the co-existence of tensile and compressive pre-buckling stresses in the plate, and can be loosely referred to as the *membrane boundary layer*. The other is just a consequence of the fact that in thin plates bending effects appear as a singular perturbation to
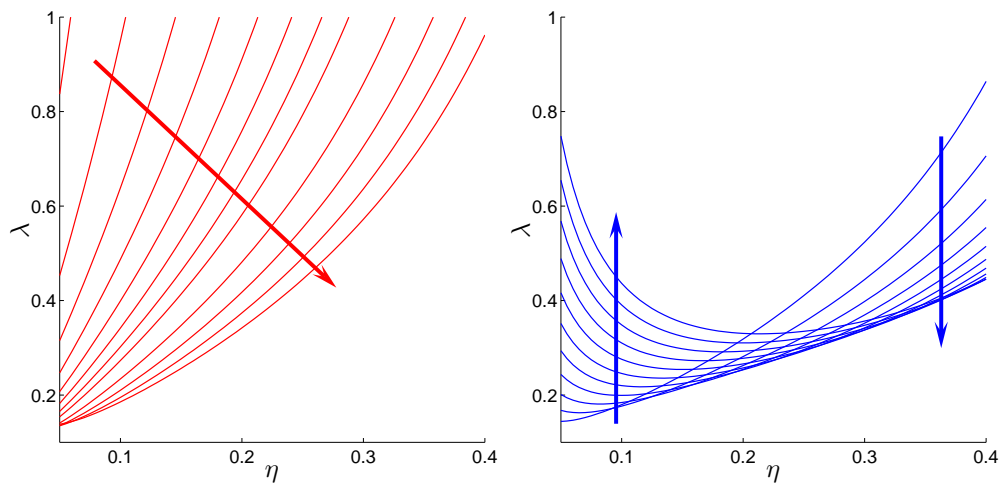
Figure 1-7: Dependence of the response curves $\lambda = \lambda(\eta; n)$ for the radially stretched annulus discussed in [47] when $\mu = 400$. The red curves on the left illustrate the *membrane-like* behaviour ($n \ll \mu^{1/2}$) while the blue curves on the right describe the *plate-like* effect ($n \geq \mu^{1/2}$). The arrows indicate the direction of increasing $n \in \mathbb{N}$.
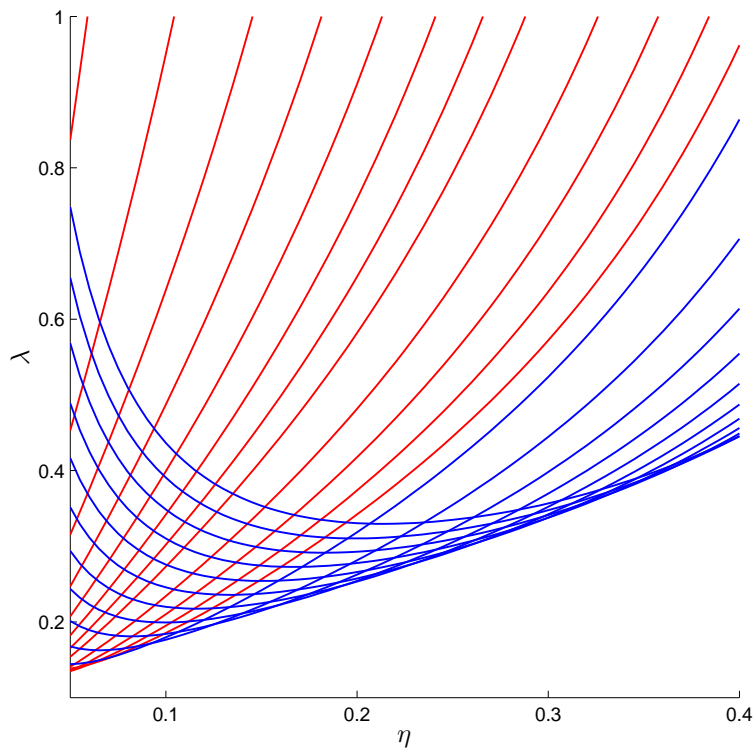
Figure 1-8: The superposition of the two families of curves recorded in Fig. 1-7. Note that for $\eta \geq 0.1$ the *neutral stability envelope* involves only the blue curves.

stretching, so we can label this second one as the *bending boundary layer*. To make transparent the ideas put forth in [41] we need to be a bit more specific, although we shall try to maintain a general tone.

After the introduction of the appropriate boundary-layer variables it was assumed that as

$\mu \to \infty$ the critical mode number would expand as

$$n = N_0\mu^{3/4} + N_1\mu^{1/4} + N_2\mu^{-1/4} + \dots, \qquad (1.19)$$

where $N_j \in \mathbb{R}$ were constants that had to be fixed by ensuring that (1.16) was minimised. To this end the eigenvalue was also assumed to have a representation of the form

$$\lambda = \lambda_0 + \lambda_1\mu^{-1/2} + \lambda_2\mu^{-1} + \dots. \qquad (1.20)$$

The coefficient λ_0 corresponded to the value of λ for which the the prebuckling azimuthal stresses first became equal to zero in the plane membrane case ($\mu = 0$); the remaining λ_j ($j \geq 1$) turned out to be available from the boundary-layer analysis mentioned above. Interestingly enough, the dependence of the coefficients in (1.20) on the N_j's that feature in (1.19) displayed a certain pattern that allowed the strategy to work consistently to any degree of accuracy required. In most of the published works (e.g., [32, 33, 34, 40, 41]) the first term in the expansion (1.19) was sufficient, although higher-order calculations were shown to be feasible in [44]. In general λ_1 depends only on N_0 (and other given parameters), i.e. $\lambda_1 = \lambda_1(N_0)$. From (1.19) and (1.20), it transpires that $\lambda = \lambda(N_0, N_1, \dots)$, so that the critical envelope is determined by the conditions

$$\frac{\partial \lambda}{\partial N_j} = 0, \qquad j = 0, 1, 2, \dots.$$

Asymptotically, this demands that $\partial\lambda_1/\partial N_0 = 0$, an equation that immediately identifies the critical value of N_0, say, N_0^*. Following a lengthy matching process of the asymptotic solutions in the two boundary layers mentioned above, eventually leads to an expression of λ_2 as a function of both N_0 and N_1, i.e. $\lambda_2 = \lambda_2(N_0, N_1)$, where the dependence on N_1 is linear. While this might seem as an impasse at this stage in the solution, evaluating λ_2 at $N_0 = N_0^*$ removes the dependence on N_1 and one is then able to get a three-term asymptotic approximation in (1.20) even though it is just the first term in the other expansion (1.19) that is available. If the calculations are taken to higher orders one finds that $\lambda_3 = \lambda_3(N_0, N_1, N_2)$ and the dependence on N_1 is now quadratic, whereas that on N_2 is linear. The stationarity condition $\partial\lambda_3/\partial N_1 = 0$ yields the critical value of N_1, say, N_1^*, and so on. In certain cases (e.g., see [42]) some variations of this strategy were found, in the sense that $\mu^{-1/4}$ rather than $\mu^{-1/2}$ entered in the expansion (1.20) and some of the coefficients λ_j in that formula were identically zero on evaluating them at $N_0 = N_0^*$. However, the quadratic and linear dependence already mentioned, as well as the partial derivative conditions demanded by the desired criticality, were recurring features in all of the examples studied.

1.4.3   Numerical strategies

Tension field theories do not require any special numerical techniques since the small thickness of the plates or shells to which they apply is left out. Finite element simulations have been used to study the wrinkling phenomena far away from the initial bifurcation point that marks their onset.

The problems discussed in this Thesis are governed by PDE's, which are subsequently reduced to ODE's via the customary normal-mode reduction in elastic stability (e.g., [3, 19, 119]). The traditional method of choice for solving boundary eigenvalue problems associated with ordinary differential equations is the *determinantal method* (e.g., see [65]). However, such approaches turn out to be ineffective when employed for problems with turning points; this is exactly the case when partial wrinkling is present. Such difficulties have been long recognised in other fields, although in Solid Mechanics these findings are much more recent (e.g., [106]). For example, in the Fluid Mechanics literature it has been known for some time that strategies based on the determinantal method are doomed to failure when used to solve the Orr-Sommerfeld equation (e.g., see [53]), an archetypal example of fourth-order differential equation with a turning point (although its nature is rather different from the kind of TP encountered in partial wrinkling). Haughton and Orr [66] reported similar difficulties when trying to solve the linearised eversion problem for hyperelastic cylindrical shells (incidentally their problem also features a turning point).

A more successful technique is the *compound matrix method* described succinctly in [53] and reviewed in considerably more detail by Lindsay and Rooney in [81]. The gist of this method is the introduction of some auxiliary variables that are subsequently found to satisfy an auxiliary higher-order linear system of differential equations that must be integrated so that a certain target condition is met at one of the endpoints of the integration range. Unfortunately, even this technique has its own limitations because the dimension of the auxiliary system tends to grow quickly. For example, for a fourth-order problem the auxiliary system contains six equations, while for one of sixth-order the system has twenty equations. While this is might still look reasonable from a practical point of view, matters get out of hand for higher-order equations, as for an eight-order problem one would have to integrate a system comprising seventy equations (even generating the relevant auxiliary equations is nothing short of a Herculean task). Particular details of the compound matrix calculations relevant to the problems of this Thesis appear in *Appendix B*.

Other methods that could be used to solve the eigenvalue problems in this Thesis include standard packages based on finite differences or collocation methods, such as the `Matlab` suite 'sbvp' [10] or the standard boundary-value solver 'bvp4c'. Before concluding our short account of the numerical procedures adopted in this Thesis, it is interesting to point out a different strategy that is usually insensitive to the presence of turning points and can be brought to bear on a whole range of situations involving linear bifurcations. This is rooted in the classical

perturbation method used extensively by Timoshenko and Gere [119] for simple beam and truss structures. Recently, Jillella and Peddeson [71] followed up on some remarks made by Coman in the introductory part of reference [37], and presented results obtained by this method for the radially stretched annulus analysed in [41, 47].

The key observation regarding this approach is that the linear elastic stability problem can be fictitiously perturbed by introducing an arbitrary imperfection, so that the governing equations take the form

$$\mathcal{M}[\boldsymbol{\Phi}] - \lambda \mathcal{N}[\boldsymbol{\Phi}] = \boldsymbol{f} \, , \tag{1.21}$$

where $\mathcal{M}$ and $\mathcal{N}$ are some differential operators and the equation is typically solved subject to homogeneous boundary conditions. Here λ plays the role of a loading parameter, while the *arbitrary* function $\boldsymbol{f}$ characterises the degree of imperfection; the unknown $\boldsymbol{\Phi}$ and the (fixed) right-hand side $\boldsymbol{f}$ are possibly multi-dimensional vector fields.

The original linear elastic stability problem corresponds to setting $\boldsymbol{f} \equiv \boldsymbol{0}$. If $\mathcal{N} = \mathcal{I}$ (the identity operator) and the eigenproblem has only a discrete (simple) spectrum consisting of an infinite sequence of numbers $\{\lambda_j\}_{j \geq 0}$, it is a standard fact that

$$\boldsymbol{\Phi} = \sum_{j=0}^{\infty} \frac{\beta_j}{\lambda - \lambda_j} \boldsymbol{\Phi}_j \, , \tag{1.22}$$

where $\{\boldsymbol{\Phi}_j\}_{j \geq 0}$ denotes the corresponding set of eigenfunctions and $\beta_j \in \mathbb{R}$ are uniquely determined by $\boldsymbol{f}$ (e.g., see [16]). In deriving the above expansion it was assumed that the eigenfunctions form a complete set, an issue that is far from trivial when the eigenproblem is not self-adjoint. It is obvious that as $\lambda \to \lambda_{j_0}^{\pm}$ then $\boldsymbol{\Phi} \to \infty$, irrespective of how small the right-hand side $\boldsymbol{f}$ is – a clear hallmark of structural instability. (The usual Fredholm solvability condition is not invoked here because the right-hand side in (1.21) is understood as being arbitrary; while it may be true that in some instances $\beta_{j_0} = 0$ and hence $\boldsymbol{\Phi}$ remains bounded as $\lambda \to \lambda_{j_0}$, this is an exceptional situation that one can choose to ignore in a general discussion.) In summary, within this context one sets out by fixing an arbitrary (constant) value for the right-hand side of (1.21), followed by solving the resulting boundary-value problem for a sequence of values of λ increasing from some reference value (usually, zero). The approach towards the first eigenvalue is signalled by a sharp increase of the L^2-norm of the solution and the inability of the computer code to go past a certain critical value of λ – this represents an approximation of the desired quantity (see Figure 7 of [36] where the technique was applied to the secondary bifurcations of a sandwich panel). Modifications of the underlying ideas presented above to the case when $\mathcal{N} \neq \mathcal{I}$ or the eigenvalues of the homogeneous version of (1.21) have higher multiplicity can be adapted from the general theory given by Collatz in [27].

1.5 A guide to the Thesis

The Thesis aims to probe further into some of the open questions that surface in relation to the literature reviewed above. Generally speaking this will involve studying a number of linear eigenvalue problems by using a mixture of both numerical and asymptotic techniques.

We start in *Chapter 2* with a full set of coordinate-free derivations of Föppl-von Kármán plate theory (FvK) and the associated buckling equations for a general anisotropic linear elastic plate. This set of equations is then adapted to the isotropic plate case, and a further case for plates subject to in-plane loading.

Then in *Chapter 3*, a *Hybrid Energy Method* is proposed for the wrinkling of rectangular and annular plates subject to tensile loads. The route taken here is based on the leading order (simplest) asymptotic approximations already obtained by Coman *et al.* [29, 41, 44, 47], but is rather different from the earlier studies since it employs a modified energy method akin to *Hybrid Galerkin Technique* (HGT) of Geer and Andersen [4, 5, 6]. It is shown that this strategy allows a more faithful description of the numerical simulations previously reported in the literature, even when the asymptotic parameter μ (which typically must be in the range 350.0 or larger for very thin plates) is relatively small ($\mu \simeq 50.0$). Strictly speaking this method requires that the asymptotic results for both large$-$ and small$-\mu$ regimes are available, which are then combined into some sort of composite ansatz that is used in the same spirit as in the classical Galerkin or Rayleigh-Ritz methods. Since our problems involve *asymmetric* instability patterns and are quite complicated, Geer and Andersen's ideas are not immediately applicable. Nevertheless, our modification of their strategy does perform remarkably well and suggests that this is an effective line of inquiry. Furthermore, motivated by the necessity of the small$-\mu$ asymptotic results in the HGT technique, we pursue the mathematical limit $\mu \to 0$ for the equation (1.15), for both circular and rectangular geometries. The asymptotic formulae obtained tend to perform well even for $\mu \simeq 2.0$, a case which strictly speaking falls outside the theoretical range of validity for the analysis carried out in §3.3.2. The presence of two interactive boundary layers also poses some interesting challenges. The work in this chapter has been published online [50].

In *Chapter 4* we consider a novel case of a bi-annular thin elastic plate, consisting of two concentric annuli made of different elastic materials and perfectly bonded together. It is the interface (discontinuity) between the two annuli, together with the piecewise-constant mechanical parameters, that arouse our interest, and introduce some new features to the bifurcation. Due to the asymptotic features (large parameter μ) of this problem, we first discuss the existence of compressive stresses in the pre-buckling state (limit case $\mu \to \infty$). Since the formulation of pre-bucking is much more transparent than the buckling problem, we apply both analytical and numerical analysis in order to shed light on the latter problem. It transpires that there are two types of lower bounds for external loading when compressive stresses first appear in the bi-annular region. Then, to solve the buckling problem, extensive numerical simulations are carried out by using numerical strategies of an adapted version of compound matrix method,

in conjugation with an collocation solver 'sbvp'. Because now there is an interface in the annulus, the numerical simulation becomes more demanding compared to the single-annular case. For example, the compound matrix approach requires special modifications for dealing with this non-trivial feature. As shown by Lindsay in [80] this strategy is eminently amenable to generalisations for layered continua, and we take advantage of his numerical scheme to carry out our simulations. Moreover, the application of a collocation solver involves transforming the three-point fourth-order boundary value problem into an eighth-order two-point boundary value problem, with an additional trivial differential equation by letting the derivative of the eigenvalue be zero, and a normalisation equation (nonlinear) to normalise the eigenfunction. Then the nonlinear collocation-based solver 'sbvp' (for general singular & nonlinear problems) in Matlab is used to solve the transformed nonlinear eigenvalue problem. In light of the new features obtained in the pre-buckling analysis (the limit case $\mu \to \infty$), the question arises as to whether there are similar behaviours for the NSE when μ is asymptotically large. The answer to this question turns out to be positive. Another interesting problem concerns the effects of discontinuities (introduced by the interface) on the NSE and the wrinkling modes. Is it possible that the wrinkling is still triggered near the inner boundary, or the interface, or that we have two localised wrinkles on both annuli? This is accomplished by pulling the above analyses together. Given the similarities between the problem treated in this chapter and the work [47], one would also expect that the asymptotic simplification of that reference could be transposed to the bi-annular plate. This expectation is indeed confirmed and allows us to apply WKB reduction on the fairly complex eigenvalue problems, together with the justification of the reduction of the boundary and continuity conditions. This work has been published in [82] and an additional paper was submitted for publication [48] which is currently under review.

In *Chapter 5* the original motivation comes from trying to establish whether there is any parallel between the *plane stress* situations involving the instabilities of the stretched annular plate [41, 47] and a particular *plane strain* scenario. This is accomplished by looking at an infinite cylinder subject to radial stretching on the two cylindrical surfaces. The FvK theory is of course no longer applicable, so it will have to be replaced by a more suitable model. In the interest of consistency with the earlier developments [41] in which the prebuckling stresses were those given by the Linear Elasticity Lamé solution, we consider a particular set of bifurcation equations based on a simplified theory of Biot [15] (these equations appear in Novozhilov's book [94] and have been used by other investigators without giving appropriate credit – e.g., [72]). While the main equations used in *Chapter 5* are not new, we give a novel tensor derivation that clarifies the assumptions introduced and we also present a new tensorial equation in which some of the simplifications are removed. The method of solution in that chapter mirrors to a certain extent the investigations for the stretched annulus, in the sense that the normal mode reduction leaves us with an eigenvalue problem in which we have the (unknown) mode number that has to be determined by minimising a relation of the form (1.16). Unlike in the

plate problem, this time there is no obvious asymptotic parameter present in the governing equations. But the main challenge in this problem comes from the fact that the second-order differential operators in the eigenvalue problems have variable coefficients and can exhibit loss of ellipticity in some regions of the annulus. This was not the case with the work based on (1.5) since the bi-Laplacian guarantees ellipticity, despite the fact that the membrane equations $(D = 0)$ are of mixed type when one of the principal stresses of $\mathring{\boldsymbol{N}}$ is negative. Also, now the topology of the response curves no longer resembles the familiar picture seen in the plane stress situations. Furthermore, because we are dealing with a traction boundary-value problem we have to account for the satisfaction of the Shapiro-Lopatinskij [54] condition which turns out to be violated in some cases. So the picture that emerges from our analysis strongly suggests that, at least for the particular St Venant-Kirchhoff constitutive law used here, the elastic instability involves either the critical mode number $n = 2$ or $n = \infty$. Strictly speaking, the latter is not exactly a form of structural instability but a manifestation of material failure. The work in this chapter has been published in [49].

In *Chapter 6*, some key results and remarks of this Thesis are summarised, followed by a brief description of potential further work.

Chapter 2

Föppl–von Kármán plate theory and bifurcation equations

In this chapter we will formulate the (Föppl–von Kármán) FvK equations and the corresponding bifurcation equations (both weak form and strong form with natural boundary conditions) for a thin plate of anisotropic linear elastic material by using a coordinate-free approach and the *Calculus of Variations* (CV) strategy as stated in §1.2.

As is well known, a plate is defined as a plane structural element with small thickness compared to the planar dimensions [118]. In Mechanics, plates theories reduce a three-dimensional problem into a two-dimensional problem by taking advantage of the disparity between the thickness and planar dimensions. Strictly speaking, all plate theories are approximate in terms of certain assumptions. In general, the more 'accurate' the theory is, the more demanding it becomes for solving it either numerically or analytically. For a given problem, it becomes a compromise to choose an appropriate plate theory between the accuracy and the calculation expense.

In this Thesis we will employ the classical Föppl–von Kármán (FvK) plate theory, as this has been repeatedly proven to be a versatile model able to well describe a wide variety of physical phenomena in thin planar structures (for example, see [8]).

Even though the derivation of this set of equations is available in a number of textbooks (such as [3, 19, 20, 26, 119]), it is still necessary to record here the full derivation based on the minimum energy principle (CV) for the following reasons:

- In the literature, the derivations of this set equations are limited to employing either Cartesian coordinates or polar coordinates;

- the plates are generally confined to isotropic or orthotropic elastic materials;

- the formulation is only in strong form based on the equilibrium criterion, and the derivations for boundary conditions are often left vague;

- the connections between this plate theory and three dimensional deformation are not clear.

In this chapter, the derivation is carried out in terms of tensorial algebra and Variational Principles. One of the merits is that it offers us the freedom in choosing particular coordinates for particular problems, as a tensorial derivation is used. Since no direct reference is made to rectangular or polar coordinates. In addition, mistakes in derivation can be avoided as far as possible due to the conciseness of the tensorial notation. Another advantage is, CV can furnish automatically the full set of boundary conditions once a variational structure for the loading is available. For example, in the derivation of interfacial conditions, this strategy helps us to circumvent the fallible continuity conditions, see *Chapter 4*.

This chapter is organised as follows. We first use CV to derive a set of governing equations for both the basic state (in §2.1) and the bifurcation state (in §2.2). The derivations of both weak forms and strong forms (together with their complementary boundary conditions) for both states are obtained in this process. Also, the material is assumed to be generally anisotropic elastic which is applicable to model anisotropic composite thin plates. This set of equations is then adapted to the isotropic linear elastic plate case (in §2.3), and a further case for plates subject to in-plane loading (as in §2.4) which will be used in *Chapter 3* (weak form) and *Chapter 4* (strong form).

2.1 Energy formulation on FvK equations

We assume a plate occupying the region $\Omega \times [-h/2, h/2]$, where $\Omega \subset \mathbb{R}^2$ is the midplane surface of the plate, h the thickness. Without losing generality, we use vector $\boldsymbol{x} + z\hat{\boldsymbol{n}}$ to describe the position of any point within the plate, where $\boldsymbol{x} \in \Omega$ denotes the projection of the point on the midplane, $\hat{\boldsymbol{n}}$ is the unit normal to the midplane. Notice that $\boldsymbol{x}$ is a two-dimensional vector with component form x_α, where the index α ranges over the value $\{1, 2\}$, and we do not follow any particular reference coordinate in the two-dimensional (midplane) region. The in-plane displacement is defined as $\boldsymbol{v} := (u, v)$. $z \in [-h/2, h/2]$ stands for the lateral coordinate with the corresponding displacement described by w.

For *thin* plates, the well-known Love–Kirchhoff hypothesis is customarily taken, which reduces the three-dimensional problem into a two-dimensional one by expressing the displacement field as

$$\boldsymbol{u} = \boldsymbol{v} - z\boldsymbol{\nabla}w + w\hat{\boldsymbol{n}}, \tag{2.1}$$

where $\boldsymbol{\nabla}$ is the two dimensional *gradient* operator on the in-plane surface, with component form $\nabla_\alpha, \alpha \in \{1, 2\}$. For thick plates, displacement field takes the form

$$\boldsymbol{u} = \boldsymbol{v} - f(z)\boldsymbol{\phi} + w\hat{\boldsymbol{n}},$$

where $\boldsymbol{\phi}$ is the bending rotation vector. For example, $f(z) = z$ is for the first-order shear deformation theory (Reissner-Mindlin [89, 102] plate theory). For higher-order shear deformation theories, Reddy [100] and Shi [112] assume

$$f(z) = z(1 - \frac{4z^2}{3h^2}) \qquad \text{and} \qquad f(z) = \frac{5}{4}z(1 - \frac{4z^2}{3h^2})$$

respectively.

In this work, we only take the displacement assumption (2.1) in classical plate theory for a thin plate. By taking the leading order terms, the Lagrange strain tensor is generally reduced to

$$\boldsymbol{E} \simeq (\boldsymbol{\nabla} \otimes \boldsymbol{v})^s + \frac{1}{2}(\boldsymbol{\nabla}w) \otimes (\boldsymbol{\nabla}w) - z\boldsymbol{\nabla} \otimes \boldsymbol{\nabla}w \,, \tag{2.2}$$

where the symmetric term $(\boldsymbol{\nabla} \otimes \boldsymbol{v})^s := (\boldsymbol{\nabla} \otimes \boldsymbol{v} + \boldsymbol{v} \otimes \boldsymbol{\nabla})/2$. Here, we introduce the stretching strain tensor $\boldsymbol{E}_s$ experienced by the midplane and the bending strain tensor $\boldsymbol{E}_b$ which is purely caused by the out-of-plane displacement.

$$\boldsymbol{E}_s := (\boldsymbol{\nabla} \otimes \boldsymbol{v})^s + \frac{1}{2}(\boldsymbol{\nabla}w) \otimes (\boldsymbol{\nabla}w) \,, \tag{2.3a}$$

$$\boldsymbol{E}_b := -z\boldsymbol{\nabla} \otimes \boldsymbol{\nabla}w \,, \tag{2.3b}$$

such that $\boldsymbol{E} = \boldsymbol{E}_s + \boldsymbol{E}_b$.

For a conservative system, the total potential energy $\mathcal{V}$ is composed of two parts: the potential energy of strains $\mathcal{E}$ and the potential of the external forces $\mathcal{V}_e$, namely,

$$\mathcal{V} = \mathcal{E} + \mathcal{V}_e \,, \tag{2.4}$$

which is the *weak form* for the equilibrium state. Here, another assumption for the FvK equations is: the plate undergoes large deflections but small strains such that the referential and spatial description can be assumed to coincide. If linear Hooke's law is assumed for the plate, the strain energy of a plate can be given by

$$\mathcal{E}(\boldsymbol{u}) := \frac{1}{2} \int_{\Omega \times h} \boldsymbol{E} : \mathbb{C} : \boldsymbol{E} \, \mathrm{d}V \,. \tag{2.5}$$

where $\mathbb{C}$ is a symmetric fourth-order stiffness tensor, with 6 independent components for general anisotropic linear elastic plates under plane stress deformation. If external forces do not change (both magnitude and directions) during the deformation, its potential energy takes the form

$$\mathcal{V}_e = -\int_{\Omega} pw \, \mathrm{d}A - \int_{\partial\Omega} (\boldsymbol{q} \cdot \boldsymbol{v} + R_n \nabla_n w + Vw) \, \mathrm{d}S \,, \tag{2.6}$$

where $\mathrm{d}A$ is the area element of the midplane, while $\mathrm{d}S$ represents the line element of the midplane's edge; p is the stress applied on the midplane; $\boldsymbol{q}$, R_n and V represent in-plane external

stresses, the moment loads (normal to the boundary) and the lateral shear forces applied on the boundary $\partial\Omega$. Indeed, the external loading assumed in (2.6) is only a specific case in the static problem, which can be easily adapted to other situations. For example, in dynamic analysis, we expect an additional kinetic energy term

$$\mathcal{V}_k = \frac{1}{2}\int_{\Omega\times h}\rho\dot{\boldsymbol{u}}\cdot\dot{\boldsymbol{u}}\,\mathrm{d}V\,,$$

where ρ is the density and $\dot{\boldsymbol{u}}$ represents the first derivative of $\boldsymbol{u}$ with respect to time. For this more general case, the CV for the dynamic analysis, is actually *Hamilton's principle*. However, in this Thesis, we only discuss static problems, and consider the kinetic term to be identically zero.

Substituting (2.3) into (2.5), the total strain energy is composed of bending energy and stretching energy $\mathcal{E} = \mathcal{E}_b + \mathcal{E}_s$, where the bending energy is given in the form below associated to the bending strain tensor

$$\mathcal{E}_b(\boldsymbol{u}) := \frac{1}{2}\int_{\Omega\times h}\boldsymbol{E}_b : \mathbb{C} : \boldsymbol{E}_b\,\mathrm{d}V = \frac{1}{2}\int_{\Omega}(\boldsymbol{\nabla}\otimes\boldsymbol{\nabla}w) : \mathbb{D} : (\boldsymbol{\nabla}\otimes\boldsymbol{\nabla}w)\,\mathrm{d}A\,, \qquad (2.7)$$

where $\mathbb{D}$ is the bending stiffness tensor of the plate

$$\mathbb{D} := \int_{-\frac{h}{2}}^{\frac{h}{2}} z^2\mathbb{C}\,\mathrm{d}z\,. \qquad (2.8)$$

If the elasticity coefficients do not vary with the thickness, then $\mathbb{D} = \mathbb{C}h^3/12$. Likewise, the stretching energy takes the form

$$\mathcal{E}_s(\boldsymbol{u}) := \frac{1}{2}\int_{\Omega\times h}\boldsymbol{E}_s : \mathbb{C} : \boldsymbol{E}_s\,\mathrm{d}V = \frac{1}{2}\int_{\Omega}\boldsymbol{E}_s : \mathbb{A} : \boldsymbol{E}_s\,\mathrm{d}A\,, \qquad (2.9)$$

by taking the membrane stiffness tensor $\mathbb{A}$ of the plate as

$$\mathbb{A} := \int_{-\frac{h}{2}}^{\frac{h}{2}} \mathbb{C}\,\mathrm{d}z\,, \qquad (2.10)$$

which takes the value $\mathbb{A} = h\mathbb{C}$ for the plates with material homogeneous in the lateral direction. Incidentally, there should be another 'coupling' energy term which couples the elongation and bending deformations. When the material is inhomogeneous in the lateral direction, this term should be considered, such as laterally layered plates or laterally functionally graded plates (e.g., see [92]). However, for a thin plate with mechanical properties constant in the thickness direction, the coupling stiffness tensor becomes $\int_{-\frac{h}{2}}^{\frac{h}{2}} z\mathbb{C}\,\mathrm{d}z = 0\mathbb{C}$, and thus this coupling energy term can be omitted. It is the latter assumption that is made for the derivations hereafter.

Next, we shall take the principle of minimum potential energy in terms of the CV to formulate the problem, and we will use the following definitions for the the first and second

variations hereafter

$$\delta\mathcal{E}(\mathring{\boldsymbol{u}})[\boldsymbol{u}_1] := \frac{\partial}{\partial\varepsilon}\mathcal{E}(\mathring{\boldsymbol{u}}+\varepsilon\boldsymbol{u}_1)\Big|_{\varepsilon=0}, \qquad \delta^2\mathcal{E}(\mathring{\boldsymbol{u}})[\boldsymbol{u}_1,\boldsymbol{u}_1] := \frac{\partial^2}{\partial\varepsilon^2}\mathcal{E}(\mathring{\boldsymbol{u}}+\varepsilon\boldsymbol{u}_1)\Big|_{\varepsilon=0}. \qquad (2.11)$$

To start, we consider the equilibrium of basic state, which requires $\delta\mathcal{E} = 0$. Here, we use '$\circ$' to denote the variables in the basic state. We assume that the configuration of the plate is described by $\mathring{\boldsymbol{u}} = \mathring{\boldsymbol{v}} + \mathring{w}\hat{\boldsymbol{n}}$. If we give an arbitrary variation to this configuration, $\mathring{\boldsymbol{u}} \to \mathring{\boldsymbol{u}}+\varepsilon\boldsymbol{u}_1$, where, $\boldsymbol{u}_1 = \boldsymbol{v}_1 + w_1\hat{\boldsymbol{n}}$, we can have both the first and second variation of potential energy by means of the definitions (2.11). The equilibrium of the plate (in basic state) is given by $\delta\mathcal{E}[\boldsymbol{u}_1] = 0$, where $\delta\mathcal{E} = \delta\mathcal{E}_b + \delta\mathcal{E}_s$.

From (2.7) we have

$$\delta\mathcal{E}_b(\mathring{\boldsymbol{u}})[\boldsymbol{u}_1] = \int_\Omega \mathring{\boldsymbol{M}} : (\boldsymbol{\nabla}\otimes\boldsymbol{\nabla}w_1)\,\mathrm{d}A\,,$$

where $\mathring{\boldsymbol{M}} := (\boldsymbol{\nabla}\otimes\boldsymbol{\nabla}\mathring{w}) : \mathbb{D} = \mathbb{D} : (\boldsymbol{\nabla}\otimes\boldsymbol{\nabla}\mathring{w})$ is the bending tensor of the plate, which is a symmetric tensor. Recalling the identity

$$\boldsymbol{\nabla}\cdot(\boldsymbol{T}\cdot\boldsymbol{a}) = (\boldsymbol{\nabla}\cdot\boldsymbol{T})\cdot\boldsymbol{a} + \boldsymbol{T}:(\boldsymbol{\nabla}\otimes\boldsymbol{a})\,, \qquad (2.12)$$

which holds for any second-order tensor $\boldsymbol{T}$ and vector $\boldsymbol{a}$, if we treat $\boldsymbol{\nabla}w_1$ as $\boldsymbol{a}$, then

$$\delta\mathcal{E}_b(\mathring{\boldsymbol{u}})[\boldsymbol{u}_1] = \int_\Omega \left[\boldsymbol{\nabla}\cdot(\mathring{\boldsymbol{M}}\cdot\boldsymbol{\nabla}w_1) - (\boldsymbol{\nabla}\cdot\mathring{\boldsymbol{M}})\cdot\boldsymbol{\nabla}w_1\right]\mathrm{d}A$$

$$= \int_{\partial\Omega} \mathring{\boldsymbol{M}}\cdot\boldsymbol{\nabla}w_1\cdot\boldsymbol{n}\,\mathrm{d}S - \int_\Omega (\boldsymbol{\nabla}\cdot\mathring{\boldsymbol{M}})\cdot\boldsymbol{\nabla}w_1\,\mathrm{d}A, \quad (2.13)$$

where, it is apparent that $\mathring{\boldsymbol{M}}\cdot\boldsymbol{\nabla}w_1\cdot\boldsymbol{n} = \mathring{\boldsymbol{M}}\cdot\boldsymbol{n}\cdot\boldsymbol{\nabla}w_1$ due to the symmetry of $\mathring{\boldsymbol{M}}$. In order to simplify the first term further, it helps to introduce the local system of basis vectors $\{\boldsymbol{n}, \boldsymbol{s}\}$ attached to the boundary $\partial\Omega$. Then, $\mathring{\boldsymbol{M}}\cdot\boldsymbol{n}$ can be decomposed into *bending moment* $\mathring{M}_b$ and *twisting moment* $\mathring{M}_t$

$$\mathring{M}_b := \mathring{\boldsymbol{M}} : (\boldsymbol{n}\otimes\boldsymbol{n}) = (\boldsymbol{\nabla}\otimes\boldsymbol{\nabla}\mathring{w}):\mathbb{D}:(\boldsymbol{n}\otimes\boldsymbol{n})\,, \qquad (2.14a)$$

$$\mathring{M}_t := \mathring{\boldsymbol{M}} : (\boldsymbol{n}\otimes\boldsymbol{s}) = (\boldsymbol{\nabla}\otimes\boldsymbol{\nabla}\mathring{w}):\mathbb{D}:(\boldsymbol{n}\otimes\boldsymbol{s})\,. \qquad (2.14b)$$

Furthermore, the two-dimensional gradient operator $\boldsymbol{\nabla}$ can be rewritten in the form

$$\boldsymbol{\nabla} := \boldsymbol{n}\frac{\partial}{\partial n} + \boldsymbol{s}\frac{\partial}{\partial s} := \boldsymbol{n}\nabla_n + \boldsymbol{s}\nabla_s\,.$$

so, $\boldsymbol{\nabla}\mathring{w} = \boldsymbol{n}\nabla_n\mathring{w} + \boldsymbol{s}\nabla_s\mathring{w}$. Here we assume that the boundary $\partial\Omega$ is made of closed curves, then by using the identity (A.8) recorded in *Appendix A*, we have

$$\oint_{\partial\Omega} \mathring{\boldsymbol{M}}\cdot\boldsymbol{n}\cdot\boldsymbol{\nabla}w_1\,\mathrm{d}S = \oint_{\partial\Omega}\left\{\left[\mathring{\boldsymbol{M}}:(\boldsymbol{n}\otimes\boldsymbol{n})\right](\boldsymbol{\nabla}w_1\cdot\boldsymbol{n}) + \left[\mathring{\boldsymbol{M}}:(\boldsymbol{n}\otimes\boldsymbol{s})\right](\boldsymbol{\nabla}w_1\cdot\boldsymbol{s})\right\}\mathrm{d}S$$

$$= \oint_{\partial\Omega} \left[\mathring{\boldsymbol{M}} : (\boldsymbol{n} \otimes \boldsymbol{n}) \right] (\boldsymbol{\nabla} w_1 \cdot \boldsymbol{n}) \, \mathrm{d}S - \oint_{\partial\Omega} \boldsymbol{\nabla} \left[\mathring{\boldsymbol{M}} : (\boldsymbol{n} \otimes \boldsymbol{s}) \right] \cdot \boldsymbol{s} \, w_1 \, \mathrm{d}S$$

where,

$$\boldsymbol{\nabla} \left[\mathring{\boldsymbol{M}} : (\boldsymbol{n} \otimes \boldsymbol{s}) \right] \cdot \boldsymbol{s} = \boldsymbol{\nabla} \left\{ \mathbb{D} \vdots \left[(\boldsymbol{\nabla} \otimes \boldsymbol{\nabla}\mathring{w}) \otimes \boldsymbol{n} \otimes \boldsymbol{s} \right] \right\} \cdot \boldsymbol{s} \,,$$

hereafter, we introduce ':' and '$\vdots$' which stand for the triple and quadruple contractions respectively; for their definitions see *Appendix A*.

The second term on the right hand side of (2.13) can be transformed further using the *Divergence Theorem*

$$\int_\Omega (\phi \boldsymbol{\nabla} \cdot \boldsymbol{a} + \boldsymbol{a} \cdot \boldsymbol{\nabla}\phi) \, \mathrm{d}A = \int_{\partial\Omega} (\boldsymbol{a} \cdot \boldsymbol{n})\phi \, \mathrm{d}S \,. \tag{2.15}$$

By letting $\boldsymbol{\nabla} \cdot \mathring{\boldsymbol{M}} \to \boldsymbol{a}$ and $w_1 \to \phi$, we find that

$$\int_\Omega (\boldsymbol{\nabla} \cdot \mathring{\boldsymbol{M}}) \cdot \boldsymbol{\nabla} w_1 \, \mathrm{d}A = \int_{\partial\Omega} \left[(\boldsymbol{\nabla} \cdot \mathring{\boldsymbol{M}}) \cdot \boldsymbol{n} \right] w_1 \, \mathrm{d}S - \int_\Omega \left[\boldsymbol{\nabla} \cdot (\boldsymbol{\nabla} \cdot \mathring{\boldsymbol{M}}) \right] w_1 \, \mathrm{d}A \,.$$

Here,

$$\boldsymbol{\nabla} \cdot \mathring{\boldsymbol{M}} = \boldsymbol{\nabla} \cdot \left[\mathbb{D} : (\boldsymbol{\nabla} \otimes \boldsymbol{\nabla}\mathring{w}) \right] = \mathbb{D} \vdots (\boldsymbol{\nabla} \otimes \boldsymbol{\nabla} \otimes \boldsymbol{\nabla}\mathring{w})$$

and

$$\boldsymbol{\nabla} \cdot (\boldsymbol{\nabla} \cdot \mathring{\boldsymbol{M}}) = \boldsymbol{\nabla} \cdot \left\{ \boldsymbol{\nabla} \cdot \left[\mathbb{D} : (\boldsymbol{\nabla} \otimes \boldsymbol{\nabla}\mathring{w}) \right] \right\} = \mathbb{D} \vdots (\boldsymbol{\nabla} \otimes \boldsymbol{\nabla} \otimes \boldsymbol{\nabla} \otimes \boldsymbol{\nabla}\mathring{w}) \,,$$

which are valid for any constant stiffness tensor $\mathbb{D}$ for a general linear elastic material. Therefore, the bending energy in (2.7) yields

$$\delta\mathcal{E}_b(\mathring{\boldsymbol{u}})[\boldsymbol{u}_1] = \int_{\partial\Omega} \left\{ \mathring{\boldsymbol{M}} \cdot \boldsymbol{n} \cdot \boldsymbol{\nabla} w_1 - \left[\mathbb{D} \vdots (\boldsymbol{\nabla} \otimes \boldsymbol{\nabla} \otimes \boldsymbol{\nabla}\mathring{w}) \right] \cdot \boldsymbol{n} w_1 \right\} \mathrm{d}S + \int_\Omega \mathbb{D} \vdots (\boldsymbol{\nabla} \otimes \boldsymbol{\nabla} \otimes \boldsymbol{\nabla} \otimes \boldsymbol{\nabla}\mathring{w}) w_1 \, \mathrm{d}A \,. \tag{2.16}$$

Next we shall consider $\delta\mathcal{E}_s(\mathring{\boldsymbol{u}})[\boldsymbol{u}_1]$. When applying an arbitrary variation $\boldsymbol{u}_1$ onto $\mathring{\boldsymbol{u}} \to \mathring{\boldsymbol{u}} + \varepsilon\boldsymbol{u}_1$ ($\boldsymbol{u}_1 = \boldsymbol{v}_1 + w_1\hat{\boldsymbol{n}}$), the stretching strain becomes

$$\boldsymbol{E}_s = \mathring{\boldsymbol{E}}_s + \varepsilon\boldsymbol{E}_{s1} + \varepsilon^2 \boldsymbol{E}_{s2} + \cdots \,,$$

where, '$\cdots$' stands for the higher-order terms, and

$$\mathring{\boldsymbol{E}}_s := (\boldsymbol{\nabla} \otimes \mathring{\boldsymbol{v}})^s + \frac{1}{2}(\boldsymbol{\nabla}\mathring{w}) \otimes (\boldsymbol{\nabla}\mathring{w}) \,,$$

$$\boldsymbol{E}_{s1} := (\boldsymbol{\nabla} \otimes \boldsymbol{v}_1)^s + [(\boldsymbol{\nabla}\mathring{w}) \otimes (\boldsymbol{\nabla} w_1)]^s \,,$$

$$\boldsymbol{E}_{s2} := \frac{1}{2}(\boldsymbol{\nabla} w_1) \otimes (\boldsymbol{\nabla} w_1) \,.$$

Taking the first variation of the stretching energy (2.9) in terms of the definition in $(2.11)_1$ we

have

$$\delta\mathcal{E}_s(\mathring{\boldsymbol{u}})[\boldsymbol{u}_1] = \int_\Omega \mathring{\boldsymbol{E}}_s : \mathbb{A} : \boldsymbol{E}_{s1}\,\mathrm{d}A = \int_\Omega \left[\mathring{\boldsymbol{N}} : (\boldsymbol{\nabla}\otimes\boldsymbol{v}_1)^s + \mathring{\boldsymbol{N}} : (\boldsymbol{\nabla}\mathring{w}\otimes\boldsymbol{\nabla}w_1)^s\right]\,\mathrm{d}A\,, \quad (2.17)$$

where, we have introduced the symmetric tensor $\mathring{\boldsymbol{N}} := \mathring{\boldsymbol{E}}_s : \mathbb{A} = \mathbb{A} : \mathring{\boldsymbol{E}}_s$, which is the membrane stress tensor in the basic state. Notice that for a general symmetric second-order tensor $\boldsymbol{T}$, we have

$$\boldsymbol{T} : (\boldsymbol{a}\otimes\boldsymbol{b})^s = \boldsymbol{T} : (\boldsymbol{a}\otimes\boldsymbol{b}) = \boldsymbol{T} : (\boldsymbol{b}\otimes\boldsymbol{a}) = (\boldsymbol{T}\cdot\boldsymbol{b})\cdot\boldsymbol{a} = (\boldsymbol{T}\cdot\boldsymbol{a})\cdot\boldsymbol{b}\,, \quad (2.18)$$

which is valid for any vectors $\boldsymbol{a}$ and $\boldsymbol{b}$. So, we can drop the symmetric superscript in (2.17). By using the identity (2.12),

$$\int_\Omega \mathring{\boldsymbol{N}} : (\boldsymbol{\nabla}\otimes\boldsymbol{v}_1)\,\mathrm{d}A = \int_\Omega \left[\boldsymbol{\nabla}\cdot(\mathring{\boldsymbol{N}}\cdot\boldsymbol{v}_1) - (\boldsymbol{\nabla}\cdot\mathring{\boldsymbol{N}})\cdot\boldsymbol{v}_1\right]\,\mathrm{d}A$$

$$= \int_{\partial\Omega} (\mathring{\boldsymbol{N}}\cdot\boldsymbol{v}_1)\cdot\boldsymbol{n}\,\mathrm{d}S - \int_\Omega (\boldsymbol{\nabla}\cdot\mathring{\boldsymbol{N}})\cdot\boldsymbol{v}_1\,\mathrm{d}A\,,$$

where $(\mathring{\boldsymbol{N}}\cdot\boldsymbol{v}_1)\cdot\boldsymbol{n} = (\mathring{\boldsymbol{N}}\cdot\boldsymbol{n})\cdot\boldsymbol{v}_1$, since $\mathring{\boldsymbol{N}} = \mathring{\boldsymbol{N}}^T$. Repeated application of the identity (2.18) and the *Divergence Theorem* (2.15) yields

$$\int_\Omega \mathring{\boldsymbol{N}} : (\boldsymbol{\nabla}\mathring{w}\otimes\boldsymbol{\nabla}w_1)\,\mathrm{d}A = \int_\Omega (\mathring{\boldsymbol{N}}\cdot\boldsymbol{\nabla}\mathring{w})\cdot\boldsymbol{\nabla}w_1\,\mathrm{d}A$$

$$= \int_{\partial\Omega} \left[(\mathring{\boldsymbol{N}}\cdot\boldsymbol{\nabla}\mathring{w})\cdot\boldsymbol{n}\right]w_1\,\mathrm{d}S - \int_\Omega \left[\boldsymbol{\nabla}\cdot(\mathring{\boldsymbol{N}}\cdot\boldsymbol{\nabla}\mathring{w})\right]w_1\,\mathrm{d}A\,.$$

Furthermore, the variation of the external loading base on (2.6) becomes

$$\delta\mathcal{V}_e = -\int_\Omega pw_1\,\mathrm{d}A - \int_{\partial\Omega} (\boldsymbol{q}\cdot\boldsymbol{v}_1 + R_n\nabla_n w_1 + Vw_1)\,\mathrm{d}S\,. \quad (2.19)$$

If we sum up (2.16), (2.17) and (2.19), the equilibrium of the system requires

$$\delta\mathcal{E}(\mathring{\boldsymbol{u}})[\boldsymbol{u}_1] = \int_\Omega \left\{\left[\mathbb{D}\vdots(\boldsymbol{\nabla}\otimes\boldsymbol{\nabla}\otimes\boldsymbol{\nabla}\otimes\boldsymbol{\nabla}\mathring{w}) - \boldsymbol{\nabla}\cdot(\mathring{\boldsymbol{N}}\cdot\boldsymbol{\nabla}\mathring{w}) - q\right]w_1 - (\boldsymbol{\nabla}\cdot\mathring{\boldsymbol{N}})\cdot\boldsymbol{v}_1\right\}\,\mathrm{d}A$$

$$(2.20a)$$

$$+ \int_{\partial\Omega} \left\{\left[(\mathring{\boldsymbol{N}}\cdot\boldsymbol{\nabla}\mathring{w} - \mathbb{D}\vdots(\boldsymbol{\nabla}\otimes\boldsymbol{\nabla}\otimes\boldsymbol{\nabla}\mathring{w}))\cdot\boldsymbol{n} - \boldsymbol{\nabla}\big(\mathbb{D}\vdots(\boldsymbol{\nabla}\otimes\boldsymbol{\nabla}\mathring{w}\otimes\boldsymbol{n}\otimes\boldsymbol{s})\big)\cdot\boldsymbol{s} - V\right]w_1\right.$$

$$\left. + (\mathring{\boldsymbol{N}}\cdot\boldsymbol{n} - \boldsymbol{q})\cdot\boldsymbol{v}_1 + \left[\mathring{\boldsymbol{M}} : (\boldsymbol{n}\otimes\boldsymbol{n})(\boldsymbol{\nabla}w_1\cdot\boldsymbol{n}) - R_n\right]\cdot\boldsymbol{\nabla}w_1\right\}\,\mathrm{d}S = 0\,. \quad (2.20b)$$

Using standard variational calculus arguments, we can obtain the equilibrium equation (*strong form*) for the basic state from (2.20a), and the associated boundary conditions from (2.20b), corresponding to the *weak form* (2.4) for equilibrium. Due to the arbitrariness of the $\boldsymbol{v}_1$ and

w_1, the equilibrium equations for the basic state can be cast as

$$\mathbb{D} \vdots (\boldsymbol{\nabla} \otimes \boldsymbol{\nabla} \otimes \boldsymbol{\nabla} \otimes \boldsymbol{\nabla} \mathring{w}) - \boldsymbol{\nabla} \cdot (\mathring{\boldsymbol{N}} \cdot \boldsymbol{\nabla} \mathring{w}) = p \,, \tag{2.21a}$$

$$\boldsymbol{\nabla} \cdot \mathring{\boldsymbol{N}} = \boldsymbol{0} \,, \tag{2.21b}$$

where, in (2.21a), we notice that

$$\boldsymbol{\nabla} \cdot (\mathring{\boldsymbol{N}} \cdot \boldsymbol{\nabla} \mathring{w}) = (\boldsymbol{\nabla} \cdot \mathring{\boldsymbol{N}}) \cdot \boldsymbol{\nabla} \mathring{w} + \mathring{\boldsymbol{N}} : (\boldsymbol{\nabla} \otimes \boldsymbol{\nabla} \mathring{w}) = \mathring{\boldsymbol{N}} : (\boldsymbol{\nabla} \otimes \boldsymbol{\nabla} \mathring{w}) \,.$$

because of (2.21b). This set of coupled equations (2.21) is frequently used as an alternative form of von Kármán equations, and is valid for anisotropic linear elastic plates.

To obtain the boundary conditions from (2.20b), we need to employ the decompositions again. For example, we can decompose $\boldsymbol{v}$ in terms of $\boldsymbol{n}, \boldsymbol{s}$ by letting $v_n = \boldsymbol{v} \cdot \boldsymbol{n}$ while $v_s = \boldsymbol{v} \cdot \boldsymbol{s}$ (same decomposition applies for $\boldsymbol{q}$). Also, $\mathring{\boldsymbol{N}} \cdot \boldsymbol{n}$ can be decomposed into two components in $\boldsymbol{n}$ and $\boldsymbol{s}$ directions along the boundary $\partial\Omega$, namely, the *normal resultant* $\mathring{N}_n$ and the *shear resultant* $\mathring{N}_n$ (recalling the identity (2.18), for example, $\mathring{\boldsymbol{N}} : (\boldsymbol{n} \otimes \boldsymbol{s}) = \mathring{\boldsymbol{N}} \cdot \boldsymbol{n} \cdot \boldsymbol{s}$)

$$\mathring{N}_n := \mathring{\boldsymbol{N}} : (\boldsymbol{n} \otimes \boldsymbol{n}) = \left[(\boldsymbol{\nabla} \otimes \mathring{\boldsymbol{v}})^s + \frac{1}{2} (\boldsymbol{\nabla} \mathring{w}) \otimes (\boldsymbol{\nabla} \mathring{w}) \right] : \mathbb{A} : (\boldsymbol{n} \otimes \boldsymbol{n}) \,, \tag{2.22a}$$

$$\mathring{N}_s := \mathring{\boldsymbol{N}} : (\boldsymbol{n} \otimes \boldsymbol{s}) = \left[(\boldsymbol{\nabla} \otimes \mathring{\boldsymbol{v}})^s + \frac{1}{2} (\boldsymbol{\nabla} \mathring{w}) \otimes (\boldsymbol{\nabla} \mathring{w}) \right] : \mathbb{A} : (\boldsymbol{n} \otimes \boldsymbol{s}) \,. \tag{2.22b}$$

By applying the standard calculus of variation arguments to (2.20b), we can deduce the following boundary conditions on the boundary $\partial\Omega$ (or some disjoint parts of it)

$$\text{either} \quad \mathring{N}_n = q_n \quad \text{or} \quad \mathring{v}_n \quad \text{specified} \,, \tag{2.23a}$$

$$\text{either} \quad \mathring{N}_s = q_s \quad \text{or} \quad \mathring{v}_s \quad \text{specified} \,, \tag{2.23b}$$

$$\text{either} \quad \mathring{M}_b = R_n \quad \text{or} \quad \frac{\partial \mathring{w}}{\partial n} \quad \text{specified} \,, \tag{2.23c}$$

$$\text{either} \quad \mathring{S}_v = V \quad \text{or} \quad \mathring{w} \quad \text{specified} \,, \tag{2.23d}$$

where $\mathring{S}_v := \left[\mathring{\boldsymbol{N}} \cdot \boldsymbol{\nabla} \mathring{w} - \mathbb{D} \vdots (\boldsymbol{\nabla} \otimes \boldsymbol{\nabla} \otimes \boldsymbol{\nabla} \mathring{w}) \right] \cdot \boldsymbol{n} - \boldsymbol{\nabla} \left\{ \mathbb{D} \vdots \left[(\boldsymbol{\nabla} \otimes \boldsymbol{\nabla} \mathring{w}) \otimes \boldsymbol{n} \otimes \boldsymbol{s} \right] \right\} \cdot \boldsymbol{s}$ is the *vertical shear force* along the boundary.

2.2 Bifurcation equations

As mentioned earlier in §1.2, the stability of a conservative system is indicated by the second variation of the total potential energy. With the application of $(2.11)_2$ on the bending energy

(2.7), we obtain

$$\delta^2 \mathcal{E}_b(\mathring{\boldsymbol{u}})[\boldsymbol{u}_1, \boldsymbol{u}_1] = \int_\Omega (\boldsymbol{\nabla} \otimes \boldsymbol{\nabla} w_1) : \mathbb{D} : (\boldsymbol{\nabla} \otimes \boldsymbol{\nabla} w_1) \, \mathrm{d}A \,, \tag{2.24}$$

while for the stretching part as in (2.9), we have

$$\delta^2 \mathcal{E}_s(\mathring{\boldsymbol{u}})[\boldsymbol{u}_1, \boldsymbol{u}_1] = \int_\Omega \left(2\mathring{\boldsymbol{E}}_s : \mathbb{A} : \boldsymbol{E}_{s2} + \boldsymbol{E}_{s1} : \mathbb{A} : \boldsymbol{E}_{s1} \right) \mathrm{d}A$$

$$= \int_\Omega \mathring{\boldsymbol{N}} : (\boldsymbol{\nabla} w_1 \otimes \boldsymbol{\nabla} w_1) \, \mathrm{d}A + \int_\Omega \boldsymbol{N}_1 : (\boldsymbol{\nabla} \otimes \boldsymbol{v}_1 + \boldsymbol{\nabla} \mathring{w} \otimes \boldsymbol{\nabla} w_1)^s \, \mathrm{d}A \,, \quad (2.25)$$

where $\boldsymbol{N}_1 := \mathbb{A} : \boldsymbol{E}_{s1} = \mathbb{A} : (\boldsymbol{\nabla} \otimes \boldsymbol{v}_1 + \boldsymbol{\nabla} \mathring{w} \otimes \boldsymbol{\nabla} w_1)^s$. While for the second variation of the potential energy of external load is zero in light of (2.6), namely, $\delta^2 \mathcal{V}_e \equiv 0$. Summing up (2.24) and (2.25) we have the *weak form* of the bifurcation equation

$$\delta^2 \mathcal{V}(\mathring{\boldsymbol{u}})[\boldsymbol{u}_1, \boldsymbol{u}_1] = \int_\Omega \Big[(\boldsymbol{\nabla} \otimes \boldsymbol{\nabla} w_1) : \mathbb{D} : (\boldsymbol{\nabla} \otimes \boldsymbol{\nabla} w_1)$$

$$+ \mathring{\boldsymbol{N}} : (\boldsymbol{\nabla} w_1 \otimes \boldsymbol{\nabla} w_1) + \boldsymbol{N}_1 : (\boldsymbol{\nabla} \otimes \boldsymbol{v}_1 + \boldsymbol{\nabla} \mathring{w} \otimes \boldsymbol{\nabla} w_1)^s \Big] \mathrm{d}A \equiv 0 \,. \quad (2.26)$$

In order to obtain the neutral stability (critical buckling) state $\mathring{\boldsymbol{u}}$ and $\boldsymbol{u}_1$, we should have $\delta \left\{ \delta^2 \mathcal{E}(\mathring{\boldsymbol{u}}_C, \boldsymbol{u}_{1C}) \right\} [\delta \boldsymbol{u}_1] = 0$ according to the Trefftz criterion. Here, $\delta \boldsymbol{u}_1$ is the variation given to $\boldsymbol{u}_1$, namely, $\boldsymbol{u}_1 = \boldsymbol{v}_1 + w_1 \hat{\boldsymbol{n}} \to \boldsymbol{u}_1 = \boldsymbol{v}_1 + \varepsilon \delta \boldsymbol{v}_1 + (w_1 + \varepsilon \delta w_1) \hat{\boldsymbol{n}}$. By considering (2.24) in terms of $(2.11)_2$, we obtain

$$\delta \left\{ \delta^2 \mathcal{E}_b(\mathring{\boldsymbol{u}}, \boldsymbol{u}_1) \right\} [\delta \boldsymbol{u}_1] = 2 \int_{\partial\Omega} \left\{ \boldsymbol{M}_1 \cdot \boldsymbol{n} \cdot \boldsymbol{\nabla} \delta w_1 - \left[\mathbb{D} \vdots (\boldsymbol{\nabla} \otimes \boldsymbol{\nabla} \otimes \boldsymbol{\nabla} w_1) \right] \cdot \boldsymbol{n} \delta w_1 \right\} \mathrm{d}S$$

$$+ 2 \int_\Omega \mathbb{D} \vdots (\boldsymbol{\nabla} \otimes \boldsymbol{\nabla} \otimes \boldsymbol{\nabla} \otimes \boldsymbol{\nabla} w_1) \delta w_1 \, \mathrm{d}A \,. \quad (2.27)$$

where $\boldsymbol{M}_1 := \mathbb{D} : (\boldsymbol{\nabla} \otimes \boldsymbol{\nabla} w_1)$ is the linear term of bending tensor caused by the variation $\delta \boldsymbol{u}_1$, and the first term can be decomposed further following similar procedure after (2.13). Here we omit this for simplicity. The stretching part in (2.25) becomes

$$\delta \left\{ \delta^2 \mathcal{E}_s(\mathring{\boldsymbol{u}}, \boldsymbol{u}_1) \right\} [\delta \boldsymbol{u}_1] = 2 \int_{\partial\Omega} \left[(\boldsymbol{N}_1 \cdot \delta \boldsymbol{v}_1) \cdot \boldsymbol{n} + (\mathring{\boldsymbol{N}} \cdot \boldsymbol{\nabla} w_1 + \boldsymbol{N}_1 \cdot \boldsymbol{\nabla} \mathring{w}) \cdot \boldsymbol{n} \delta w_1 \right] \mathrm{d}S$$

$$- 2 \int_\Omega \left\{ (\boldsymbol{\nabla} \cdot \boldsymbol{N}_1) \cdot \delta \boldsymbol{v}_1 + \left[\boldsymbol{\nabla} \cdot (\mathring{\boldsymbol{N}} \cdot \boldsymbol{\nabla} w_1) + \boldsymbol{\nabla} \cdot (\boldsymbol{N}_1 \cdot \boldsymbol{\nabla} \mathring{w}) \right] \delta w_1 \right\} \mathrm{d}A \,. \quad (2.28)$$

Summing up (2.27) and (2.28) we have

$$\delta \left\{ \delta^2 \mathcal{E}(\mathring{\boldsymbol{u}}, \boldsymbol{u}_1) \right\} [\delta \boldsymbol{u}_1] = 2 \int_\Omega \left[\Gamma \delta w_1 - (\boldsymbol{\nabla} \cdot \boldsymbol{N}_1) \cdot \delta \boldsymbol{v}_1 \right] \mathrm{d}A \tag{2.29a}$$

$$+ 2 \int_{\partial\Omega} \left\{ (\boldsymbol{\chi} \cdot \boldsymbol{n} - \boldsymbol{\zeta} \cdot \boldsymbol{s}) \delta w_1 + \boldsymbol{N}_1 \cdot \boldsymbol{n} \cdot \delta \boldsymbol{v}_1 + \boldsymbol{M}_1 : (\boldsymbol{n} \otimes \boldsymbol{n}) \left[\boldsymbol{\nabla}(\delta w_1) \cdot \boldsymbol{n} \right] \right\} \mathrm{d}S \,, \quad (2.29b)$$

where

$$\Gamma := \mathbb{D} \vdots (\boldsymbol{\nabla} \otimes \boldsymbol{\nabla} \otimes \boldsymbol{\nabla} \otimes \boldsymbol{\nabla} w_1) - \boldsymbol{\nabla} \cdot (\mathring{\boldsymbol{N}} \cdot \boldsymbol{\nabla} w_1) - \boldsymbol{\nabla} \cdot (\boldsymbol{N}_1 \cdot \boldsymbol{\nabla} \mathring{w}) \,,$$

$$\boldsymbol{\chi} := \mathring{\boldsymbol{N}} \cdot \boldsymbol{\nabla} w_1 + \boldsymbol{N}_1 \cdot \boldsymbol{\nabla} \mathring{w} - \mathbb{D} \vdots (\boldsymbol{\nabla} \otimes \boldsymbol{\nabla} \otimes \boldsymbol{\nabla} w_1) \,,$$

$$\boldsymbol{\zeta} := \boldsymbol{\nabla} \big[\mathbb{D} \vdots (\boldsymbol{\nabla} \otimes \boldsymbol{\nabla} w_1 \otimes \boldsymbol{n} \otimes \boldsymbol{s}) \big] \,.$$

Similarly, we have

$$\boldsymbol{\nabla} \cdot (\mathring{\boldsymbol{N}} \cdot \boldsymbol{\nabla} w_1) = \mathring{\boldsymbol{N}} : (\boldsymbol{\nabla} \otimes \boldsymbol{\nabla} w_1) \quad \text{and} \quad \boldsymbol{\nabla} \cdot (\boldsymbol{N}_1 \cdot \boldsymbol{\nabla} \mathring{w}) = \boldsymbol{N}_1 : (\boldsymbol{\nabla} \otimes \boldsymbol{\nabla} \mathring{w}) \,.$$

Using some basic arguments in calculus of variations we arrive at the coupled governing equation (*strong form*) for bifurcation based on (2.29a)

$$\mathbb{D} \vdots (\boldsymbol{\nabla} \otimes \boldsymbol{\nabla} \otimes \boldsymbol{\nabla} \otimes \boldsymbol{\nabla} w_1) - \mathring{\boldsymbol{N}} : (\boldsymbol{\nabla} \otimes \boldsymbol{\nabla} w_1) - \boldsymbol{N}_1 : (\boldsymbol{\nabla} \otimes \boldsymbol{\nabla} \mathring{w}) = 0 \,, \tag{2.30a}$$

$$\boldsymbol{\nabla} \cdot \boldsymbol{N}_1 = \boldsymbol{0} \,. \tag{2.30b}$$

This set of coupled bifurcation equations is to be considered under appropriate boundary conditions, which can be obtained from (2.29b). The derivation is similar with that when we derive the boundary conditions for the *FvK* equations. In the interest of brevity, we only record the final results, as follows

$$\text{either} \quad N_{1n} = 0 \quad \text{or} \quad v_{1n} \quad \text{specified} \,, \tag{2.31a}$$

$$\text{either} \quad N_{1s} = 0 \quad \text{or} \quad v_{1s} \quad \text{specified} \,, \tag{2.31b}$$

$$\text{either} \quad M_{1b} = 0 \quad \text{or} \quad \frac{\partial w_1}{\partial n} \quad \text{specified} \,, \tag{2.31c}$$

$$\text{either} \quad S_{1v} = 0 \quad \text{or} \quad w_1 \quad \text{specified} \,, \tag{2.31d}$$

where,

$$N_{1n} = \boldsymbol{N}_1 : (\boldsymbol{n} \otimes \boldsymbol{n}) = (\boldsymbol{\nabla} \otimes \boldsymbol{v}_1 + \boldsymbol{\nabla} \mathring{w} \otimes \boldsymbol{\nabla} w_1)^s : \mathbb{A} : (\boldsymbol{n} \otimes \boldsymbol{n}) \,,$$

$$N_{1s} = \boldsymbol{N}_1 : (\boldsymbol{n} \otimes \boldsymbol{s}) = (\boldsymbol{\nabla} \otimes \boldsymbol{v}_1 + \boldsymbol{\nabla} \mathring{w} \otimes \boldsymbol{\nabla} w_1)^s : \mathbb{A} : (\boldsymbol{n} \otimes \boldsymbol{s}) \,,$$

$$M_{1b} = \boldsymbol{M}_1 : (\boldsymbol{n} \otimes \boldsymbol{n}) = (\boldsymbol{\nabla} \otimes \boldsymbol{\nabla} w_1) : \mathbb{D} : (\boldsymbol{n} \otimes \boldsymbol{n}) \,,$$

$$S_{1v} = \big[\mathring{\boldsymbol{N}} \cdot \boldsymbol{\nabla} w_1 + \boldsymbol{N}_1 \cdot \boldsymbol{\nabla} \mathring{w} - \mathbb{D} \vdots (\boldsymbol{\nabla} \otimes \boldsymbol{\nabla} \otimes \boldsymbol{\nabla} w_1) \big] \cdot \boldsymbol{n} - \boldsymbol{\nabla} \Big\{ \mathbb{D} \vdots \big[(\boldsymbol{\nabla} \otimes \boldsymbol{\nabla} w_1) \otimes \boldsymbol{n} \otimes \boldsymbol{s} \big] \Big\} \cdot \boldsymbol{s} \,.$$

So far the formulation is for anisotropic elastic plates subject to both in-plane and lateral loads; next we specialise this formulation to isotropic plates as in §2.3, which is further reduced to plates under in-plane loading only, as recorded in §2.4.

It's worth highlighting that we can also arrive at the bifurcation equations by using the

MAE method. By applying the linearisation process as outlined in §1.2 to the equilibrium equation (2.21), we can also arrive at the governing equation for the bifurcation as (2.30). The corresponding boundary conditions (2.31) can be obtained by applying the MAE manipulations on the boundary conditions of the basic state (2.23).

2.3 Formulation for isotropic elastic plates

Next we will reduce the formulation for the general anisotropic plate in the last section to the special case when the plate is made of the St. Venant–Kirchhoff (isotropic) material. We confine ourselves to this isotropic linear elastic material for all the problems to be discussed in this Thesis. The stiffness tensor for the St. Venant–Kirchhoff material is

$$\mathbb{C} = \frac{E\nu}{1-\nu^2} \boldsymbol{I} \otimes \boldsymbol{I} + \frac{E}{2(1+\nu)} \mathbb{I},$$

where E and ν denote Young's modulus and Poisson ratio respectively; $\boldsymbol{I}$ is the second-order identity tensor (with the component form $g_{\alpha\beta}g_{\gamma\delta}$), while $\mathbb{I}$ is the symmetric part of the fourth-order identity tensor whose entries are $(g_{\alpha\gamma}g_{\beta\delta} + g_{\alpha\delta}g_{\beta\gamma})/2$. Therefore, the component form of $\mathbb{C}$ reads,

$$\mathbb{C}_{\alpha\beta\gamma\delta} = \frac{E}{1-\nu^2} \left[\nu g_{\alpha\beta}g_{\gamma\delta} + \frac{1-\nu}{2}(g_{\alpha\gamma}g_{\beta\delta} + g_{\alpha\delta}g_{\beta\gamma}) \right].$$

According to the definitions of $\mathbb{A}$ and $\mathbb{D}$ in (2.8) and (2.10), we have

$$\mathbb{A} := h\mathbb{C} = A[\nu\boldsymbol{I} \otimes \boldsymbol{I} + (1-\nu)\mathbb{I}], \qquad \mathbb{D} = \frac{h^3}{12}\mathbb{C} = D[\nu\boldsymbol{I} \otimes \boldsymbol{I} + (1-\nu)\mathbb{I}]$$

where

$$A = \frac{Eh}{1-\nu} \quad \text{and} \quad D = \frac{Eh^3}{12(1-\nu^2)}$$

are the bending and the in-plane stiffnesses of the plate.

Now we aim to obtain the equilibrium equation (2.21) and the boundary conditions (2.23) for an isotropic plate. Using the identities recorded in *Appendix A*, we have

$$\mathbb{D} \vdots (\boldsymbol{\nabla} \otimes \boldsymbol{\nabla} \otimes \boldsymbol{\nabla} \otimes \boldsymbol{\nabla}\mathring{w}) = D\nabla^4\mathring{w},$$

$$\mathbb{D} : (\boldsymbol{\nabla} \otimes \boldsymbol{\nabla} \otimes \boldsymbol{\nabla}\mathring{w}) = D\boldsymbol{\nabla}(\nabla^2\mathring{w}),$$

$$\mathring{\boldsymbol{N}} := \mathbb{A} : \left[(\boldsymbol{\nabla} \otimes \mathring{\boldsymbol{v}})^s + \frac{1}{2}\boldsymbol{\nabla}\mathring{w} \otimes \boldsymbol{\nabla}\mathring{w} \right] = A \left\{ \nu(\boldsymbol{\nabla} \cdot \mathring{\boldsymbol{v}} + \frac{1}{2}|\boldsymbol{\nabla}\mathring{w}|^2)\boldsymbol{I} + (1-\nu) \left[(\boldsymbol{\nabla} \otimes \mathring{\boldsymbol{v}})^s + \frac{1}{2}\boldsymbol{\nabla}\mathring{w} \otimes \boldsymbol{\nabla}\mathring{w} \right] \right\},$$

$$\mathring{\boldsymbol{M}} := \mathbb{D} : (\boldsymbol{\nabla} \otimes \boldsymbol{\nabla}\mathring{w}) = D \left[\nu\nabla^2\mathring{w}\boldsymbol{I} + (1-\nu)\boldsymbol{\nabla} \otimes \boldsymbol{\nabla}\mathring{w} \right],$$

where $|\boldsymbol{\nabla}\mathring{w}|^2 := \boldsymbol{\nabla}\mathring{w} \cdot \boldsymbol{\nabla}\mathring{w}$. Therefore, the governing equation for the equilibrium of an isotropic

elastic plate becomes

$$D\nabla^4\mathring{w} - \mathring{\boldsymbol{N}} : (\boldsymbol{\nabla} \otimes \boldsymbol{\nabla}\mathring{w}) = 0 \,, \tag{2.32a}$$

$$\boldsymbol{\nabla} \cdot \mathring{\boldsymbol{N}} = \boldsymbol{0} \,. \tag{2.32b}$$

By substituting the simplified terms obtained earlier into (2.22) and (2.14), we can also obtain the following specific terms in the boundary conditions (2.23)

$$\mathring{N}_n = \mathring{\boldsymbol{N}} : (\boldsymbol{n} \otimes \boldsymbol{n}) = A\left\{\nu(\boldsymbol{\nabla} \cdot \mathring{\boldsymbol{v}} + \frac{1}{2}|\boldsymbol{\nabla}\mathring{w}|^2) + (1-\nu)\left[\nabla_n v_n + \frac{1}{2}(\nabla_n\mathring{w})^2\right]\right\}$$

$$= A\left\{\nabla_n\mathring{v}_n + \frac{1}{2}(\nabla_n\mathring{w})^2 + \nu\left[\nabla_s\mathring{v}_s + \frac{1}{2}(\nabla_s\mathring{w})^2\right]\right\} \,,$$

$$\mathring{N}_s = \mathring{\boldsymbol{N}} : (\boldsymbol{n} \otimes \boldsymbol{s}) = \frac{A(1-\nu)}{2}(\nabla_n v_s + \nabla_s v_n + \nabla_n\mathring{w}\nabla_s\mathring{w}) \,,$$

$$\mathring{M}_b = \mathring{\boldsymbol{M}} : (\boldsymbol{n} \otimes \boldsymbol{n}) = D\left[\nu\nabla^2\mathring{w} + (1-\nu)\nabla_n^2\mathring{w}\right] = D(\nabla_n^2\mathring{w} + \nu\nabla_s^2\mathring{w}) \,,$$

$$\mathring{M}_t = \mathring{\boldsymbol{M}} : (\boldsymbol{n} \otimes \boldsymbol{s}) = (1-\nu)\nabla_n\nabla_s\mathring{w} \,,$$

$$\mathring{S}_v = \mathring{\boldsymbol{N}} \cdot \boldsymbol{\nabla}\mathring{w} \cdot \boldsymbol{n} - D\left[\nabla_n(\nabla^2\mathring{w}) + (1-\nu)\nabla_s(\nabla_n\nabla_s\mathring{w})\right] \,,$$

where we have used the definition $\nabla^2\mathring{w} = \nabla_n^2\mathring{w} + \nabla_s^2\mathring{w}$, and $\nabla_n^2(\bullet) := \nabla_n(\nabla_n\bullet)$, $\nabla_s^2(\bullet) := \nabla_s(\nabla_s\bullet)$.

Furthermore, following similar derivations as above, we can arrive at the following bifurcation equations for the isotropic case

$$D\nabla^4 w_1 - \mathring{\boldsymbol{N}} : (\boldsymbol{\nabla} \otimes \boldsymbol{\nabla} w_1) - \boldsymbol{N}_1 : (\boldsymbol{\nabla} \otimes \boldsymbol{\nabla}\mathring{w}) = 0 \,, \tag{2.33a}$$

$$\boldsymbol{\nabla} \cdot \boldsymbol{N}_1 = \boldsymbol{0} \,. \tag{2.33b}$$

The boundary conditions (2.31) for bifurcation state can be deduced in a similar way as for the equilibrium, just by replacing all the terms with superscript $(\mathring{\bullet})$ with subscript $(\bullet)_1$, with the exception of $\boldsymbol{N}_1$ (therefore N_{1n}, N_{1s}) and S_{1v}

$$\boldsymbol{N}_1 = A\left[\nu(\boldsymbol{\nabla} \cdot \boldsymbol{v}_1 + \boldsymbol{\nabla}\mathring{w} \cdot \boldsymbol{\nabla} w_1)\boldsymbol{I} + (1-\nu)\left(\boldsymbol{\nabla} \otimes \boldsymbol{v}_1 + \boldsymbol{\nabla}\mathring{w} \otimes \boldsymbol{\nabla} w_1\right)^s\right] \,.$$

Finally,

$$N_{1n} = A\left[\nu(\boldsymbol{\nabla} \cdot \boldsymbol{v}_1 + \boldsymbol{\nabla}\mathring{w} \cdot \boldsymbol{\nabla} w_1) + (1-\nu)\left(\nabla_n v_{1n} + \nabla_n\mathring{w}\nabla_n w_1\right)\right]$$

$$= A\left[\nabla_n v_{1n} + \nabla_n\mathring{w}\nabla_n w_1 + \nu(\nabla_s v_{1s} + \nabla_s\mathring{w}\nabla_s w_1)\right] \,,$$

$$N_{1s} = \frac{A(1-\nu)}{2}(\nabla_n v_{1s} + \nabla_s v_{1n} + \nabla_n\mathring{w}\nabla_s w_1 + \nabla_s\mathring{w}\nabla_n w_1) \,,$$

$$M_{1b} = D(\nabla_n^2 w_1 + \nu\nabla_s^2 w_1) \,,$$

$$M_{1t} = (1 - \nu)\nabla_n \nabla_s w_1 \,,$$

$$S_{1v} = (\mathring{\boldsymbol{N}} \cdot \boldsymbol{\nabla} w_1 + \boldsymbol{N}_1 \cdot \boldsymbol{\nabla} \mathring{w}) \cdot \boldsymbol{n} - D\left[\nabla_n(\nabla^2 w_1) + (1 - \nu)\nabla_s(\nabla_n \nabla_s w_1)\right] \,.$$

2.4 Formulation for isotropic plates under in-plane loading

The problems to be discussed in *Chapter 3* and *Chapter 4* will be bifurcation problem of plates under in-plane loading only. So in this section we discuss the related simplifications for the weak forms and the strong forms for the equilibrium and stability of isotropic plates under in-plane loading. When a plate is subject to in-plane loads only, in (2.6), $p \equiv 0$ on Ω; $\boldsymbol{q} \neq \boldsymbol{0}, R_n = 0, V = 0$ along the boundary $\partial\Omega$. In this case, the out-of-plane displacement in the basic state is identically zero, namely, $\mathring{w} \equiv 0$. The first variation of the total potential energy (2.20) becomes

$$\delta\mathcal{V}(\mathring{\boldsymbol{u}})[\boldsymbol{u}_1] = \delta\mathcal{E}_s(\mathring{\boldsymbol{u}})[\boldsymbol{u}_1] + \delta\mathcal{V}_e(\mathring{\boldsymbol{u}})[\boldsymbol{u}_1] = \int_{\partial\Omega}(\mathring{\boldsymbol{N}} \cdot \boldsymbol{n} - \boldsymbol{q}) \cdot \boldsymbol{v}_1 \, \mathrm{d}S - \int_\Omega (\boldsymbol{\nabla} \cdot \mathring{\boldsymbol{N}}) \cdot \boldsymbol{v}_1 \, \mathrm{d}A = 0 \,, \quad (2.34)$$

since $\delta\mathcal{E}_b \equiv 0$. The second variation of bending energy (2.24) is reduced to

$$\delta^2\mathcal{E}_b(\mathring{\boldsymbol{u}})[\boldsymbol{u}_1, \boldsymbol{u}_1] = 2D\int_\Omega \left\{(\nabla^2 w_1)^2 - (1 - \nu)[w_1, w_1]\right\} \mathrm{d}A \,, \quad (2.35)$$

where $\nabla^4 := \left(\nabla^2\right)^2$ stands for the bi-Laplacian operator, and

$$D = \frac{Eh^3}{12(1 - \nu^2)}$$

is the bending stiffness of the isotropic plate; the bracket is Monge-Ampère bracket which is defined as $[f, g] := (\nabla^2 f)(\nabla^2 g) - (\boldsymbol{\nabla} \otimes \boldsymbol{\nabla} f) : (\boldsymbol{\nabla} \otimes \boldsymbol{\nabla} g)$. However, back to the stretching energy, it is customarily assumed (for example, see [3, 119]) that the plate's midplane is inextensible during buckling (but was not applied to basic state); the condition for this reads

$$\boldsymbol{E}_s := (\boldsymbol{\nabla} \otimes \boldsymbol{v})^s + \frac{1}{2}(\boldsymbol{\nabla} w) \otimes (\boldsymbol{\nabla} w) = \boldsymbol{O} \,;$$

therefore, if we give a variation $\varepsilon\boldsymbol{u}_1 := \varepsilon(\boldsymbol{v}_1 + w_1\hat{\boldsymbol{n}})$ to the above condition, we have

$$\boldsymbol{E}_{s1} = \delta\boldsymbol{E}_s[\boldsymbol{u}_1] = [\boldsymbol{\nabla} \otimes \boldsymbol{v}_1 + (\boldsymbol{\nabla}\mathring{w}) \otimes (\boldsymbol{\nabla} w_1)]^s = \boldsymbol{O} \,. \quad (2.36)$$

Under such assumption, we also have $\boldsymbol{N}_1 = \boldsymbol{O}$. According to [3] such an approximation is equivalent to asking for the Gaussian curvature of the deformed plate midplane be identically zero or, equivalently, that this surface be developable during buckling. Thus, the second variation

of the stretching energy (2.25) becomes

$$\delta^2 \mathcal{E}_s(\mathring{\boldsymbol{u}})[\boldsymbol{u}_1, \boldsymbol{u}_1] = 2 \int_\Omega \mathring{\boldsymbol{N}} : \left[(\boldsymbol{\nabla} w_1) \otimes (\boldsymbol{\nabla} w_1) \right]. \tag{2.37}$$

Adding two part (2.35), (2.37) together, we have the *weak form* for bifurcation

$$\delta^2 \mathcal{V}(\mathring{\boldsymbol{u}})[\boldsymbol{u}_1, \boldsymbol{u}_1] := 2D \int_\Omega \left\{ (\nabla^2 w_1)^2 - (1-\nu)[w_1, w_1] \right\} \mathrm{d}A + 2 \int_\Omega \mathring{\boldsymbol{N}} : (\boldsymbol{\nabla} w_1 \otimes \boldsymbol{\nabla} w_1) \, \mathrm{d}A, \tag{2.38}$$

which will be used in *Chapter 3*.

Consider a plate only subject to in-plane loading, which is initially flat with condition $\mathring{w} \equiv 0$, then the equilibrium equations (2.32) in the basic state are reduced to

$$\boldsymbol{\nabla} \cdot \mathring{\boldsymbol{N}} = \boldsymbol{0}, \tag{2.39}$$

where $\mathring{\boldsymbol{N}}$ denotes the linearised membrane stress tensor corresponding to the basic state (not necessarily constant) obtained by solving the reduced governing equation for the basic state (2.39). If we take a further inextensional assumption, then $\boldsymbol{N}_1 = \mathbb{A} : \boldsymbol{E}_{s1} = \boldsymbol{O}$, and the bifurcation equations (*strong form*) (2.33) become

$$D\nabla^4 w_1 - \mathring{\boldsymbol{N}} : (\boldsymbol{\nabla} \otimes \boldsymbol{\nabla} w_1) = 0, \tag{2.40a}$$

$$\boldsymbol{\nabla} \cdot \boldsymbol{N}_1 = \boldsymbol{0}. \tag{2.40b}$$

Notice that this is a set of coupled equations. As the inextensible midplane assumption has been taken, the second equation (2.40b) will vanish due to (2.36). In this case, only the first equation (2.40a) that must be investigated for finding the eigenvalues (λ is usually present in the expression of $\mathring{\boldsymbol{N}}$). Although the assumption made in (2.36) is in general violated, the determination of the neutrally stable configurations using this hypothesis is acceptable for very thin elastic plates (for instance, as shown in [47], the results for the critical buckling obtained from a decoupled version of (2.40a) alone confirm those from the coupled version of (2.40) in [59]). However, coupling between bending and stretching becomes important when $\mathring{w} \neq 0$, or the plate enters the post-buckling regime.

Moreover, complementary boundary conditions (2.23) for the basic state (when solving (2.39)) need to be specified

$$\text{either} \quad \mathring{N}_n = q_n \quad \text{or} \quad \mathring{v}_n \quad \text{specified}, \tag{2.41a}$$

$$\text{either} \quad \mathring{N}_s = q_s \quad \text{or} \quad \mathring{v}_s \quad \text{specified}, \tag{2.41b}$$

where

$$\mathring{N}_n = A(\nabla_n \mathring{v}_n + \nu \nabla_s \mathring{v}_s), \qquad \mathring{N}_s = \frac{A(1-\nu)}{2}(\nabla_n \mathring{v}_s + \nabla_s \mathring{v}_n).$$

The boundary conditions in (2.31) are simplified to

$$\text{either} \quad M_{1b} = 0 \quad \text{or} \quad \frac{\partial w_1}{\partial n} \quad \text{specified}, \tag{2.42a}$$

$$\text{either} \quad S_{1v} = 0 \quad \text{or} \quad w_1 \quad \text{specified}, \tag{2.42b}$$

when solving the bifurcation equations (2.40a), where

$$M_{1b} = D(\nabla_n^2 w_1 + \nu \nabla_s^2 w_1), \quad M_{1t} = (1 - \nu)\nabla_n \nabla_s w_1,$$

$$S_{1v} = (\mathring{\boldsymbol{N}} \cdot \boldsymbol{\nabla} w_1) \cdot \boldsymbol{n} - D \left[\nabla_n (\nabla^2 w_1) + (1 - \nu)\nabla_s (\nabla_n \nabla_s w_1) \right].$$

2.5 Conclusions

In this chapter we have provided a complete formulation on the classic plate theory (Föppl–von Kármán equations) for anisotropic linear elastic thin plates by using a coordinate-free approach. This includes the weak and strong form (with boundary conditions) for both the basic state and the bifurcation state in bifurcation analysis.

This was accomplished by first assuming the Love–Kirchhoff displacement field, which is plugged into the energy functional to get the weak forms for both the basic and bifurcation states. Then CV is employed to get both the governing equations (strong forms) and natural boundary conditions from their corresponding weak forms. These equations can be used for any geometries such as rectilinear and polar coordinates due to the coordinate-free approach we have used.

This set of equations is straightforward to reduce to a specific anisotropic material (such as isotropic, orthotropic, transversely-isotropic, etc) by only evaluating the corresponding fourth-order stiffness tensor in the equations. The fourth-order stiffness tensors for different kinds anisotropic material are given in [58]. The procedure for obtaining the natural boundary conditions in this chapter can be modified slightly to formulate the continuity conditions along the contacts in planar-composite structures (see *Chapter 4* as an example).

Then this set of equations is specialised for isotropic linear elastic plates and a further case for plates subject to in-plane loading only, both in weak form (to be used in *Chapter 3*) and strong form (to be involved in *Chapter 4*).

Chapter 3

A hybrid energy method for a class of eigenvalue problems related to edge-buckling in thin plates

3.1 Introduction

Approximation schemes such as the Rayleigh–Ritz method or the Galerkin technique have played a historical role in the development of the theory of elastic stability [3, 119]. They are still used on a large scale in the engineering community and feature most prominently as the basis of sophisticated finite element computer packages. The use of the more basic "incarnations" of these two methods (in the spirit of Timoshenko's book, for example) represents one of the most expedient ways for solving buckling problems with a relatively modest amount of effort. Unfortunately, these more basic versions are not well suited for describing localised eigendeformations unless one is prepared to allow for a large number of terms in the corresponding approximations.

The problems we are interested in this chapter have been discussed by Coman *et al* [29, 41, 44, 47] with the help of singular perturbation techniques. In what follows the emphasis will be on improving those results and looking at some features that were not touched upon in the previous investigations. As pointed out in the literature review in *Chapter 1*, the papers just cited dealt with the linear bifurcation equations related to the partial wrinkling of stretched thin elastic plates (for details of the precise setting see Figures 3-1 and 3-8 later in this chapter). Among other things, it was discovered that these equations were intimately controlled by a typically large dimensionless parameter $\mu \gg 1$ (whose definition was problem-dependent).

Regular/periodic features of the eigendeformation in one of the two principal directions of the pre-buckling state of stress facilitated the reduction of the corresponding partial differential equations to ordinary differential equations for an unknown transverse amplitude function W. The eigenvalue λ and the eigenfunction W were then represented as power series in $\mu^{-1/2}$, i.e.

$$\begin{Bmatrix} \lambda \\ W \end{Bmatrix} = \sum_{j=0}^{\infty} \begin{Bmatrix} \lambda_j \\ W_j \end{Bmatrix} \mu^{-j/2}, \tag{3.1}$$

with the coefficients $\lambda_j \in \mathbb{R}$ and the functions W_j determined sequentially through a sequence of lengthy calculations. An indication of the role played by the size of μ on the accuracy of the approximations derived in [29, 41, 44, 47] is included in *Tables 3.1 and 3.2* .

Table 3.1: Typical comparisons for the critical edge-buckling loads λ_C of the clamped rectangular plate studied in [29, 44]: direct numerical simulations (NUM), two-term asymptotic results ($ASY\,I$), and three-term asymptotic expressions ($ASY\,II$); the relative errors ($R.E.$) of the last two sets of data with respect to the first are recorded in the last two columns.

μ	NUM	ASY (I)	ASY (II)	$R.E.$ I (%)	$R.E.$ II (%)
400.0	0.213362	0.205769	0.212336	3.5588	0.4809
200.0	0.238152	0.221965	0.235099	6.7969	1.2819
80.0	0.300362	0.254101	0.286936	15.4015	4.4697
60.0	0.333067	0.267628	0.311407	19.6475	6.5030
40.0	0.399122	0.290318	0.355988	27.2608	10.8073
10.0	1.226536	0.413969	0.676648	66.2489	44.8326

Table 3.2: Same data as in *Table 3.1*, but for the annular plate discussed in [41, 47] (with the corrected term λ_2^* as given in our §3.4). Here the ratio of the two radii of the annulus (η) is equal to 0.1.

μ	NUM	$ASY(I)$	$ASY(II)$	$R.E.$ I (%)	$R.E.$ II (%)
1200.0	0.197795	0.177290	0.195899	10.3668	0.9583
800.0	0.229288	0.197506	0.225421	13.8611	1.6867
400.0	0.311650	0.243140	0.298969	21.9830	4.0691
200.0	0.454089	0.307676	0.419334	32.2432	7.6538
80.0	0.854713	0.435724	0.714869	49.0210	16.3616
60.0	1.081105	0.489620	0.861813	54.7111	20.2841
40.0	1.556522	0.580031	1.138320	62.7354	26.8677
10.0	7.743505	1.072726	3.305881	86.1468	57.3077

It must be clear from this data that the asymptotic formulae perform admirably well for the

range they were intended to, but as μ decreases their reliability deteriorates fast. This trend is more pronounced in the case of the annular plate, so the question arises: can those results be improved?

As pointed out in [47], typical values of the non-dimensional parameter μ for annular thin films are in the vicinity of 300.0 or larger, but smaller numbers are also relevant to practical applications. Thus, extending the results in the aforementioned works to a broader range of values for the stiffness parameter μ would be desirable. Furthermore, from a strictly mathematical point of view the limit $\mu \to 0$ is also of interest, although this case does not have an immediate physical connotation.

The route we choose to pursue the answer to the question posed above is related to the so-called *Hybrid Galerkin Method* discussed at length by Geer and Andersen in a number of interesting papers [4, 5, 6] (the idea of using boundary-layer type functions in conjunction with Galerkin methods can be traced back to much earlier studies like that of Di Prima [52], for example). Their method is based on replacing the asymptotic gauges with arbitrary constants in known asymptotic expansions, that are subsequently determined by following the same pattern as in the classical version of the Galerkin scheme. We shall make the ideas more precise in §3.2, but here we confine ourselves to reviewing some related efforts.

Gristchack *et al.* [63] have used the classical WKB method in conjunction with the theory developed in [4, 5, 6] to determine the state of stress in an orthotropic elastic conical shell subjected to axial loading, while in [64] they dealt with the problem of dynamic loading for a piezoelectric sandwich plate. Whiting [126] modified existing multiple-scale results for buckling of a long strut on a nonlinear Winkler foundation, and used them as a starting point for his Galerkin procedure. That study was later extended by Wadee *et al.* [124] for the stability of single-hump localised solutions in the same particular context. The very good accuracy obtained in all of these works is indicative of the high efficiency and reliability of the hybrid approximation methods.

This chapter is organised as follows. We start by setting the stage in the next section, where the main ingredients of the energy method for elastic plates are briefly recalled. In §3.3 we discuss the details of the modification we introduce for the case of the rectangular plate studied in [29, 44]. It is shown that the results obtained with the current strategy do improve upon the previous studies, especially for $\mu \simeq 20.0$ to 300.0, but difficulties are still encountered for $\mu \lesssim 7.0$. Partly motivated by this occurrence, we discuss the regular perturbation case $\mu \to 0$ and establish that the relative errors of the new approximations are within 5% for $0 < \mu \lesssim 2.0$; while the work in §3.3.2 is pursued from a purely mathematical perspective, it is particularly gratifying that its range of validity extends well beyond its theoretical limitations. The more difficult problem of the stretched annular plate investigated in [41, 47] is tackled in §3.4 by using the same hybrid energy method. Again, comparisons with the earlier results and direct numerical simulations of the original equation show a marked improvement.

3.2 The Hybrid Energy Method

In this section, we outline the strategy of the hybrid energy method, which is clarified by comparisons with the *Rayleigh–Ritz* and *Galerkin* methods.

In the current hybrid energy method, we need to make use of the *weak form* of the bifurcation equation. For example, in the problems to be discussed in this chapter, we recall (2.38) as formulated in *Chapter 2*

$$\delta^2 \mathcal{E}(\lambda, \boldsymbol{u}_1) = 2D \int_\Omega \left\{ (\nabla^2 w_1)^2 - (1 - \nu)[w_1, w_1] \right\} \mathrm{d}A + 2 \int_\Omega \mathring{\boldsymbol{N}} : (\boldsymbol{\nabla} w_1 \otimes \boldsymbol{\nabla} w_1) \, \mathrm{d}A = 0 \, .$$

Here the expression $\delta^2 \mathcal{E}(\lambda, \boldsymbol{u}_1)$ represents $\delta^2 \mathcal{E}(\mathring{\boldsymbol{u}})[\boldsymbol{u}_1, \boldsymbol{u}_1]$ as in (2.38), since $\mathring{\boldsymbol{u}} = \mathring{\boldsymbol{u}}(\lambda)$ is determined by the external loading parameter λ by solving the pre-buckling problem. (Notice that the pre-buckling stress tensor $\mathring{\boldsymbol{N}}$ depends on $\mathring{\boldsymbol{u}}$ and therefore on λ.) The determination of the neutrally stable buckling configurations is obtained from the well-known Trefftz criterion,

$$\delta \left\{ \delta^2 \mathcal{E}(\lambda, \boldsymbol{u}_1) \right\} [\delta \boldsymbol{u}_1] = 0 \, , \tag{3.2}$$

that must be satisfied by all $\delta \boldsymbol{u}_1 = \delta \boldsymbol{v}_1 + (\delta w_1)\hat{\boldsymbol{n}}$ compatible with the geometrical boundary conditions; this variational problem defines the critical eigenvalue, $\lambda = \lambda_C$, and the infinitesimal buckling mode, $\boldsymbol{u}_1 = \boldsymbol{u}_{1C}$.

Now we recall some fundamental ideas of Rayleigh–Ritz method. The equation (3.2) forms the basis of the classical Rayleigh–Ritz method. By expanding the unknown transverse eigendisplacement in the form

$$w \simeq w_k := \sum_{j=1}^k C_j \phi_j \, ,$$

where $C_j \in \mathbb{R}$ $(j = 1, 2, \ldots, k)$ are undetermined constants, and the test functions $\{\phi_j\}$ are a priori known and assumed to satisfy the kinematic boundary conditions for the problem at hand, the Trefftz criterion (3.2) translates into the criticality conditions

$$\frac{\partial}{\partial C_i} \left[\delta^2 \mathcal{E}(\lambda, \boldsymbol{u}_1) \right] = 0 \, , \qquad i = 1, 2, \ldots, k \, . \tag{3.3}$$

This typically represents a generalised matrix eigenvalue problem of the form $A = \lambda B$, for some known square matrices A and B, which can be solved without difficulty.

The strategy we propose in this work differs in several respects from the classical method. For example, to allow convergence in the $L^2(\Omega)$-norm of the sequence of approximations in this classical approach one would have to require that the shape functions $\{\phi_i\}$ form a complete set in Ω; the agreement with the actual solution usually improves by increasing $k \in \mathbb{N}$. Our choice of basis functions does not fulfil such requirements as it is informed by the asymptotic analysis developed in [41, 44]. Also, the kinematic boundary conditions are satisfied only approximately, unlike in the classical case.

For the sake of completeness, next we give a short overview of the Hybrid Galerkin Method of Geer and Andersen [4, 5]. The strategy is applicable to general equations of the form

$$\mathcal{L}(u; \varepsilon) = 0\,, \tag{3.4}$$

where $\mathcal{L}$ is a differential operator and $\varepsilon \in \mathbb{R}$ is some parameter. The operator involved in the above equation may depend on several other parameters (which here are not mentioned explicitly), but it is just the behaviour of ε around some specific values ε_j $(j = 1, 2, \ldots, q)$ which is of interest. In most cases $\varepsilon_1 = 0$ and $\varepsilon_2 = +\infty$, although in principle $q \geq 3$ does not pose any sort of complications. When applied to problems such as (3.4), which do not necessarily have a variational structure, the technique is essentially a modification of the classical Galerkin method. Our interest is, however, in conservative elastic stability problems, so we shall adapt the theory of [4, 5, 6] to the Rayleigh–Ritz (energy) approach. It is well known [79] that the two classical versions are in fact equivalent to each other for such problems. Hence there is no loss of generality in our exposition.

The first step consists of generating asymptotic expansions for $\varepsilon \to \varepsilon_j$ for each $j = 1, 2, \ldots, q$, which we can formally write

$$u = u_0 + \sum_{s=1}^{n_i-1} u_s^{(i)} \delta_s^{(i)}(\varepsilon) + \mathcal{O}(\delta_{n_i}(\varepsilon))\,,$$

where u_0 is the leading order expansion and the gauge functions $\left\{ \delta_s^{(i)}(\varepsilon) \right\}$ $(s = 1, 2, \ldots, n_i-1)$ are specific to the problem at hand.

In the second step we have two alternative treatment schemes.

One is taking the above asymptotic expansion for u to a certain order, using this as an ansatz. Then we plug this ansatz directly into the weak form $\delta^2 \mathcal{E}(\lambda)[\boldsymbol{u}_{1C}, \boldsymbol{u}_{1C}] = 0$, which ends up with an equation in terms of λ and other parameters (not explicit). By solving this equation we could obtain λ as a function of other parameters. Notice in this treatment, we did not use the idea of Rayleigh–Ritz (3.3). Instead, we just assume that this variational effect (3.3) is already (asymptotically) embedded in the asymptotics $\boldsymbol{u}_{1C} \simeq u$, which were obtained from the bifurcation equation (strong form together with the boundary conditions).

Alternatively, we can follow a Rayleigh–Ritz strategy by discarding the gauge functions and selecting a subset of $\left\{ u_s^{(i)} \right\}$, with $s = 1, 2, \ldots, n_i - 1$ and $i = 1, 2, \ldots, q$, to construct the ansatz

$$u = u_0 + \sum_{s=1}^{Q} C_s u_s\,, \tag{3.5}$$

with $Q \leq \sum_{j=1}^{q} n_j$. The unknowns C_s are determined exactly as in the classical energy method by applying both the weak form for bifurcation $\delta^2 \mathcal{E}(\lambda)[\boldsymbol{u}_1, \boldsymbol{u}_1] = 0$ and the stationarity conditions (3.3).

Obviously, the results obtained from the latter treatment are expected to be more accurate, because we have introduced freedom to the ansatz, and the eigenfunction u can be approximated better. However, this procedure is much more expensive from a computational point of view, and can easily cause convergence problem in numerical calculations. In contrast, the former treatment is more straightforward and computationally economic, and is later proven to be an accurate and efficient strategy. So in this work we choose the former strategy.

In the Galerkin and Rayleigh–Ritz methods increasing the number of test functions does not pose any serious difficulties because of the conditions in (3.3) end up with linear algebra system. Unfortunately, this is not the case with the hybrid methods and that is why it is important to keep the terms of expansion for u small.

Depending on the nature of the features studied with this method, it is important to allow for variations from the above strategy. For example, in the post-buckling analyses discussed by Wadee *et al.* [124] and Whitting [126] for compressed beams on nonlinear Winkler foundations it was found helpful to introduce some extra degrees of freedom that made the ansatz (3.5) nonlinear (in the sense that some of the C's entered in the expression of the gauge functions as well – see equation (16) in [124]).

3.3 Rectangular plate

A detailed numerical and asymptotic analysis for the edge-buckling of a stretched elastic plate subjected to in-plane bending was carried out in [29, 44]. For the sake of completeness here we include an outline of the model and a summary of some of the main results.

The rectangular thin elastic plate of length $2a$, width b, and thickness h ($h/b \ll 1$) corresponds to the situation illustrated in Figure 3-1; it is assumed to occupy the domain

$$\Omega \equiv \left\{ (x,y) \in \mathbb{R}^2 \,|\, -a \leq x \leq a\,, 0 \leq y \leq b \right\}.$$

The plate is stretched by normal stresses σ_0 in the y-direction, while on the two lateral edges it is subjected to the loads P at the midpoints. Further in-plane bending moments M act simultaneously, as indicated in the aforementioned figure. Under the combined action of these loads the plate develops a region of compressive stresses adjacent to one of the long edges, leading eventually to a regular wrinkling pattern in the $x-$direction (for a certain critical value of the ratio M/P). With the short sides taken as simply supported, the linearised Föppl–von Kármán buckling equation used for describing the bifurcations of this plate is reduced to an ODE by expressing the transverse displacement in the form

$$w(x,y) = W(y)\sin(A_m x).$$
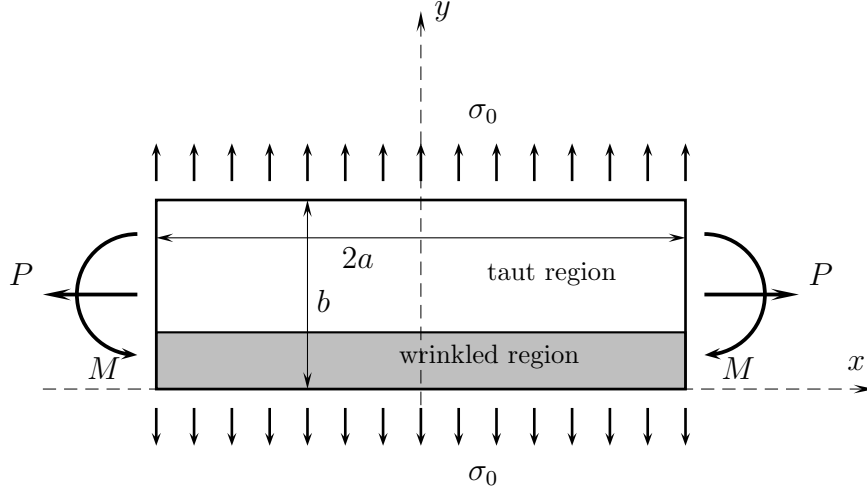
Figure 3-1: Stretched thin film under in-plane bending.

Eventually, it transpires that

$$W''''(y) + \mathcal{P}_1(\mu, A_m)W''(y) + \mathcal{P}_2(y; \mu, A_m)W(y) = 0\,, \qquad 0 < y < 1\,, \tag{3.6}$$

where

$$\mathcal{P}_1(\mu, A_m) := -(\mu^2 + 2A_m^2)\,,$$
$$\mathcal{P}_2(y; \mu, A_m) := A_m^2 \left\{ A_m^2 + 6\mu^2 \left[2\lambda y - \left(\lambda - \frac{1}{6} \right) \right] \right\}\,,$$

and

$$\eta := \frac{a}{b}, \qquad A_m := \frac{m\pi}{\eta}, \qquad \lambda := \frac{M}{Pb}\,,$$

$$\mu^2 := 12(1 - \nu^2) \left(\frac{\sigma_0}{E} \right) \left(\frac{b}{h} \right)^2\,;$$

differentiation with respect to y is indicated by a dash $(\cdot)'$. The mode number $m \in \mathbb{N}$ is uniquely determined by identifying the global minimum of the curve $\lambda = \lambda(A_m)$. We shall use the appellative 'critical' in relation to these values.

The same normal-mode solution transforms the boundary conditions along the long edges into relatively simple expressions. In the case of clamped edges they take the form

$$W = W' = 0 \qquad \text{at} \qquad y = 0, 1\,, \tag{3.7}$$

while for the free-edge case we have

$$W'' - \nu A_m^2 W = 0 \qquad\qquad \text{at} \qquad y = 0, 1\,, \tag{3.8a}$$
$$W''' - \left[\mu^2 + (2 - \nu)A_m^2 \right] W = 0 \qquad \text{at} \qquad y = 0, 1\,. \tag{3.8b}$$

Finally, the work in [44] provides the asymptotic expansion for the critical buckling load λ_C and the corresponding critical buckling mode number (proportional to A_m^C below) in the form

$$W = W_0(Y) + \mu^{-1/2}W_1(Y) + \mu^{-1}W_2(Y) + \mu^{-3/2}W_3(Y) + \mathcal{O}(\mu^{-2}), \qquad Y := \mu^{1/2}y, \quad \text{(3.9a)}$$

$$\lambda_C = \lambda_0 + \lambda_{1i}^*\mu^{-1/2} + \lambda_{2i}^*\mu^{-1} + \mathcal{O}(\mu^{-3/2}), \quad \text{for} \quad i = 1,\, 2, \quad \text{(3.9b)}$$

$$(A_m^C)^2 = M_{0i}^*\mu^{3/2} + M_{1i}^*\mu + \mathcal{O}(\mu^{1/2}), \quad \text{for} \quad i = 1,\, 2, \quad \text{(3.9c)}$$

where the extra subscript '1' is used to indicate the values for the free-edge case, and '2' applies to the clamped-edge approximation. The coefficients that appear in (3.9) are recorded below and are identified through a sequence of lengthy matched asymptotic calculations,

$$\lambda_0 = 1/6, \qquad M_{02}^* = 1.17306, \quad M_{01}^* = 0.62912,$$

$$\lambda_{12}^* = 0.78204, \quad \lambda_{22}^* = 2.62679, \quad M_{12}^* = 0.79737,$$

$$\lambda_{11}^* = 0.41941, \quad \lambda_{21}^* = 0.65966 - 0.11111\nu^2, \quad M_{11}^* = 0.39579 - 0.66666\nu^2.$$

Details on the W_j−terms in the expansion of the eigenfunctions are given in the next section (as adapted to our immediate purposes). The comparison between these asymptotic results and numerics showed good agreement for both the two- and three-term approximations when $\mu \gg 1$; the question here is whether or not this assumption can be relaxed without affecting the accuracy.

3.3.1 Hybrid energy method

We start by noticing that setting $\boldsymbol{u}_1 \to \boldsymbol{u}_{1C}$ in (3.2) gives

$$\delta^2 E(\lambda)[\boldsymbol{u}_{1C}, \boldsymbol{u}_{1C}] = 0; \quad \text{(3.10)}$$

in the case of our rectangular plate this equation assumes the form

$$\int_0^1 \left[W''^2(y) + (\mu^2 + 2A_m^2)W'^2(y) + \mathcal{P}_2(y; \mu, A_m)W^2(y) \right] dy = 0. \quad \text{(3.11)}$$

Alternatively, the energy integral (3.11) can be also obtained by multiplying equation (3.6) by $W \equiv W(y)$ and then integrating the resulting expression over $[0,1]$ with the help of the corresponding boundary conditions and the integration by parts formula.

As already pointed out, since our main interest lies with the approximation of the envelope of the neutral stability curves, we are essentially looking for eigenvalues satisfying $\partial\lambda/\partial A_m = 0$. On applying

$$\frac{\partial\left\{\delta^2 E(\lambda)[\boldsymbol{u}_{1C}, \boldsymbol{u}_{1C}]\right\}}{\partial(A_m^2)} = 0, \quad \text{(3.12)}$$

we derive an extra integral constraint applicable to the case in which the long edges are clamped,

$$\int_0^1 \left\{ W'^2(y) + \left[A_m^2 + 3\mu^2 \left(2\lambda y - \left(\lambda - \frac{1}{6} \right) \right) \right] W^2(y) \right\} \mathrm{d}y = 0\,. \tag{3.13}$$

An different route for arriving at equation (3.13) was taken by Coman and Bassom in [44], and it relies on the use of the Fredholm solvability condition for a certain inhomogeneous fourth-order ODE. In the next chapter we shall extend their approach to the case of a bi-annular plate which involves a set of interfacial conditions.

The counterpart of (3.13) for the case when the long edges of the plate are 'free' rather than 'clamped' is obtained similarly, with the only difference that this time we need to make use of the boundary conditions (3.8). The final result reads

$$\int_0^1 \left\{ -\nu W(y) W''(y) + (1-\nu) W'^2(y) + \left[A_m^2 + 3\mu^2 \left(2\lambda y - \left(\lambda - \frac{1}{6} \right) \right) \right] W^2(y) \right\} \mathrm{d}y = 0\,. \tag{3.14}$$

A possible candidate for the ansatz of our hybrid energy method is

$$\lambda_C = \lambda_0 + \lambda_{1j}^* c_1\,, \quad (A_m^C)^2 = M_{0j}^* c_2\,, \tag{3.15a}$$

$$W(y) = W_0(y) + W_1(y) c_3 + \dots\,, \tag{3.15b}$$

where

$$W_0(y) = \mathrm{Ai}\left(\omega \mu^{1/2} y + \zeta_{0j} \right)\,, \qquad \omega := (2 M_{0i}^*)^{1/3}\,. \tag{3.16}$$

Here, $W_0(Y)$ in (3.9a) is expressed in terms of y, ζ_{0j} denotes the first zero of the equation $Ai^{(j)}(\zeta) = 0$ ($j = 1, 2$): for the free-edge case we take $\zeta_{01} \simeq -1.01879$, while for clamped edges, $\zeta_{02} \simeq -2.3381$. The expression of $W_1(y)$ is not given here because of its high complexity, but it can be found in [44] (see equations (16) and (17) in that reference).

The above approximation is obtained from (3.9) in which the powers of μ have been replaced by the arbitrary constants c_i ($i = 1, \dots, n$); for notational simplicity we let $\mathbf{c} := [c_1, c_2, \dots, c_n]$. Note that (3.15a) do not require more terms as in (3.9b) or (3.9c) – it is just the expansion (3.15b) that could potentially improve the accuracy of our numerical strategy.

If we confine ourselves to the case when just $W_0(y)$ is used in (3.15b) we essentially end up with two unknowns for which we need only two equations. Substituting (3.15) into the integral constraint (3.11) yields a first nonlinear equation in the c_i's, which we shall identify by the notation $f_1(\mathbf{c}) = 0$. A second equation is obtained by plugging the same ansatz into either (3.13) or (3.14); this will generically be referred to as $f_2(\mathbf{c}) = 0$. Thus, we get two nonlinear equations in two unknowns. Here, we provide some details and possible simplifications in the calculations that lead to these equations for the case of a clamped-edge plate.

To start, we rewrite the energy integral in (3.11) in the form

$$\int_0^1 \left[W''^2(y) - \mathcal{P}_1(\mu; A_m)W'^2(y) + \mathcal{R}_1(\mu; A_m, \lambda)W^2(y) + \mathcal{R}_2(\mu; A_m, \lambda)yW^2(y) \right] \mathrm{d}y = 0 \,, \quad (3.17)$$

where

$$\mathcal{R}_1(\mu; A_m, \lambda) := A_m^2 \left[A_m^2 - 6\mu^2 \left(\lambda - \frac{1}{6} \right) \right] \,,$$

$$\mathcal{R}_2(\mu; A_m, \lambda) := 12\mu^2 A_m^2 \lambda \,.$$

As mentioned earlier, we choose an ansatz based on the leading-order asymptotic predictions

$$W(y) = \mathrm{Ai}(ky + \zeta_{02}) \,,$$

where 'Ai' is the usual Airy function of the first kind, $k := \mu^{1/2}\omega = \mu^{1/2}(2M_{02}^*)^{1/3}$, and M_{02}^* is a constant that has already been mentioned in §3.3. To simplify the notation we introduce the variable $Z := ky + \zeta_{02}$, so that now $W(y) = \mathrm{Ai}(Z)$, and notice that

$$\frac{\mathrm{d}^n(\cdot)}{\mathrm{d}y^n} = k^n \frac{\mathrm{d}^n(\cdot)}{\mathrm{d}Z^n} \,, \quad (3.18)$$

$$Z\big|_{y=0} = \zeta_{02} =: a_1 \quad \text{and} \quad Z\big|_{y=1} = k + \zeta_0 =: a_2 \,; \quad (3.19)$$

the reason for re-labelling the first zero of the Airy function is to provide a more uniform notation in the subsequent calculations.

By using the change of variable indicated above, the integrals in (3.17) can be recast as follows

$$\int_0^1 \left[\frac{\mathrm{d}^2 W(y)}{\mathrm{d}y^2} \right]^2 \mathrm{d}y = \int_{a_1}^{a_2} \left[k^2 \frac{\mathrm{d}^2 W(Z)}{\mathrm{d}Z^2} \right]^2 \frac{1}{k} \mathrm{d}Z = k^3 \int_{a_1}^{a_2} Z^2 W^2(Z) \mathrm{d}Z \,,$$

$$\int_0^1 \left[\frac{\mathrm{d}W(y)}{\mathrm{d}y} \right]^2 \mathrm{d}y = \int_{a_1}^{a_2} \left[k \frac{\mathrm{d}W(Z)}{\mathrm{d}Z} \right]^2 \frac{1}{k} \mathrm{d}Z = k \int_{a_1}^{a_2} \left[\frac{\mathrm{d}W(Z)}{\mathrm{d}Z} \right]^2 \mathrm{d}Z \,,$$

$$\int_0^1 W^2(y) \mathrm{d}y = \frac{1}{k} \int_{a_1}^{a_2} W^2(Z) \mathrm{d}Z \,,$$

$$\int_0^1 yW^2(y) \mathrm{d}y = \frac{1}{k^2} \int_{a_1}^{a_2} ZW^2(Z) \mathrm{d}Z - \frac{a_1}{k^2} \int_{a_1}^{a_2} W^2(Z) \mathrm{d}Z \,.$$

Therefore, equation (3.17) can be reformulated further as

$$k^3 T_1 - k\mathcal{P}_1(\mu; A_m)T_2 + \left[\frac{\mathcal{R}_1(\mu; A_m, \lambda)}{k} - \frac{a_1 \mathcal{R}_2(\mu; A_m, \lambda)}{k^2} \right] T_3 + \frac{\mathcal{R}_2(\mu; A_m, \lambda)}{k^2} T_4 = 0 \,, \quad (3.20)$$

where

$$T_1 := \int_{a_1}^{a_2} \left[\frac{\mathrm{d}W^2(Z)}{\mathrm{d}Z^2} \right]^2 \mathrm{d}Z\,, \qquad T_2 := \int_{a_1}^{a_2} \left[\frac{W(Z)}{\mathrm{d}Z} \right]^2 \mathrm{d}Z\,,$$

$$T_3 := \int_{a_1}^{a_2} W^2(Z)\mathrm{d}Z\,, \qquad\qquad T_4 := \int_{a_1}^{a_2} ZW^2(Z)\mathrm{d}Z\,.$$

Reference [2] provides us with a set of interesting formulae that facillitate the simplification of integrals of products of Airy functions. That strategy will be applied in the context of (3.20) as indicated below

$$T_1 := \int_{a_1}^{a_2} Z^2\mathrm{Ai}^2(Z)\mathrm{d}Z = \frac{1}{5}\Big[2\Big\{ Z\mathrm{Ai}(Z)\mathrm{Ai}'(Z) - \frac{1}{2}\mathrm{Ai}^2(Z) \Big\} - Z^2\mathrm{Ai}'^{\,2}(Z) + Z^3\mathrm{Ai}^2(Z) \Big]_{a_1}^{a_2}\,,$$
$$\tag{3.21a}$$

$$T_2 := \int_{a_1}^{a_2} \mathrm{Ai}'^{\,2}(Z)\mathrm{d}Z = \frac{1}{3}\Big[2\mathrm{Ai}(Z)Ai'(Z) + Z\mathrm{Ai}'^{\,2}(Z) - Z^2\mathrm{Ai}^2(Z) \Big]_{a_1}^{a_2}\,, \tag{3.21b}$$

$$T_3 := \int_{a_1}^{a_2} \mathrm{Ai}^2(Z)\mathrm{d}Z = \Big[Z\mathrm{Ai}^2(Z) - \mathrm{Ai}'^{\,2}(Z) \Big]_{a_1}^{a_2}\,, \tag{3.21c}$$

$$T_4 := \int_{a_1}^{a_2} Z\mathrm{Ai}^2(Z)\mathrm{d}Z = \frac{1}{3}\Big[\mathrm{Ai}(Z)Ai'(Z) - Z\mathrm{Ai}'^{\,2}(Z) + Z^2\mathrm{Ai}^2(Z)) \Big]_{a_1}^{a_2}\,, \tag{3.21d}$$

where $[\psi]_{a_1}^{a_2} \equiv \psi(a_2) - \psi(a_1)$. As mentioned earlier, the integration limits a_1, a_2 depend only on the parameter μ. Therefore, with given μ, the quantities $T_i = T_i(\mu)$ (for $i = 1, 2, 3, 4$) can be calculated once and for all. On substituting (3.21) into (3.20) we then end up with the first equation $f_1(A_m, \lambda) = 0$.

Additionally, we have derived the integral constraint (3.13) which enforces the criticality condition $\partial\lambda/\partial A_m = 0$. For the clamped-edge rectangular plate this assumes the expression

$$\int_0^1 \Big\{ W'^2(y) + [\mathcal{R}_3(\mu; A_m, \lambda) + \mathcal{R}_4(\mu; \lambda)y]\, W^2(y) \Big\}\, \mathrm{d}y = 0\,, \tag{3.22}$$

where

$$\mathcal{R}_3(\mu; A_m, \lambda) := A_m^2 - \mu^2\left(3\lambda - \frac{1}{2} \right)\,,$$

$$\mathcal{R}_4(\mu; \lambda) := 6\mu^2\lambda\,.$$

Carrying out the same transformation on variables as for (3.17), we eventually get

$$kT_2 + \left[\frac{\mathcal{R}_3(\mu; A_m, \lambda)}{k} - \frac{a_1\mathcal{R}_4(\mu; \lambda)}{k^2} \right] T_3 + \frac{\mathcal{R}_4(\mu; \lambda)}{k^2}T_4 = 0\,, \tag{3.23}$$

where, T_2, T_3, T_4 were introduced earlier in (3.20). If we plug (3.21) into (3.23), we then obtain

the second equation $f_2(A_m, \lambda) = 0$.

To summarise, in (3.20) and (3.23) we have formulated two nonlinear equations f_1, f_2 in two unknowns A_m, λ. Since A_m and λ depend only on c_1 and c_2, according to (3.15), we essentially have two equations for these two unknowns. To complete the solution, the multi-dimensional root finding problem is transformed into a minimisation problem by considering $I(\boldsymbol{c}) := f_1^2(\boldsymbol{c}) + f_2^2(\boldsymbol{c})$, which is expected to be zero when $\boldsymbol{c} \in \mathbb{R}^2$ corresponds to our actual solution. Cast in this form the problem is then solved by using Powell's method (e.g., see [98] for details). The situation we are confronted with is not trivial because the functional that needs to be minimised is highly nonlinear. We have checked that the minima of $I(\boldsymbol{c})$ lead to values of the functional that are virtually indistinguishable from zero; this indicates that our approximate solution satisfies the neutral stability condition (3.11) and guarantees that the most dangerous mode has been captured. A final observation worth stating is that, owing to the non-quadratic nature of the functional to be minimised, providing an initial guess requires additional care. We employed a numerical continuation strategy in which the original guess was supplied by various powers of $\mu \gg 1$, as hinted by (3.9), with μ then being decreased progressively until it reached $\mathcal{O}(1)-$values. In manipulating integrals involving Airy functions a certain degree of simplification can be achieved by using the formulae in [2].

Results of this method are recorded in Figures 3-2 and 3-4 for clamped and, respectively, free-edge boundary conditions, which are followed by the corresponding relative errors with respect to the direct numerical simulations as in Figures 3-3 and 3-5. In Figures 3-2 and 3-4, the direct numerical simulations are shown with a continuous line, while the new approximations are represented by the white markers. To put things in perspective, we have also included the two- and three-term asymptotic approximations from [44] (the dot-dashed/dashed lines). It is quite remarkable that the simple-minded ansatz (3.16) informed by the leading-order asymptotic analysis of equation (3.6) outperforms by a long shot the two-term asymptotic approximation obtained through a very laborious analysis [44]. In Figure 3-3 the relative errors between the hybrid energy results and numerics tend to deteriorate, for instance, from $R.E. \simeq 5.14\%$ ($\mu = 11.0$) $R.E. \simeq 9.96\%$ ($\mu = 10.0$), although for $\mu \gtrsim 60.0$ we have $R.E. \lesssim 2.73\%$. Similar conclusions can be drawn in relation to Figure 3-4 and 3-5.

A caveat needs to be raised about our choice of test function (3.16). In the case of a clamped plate, for relatively largish values of μ (typically, greater than 10.0), this function and its derivative display exponential decay for $y \simeq 1.0$, so the constraints $W(1) = W'(1) = 0$ are satisfied asymptotically. Note that by definition $W(0) = 0$ (exactly), but $W'(0) \neq 0$. It was shown in [44] that satisfaction of the condition $W'(0) = 0$ demanded the introduction of an $\mathcal{O}(\mu^{-1})$ layer that had to be matched to the solution described by equations (3.9). Here we have disregarded this effect because the results obtained with the apparently crude choice of (3.16) already lead to values that improve considerably upon the earlier studies. In §3.6 we shall reconsider this point and look more closely at what happens if the test function is replaced by

the $\mathcal{O}(\mu^{-1})$ *composite* asymptotic approximation that partially satisfies the derivative boundary condition at $y = 0$. It is also important to keep in mind that higher-order asymptotic results are not easily available for the annulus problem discussed in §3.4.
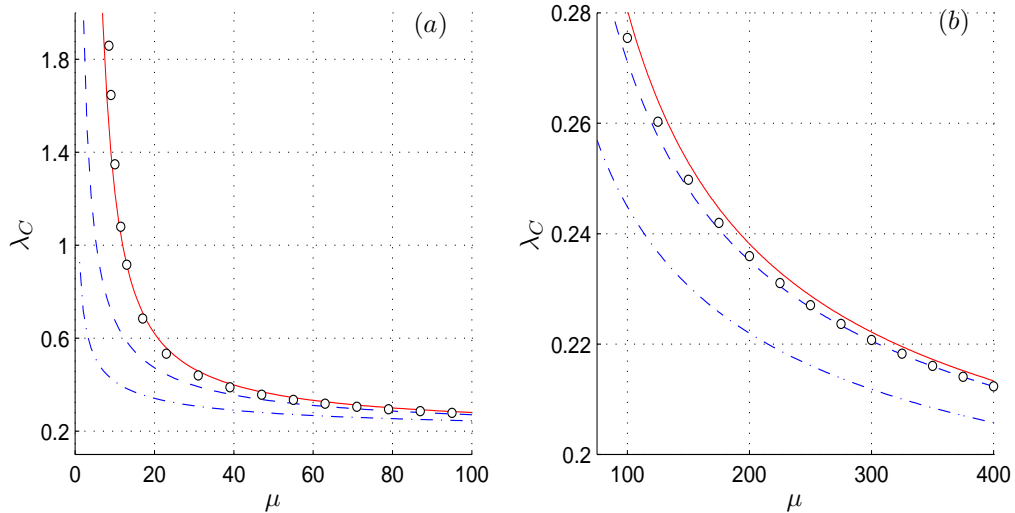
Figure 3-2: Comparisons between two- (*dot-dashed line*) and three-term (*dashed line*) asymptotic approximations of the critical eigenvalue, the hybrid energy method (*small circles*) and the corresponding direct numerical simulations (*continuous line*) for the clamped-edge rectangular plate. Both (*a*) and (*b*) are the comparisons of λ_C, but for different ranges of μ.
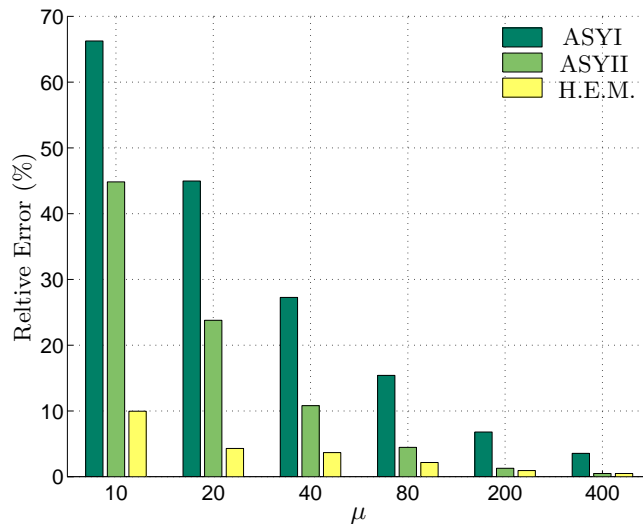
Figure 3-3: Relative errors with respect to the direct numerical simulations shown in in Fig. 3-2 for the three approximations recorded there: the two- (*ASYI*) & three- (*ASYII*) term asymptotic results for the critical eigenvalue, together with the hybrid energy method (*H. E. M.*) for the clamped-edge rectangular plate.

It might be tempting to try and improve the results already obtained, especially since $W_1(y)$ in (3.15b) is available [44]. In this case we have three unknowns, so a change of tack is imperative. The criticality conditions (3.13) or (3.14) will remain unchanged, but two further equations are obtained with the help of (3.2) in which $\delta w \rightarrow W_0(y)\sin(A_m x)$ and $\delta w \rightarrow$
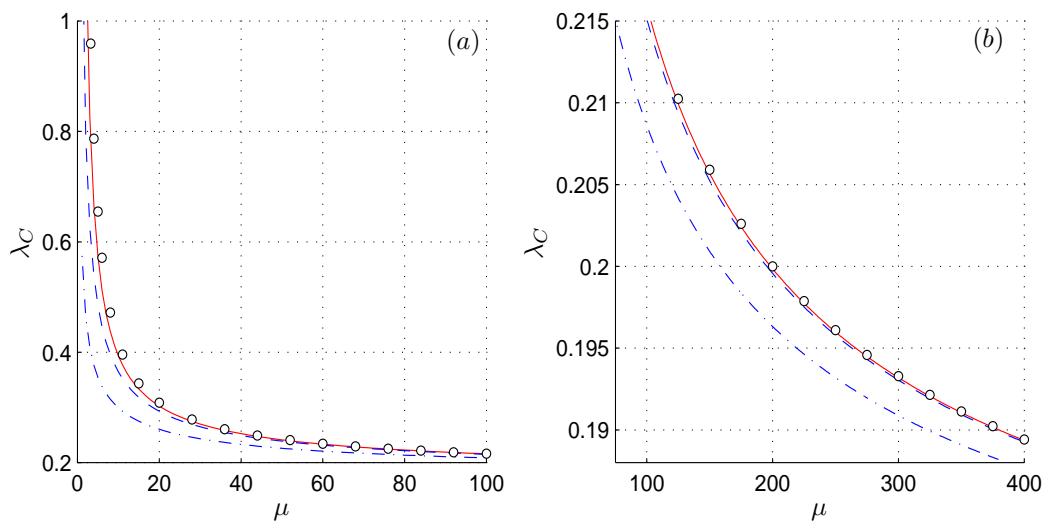
Figure 3-4: Same as per Fig. 3-2, but for the free-edge rectangular plate.
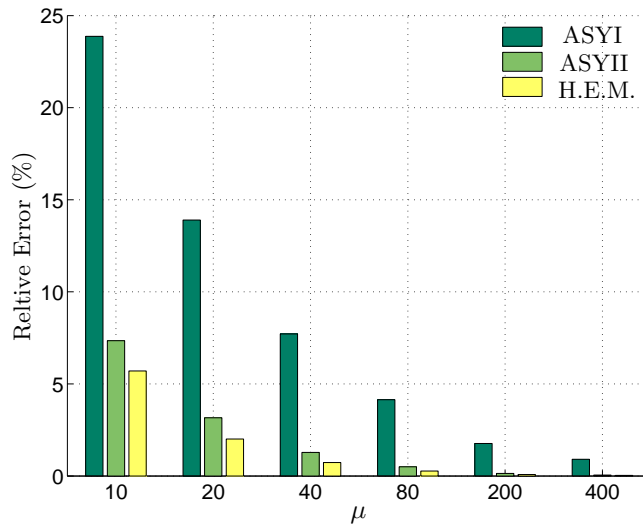
Figure 3-5: Same as per Fig. 3-3, corresponding to the results in Fig. 3-4 for the free-edge rectangular plate.

$W_1(y)\sin(A_m x)$, respectively. Doing this, however, does not lead to any noteworthy headway since the kinematic boundary condition $W'(0) = 0$ is still violated (and will continue to be so as long as we do not take into consideration the $\mathcal{O}(\mu^{-1})$ layer mentioned above).

3.3.2 The limiting case $\mu \to 0$

As already pointed out in the *Introduction*, for wrinkling it is the limit $\mu \gg 1$ that is the most interesting. However, from a mathematical point of view it would be important to understand the asymptotic structure of the opposite limit $\mu \to 0$ as well. This scenario is also relevant to the important case $\sigma_{xx} \to 0$, and it does present us with an interesting *regular perturbation* situation. We also anticipate that the range of validity for these new asymptotic results would

extend beyond their immediate limit of applicability, so they could be useful (at least in principle) as numerical guesses for the optimisation routines used in the hybrid energy method. Another motivation for the work in this section comes from the related papers of Geer and Andersen [4, 5, 6] mentioned in §3.2, although it will eventually transpire that we cannot follow their strategy very closely.

Clamped-edge boundary conditions

For a rectangular plate with clamped edges $A_m^C = \mathcal{O}(1)$ as $\mu \to 0$. At the same time, the critical eigenvalue λ_C displays a tendency to blow up, which was verified by the direct numerical simulations. This limiting behaviour is captured by the following ansatz

$$W(y) = W_0(y) + W_1(y)\mu^2 + \dots, \tag{3.24a}$$

$$\lambda = \lambda_0 \mu^{-2} + \lambda_1 + \lambda_2 \mu^2 + \dots, \tag{3.24b}$$

$$(A_m)^2 = M_0 + M_1 \mu^2 + \dots, \tag{3.24c}$$

where W_0, λ_0, and M_0 satisfy the simplified differential equation

$$W_0'''' - 2M_0^2 W_0'' + M_0\left[M_0 + 6\lambda_0(2y-1)\right]W_0 = 0, \tag{3.25}$$

that is to be solved subject to the boundary conditions

$$W_0(y) = W_0'(y) = 0, \qquad \text{at} \qquad y = 0, 1.$$

Here and in the next section we shall employ some of the labels used previously for expanding λ, A_m and W in order to avoid overdoing the notation; no confusion should arise as these derivations are independent of each other.

Note that this reduced problem depends only on the parameters λ_0 and M_0, so we can integrate it numerically once and for all to identify the values for which the curve $\lambda_0 = \lambda_0(M_0)$ has a global minimum. It is found that the critical values are $(\lambda_0^*, M_0^*) = (65.0663, 6.6399)$.

Some comparisons with direct numerical simulations are included in Figure 3-6. It can be clearly seen that the asymptotic solution for $0 < \mu \ll 1$ is applicable even for $0 < \mu \lesssim 2.0$, since its relative error is within 5% for this range of μ. Unfortunately, the asymptotic analysis can be executed only to the leading order – similar limitations were encountered in a couple of recent works [34, 42].
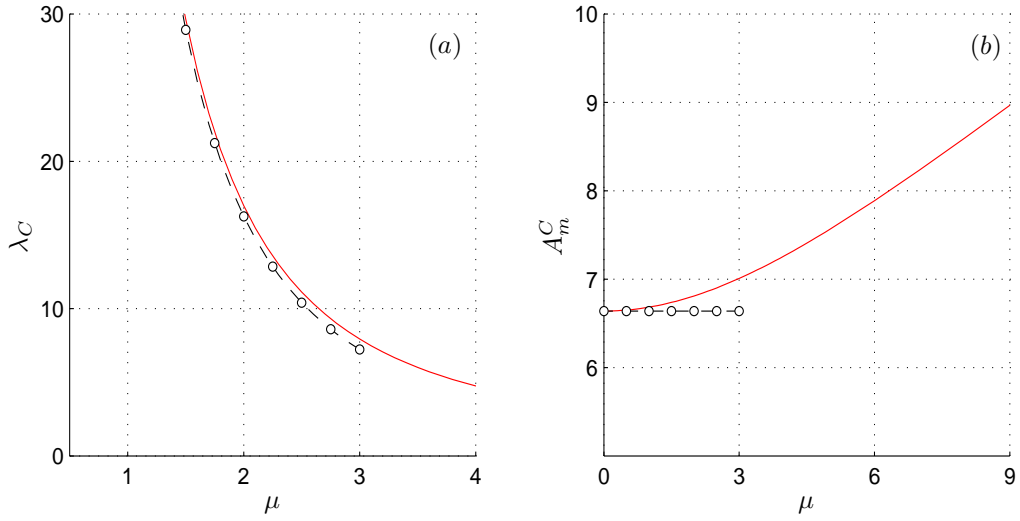
Figure 3-6: Plot (a) shows the comparison between the asymptotic approximation $\lambda_C \simeq \lambda_0^*/\mu^2$ (*circle-dashed*) and its counterpart obtained by direct numerical simulations (*continuous line*) in the case of a clamped-edge rectangular plate. Plot (b) gives an idea about a similar comparison of A_m^C involving the corresponding mode numbers.

Free edges

For the free-edge case, informed by numerical simulations, we expect the critical A_m to approach zero as $\mu \to 0$ and λ_C is found to display a similar blow-up behaviour as seen previously. However, the asymptotic structure of the limiting case is somewhat different (the asymptotic analysis from Eq. (3.26) to (3.35) was obtained by the first author of [50]. For the sake of self-consistency, they are recorded here with acknowledgement). It turns out that this time we need an ansatz of the form

$$W(y) = W_0(y) + W_1(y)\mu + W_2(y)\mu^2 + \dots, \tag{3.26a}$$

$$\lambda = \lambda_0\mu^{-1} + \lambda_1 + \lambda_2\mu + \dots, \tag{3.26b}$$

$$(A_m)^2 = M_0\mu^2 + M_1\mu^3 + \dots. \tag{3.26c}$$

Substituting (3.26) into the bifurcation equation (3.6) and setting to zero the coefficients of successive powers of μ we obtain

$$\mathcal{O}(1): \quad W_0'''' = 0, \tag{3.27a}$$

$$\mathcal{O}(\mu): \quad W_1'''' = 0, \tag{3.27b}$$

$$\mathcal{O}(\mu^2): \quad W_2'''' - (1 + 2M_0)W_0'' = 0, \tag{3.27c}$$

$$\mathcal{O}(\mu^3): \quad W_3'''' - (1 + 2M_0)W_1'' - 2M_1W_0'' + 6M_0(2y - 1)\lambda_0W_0 = 0. \tag{3.27d}$$

Similarly, plugging (3.26) into the boundary conditions (3.8), we derive the constraints that W_j (for $j = 1, 2, \dots$) must satisfy at $y = 0, 1$

$$W_0'' = 0\,, \qquad\qquad\qquad W_0''' = 0\,, \tag{3.28a}$$

$$W_1'' = 0\,, \qquad\qquad\qquad W_1''' = 0\,, \tag{3.28b}$$

$$W_2'' - \nu M_0 W_0 = 0\,, \qquad\qquad W_2''' - [1 + (2 - \nu)M_0]\,W_0' = 0\,, \tag{3.28c}$$

$$W_3'' - \nu M_0 W_1 - \nu M_1 W_0 = 0\,, \qquad W_3''' - [1 + (2 - \nu)M_0]\,W_1' - (2 - \nu)M_1 W_0' = 0\,. \tag{3.28d}$$

Finally, the critical buckling mode condition (3.14) can be expanded in powers of μ and results in the following additional constraints

$$\mathcal{O}(1): \quad \int_0^1 \left[\nu W_0 W_0'' - (1 - \nu)W_0'^2\right]\,\mathrm{d}y = 0\,, \tag{3.29a}$$

$$\mathcal{O}(\mu): \quad \int_0^1 \left[\nu W_0 W_1'' - 2(1 - \nu)W_0'W_1' + \nu W_0''W_1 + \Gamma_1\right]\,\mathrm{d}y = 0\,, \tag{3.29b}$$

$$\mathcal{O}(\mu^2): \quad \int_0^1 \left[\nu W_0 W_2'' - 2(1 - \nu)W_0'W_2' + \nu W_0''W_2 + \Gamma_2\right]\,\mathrm{d}y = 0\,, \tag{3.29c}$$

where

$$\Gamma_1 := -\,3(2y - 1)\lambda_0 W_0^2\,,$$

$$\Gamma_2 := \nu W_1 W_1'' - (1 - \nu)W_1'^2 - 6(2y - 1)\lambda_0 W_0 W_1 - \left[M_0 + 3(2y - 1)\lambda_1 - \frac{1}{2}\right] W_0^2\,.$$

The leading order equation (3.27a) together with the boundary conditions (3.28a) leads to the general solution $W_0(y) = \gamma_1 y + \gamma_2$ in which $\gamma_1, \gamma_2 \in \mathbb{R}$ are constants that will be fixed as we go along. On substituting this W_0 into (3.29a) results in $\gamma_1 = 0$, and hence $W_0(y) = \gamma_2$; without any loss of generality we can assume $\gamma_2 = 1$.

Next, considering the equation (3.27b) subject to the end constraints (3.28b) yields

$$W_1(y) = \gamma_3 y + \gamma_4\,,$$

where $\gamma_3, \gamma_4 \in \mathbb{R}$ are constants. Note that γ_4 can be taken to be zero because of the homogeneous nature of the problem and, as we have $W_0(y)$ already, it is only γ_3 that needs to be determined. To this end, we carry on with solving the next order problem, consisting of (3.27c) in conjunction with (3.28c); some simple algebra eventually leads to

$$W_2(y) = \frac{1}{2}\nu M_0 \gamma_2 y^2\,.$$

We mention in passing that the criticality constraint (3.29b) is identically satisfied with the

information we have thus far, so we need to look at (3.29c). It transpires that

$$(1-\nu)\gamma_3^2 + \lambda_0\gamma_2\gamma_3 + \left[(1-\nu^2)M_0 + \frac{1}{2}\right]\gamma_2^2 = 0\,, \tag{3.31}$$

an equation that will be used shortly to identify λ_0. After some further manipulations, the solution of (3.27d) and (3.28d) is found to be

$$W_3''(y) = -6M_0\left(\frac{y^3}{3} - \frac{y^2}{2}\right)\lambda_0\gamma_2 + \gamma_5 y + \gamma_6\,, \tag{3.32}$$

with

$$\gamma_5 := (\nu\gamma_3 - \lambda_0\gamma_2)M_0, \qquad \gamma_6 := \nu M_1\gamma_2\,;$$

in the course of reaching equation (3.32) it also emerges that

$$\gamma_3 = -\left[\frac{M_0\lambda_0}{1 + 2(1-\nu)}\right]\gamma_2\,.$$

On substituting this value of γ_3 into (3.31) we arrive at

$$\lambda_0^2 = \frac{M_0(1-\nu^2) + \frac{1}{2}}{\omega_2 M_0 - \omega_1 M_0^2}\,, \tag{3.33}$$

where

$$\omega_1 := \frac{1-\nu}{[1+2(1-\nu)]^2} \qquad \text{and} \qquad \omega_2 := \frac{1}{1+2(1-\nu)}\,.$$

As we aim for the lowest critical load, this expression must be minimised with respect to M_0, i.e. $\partial\lambda_0^2/\partial M_0 = 0$. The result is a quadratic algebraic equation for M_0, whose unique positive root will give the critical value

$$M_0^* = \frac{-1 + \sqrt{7 + 2\nu - 4\nu^2}}{2(1-\nu^2)}\,. \tag{3.34}$$

The corresponding critical value of λ_0 is obtained by substituting (3.34) into (3.33), i.e.

$$\lambda_0^* = \lambda_0\big|_{M_0=M_0^*}\,. \tag{3.35}$$

To assess the relevance and usefulness of these last two formulae, a representative sample of comparisons between them and direct numerical simulations is summarised in Figure 3-7.
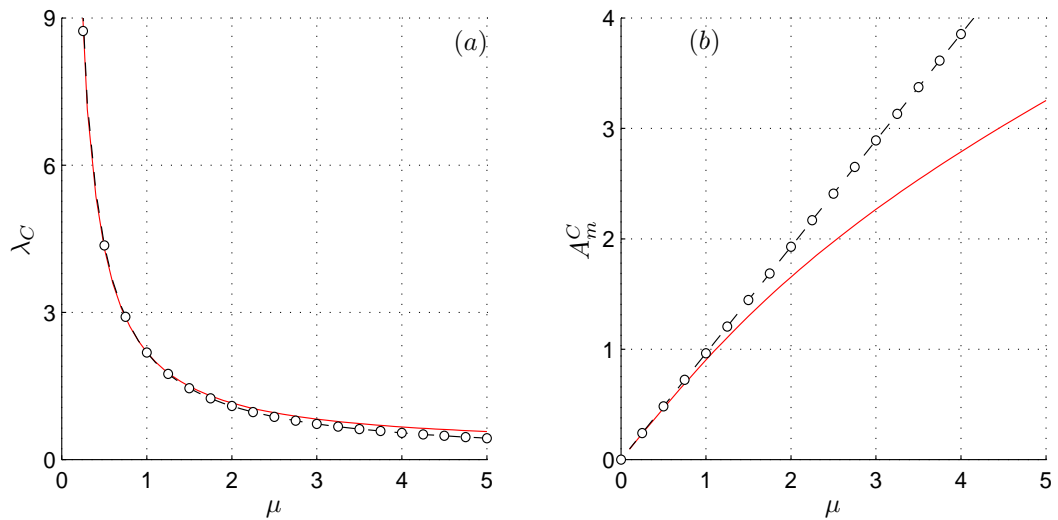
Figure 3-7: Free-edge rectangular plate: plot (a) includes the comparison between the asymptotic approximation $\lambda_C \simeq \lambda_0^*/\mu$ (*small circles*) given by (3.35) and direct numerical simulations. The accuracy of (3.26c) and (3.34) on A_m^C can be appreciated by inspecting plot (b).

The remarks made in the previous section vis-á-vis the range of applicability of the results derived for the free-edge case remain valid. Relative errors between asymptotics and numerics are roughly 5% for $0 < \mu \lesssim 2.0$. Further work, not discussed here, has shown that the term λ_1 in the asymptotic ansatz (3.26b) is negative. Once obtained, that term does improve the accuracy of the approximation as μ gets closer and closer to zero, but within the range $1.0 < \mu < 2.0$ the results become worse.

3.4 Annular plate

Full details of this model and a comprehensive asymptotic analysis can be found in [41, 47]; only the most important aspects are highlighted below. We consider an annular plate with inner radius R_1, outer radius R_2, and thickness h ($h \ll R_2$) – as shown in Figure 3-8. This configuration is stretched by applying uniform radial displacement fields U_1 and U_2 on the inner and outer rims respectively. The Lamé solution for the corresponding plane stress problem reveals the presence of compressive stresses near the inner rim. Coupled with the same Föppl–von Kármán buckling equation as in §3.3, the bifurcation problem that results is reduced to an *ODE* by using the separable variables solution

$$w(r,\theta) = W(r)\cos n\theta \,,$$

where $n \in \mathbb{N}$ is the mode number (equal to half the number of identical wrinkles in the azimuthal direction). The final result reads

$$W'''' + \mathcal{P}_3(\rho)W''' + \mathcal{P}_4(\rho)W'' + \mathcal{P}_5(\rho)W' + \mathcal{P}_6(\rho)W = 0 \,, \quad \eta < \rho < 1 \,, \qquad (3.36)$$
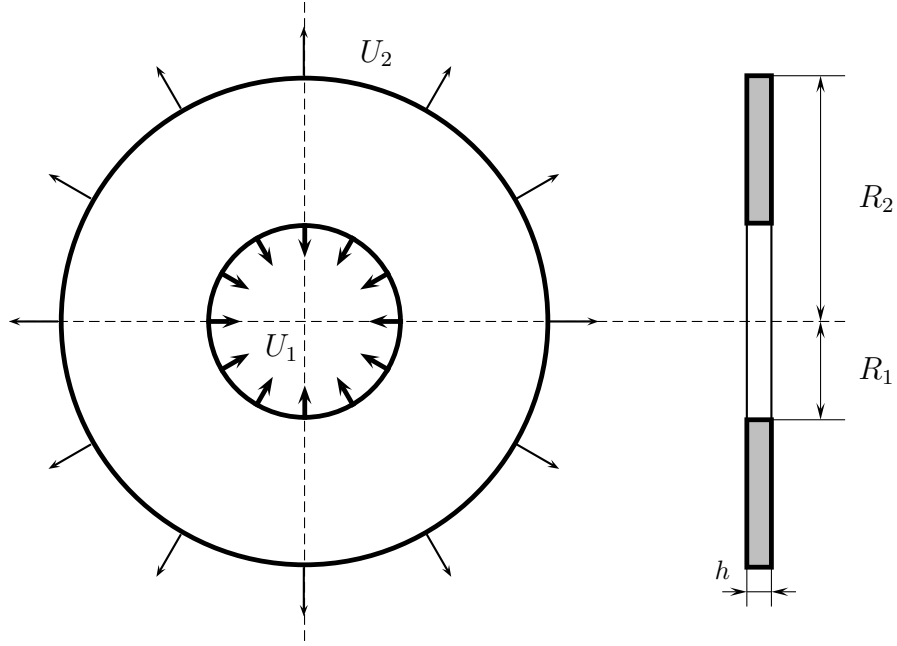
Figure 3-8: An annular plate subject to uniform displacement fields on its boundaries. For a sufficiently large ratio U_1/U_2, localised buckling emerges near the central hole.

where

$$\eta := \frac{R_1}{R_2}, \qquad \rho := \frac{r}{R_2},$$

and the rescaled W is denoted by the same letter to avoid overloading the notation. The coefficients of (3.36) are defined by

$$\mathcal{P}_3(\rho) := \frac{2}{\rho}, \qquad\qquad \mathcal{P}_4(\rho) := -\left[\frac{2n^2+1}{\rho^2} + \mu^2\left(A + \frac{B}{\rho^2}\right)\right],$$

$$\mathcal{P}_5(\rho) := \frac{1}{\rho}\left[\frac{2n^2+1}{\rho^2} - \mu^2\left(A - \frac{B}{\rho^2}\right)\right], \quad \mathcal{P}_6(\rho) := \frac{n^2}{\rho^2}\left[\frac{n^2-4}{\rho^2} + \mu^2\left(A - \frac{B}{\rho^2}\right)\right],$$

with

$$A := (1+\nu)\frac{1+\lambda\eta}{1-\eta^2}, \qquad B := (1-\nu)\frac{\eta^2+\lambda\eta}{1-\eta^2}, \tag{3.37a}$$

$$\lambda := \frac{U_1}{U_2}, \qquad \mu^2 := \frac{12U_2 R_2}{h^2}. \tag{3.37b}$$

For the sake of brevity only clamped boundary conditions are considered. In terms of the amplitude $W(\rho)$ these are

$$W(\rho) = W'(\rho) = 0 \quad \text{at} \quad \rho = 0, 1. \tag{3.38}$$

In [41, 45], Coman and Bassom provided a detailed asymptotic investigation of the aforementioned model. They showed that the neutral stability envelope can be obtained by various

expansions in suitable powers of $\mu \gg 1$,

$$W(Y) = W_0(Y) + W_1(Y)\mu^{-1/2} + \mathcal{O}(\mu^{-1}) , \qquad Y := \mu^{1/2}(\rho - \eta) \tag{3.39a}$$

$$(n_C)^2 = N_0^* \mu^{3/2} + \mathcal{O}(\mu) , \tag{3.39b}$$

$$\lambda_C = \lambda_0 + \lambda_1^* \mu^{-1/2} + \lambda_2^* \mu^{-1} + \mathcal{O}(\mu^{-3/2}) , \tag{3.39c}$$

where,

$$N_0^* = \left(\frac{2}{3} \zeta_0 \eta^2 \hat{A}_0 \right)^{3/4} , \tag{3.40a}$$

$$\lambda_0 = \frac{2\nu\eta}{1 - \nu - \eta^2(1+\nu)} , \tag{3.40b}$$

$$\lambda_1^* = 4N_0^* G , \tag{3.40c}$$

$$\lambda_2^* = 2\eta^2 G \left[4\zeta_0 (N_0^*)^{2/3} \left(G\hat{A}_1 + \frac{1}{2\eta^2} \right) + \frac{(\hat{A}_0)^{1/2}}{\eta\sqrt{2}} \right] ; \tag{3.40d}$$

$(-\zeta_0) \simeq -2.3381$ represents the first zero of the Airy function Ai, and we have introduced the notations

$$\hat{A}_0 := \frac{(1+\nu)(1+\lambda_0\eta)}{1-\eta^2} , \qquad \hat{A}_1 := \frac{(1+\nu)\eta}{1-\eta^2} , \tag{3.41a}$$

$$G := \frac{1-\eta^2}{\eta(1-\nu) - \eta^3(1+\nu)} . \tag{3.41b}$$

Note that in the expansion of $(n_C)^2$, only the critical value N_0^* is available – as pointed out in [41] the effort required to find N_1^* is significant. Thus, improving on these results is far from being a lightweight undertaking.

The hybrid energy method for the annular plate proceeds along the same route as in §3.3.1; the ansatz that we use is given by

$$\lambda \simeq \lambda_C \equiv \lambda_0 + \lambda_1^* c_1 , \quad n^2 \simeq (n_C)^2 \equiv N_0^* c_2 , \quad W(\rho) = W_0(\rho) + W_1(\rho)c_3 + \dots , \tag{3.42}$$

where

$$W_0(\rho) = \text{Ai}\left(\frac{N_0^{*1/3} \mu^{1/2}}{\eta} (\rho - \eta) + \zeta_0 \right) . \tag{3.43}$$

Since in this case $W_1(\rho)$ is not easily available, our approximation will have only two degrees of freedom (c_1 and c_2). These constants are found from (3.10), which for an annular plate becomes

$$\int_\eta^1 \left[\Pi_3 W''^2(\rho) + \Pi_4 W'^2(\rho) + \Pi_5 W^2(\rho) \right] d\rho = 0 , \tag{3.44}$$
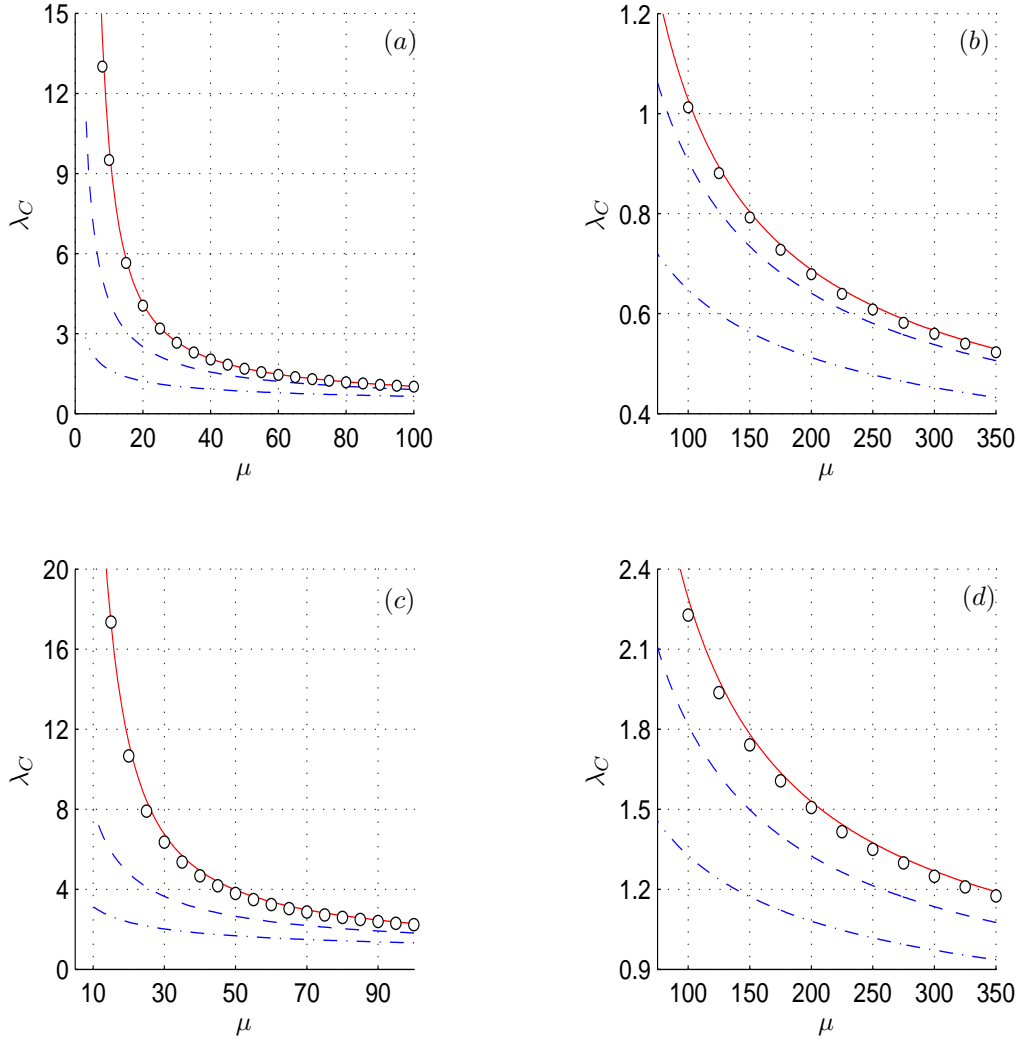
Figure 3-9: Comparisons of the various approximations of the critical eigenvalue $\lambda_C \equiv \lambda_C(\mu)$: two- (*dot-dashed line*) & three-term (*dashed line*) asymptotic results, the hybrid energy method (*small circles*), and the direct numerical results (*continuous line*) for the stretched annular plate. Here $\eta = 0.2$ in (*a*), (*b*) and $\eta = 0.4$ in (*c*), (*d*).

with

$$\Pi_3 := \rho \,, \qquad \Pi_4 := \frac{2n^2 + 1}{\rho} - \Delta_1(1 + \lambda\eta)\rho - \Delta_2 \frac{\eta(\lambda + \eta)}{\rho} \,,$$

$$\Pi_5 := \frac{n^2(n^2 - 4)}{\rho^3} - \frac{n^2}{\rho}\left(\Delta_1 - \frac{\Delta_2}{\rho^2}\right)(\lambda\eta + 1) \,,$$

and

$$\Delta_1 := \frac{\mu^2(1 + \nu)}{1 - \eta^2} \,, \qquad \Delta_2 := \frac{\mu^2(1 - \nu)}{1 - \eta^2} \,.$$

An additional equation is obtained from the criticality condition in (3.12) by replacing A_m^2 by n^2, namely,

$$\int_\eta^1 \left[\Pi_6 W'^2(\rho) + \Pi_7 W(\rho)W'(\rho) + \Pi_8 W^2(\rho)\right]\mathrm{d}\rho = 0 \,, \tag{3.45}$$

EIGENVALUE PROBLEMS & ELASTIC INSTABILITIES
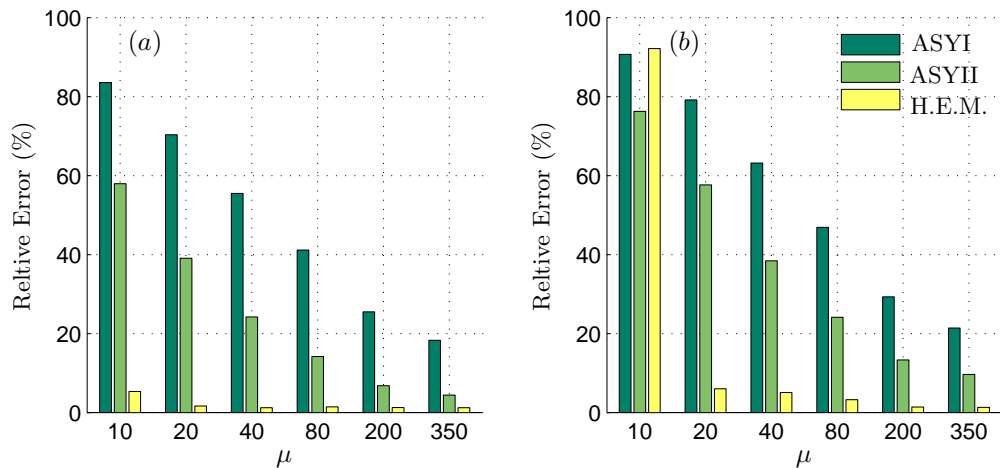
Figure 3-10: Relative errors with respect to the corresponding direct numerical solution for the three approximations seen in Fig. 3-9: two- ($ASYI$) and three-term ($ASYII$) asymptotic approximations of the critical eigenvalue $\lambda_C = \lambda_C(\mu)$, together with the hybrid energy method ($H.$ $E.$ $M.$) for a stretched annulus with $\eta = 0.2$ in (a) and $\eta = 0.4$ in (b).

where

$$\Pi_6 := \frac{2}{\rho^2}, \quad \Pi_7 := -\frac{2}{\rho^3}, \quad \Pi_8 := \frac{\mu^2}{\rho^2}\left(A - \frac{B}{\rho^2}\right) + \frac{2(n^2 - 2)}{\rho^4},$$

and the expressions of A and B were defined in (3.37). These equations will be used in the numerical strategy described in §3.3.1 and already employed in the previous section, so we omit the details.

In contrast to the rectangular plate, we now have an extra parameter, $0 < \eta < 1$, so our comparisons between asymptotic and numerics will have to reflect this new addition. Figure 3-9 shows a first set of comparisons for $\eta = 0.2$ and, respectively, $\eta = 0.4$, complemented by the corresponding relative errors plots in Figure 3-10. The results of the hybrid energy method based on the one-term ansatz (3.43) appear to perform better than both the two- and three-term asymptotic approximations derived in [41]. More specifically, when $\eta = 0.2$ as in Figure 3-10 (a), the relative errors between the values computed with the former approach and direct numerical simulations lie between 1.06% and 1.66% for μ in the range $[20.0, 350.0]$, but they tend to deteriorate quickly as $\mu \simeq 10.0$ because the boundary condition $W(1) = 0$ starts to be violated in that instance. The situation is more evident when $\eta = 0.4$ as in Figure 3-10 (b), the relative errors of the current energy method is below 6.25% to for $\mu \in [14.0, 350.0]$, but deteriorate sharply when $\mu \simeq 10.0$ ($R.E. \simeq 92.16\%$ in that case). Given our previous experience from §3.3.1 this is not unexpected.

A different set of comparisons is presented in Figures 3-11 and 3-13, which contain the neutral stability envelopes for the stretched annulus. It is known that the individual curves $\lambda = \lambda(\eta; m)$ for $m = 2, 3, \dots$ satisfy $\lim_{\eta \to 0} \lambda(\eta; m) = +\infty$, and therefore the envelope of this family of curves is expected to have the same characteristic. However, the asymptotic analysis proposed in [41] was conducted under the assumption that $\eta = \mathcal{O}_S(1)$, so the approximations of

EIGENVALUE PROBLEMS & ELASTIC INSTABILITIES
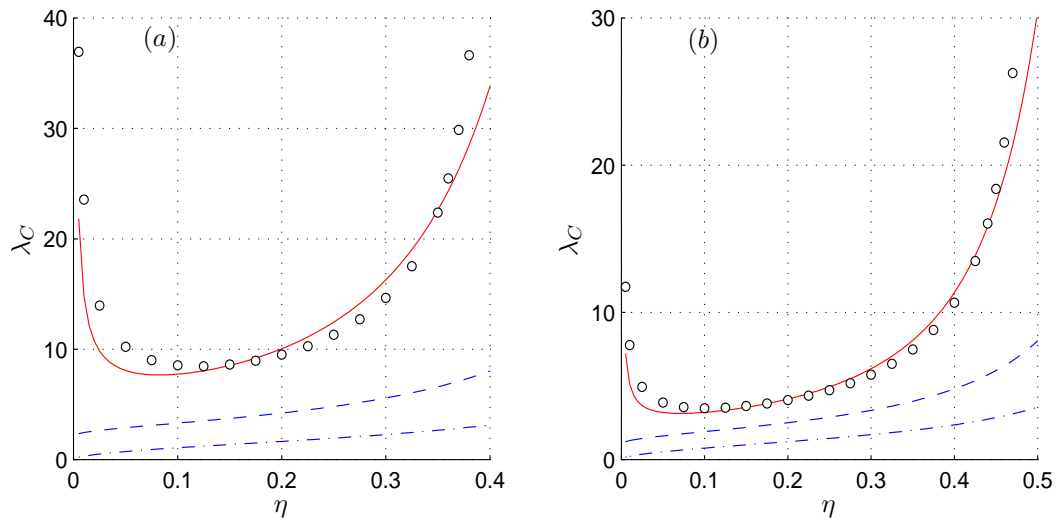
Figure 3-11: Dependence on η of the two- (*dot-dashed line*) & three-term (*dashed line*) asymptotic results, the hybrid energy method (*small circles*), and the direct numerical results (*continuous line*) for the stretched annular plate: $\mu = 10.0$ (*a*) and $\mu = 20.0$ (*b*).
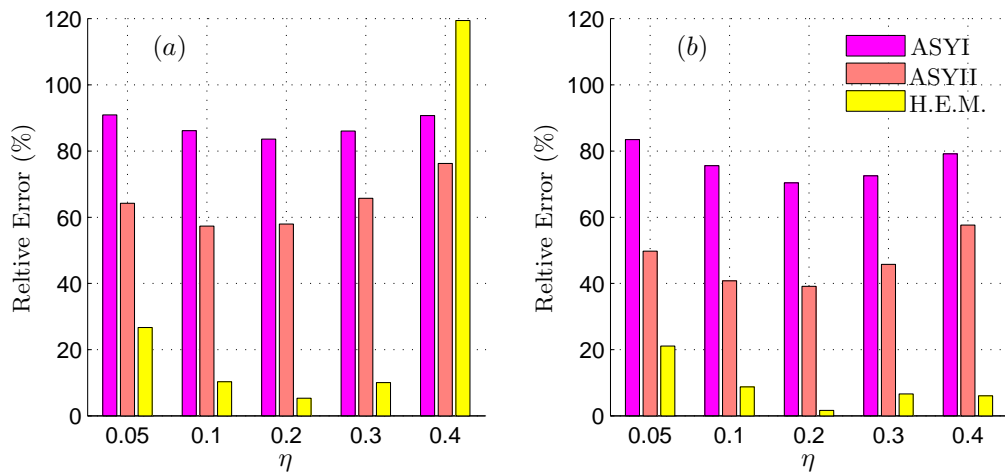
Figure 3-12: Relative errors with respect to the direct numerical solutions for two- ($ASYI$) and three-term ($ASYII$) asymptotic approximations of the critical eigenvalue $\lambda_C = \lambda_C(\eta)$ and the hybrid energy method (*H. E. M.*); the data corresponds to the information shown in Fig. 3-11 Here, $\mu = 10.0$ (*a*) and $\mu = 20.0$ (*b*).

the envelope derived there, and reproduced here as the dot-dashed/dashed lines for convenience, cannot be expected to be a faithful description of what happens for $\eta \simeq 0$. This statement does not contradict the results obtained by Coman and Bassom in [41] since for $\mu \gg 1$ the range of η for which their formula is not accurate is extremely small; in fact, it can be argued that to the level of accuracy of visual inspection their formulae perform very well for the entire range of *realistic* values of η. Indeed, (3.39c) plays the role of some sort of outer approximation for $|\eta - 1| \ll 1$ that can be complemented by a similar expression for $\eta \to 0$. Interestingly enough, the hybrid energy approximation is free of such shortcomings and it appears to follow the numerical envelope quite closely. The relative errors in Figure 3-11(a) are admittedly large

because $\mu = 10.0$, but they decrease quickly as this parameter increases. For example, in Figure 3-13(a) ($\mu = 40.0$) they are within 5.20% for $\eta \in [0.01, 0.5]$, while in Figure 3-13(d) ($\mu = 350.0$) the maximum relative error is 1.5% for $0.05 < \eta < 0.5$. We also want to point out that the blow-up of λ (both the numerical solution and our current approximations) is present in all four plots in Figure 3-13, but it is not emphasised since the $\eta-$region over which this behaviour occurs is awkward to represent graphically; furthermore, this regime has very little relevance from a practical point of view.
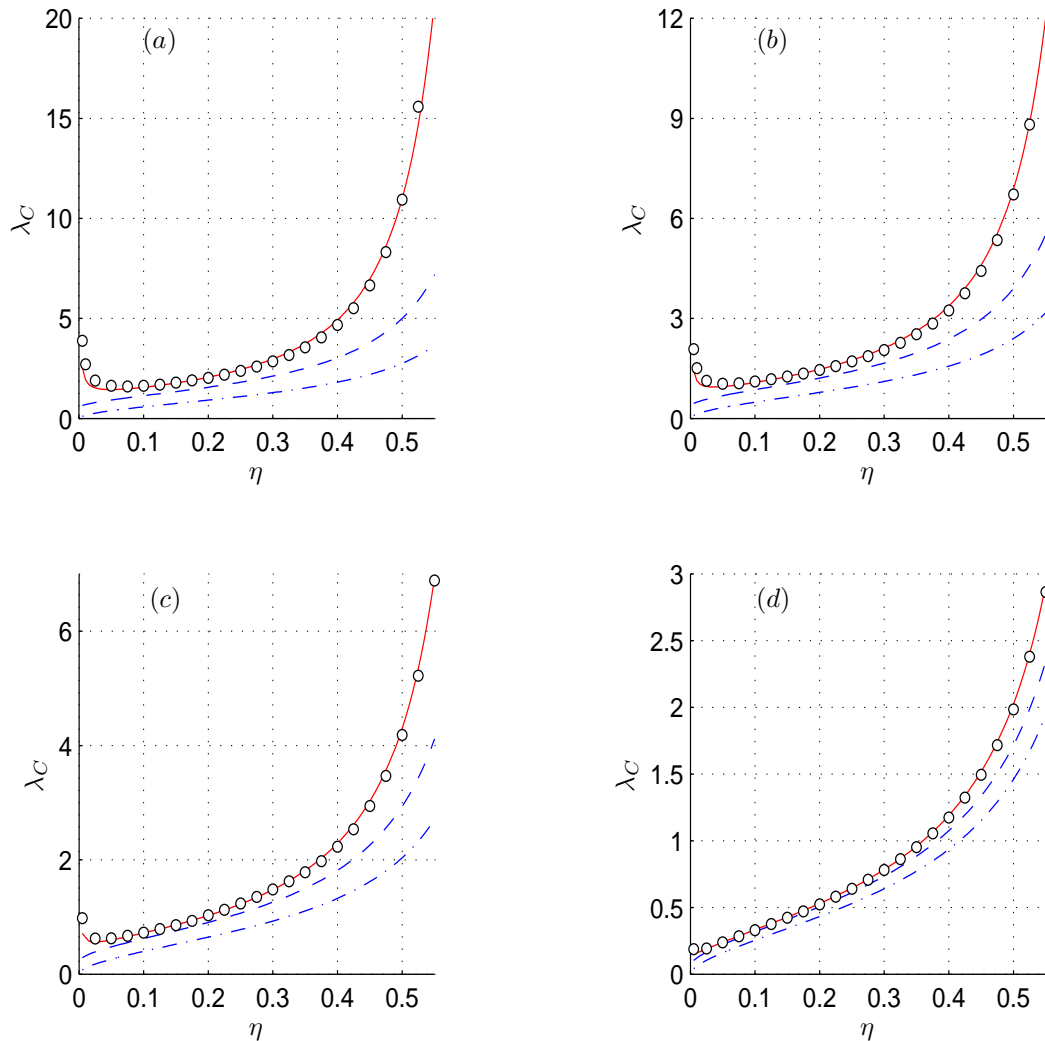
Figure 3-13: Same as per Fig. 3-11, except that $\mu = 40.0$ in (a), $\mu = 60.0$ in (b), $\mu = 100.0$ in (c), and $\mu = 350.0$ in (d).

3.4.1 The small-μ limit for the annular plate

By analogy with the clamped-edge rectangular plate, since the annular plate is also subjected to the same type of boundary constraints, we anticipate that $\lambda_C = \mathcal{O}(\mu^{-2})$ and $n_C = \mathcal{O}(1)$ when $\mu \to 0$; this expectation was also confirmed by the direct numerical simulations. Therefore, we
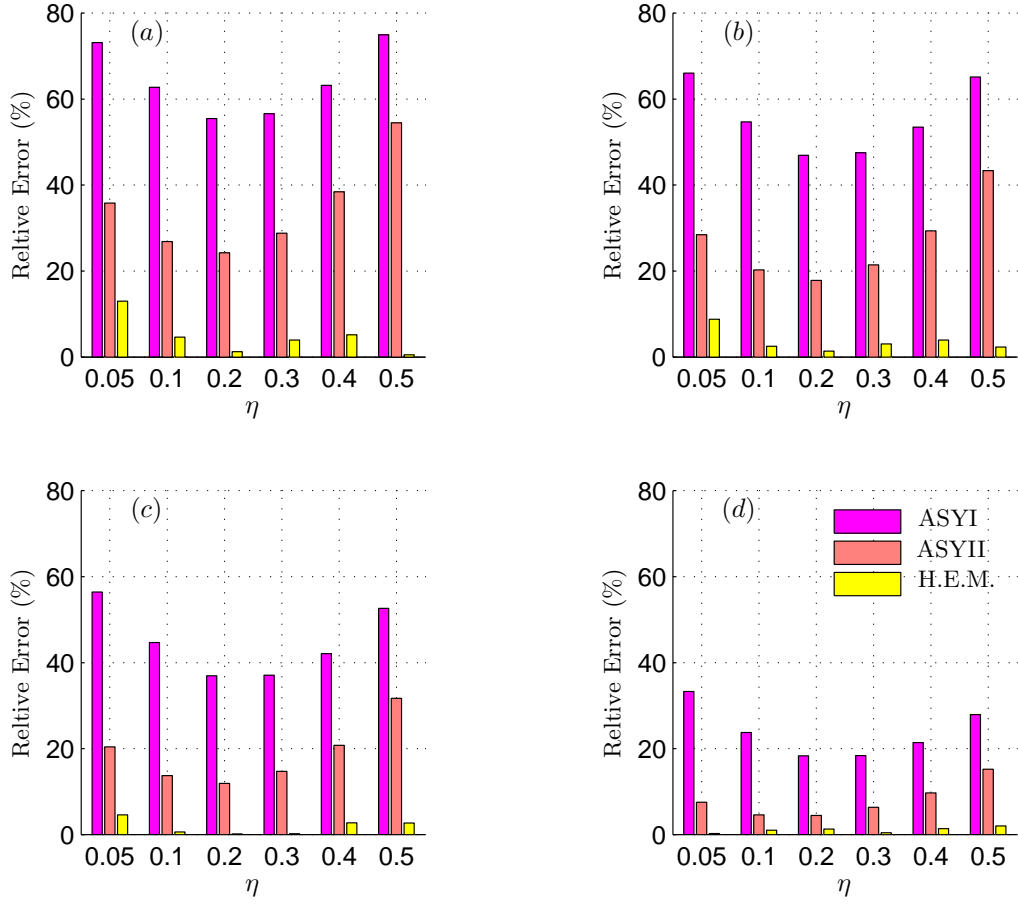
Figure 3-14: Same as per Fig. 3-12, except that $\mu = 40.0$ in (a), $\mu = 60.0$ in (b), $\mu = 100.0$ in (c), and $\mu = 350.0$ in (d), which corresponds to the (a), (b), (c), (d) in Fig. 3-13.

adopt the ansatz

$$W(\rho) = W_0(\rho) + W_1(\rho)\mu^2 + \dots, \tag{3.46a}$$

$$\lambda = \lambda_0\mu^{-2} + \lambda_1 + \lambda_2\mu^2 + \dots, \tag{3.46b}$$

$$n^2 = N_0 + N_1\mu^2 + \dots. \tag{3.46c}$$

Substituting the above formulae into the original bifurcation equation (3.36) and collecting the leading order terms, yields the simplified differential equation as

$$W_0'''' + \mathcal{C}_3(\rho)W_0''' + \mathcal{C}_2(\rho)W_0'' + \mathcal{C}_1(\rho)W_0' + \mathcal{C}_0(\rho)W_0 = 0, \tag{3.47}$$

where

$$\mathcal{C}_3(\rho) := \frac{2}{\rho}, \qquad\qquad \mathcal{C}_2(\rho) := -\left(A_0 + \frac{2N_0 + B_0 + 1}{\rho^2}\right),$$

$$\mathcal{C}_1(\rho) := \frac{1}{\rho}\left(-A_0 + \frac{2N_0 + B_0 + 1}{\rho^2}\right), \qquad \mathcal{C}_0(\rho) := \frac{N_0}{\rho^2}\left(A_0 + \frac{N_0 - B_0 - 4}{\rho^2}\right),$$

and

$$A_0 := \frac{(1+\nu)\lambda_0\eta}{1-\eta^2}, \qquad B_0 := \frac{(1-\nu)\lambda_0\eta}{1-\eta^2};$$

the boundary conditions (3.38) remain the same.

It is obvious that, when $\mu \to 0$ (the limiting situation when the rescaled bending stiffness of the plate becomes infinite), μ does not appear in both the simplified differential equation and the boundary conditions (3.38), therefore, the solutions of the simplified problem are independent of μ. However, the additional parameter η is involved here compared with the clamped-edge rectangular plate. Solving the above simplified problem, the eigenvalue $\lambda_0 = \lambda_0(\eta, N_0)$. For a given η, we have a global minimum for λ_0^* with respect to the critical N_0^*, which are shown in Figure 3-15.
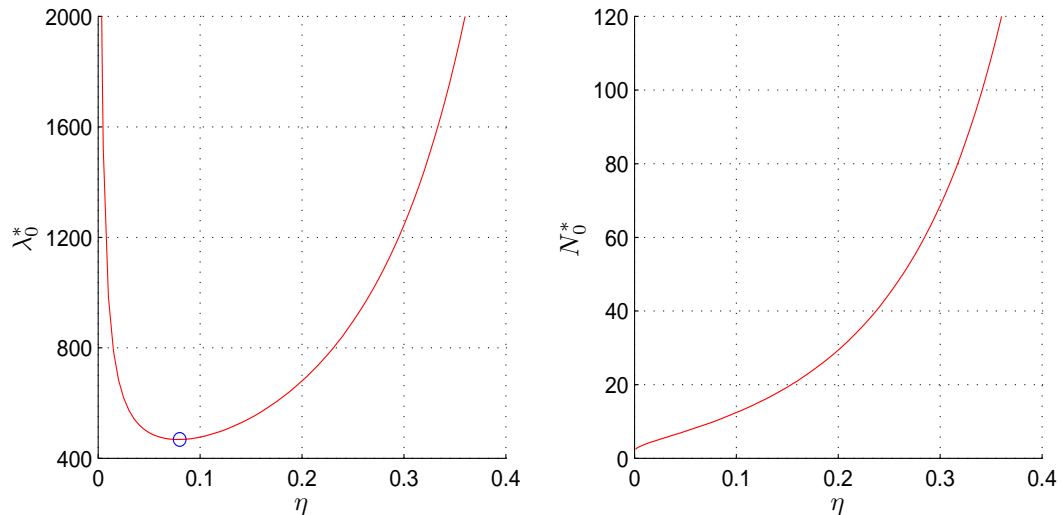
Figure 3-15: The critical eigenvalues $\lambda_0^*(\eta)$ with respect to the mode-number parameter N_0^* when solving the reduced problem equation (3.47). The right window shows the corresponding critical $N_0^*(\eta)$. Notice that, there is a minimum in the left window ($\eta \simeq 0.08, \lambda_0^* \simeq 468.1059$).

It is found from Figure 3-15 that, as η ranges from 0 to 0.4, λ_0^* shows a parabola-like tendency; moreover, $\lambda_0^*(\eta)$ has a minimum at $\eta \simeq 0.08$. It is therefore apparent that the curve of $\lambda_C(\eta)$ with $\lambda_C = \lambda_0\mu^{-2}$ also possesses a minimum near $\eta \simeq 0.08$ (for example, when $\mu = 40, 60, 100$ as in Figure 3-13 (a), (b), (c). In addition, the validity of this asymptotic approximation can also be checked by comparing its predictions with the direct numerical simulations in Figure 3-16 when $\mu = 2.0$.
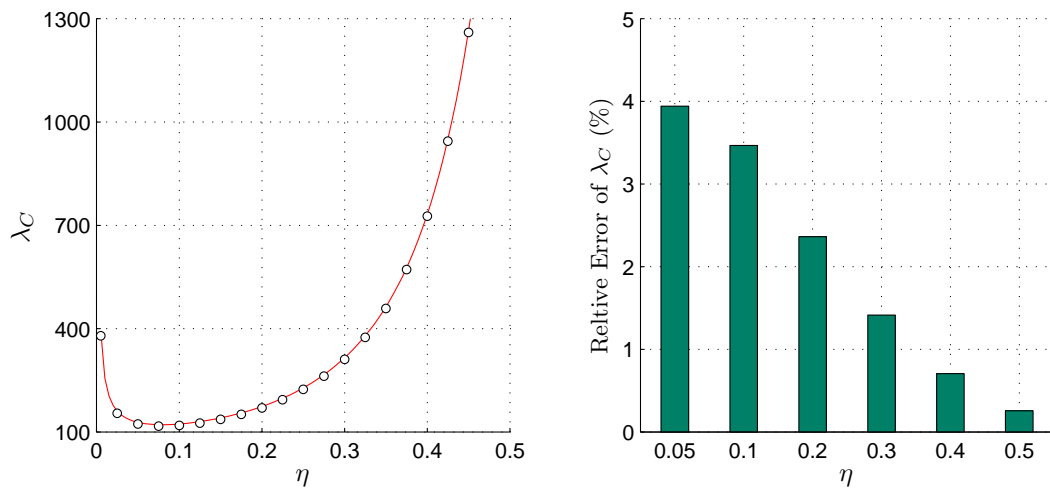
Figure 3-16: Comparison between the asymptotic approximation $\lambda_C \simeq \lambda_0^*/\mu^2$ (*continuous line*) and its counterpart obtained by direct numerical simulations (*small circles*) for an annular plate with clamped edges and $\mu = 2.0$. In the right bar chart we show the relative errors with respect to the direct numerical results, which are within 4% for the entire range of η.

It can be observed that the relative errors of asymptotic approximations for $0 < \mu \ll 1$ is even applicable for $\mu = 2.0$ ($R.E. \leq 4\%$). Similar with the clamped-edge rectangular case, only the leading order of the asymptotic analysis is worth conducting, otherwise more sophisticated numerical work is involved.

3.5 A more refined ansatz
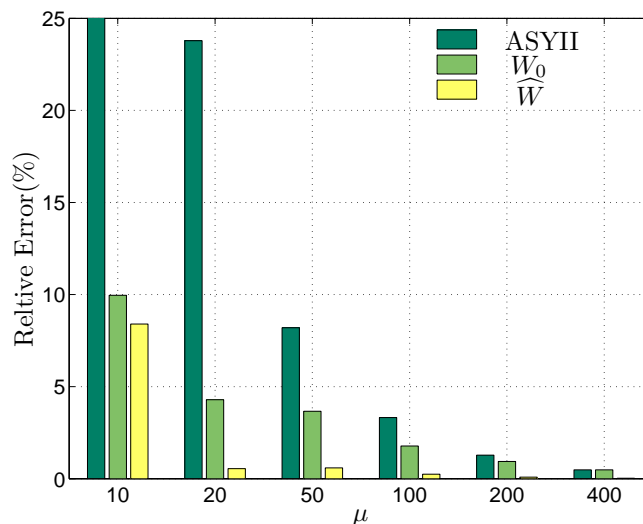
Figure 3-17: Comparison between the relative errors of several approximations on the critical eigenvalues with respect to the direct numerical simulations for the clamped-edge rectangular plate, the values of $ASYII, W_0, \widehat{W}$ shown here are the same as Tab. 3.3.

It was mentioned in §3.3.1 that a more suitable ansatz for the problems discussed in this work

Table 3.3: Comparisons between various approximations of the critical eigenvalues and direct numerical simulations (NUM) for the edge-buckling of a clamped rectangular plate. The following conventions are used: $ASYII$ represents the asymptotic result $\lambda_C := \lambda_0 + \lambda_1^* \mu^{-1/2} + \lambda_2^* \mu^{-1}$ from the paper [44]; W_0 denotes the values of λ obtained via the hybrid energy method with the simplest ansatz $W = W_0$; finally, $\widehat{W}$ is used to identify the approximate eigenvalues obtained with the test function (3.48). The relative errors with respect to the corresponding direct numerical results are recorded in the last three columns.

μ	NUM	$ASY(II)$	W_0	$\widehat{W}$	$R.E.ASY(II)$ (%)	$R.E.W_0$ (%)	$R.E.\widehat{W}$ (%)
10.0	1.226536	0.676648	1.348720	1.329550	44.8326	9.9617	8.3988
20.0	0.620428	0.472876	0.593808	0.617041	23.7824	4.2906	0.5460
30.0	0.468225	0.397007	0.448233	0.464508	15.2103	4.2696	0.7939
40.0	0.399122	0.355988	0.384502	0.396310	10.8073	3.6630	0.7045
50.0	0.359254	0.329800	0.347982	0.357133	8.1988	3.1377	0.5904
100.0	0.280448	0.271139	0.275470	0.279756	3.3196	1.7751	0.2470
200.0	0.238152	0.235099	0.235919	0.237944	1.2819	0.9377	0.0873
300.0	0.222183	0.220574	0.220768	0.222085	0.7244	0.6367	0.0443
400.0	0.213362	0.212336	0.212333	0.213306	0.4809	0.4821	0.0263

would be one which incorporates the effect of the $\mathcal{O}(\mu^{-1})$ bending layer. Prompted by that observation we shall now consider replacing W in (3.16) by

$$\widehat{W}(y) = \mathrm{Ai}(Z) + \mu^{-1/2}\left\{ \beta_1 \mathrm{Ai}'(Z) + \beta_2 \mathrm{Ai}'''(Z) + \mathrm{Ai}'(\zeta_{02})\exp(-\mu y) \right\}, \qquad (3.48)$$

where $Z := \omega \mu^{1/2} y + \zeta_{02}$ and β_j $(j = 1, 2)$ are the complicated expressions defined in equation (17) of [44]. Comparisons with various other results obtained previously are recorded in Table 3.3 and the corresponding relative errors in Figure 3-17. The data included there indicates a significant improvement over both the asymptotic results reported in [41] and the earlier results from our hybrid energy method. It can be shown that the free-edge case for the rectangular plate is amenable to a similar treatment by following the analysis available in [44], although things are considerably more involved for the annular plate. That is partly due to the fact that one has to take the asymptotic analysis of [41] to the next order.

Refining the ansatz (3.16) or (3.43) as indicated above can only provide a sensible improvement as long as μ does not get too small, typically $\mu \gtrsim 10.0$. Indeed, the analysis of Geer and Andersen in [4, 5, 6] suggests that for lower μ-values one would have to augment the Rayleigh–Ritz ansatz by terms coming from the asymptotic analysis in which $0 < \mu \ll 1$. Unfortunately, as we have already seen in §3.3.2 for the clamped plate, the expression of the corresponding eigenmodes is not immediately available in closed form. While in principle we can construct the refined ansatz and use numerical methods to carry out the programme outlined in §3.3.1, there is little scope in pursuing it as this would defeat the whole purpose of using the hybrid

energy method in the first place.

3.6   Discussion and conclusions

Motivated by recent work on the bending instabilities of thin elastic plates in tension (e.g., [41, 44]), a hybrid energy method has been proposed to improve upon those earlier results. With the help of a special ansatz informed by the asymptotic structure of the problems at hand, we have shown that the new strategy is capable of producing approximations for both the critical edge-buckling loads and the number of wrinkles that are valid for moderate values of the stiffness parameter μ. It is remarkable that the accuracy achieved is very good despite the simplicity of the ansatz employed. This leads us to believe that leading-order asymptotic approximations in other contexts (such as the two-dimensional problems in [90], for instance) could form the basis for similar energy strategies, thus circumventing the need of complicated numerical work.

In the context of asymmetric buckling problems our hybrid energy method is particularly versatile since it is able to capture the neutral stability envelope with minimum effort. Indeed, this is done by simply adding an extra integral constraint as demanded by the criticality of the eigenvalue with respect to the mode number. It is interesting to note that while the general asymptotic approach in [44] and [41] for rectangular and annular plates, respectively, was identical, its accuracy was problem-dependent. The hybrid energy method seems to be free of such shortcomings and is quite robust.

Finally, the analysis described in this chapter reinforces the duality between numerics and asymptotics. By using the techniques of asymptotic analysis one is naturally led to a correct estimate of the ansatz that needs to be used in approximate methods such as the Rayleigh–Ritz technique.

Chapter 4

The localised instabilities of a stretched bi-annular plate and the wrinkling-resistance analysis

4.1 Introduction

In the last chapter, we introduced a new energy method by taking advantage of the asymptotic feature (the instabilities are localised) and the minimal potential energy strategy. One of the examples discussed in that chapter was the localised instabilities of a stretched annular plate. The localised features therein were introduced by the stress concentration which was caused by the geometrical discontinuities of the central hole under stretching. But how will material discontinuity affect localised instabilities in a similar annular geometry? In this chapter, we will discuss a stretched bi-annular plate with piecewise-constant mechanical properties. More specifically, this bi-annular plate is composed of two fully bonded annuli, which are made of different materials with different Young's moduli and Poisson ratios.

Indeed, this can be regarded as a composite structure. A question with practical engineering application is: how do the mechanical and geometrical properties of each annulus contributes to the resistance to wrinkling? Can we have some general rules for designing thin structures when considering their abilities to resist buckling, in order to make the composite structure more efficient than any of the constituent ingredients?

The motivation of the present work originates partly from the work of Simitses and Frostig [55, 56, 114]. In [55], the authors formulated the classical buckling problem of a multi-annular plate subject to axisymmetric radial compressive loading on the boundaries or the common joints, which was followed by a numerical study of a uniformly compressed bi-annular plate using a power series method. Later, this study was expanded for a ring-stiffened annular

plate under compression, to discuss the effect of boundary conditions and its rigidities on its buckling [56, 114]. In the compressed situations, the authors discussed mainly the buckling forces of either when the mode number $n = 0$ (axisymmetric mode) or $n = 1$ (asymmetric mode). However, in light of the localised wrinkling problem in [41, 47], the wrinkling mode number in the current problem is supposed to be $n \gg 1$. In this case, the critical wrinkling mode number becomes a pivotal extra parameter for the critical wrinkling loads. Moreover, bi-annular plates experience *global* buckling under uniformly compressive stresses as in Simitses *et.al.*'s work [55, 56, 114], where all the mechanical properties of both annuli make contributions to the *global* buckling. In other words, there is no dominant effect introduced by the mechanical parameters of either sub-annular region. In the present problem, the buckling is expected to be localised in the case of the stretched single annular plate. It is interesting to see if only the mechanical properties of the localised region play the dominant role compared with the flatter region.
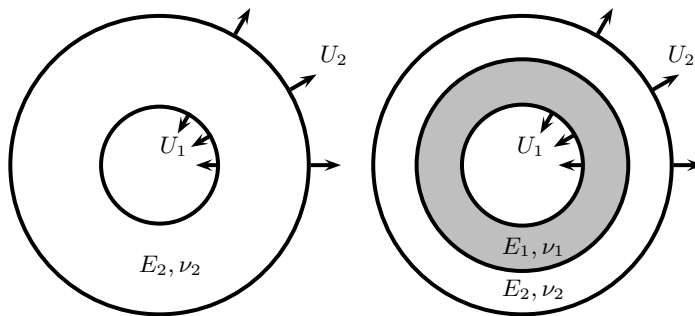
Figure 4-1: Two different annular models under the same uniform stretching displacement fields U_1, U_2. The left sketch shows a single annular plate with uniform material, while the right illustrates a bi-annular plate composed of two mechanically different annuli.

Also, comparing with the stretched single-annular plate by Coman *et al.* [41, 47], the discontinuities between the materials of the two annuli (see Fig. 4.1) raise a couple of other interesting questions:

If we recall the work done by S. Roccabiance *et. al.* [106, 107], rather than considering the homogeneous thick plate, the authors investigated the plane strain bifurcations of elastic layered structures subject to finite bending. Their analysis reveals that a multilayered structure can behave completely differently for both the basic state and the bifurcation state compared with its homogenous counterpart. For instance, a homogeneous block under bending can only possibly have one neutral axis (where the stress components are zero), and experiences surface instabilities on the compressed side when it buckles. However, a multilayered block might have several neutral axes [107]. They then pointed out that, for example, the presence of two-neutral axes might lead to long-wavelength buckling modes [106]. Returning to the stretched thin annular plate geometry, we know that in a single-annular case (in [47]), the wrinkling mode is localised near the inner rim. Then what will the wrinkling mode of a stretched layered-annular plate look like? Would it be a completely different wrinkling mode, just like the contrast between the homogeneous and multi-layered block under bending? Is it possible that

the wrinkling is still triggered near the inner boundary or the interface, or that we have two localised wrinkles on both annuli?

If we look from an alternative aspect: how do the discontinuities affect the bifurcation behaviour of a layered structure? If we get a complete understanding of this problem, it could provide us with the general rules for how the physical discontinuities influence the capabilities of anti-buckling of thin structures. It will therefore contribute to the anti-buckling design of general thin structures.

Moreover, in the single-annular case, the critical stretching load (for buckling) increases monotonically with the aspect ratio (ratio between the inner and outer radii of the annulus), the associated critical wrinkle number shows a similar trend with respect to aspect ratio. Whereas, for the stretched bi-annular plate, we might find that these monotonic relations would no longer be true in some cases.

To answer the above questions, we organise the chapter as follows. In § 4.2, we introduce the problem and record the formulation for both basic and bifurcation states within such a bi-annular geometry. For thin plates, the analysis of the pre-buckling stress distribution can always provide a fruitful indication for the wrinkling problem, which is explained in § 4.3. After appropriate rescalings, we conduct extensive numerical explorations following the numerical strategies presented in §4.4. Here, both a collocation-based solver and the compound matrix method are adopted for the eigenvalue problem (bifurcation problem) of this multi-layer structure. The response curves are shown in § 4.5.1, followed by the critical wrinkling load and the corresponding critical wrinkling modes in § 4.5.2. In these sections, we fully answer the questions raised earlier: the neutral stability envelopes NSE can be classified into two different types, *kink* and *monotonic* types. Critical wrinkling modes are not the same as for the stretched single-annular case: there are four types of wrinkling modes rather than only one: the wrinkling can be localised solely in the inner or outer annulus, or both, or localised right at the interface. Also, we present a detailed analysis to show the close connections linking the basic state, the neutral stability and the wrinkling modes, which are affected by the physical discontinuity introduced by the interface. The role played by the physical discontinuity on the prebuckling and NSE is presented in §4.6.2. Finally, motivated by the WKB analysis proposed by Coman and Haughton [47], we take advantage of the presence of a large parameter (related to the large initial stretching and small thickness, analogous to μ in last chapter) and the large value of the critical mode number, to extend that strategy to a multi-layer structure by reducing the original fourth-order eigenvalue problem into a second-order problem. For a bi-annular plate, there are four boundary conditions and four continuity conditions. We simplify the eight conditions into four by order analysis using the Laplacian expansion on an eighth-order determinant. The asymptotic results show excellent agreement with the results of the full problem. This chapter concludes with some remarks in §4.9.

4.2   Problem formulation

Let us consider a simple plane-stress situation that generalises the Lamé problem for an annular domain subject to radial stresses or displacements on its inner and outer boundaries. Rather than having uniform elastic properties, the annulus, Ω (say), is assumed to consist of two perfectly bonded concentric annular regions,

$$\Omega_I := \left\{ (r, \theta) \in \mathbb{R}^2 \mid R_1 \leq r \leq R_m, \quad 0 \leq \theta < 2\pi \right\},$$

$$\Omega_{II} := \left\{ (r, \theta) \in \mathbb{R}^2 \mid R_m \leq r \leq R_2, \quad 0 \leq \theta < 2\pi \right\},$$

that have different mechanical properties, i.e. $\Omega = \Omega_I \cup \Omega_{II}$ (details of the geometry that we have in mind can be seen in Fig. 4-2). For the sake of simplicity it will be assumed that the thicknesses of the two annuli are identical and equal to $h > 0$. The inner and outer rims of Ω are given by the curves $r = R_1$ and $r = R_2$, respectively, while $r = R_m$ indicates the location of the interface between the two concentric regions. The inner annulus (Ω_I) consists of a linearly elastic isotropic material characterised by the Young's modulus E_1 and Poisson's ratio ν_1; the outer region (Ω_{II}) is similar, but its material is described by the elastic constants E_2 and ν_2. Moreover, the inner and outer rims are assumed to subject to displacement field U_1 (inward) and U_2 (outward) respectively.
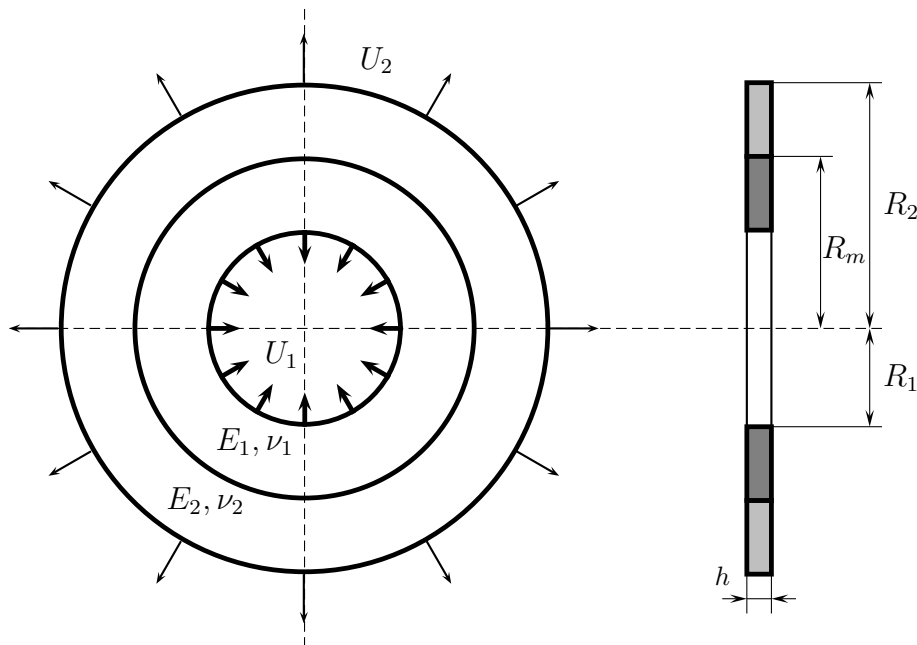
Figure 4-2: A bi-annular plate stretched by applied uniform displacements on both its inner and outer edges. The two constituent parts Ω_I and Ω_{II} are assumed to be perfectly bonded together.

Now we will apply the linearised FvK equations obtained in §2 to the present problem. As usual, with this kind of problem, we adopt a cylindrical system of coordinates with origin at

the centre of Ω and the $z-$ axis perpendicular to it. Therefore, the operators are defined as

$$\nabla_r := \frac{\partial}{\partial r}\,, \quad \nabla_\theta := \frac{1}{r}\frac{\partial}{\partial \theta}\,, \quad \nabla_{rr} := \frac{\partial^2}{\partial r^2}\,, \quad \nabla_{r\theta} := \frac{1}{r}\frac{\partial^2}{\partial r \partial \theta} - \frac{1}{r^2}\frac{\partial}{\partial \theta}\,,$$

$$\nabla_{\theta\theta} := \frac{1}{r}\frac{\partial}{\partial r} + \frac{1}{r^2}\frac{\partial^2}{\partial \theta^2}\,, \quad \nabla^2 := \nabla_{rr} + \nabla_{\theta\theta}\,, \quad \boldsymbol{\nabla} := \begin{bmatrix} \nabla_r \\ \nabla_\theta \end{bmatrix}\,, \quad \boldsymbol{\nabla} \otimes \boldsymbol{\nabla} := \begin{bmatrix} \nabla_{rr} & \nabla_{r\theta} \\ \nabla_{r\theta} & \nabla_{\theta\theta} \end{bmatrix}\,,$$

$$(4.1)$$

For notational convenience, we use the labels $j = I$ or II to indicate the variables in the two regions: Ω_I, Ω_{II}, and use C_1, C_2 and C_m to represent the circular boundaries at $r = R_1, R_2$ and R_m respectively. By recalling (2.34), the equilibrium of the basic state of the bi-annular plate requires

$$\delta\mathcal{E}(\mathring{\boldsymbol{u}})[\boldsymbol{h}] = 2\int_{C_1+C_m} \left[\mathring{\boldsymbol{N}}^I \cdot (\delta\mathring{\boldsymbol{v}}^I) \right] \cdot \boldsymbol{n}^I \, \mathrm{d}S + 2\int_{C_2+C_m} \left[\mathring{\boldsymbol{N}}^{II} \cdot (\delta\mathring{\boldsymbol{v}}^{II}) \right] \cdot \boldsymbol{n}^{II} \, \mathrm{d}S$$

$$- 2\int_{\Omega_I} (\boldsymbol{\nabla} \cdot \mathring{\boldsymbol{N}}^I) \cdot \delta\mathring{\boldsymbol{v}}^I \, \mathrm{d}A - 2\int_{\Omega_{II}} (\boldsymbol{\nabla} \cdot \mathring{\boldsymbol{N}}^{II}) \cdot \delta\mathring{\boldsymbol{v}}^{II} \, \mathrm{d}A \equiv 0\,. \qquad (4.2)$$

In addition, the forced boundary conditions are prescribed as

$$\mathring{\boldsymbol{v}}^I = (-U_1, 0)\,, \quad \delta\mathring{\boldsymbol{v}}^I \equiv \boldsymbol{0} \quad \text{on } C_1\,, \qquad \mathring{\boldsymbol{v}}^{II} = (U_2, 0)\,, \quad \delta\mathring{\boldsymbol{v}}^{II} \equiv \boldsymbol{0} \quad \text{on } C_2\,,$$

where U_1, $U_2 > 0$ are given. Notice that (4.2) should be valid for any variation $\delta\mathring{\boldsymbol{v}}^{(j)}$ that satisfies the above forced boundary conditions, so we have the *strong form* for equilibrium in basic state

$$\boldsymbol{\nabla} \cdot \mathring{\boldsymbol{N}}^{I,II} \equiv 0 \quad \text{in} \quad \Omega_{I,II}\,, \qquad (4.3)$$

which leads to the classical Lamé solution if we assume axial symmetry. Assuming $\mathring{u}_r \equiv \mathring{u}_r(r,\theta)$ and $\mathring{u}_\theta = \mathring{u}_\theta(r,\theta)$ denote the radial and the azimuthal displacements respectively, this reduces to the equivalent conditions

$$\mathring{u}_r = U(r) \qquad \text{and} \qquad \mathring{u}_\theta \equiv 0\,,$$

where the function $U(r)$ fully characterises the displacements undergone by the points in the annulus. By using the definitions of the linear elastic strains in polar coordinates,

$$\mathring{\varepsilon}_{rr} = \frac{\partial \mathring{u}_r}{\partial r}, \quad \mathring{\varepsilon}_{rr} = \frac{1}{r}\left(\mathring{u}_r + \frac{\partial \mathring{u}_\theta}{\partial \theta} \right), \quad \mathring{\varepsilon}_{r\theta} = \frac{1}{2r}\left(\frac{\partial \mathring{u}_r}{\partial r} + r\frac{\partial \mathring{u}_\theta}{\partial r} - \mathring{u}_\theta \right)\,,$$

it is immediately found that

$$\mathring{\varepsilon}_{rr} = U'(r), \quad \mathring{\varepsilon}_{\theta\theta} = \frac{U(r)}{r}, \quad \mathring{\varepsilon}_{r\theta} \equiv 0\,, \qquad (4.4)$$

where the dash indicates differentiation with respect to the radial coordinate $R_1 \le r \le R_2$.

We shall use these expressions in Hooke's law for plane-stress elasticity

$$\mathring{\sigma}_{rr} = \frac{E}{1-\nu^2}(\mathring{\varepsilon}_{rr} + \nu\mathring{\varepsilon}_{\theta\theta}), \quad \mathring{\sigma}_{\theta\theta} = \frac{E}{1-\nu^2}(\mathring{\varepsilon}_{\theta\theta} + \nu\mathring{\varepsilon}_{rr}), \tag{4.5}$$

where

$$E = \begin{cases} E_1 & \text{in} \quad \Omega_I, \\ E_2 & \text{in} \quad \Omega_{II}, \end{cases} \qquad \nu = \begin{cases} \nu_1 & \text{in} \quad \Omega_I, \\ \nu_2 & \text{in} \quad \Omega_{II}. \end{cases}$$

Based on the above assumptions, the linear equilibrium equation of the annular plate takes the form

$$\frac{d}{dr}(r\mathring{N}_{rr}) + \mathring{N}_{\theta\theta} = 0,$$

in which the resultant membrane forces can be expressed as $\mathring{N}_{rr} = h\mathring{\sigma}_{rr}$ and $\mathring{N}_{\theta\theta} = h\mathring{\sigma}_{\theta\theta}$. Since the thickness h has been assumed to be the same all over the two annuli, the equilibrium equation for the pre-buckling state is in fact $(r\mathring{\sigma}_{rr})_{,r} + \mathring{\sigma}_{\theta\theta} = 0$. Substituting (4.4) and (4.5) into this last equation leads to

$$r^2 U''(r) + rU'(r) - U(r) = 0, \tag{4.6}$$

with the general solution

$$U(r) = br + \frac{c}{r}, \tag{4.7}$$

where the constants $b, c \in \mathbb{R}$ are arbitrary. This expression is valid for both the inner and the outer regions of Ω, but with different constants. We shall use the notations (j) to represent quantities relevant to either Ω_I or Ω_{II}, and take the corresponding two solutions

$$U^I(r) = b^I r + \frac{c^I}{r}, \quad r \in [R_1, R_m], \tag{4.8a}$$

$$U^{II}(r) = b^{II} r + \frac{c^{II}}{r}, \quad r \in [R_m, R_2], \tag{4.8b}$$

that are valid in Ω_I and Ω_{II}, respectively. The four arbitrary constants $b^{(j)}$, $c^{(j)}$ are to be determined by imposing the boundary constraints on the inner and outer rims of Ω, together with the continuity conditions along the interface $r = R_m$. Assuming that uniform radial displacements are applied on $r = R_1$ and $r = R_2$, the boundary conditions are

$$U^I(R_1) = -U_1 \qquad \text{and} \qquad U^{II}(R_2) = U_2, \tag{4.9}$$

where $U_1, U_2 > 0$ are given. Moreover, the continuity of displacement at $r = R_m$ indicates that $\mathring{v}^I = \mathring{v}^{II}$, $\delta\mathring{v}^I = \delta\mathring{v}^{II}$ and $\boldsymbol{n}^I = -\boldsymbol{n}^{II} = \boldsymbol{e}_r + 0\boldsymbol{e}_\theta$ along the interface $r = R_m$, the rest of the

terms in (4.2) read

$$2 \int_{C_m} \left(\mathring{\boldsymbol{N}}^I - \mathring{\boldsymbol{N}}^{II} \right) \cdot \boldsymbol{n}^I \cdot (\delta \mathring{\boldsymbol{v}}^I) \, \mathrm{d}S \equiv 0 \,.$$

Taking into account the constant thickness of the two sub-annular regions, the continuity condition at $r = R_m$ for the basic state can be written as

$$U^I(R_m) = U^{II}(R_m) \qquad \text{and} \qquad \mathring{\sigma}_{rr}^I(R_m) = \mathring{\sigma}_{rr}^{II}(R_m) \,. \tag{4.10}$$

We introduce the non-dimensional variables

$$\lambda := \frac{U_1}{U_2}, \qquad \gamma := \frac{E_1}{E_2} \,, \tag{4.11}$$

and then substitute the general expressions (4.8) into (4.9) and (4.10). The result is a linear system of four equations for the four constants $b^{(j)}, c^{(j)}$,

$$b^I R_1 + \frac{c^I}{R_1} = -\lambda U_2 \,,$$

$$b^{II} R_2 + \frac{c^{II}}{R_2} = U_2 \,,$$

$$b^I R_m + \frac{c^I}{R_m} = b^{II} R_m + \frac{c^{II}}{R_m} \,,$$

$$\kappa_1 b^I - \kappa_2 \frac{c^I}{R_m^2} = \kappa_3 b^{II} - \kappa_4 \frac{c^{II}}{R_m^2} \,,$$

where

$$\kappa_1 := \frac{\gamma}{1 - \nu_1}, \quad \kappa_2 := \frac{\gamma}{1 + \nu_1}, \quad \kappa_3 := \frac{1}{1 - \nu_2}, \quad \kappa_4 := \frac{1}{1 + \nu_2} \,.$$

After lengthy calculations we find that $b^{I,II}$ are given as the product between certain non-dimensional factors and U_2/R_2, while in $c^{I,II}$ the dimensionless factors are multiplied by $U_2 R_2$. We can further rescale our variables by introducing

$$\rho := \frac{r}{R_2}, \quad \eta_1 := \frac{R_1}{R_2}, \quad \eta_2 := \frac{R_m}{R_2} \,, \tag{4.12a}$$

$$\overline{U}_1 := \frac{U_1}{R_2}, \quad \overline{U}_2 := \frac{U_2}{R_2} \,, \tag{4.12b}$$

so that Ω is now defined by $\eta_1 \leq \rho \leq 1$ and the interface has equation $\rho = \eta_2$; henceforth, the bars on the dimensionless U_1 and U_2 will be omitted for the sake of simplicity. In terms of these new variables the expressions of the coefficients in the basic state are

$$b^I = \frac{1}{\Delta} \left\{ \left[(\kappa_3 + \kappa_2) \eta_2{}^2 - \kappa_2 + \kappa_4 \right] \eta_1 \lambda + (\kappa_4 + \kappa_3) \eta_2{}^2 \right\} \,, \tag{4.13a}$$

$$c^I = -\frac{1}{\Delta} \left\{ \left[(\kappa_3 - \kappa_1) \eta_2^2 + (\kappa_1 + \kappa_4) \right] \eta_1 \lambda + (\kappa_4 + \kappa_3) \eta_1{}^2 \right\} \eta_2^2 \,, \tag{4.13b}$$

$$b^{II} = \frac{1}{\Delta} \Big[(\kappa_2 + \kappa_1) \, \eta_2^2 \eta_1 \lambda + (\kappa_2 - \kappa_4) \, \eta_1^2 + (\kappa_1 + \kappa_4) \, \eta_2^2 \Big] \,, \tag{4.13c}$$

$$c^{II} = -\frac{1}{\Delta} \Big[(\kappa_2 + \kappa_1) \, \eta_1 \lambda + (\kappa_3 + \kappa_2) \, \eta_1^2 + (\kappa_1 - \kappa_3) \, \eta_2^2 \Big] \eta_2^2 \,, \tag{4.13d}$$

where

$$\Delta := \big[\kappa_2 - \kappa_4 - (\kappa_3 + \kappa_2) \, \eta_2^2 \big] \eta_1^2 + \big[(\kappa_3 - \kappa_1) \, \eta_2^2 + \kappa_1 + \kappa_4 \big] \eta_2^2 \,. \tag{4.14}$$

Since $\Delta \equiv \Delta(\eta_1, \eta_2)$ defined by (4.14) appears as a denominator in the expression of the coefficients that enter in the basic state (4.8), we need to investigate whether this quantity can ever be equal to zero. By introducing $\xi := \eta_2/\eta_1 > 1$, it is a routine exercise to show that

$$\frac{\Delta}{\eta_1^2} = (\kappa_4 + \kappa_3 \eta_2^2)(\xi^2 - 1) + (\kappa_2 + \kappa_1 \xi^2)(1 - \eta_2^2) \,,$$

which is evidently strictly positive.

We are now going to couple the basic state of the previous section with the linearised bifurcation equation. Owing to the presence of two different regions in the annulus, this equation will have to be written separately in each of them. Letting w^I and w^{II} be the out-of-plane displacements experienced by the two annular parts as a result of wrinkling, (2.40a) leads to the below bifurcation equations (*strong form* for bifurcation) due to the arbitrariness of $\delta w^{(j)}$

$$D_{(j)} \nabla^4 w^{(j)} - \mathring{\boldsymbol{N}}^{(j)} : (\boldsymbol{\nabla} \otimes \boldsymbol{\nabla} w^{(j)}) = 0 \quad \text{in} \quad \Omega_{(j)} \,, \tag{4.15}$$

which is applicable to the inner and outer sub-annular regions by taking $j = I$ and II respectively, namely,

$$D_I \nabla^4 w^I - h \left[\mathring{\sigma}_{rr}^I \frac{\partial^2 w^I}{\partial r^2} + \mathring{\sigma}_{\theta\theta}^I \frac{1}{r} \left(\frac{\partial w^I}{\partial r} + \frac{1}{r} \frac{\partial^2 w^I}{\partial \theta^2} \right) \right] = 0 \quad \text{in} \quad \Omega_I \,, \tag{4.16a}$$

$$D_{II} \nabla^4 w^{II} - h \left[\mathring{\sigma}_{rr}^{II} \frac{\partial^2 w^{II}}{\partial r^2} + \mathring{\sigma}_{\theta\theta}^{II} \frac{1}{r} \left(\frac{\partial w^{II}}{\partial r} + \frac{1}{r} \frac{\partial^2 w^{II}}{\partial \theta^2} \right) \right] = 0 \quad \text{in} \quad \Omega_{II} \,, \tag{4.16b}$$

where

$$D^I := \frac{E_1 h}{12(1 - \nu_1^2)} \,, \qquad D^{II} := \frac{E_2 h}{12(1 - \nu_2^2)} \,,$$

denote the (different) bending stiffnesses in Ω_I and Ω_{II}, respectively, while

$$\nabla^4 := \left(\nabla^2 \right)^2 = \left(\frac{\partial^2}{\partial r^2} + \frac{1}{r} \frac{\partial}{\partial r} + \frac{1}{r^2} \frac{\partial^2}{\partial \theta^2} \right)^2$$

stands for the usual bi-Laplacian operator in polar coordinates.

The bifurcation equations can be rescaled by using the dimensionless variables already introduced in (4.11) and (4.12). Some further substitutions are required to complete the process,

and we state these explicitly for the sake of completeness

$$w^{(j)} \to \frac{w^{(j)}}{h}\,, \qquad D_{(j)} \to \frac{h^2}{12U_2R_2} =: \mu^{-2}\,. \tag{4.17}$$

(Although in switching from the independent variable 'r' to 'ρ' it would have been possible to re-label the radial stresses as $\mathring{\sigma}_{\rho\rho}$, we keep the original notation as that seems more intuitive.)

The rescaled pre-bifurcation stress can be expressed in terms of the non-dimensional constants found in (4.13) as recorded below

$$\begin{bmatrix} \mathring{\sigma}_{rr}^{(j)} \\[2ex] \mathring{\sigma}_{\theta\theta}^{(j)} \end{bmatrix} \to \begin{bmatrix} 1 + \nu_{(j)} & -\dfrac{1-\nu_{(j)}}{\rho^2} \\[2ex] 1 + \nu_{(j)} & \dfrac{1-\nu_{(j)}}{\rho^2} \end{bmatrix} \begin{bmatrix} b^{(j)} \\[2ex] c^{(j)} \end{bmatrix}\,, \qquad j \in \{I, II\}\,. \tag{4.18}$$

We can write the rescaled versions of (4.15) in the compact form

$$\mu^{-2}\nabla^4 w^{(j)} - h\left[\mathring{\sigma}_{rr}^{(j)}\frac{\partial^2 w^{(j)}}{\partial\rho^2} + \mathring{\sigma}_{\theta\theta}^{(j)}\frac{1}{\rho}\left(\frac{\partial w^{(j)}}{\partial\rho} + \frac{1}{\rho}\frac{\partial^2 w^{(j)}}{\partial\theta^2}\right)\right] = 0\,, \tag{4.19}$$

where μ^{-2} is usually a very small parameter ($0 < \mu^{-1} \ll 1$) for plates that are very thin or highly stretched (within the limits of the theory employed in our investigations).

The solution strategy for solving these equations mirrors closely the related approach taken by Coman *et al.* in [41, 47]). By looking for solutions with separable variables we consider

$$w^{(j)}(\rho, \theta) = W^{(j)}(\rho)\cos(n\theta)\,, \quad j \in \{I, II\}\,, \tag{4.20}$$

where $n \in \mathbb{N}$ represents the mode number (equal to half the number of regular wrinkles in the azimuthal direction), and the unknown amplitudes $W^{I,II}$ will be found by solving some simpler ordinary differential equations. We mention in passing that the mode number n must be the same in both Ω_I and Ω_{II}, otherwise there would be certain discontinuities between the wrinkled configurations of these two regions (which would contradict the perfect bond initially assumed to exist between these parts).

On substituting the ansatz (4.20) into (4.19), after eliminating the multiplicative common term $\cos n\theta$, we are left with solving two ordinary differential equations

$$\frac{d^4W^{(j)}}{d\rho^4} + \mathcal{C}_3^{(j)}(\rho)\frac{d^3W^{(j)}}{d\rho^3} + \mathcal{C}_2^{(j)}(\rho)\frac{d^2W^{(j)}}{d\rho^2} + \mathcal{C}_1^{(j)}(\rho)\frac{dW^{(j)}}{d\rho} + \mathcal{C}_0^{(j)}(\rho)W^{(j)} = 0\,, \quad \rho \in \Lambda_{(j)}\,, \tag{4.21}$$

where

$$\mathcal{C}_3^{(j)}(\rho) := \frac{2}{\rho}, \qquad\qquad \mathcal{C}_2^{(j)}(\rho) := -\left[\frac{2n^2+1}{\rho^2} + \mu^2\,\mathring{\sigma}_{\rho\rho}^{(j)}(\rho)\right],$$

$$\mathcal{C}_1^{(j)}(\rho) := \frac{1}{\rho}\left[\frac{2n^2+1}{\rho^2} - \mu^2\,\mathring{\sigma}_{\theta\theta}^{(j)}(\rho)\right], \quad \mathcal{C}_0^{(j)}(\rho) := \frac{n^2}{\rho^2}\left[\frac{n^2-4}{\rho^2} + \mu^2\,\mathring{\sigma}_{\theta\theta}^{(j)}(\rho)\right].$$

where $j = I$ or II is adopted, respectively, to describe the buckling equations of the inner and outer sub-regions. These two equations must be supplemented with appropriate boundary conditions. Using the rescaling introduced and the normal mode approach introduced earlier on, the clamped boundary conditions on $\rho = \eta_1, 1$ are

$$W^I(\eta_1) = \left.\frac{dW^I}{d\rho}\right|_{\rho=\eta_1} = 0 \quad \text{and} \quad W^{II}(1) = \left.\frac{dW^{II}}{d\rho}\right|_{\rho=1} = 0. \tag{4.22}$$

The continuity conditions along the interface are slightly more demanding. For example, the kinematic continuity on the interface requires that

$$w^I = w^{II}, \quad \boldsymbol{\nabla}w^I = \boldsymbol{\nabla}w^{II} \quad \text{at} \quad r = R_m. \tag{4.23}$$

The same rule goes for its variation, so $\delta w^I = \delta w^{II}$, $\boldsymbol{\nabla}(\delta w^I) = \boldsymbol{\nabla}(\delta w^{II})$ on the interface.

In §2.4 we have derived the boundary conditions for isotropic plates under in-plane loading. However, when we pursue the interfacial conditions, we need to be more careful – we should start from the integrals in (2.29b) which include the full information of the unit normal $\boldsymbol{n}$ or unit shear $\boldsymbol{s}$. Following a similar process as in (4.2), we can have one of the continuity conditions by applying (2.29b) along the interface (the subscript '1' has been dropped for notational convenience and the inextensible midplane assumption has been taken)

$$\sum_{j=I,II} \int_{C_m} \left\{ \left[\mathring{\boldsymbol{N}}^{(j)} \cdot \boldsymbol{\nabla}w^{(j)} - \mathbb{D}_{(j)} \vdots (\boldsymbol{\nabla} \otimes \boldsymbol{\nabla} \otimes \boldsymbol{\nabla}w^{(j)}) \right] \cdot \boldsymbol{n}^{(j)} \right.$$
$$\left. - \boldsymbol{\nabla} \left[\mathbb{D}_{(j)} \vdots (\boldsymbol{\nabla} \otimes \boldsymbol{\nabla}w^{(j)} \otimes \boldsymbol{n}^{(j)} \otimes \boldsymbol{s}^{(j)}) \right] \cdot \boldsymbol{s}^{(j)} \right\} (\delta w^{(j)}) \, \mathrm{d}S \equiv 0, \tag{4.24}$$

where $j = I$ defines the variables in Ω_I on the interface, while, II denotes those in Ω_{II} on the interface, but in opposite direction, namely, $\boldsymbol{n}^I = -\boldsymbol{n}^{II} = \boldsymbol{e}_r, \boldsymbol{s}^I = -\boldsymbol{s}^{II} = \boldsymbol{e}_\theta$. Therefore, $\boldsymbol{n}^I \otimes \boldsymbol{s}^I = \boldsymbol{n}^{II} \otimes \boldsymbol{s}^{II}$, and (4.24) becomes

$$\int_{C_m} \left\{ \left[-\mathbb{D}_I \vdots (\boldsymbol{\nabla} \otimes \boldsymbol{\nabla} \otimes \boldsymbol{\nabla}w^I) + \mathbb{D}_{II} \vdots (\boldsymbol{\nabla} \otimes \boldsymbol{\nabla} \otimes \boldsymbol{\nabla}w^{II}) \right] \cdot \boldsymbol{n}^I \right.$$
$$\left. + \boldsymbol{\nabla} \left[-\mathbb{D}_I \vdots (\boldsymbol{\nabla} \otimes \boldsymbol{\nabla}w^I \otimes \boldsymbol{n}^I \otimes \boldsymbol{s}^I) + \mathbb{D}_{II} \vdots (\boldsymbol{\nabla} \otimes \boldsymbol{\nabla}w^{II} \otimes \boldsymbol{n}^I \otimes \boldsymbol{s}^I) \right] \cdot \boldsymbol{s}^I \right\} (\delta w^I) \, \mathrm{d}S \equiv 0.$$

Specialising the bending stiffness tensor $\mathbb{D}$ to the St. Venant–Kirchhoff material case (as in §2.3), the arbitrariness of $\delta w^I = \delta w^{II}$ leads to the following continuity constraint on C_m

$$-D_I\big[\nabla_r(\nabla^2 w^I)+(1-\nu_1)\nabla_\theta(\nabla_r\nabla_\theta w^I)\big] = -D_{II}\big[\nabla_r(\nabla^2 w^{II})+(1-\nu_2)\nabla_\theta(\nabla_r\nabla_\theta w^{II})\big], \tag{4.25}$$

in which we have already made use of the simplification $\mathring{\boldsymbol{N}}^I \cdot \boldsymbol{\nabla}w^I = \mathring{\boldsymbol{N}}^{II} \cdot \boldsymbol{\nabla}w^{II}$ along C_m that follows from (4.10) and (4.23). We observe that (4.25) is the equilibrium of the vertical shear force resultants on the interface.

Eigenvalue problems & elastic instabilities

We can conduct similar operations on (2.42a) along the interface C_m, which leads to

$$\sum_{j=I,II} \int_{C_m} \mathbb{D} \vdots \left(\boldsymbol{\nabla} \otimes \boldsymbol{\nabla} w^{(j)} \otimes \boldsymbol{n}^{(j)} \otimes \boldsymbol{n}^{(j)} \right) \left[\boldsymbol{\nabla} (\delta w^{(j)}) \cdot \boldsymbol{n}^{(j)} \right] \, \mathrm{d}S \equiv 0 \,.$$

According to the arbitrariness of $\boldsymbol{\nabla}(\delta w^{(j)}) \cdot \boldsymbol{n}^{(j)}$ along C_m, we eventually have another continuity condition

$$D_I(\nabla_{rr} w^I + \nu_1 \nabla_{\theta\theta} w^I) = D_{II}(\nabla_{rr} w^{II} + \nu_2 \nabla_{\theta\theta} w^{II}) \,, \tag{4.26}$$

which states the equilibrium of the bending moments on the interface.

To summarise, at the interface $r = R_m$ we have the kinematic and mechanical continuity conditions recorded below,

$$w^I(R_m) = w^{II}(R_m), \qquad \left. \frac{\partial w^I}{\partial r} \right|_{r=R_m} = \left. \frac{\partial w^{II}}{\partial r} \right|_{r=R_m}, \tag{4.27a}$$

$$M^I(R_m) = M^{II}(R_m) \,, \qquad Q^I(R_m) = Q^{II}(R_m) \,. \tag{4.27b}$$

The quantities that appear in (4.27b) are defined by

$$M^{(j)} := D_{(j)} \left[\frac{\partial^2 w^{(j)}}{\partial r^2} + \frac{\nu_{1,2}}{r} \left(\frac{\partial w^{(j)}}{\partial r} + \frac{1}{r} \frac{\partial^2 w^{(j)}}{\partial \theta^2} \right) \right] \,,$$

$$Q^{(j)} := -D_{(j)} \left[\frac{\partial}{\partial r} \left(\nabla^2 w^{(j)} \right) + \frac{1 - \nu_{(j)}}{r} \frac{\partial^2}{\partial r \partial \theta} \left(\frac{1}{r} \frac{\partial w^{(j)}}{\partial \theta} \right) \right] + \mathring{N}_{rr}^{(j)} \nabla_r w^{(j)} \,,$$

and represent the bending moment and the vertical shear force, respectively, where the terms $\mathring{N}_{rr}^{(j)} \nabla_n w^{(j)}$ in $Q^{(j)}$ are cancelled out in (4.27b) as mentioned earlier. Here we take the chance to point out that the continuity conditions Eq. (10) in [55] and Eq. (9) in [56] are problematic, which make the mistakes

$$\widehat{Q^I}(R_m) = -\widehat{Q^{II}}(R_m) \,,$$

where

$$\widehat{Q^{(j)}} := -D_{(j)} \left[\underline{\frac{\partial}{\partial r} \left(\nabla^2 w^{(j)} \right)} + \frac{1 - \nu_{(j)}}{r} \underline{\frac{\partial}{\partial \theta} \left(\frac{1}{r} \frac{\partial w^{(j)}}{\partial \theta} \right)} \right] + \frac{\mathring{N}_{rr}^{(j)}}{D_{(j)}} \frac{\partial w^{(j)}}{\partial r} \,.$$

Comparing the expression for $Q^{(j)}$ we obtained in (4.27b), there are three discrepancies. First, the terms $\widehat{Q^{(j)}}$ on either side of their equation are of opposite sign, thus the terms $\mathring{N}_{rr}^{(j)}(R_m)$ are not cancelled out for equilibrium, which does not make sense from a physical point of view. The second difference presents in the derivative order of $w^{(j)}$ (with respect to variables r and θ) in the two underlined terms, obviously, the first term is of third-order while the latter is second-order, which is mathematically problematic. Moreover, we can observe that $D_{(j)}$ multiplies the bracket, but is in the denominator of the last term, which raises a dimensional mistake. As will be pointed out in §4.8, the continuity conditions (4.27b) are not the leading order condition compared with the forced interfacial conditions (4.27a). Therefore, it will not affect the final

results significantly (especially for the compressed bi-annular cases in [55, 56]), but it caused some singularity problems in numerical calculations when we tried their formulation in our stretched bi-annular case.

The above derivation leads us to believe that the tensorial formulation based on the minimum energy principle can help us avoid mistakes in derivation especially for comparatively complex constraints.

After using the rescalings introduced earlier on, and employing the normal-mode approach (4.20), the kinematic continuity conditions (4.23) and the natural continuity conditions in (4.25), (4.26) lead to the rescaled continuity conditions at $\rho = \eta_2$

$$W^I = W^{II} , \tag{4.28a}$$

$$\frac{dW^I}{d\rho} = \frac{dW^{II}}{d\rho} , \tag{4.28b}$$

$$\beta_1 \left(\frac{d^2W^I}{d\rho^2} + \frac{\nu_1}{\eta_2} \frac{dW^I}{d\rho} - \frac{\nu_1 n^2}{\eta_2^2} W^I \right) = \beta_2 \left(\frac{d^2W^{II}}{d\rho^2} + \frac{\nu_2}{\eta_2} \frac{dW^{II}}{d\rho} - \frac{\nu_2 n^2}{\eta_2^2} W^{II} \right) , \tag{4.28c}$$

$$\beta_1 \left[\frac{d^3W^I}{d\rho^3} + \frac{1}{\eta_2} \frac{d^2W^I}{d\rho^2} - \left(\frac{1 + (2 - \nu_1)n^2}{\eta_2^2} \right) \frac{dW^I}{d\rho} + \frac{(3 - \nu_1)n^2}{\eta_2^3} W^I \right]$$

$$= \beta_2 \left[\frac{d^3W^{II}}{d\rho^3} + \frac{1}{\eta_2} \frac{d^2W^{II}}{d\rho^2} - \left(\frac{1 + (2 - \nu_2)n^2}{\eta_2^2} \right) \frac{dW^{II}}{d\rho} + \frac{(3 - \nu_2)n^2}{\eta_2^3} W^{II} \right] , \tag{4.28d}$$

where

$$\beta_1 := \frac{\gamma}{1 - \nu_1^2} \qquad \text{and} \qquad \beta_2 := \frac{1}{1 - \nu_2^2} .$$

4.3 Basic state

Next, we are going to study the existence of azimuthal compressive stresses in Ω as in Eq. (4.18) and classify all the possible situations. Hereafter, we will refer to the analysis for prebuckling azimuthal stresses as $PBAS$ analysis for clarity.

As mentioned in § 1, the compressive component(s) in the prebuckling stress $\mathring{\boldsymbol{N}}$ is a key term in the bifurcation equation to determine the critical bucking state for the thin (slender) elastic structures. Because from a mathematical point of view, in the bifurcation equation Eq. (4.21), the rescaled prebuckling stresses $\mathring{\sigma}_{rr}^{(j)}, \mathring{\sigma}_{\theta\theta}^{(j)}$ are multiplied by a large parameter μ^2, which characterises the slenderness of the stretched bi-annular plate. It introduces a singular-perturbation feature into this eigenproblem. As $\mu \to \infty$, the original fourth-order differential equation collapse to a second-order equation, in which, the point where $\mathring{\sigma}_{\theta\theta}(\bar{\rho}) = 0$ acts as the turning point of the reduced problem. For the sake of classifying convenience, here we introduce a terminology 'Nodal Hoop Point' (NHP), which denotes the point of $\bar{\rho}$ where $\mathring{\sigma}_{\theta\theta}(\bar{\rho}) = 0$.

For a stretched bi-annular plate, the $PBAS$ are complicated compared with the model

Table 4.1: Classifications of prebuckling azimuthal stresses $(PBAS)$ $\mathring{\sigma}_{\theta\theta}(\rho)$ in the stretched bi-annular elastic plate. $I_{a,b}, II_{a,b}$ are the quantities defined in (4.29). The black bullets on the dashed lines in each sketches identify the location of the nodal hoop points (NHP) $\eta_1 < \overline{\rho} < 1$ for which $\mathring{\sigma}_{\theta\theta}(\overline{\rho}) = 0$. The coloured blocks following the notations such as $\mathcal{B}, \mathcal{G}$ indicate the background types of the pre-bifurcation hoop stresses to be used later on, e.g., Figs. 4-3 to 4-9.

Shift-down style		Shift-up style	
	$\mathcal{B}_1$, ▫ $1NHP$ in Ω_I $I_a < 0 < I_b$, $II_a, II_b > 0$, and $I_b < II_a$		$\mathcal{B}_2$, ▫ $1NHP$ in Ω_I $I_a < 0 < I_b$, $II_a, II_b > 0$, and $I_b < II_a$
	$\mathcal{R}$, ▫ $2NHP$ in $\Omega_{I,II}$ $I_a < 0 < I_b$ and $II_a < 0 < I_b$		$\mathcal{K}$, ▫ $0NHP$ $I_a < I_b < 0$ and $0 < II_a < II_b$
	$\mathcal{G}_1$, ▫ $1NHP$ in Ω_{II} $I_a, I_b < 0$ and $II_a < 0 < II_b$		$\mathcal{G}_2$, ▫ $1NHP$ in Ω_{II} $II_a < 0 < II_b$ and $I_a < I_b < 0$
	$\mathcal{Y}$, ▫ $1NHP$ in Ω_{II} $I_a, I_b > 0$ and $II_a < 0 < II_b$		

discussed in [41, 47] with only one NHP. When S. Roccabiance *et. al.* [107] considered the plane strain bifurcation of a layered thick block, they pointed out that the stress distribution in the basic state is complex and is in itself interesting, and it may have more than one neutral axis (counterpart of the NHP in our problem). Similarly, we expect that the curves of $PBAS$ of the stretched bi-annular plate might have more than one NHP, and there are a variety of situations in terms of the combinations of the positive and negative $PBAS$ regions which are separated by the NHP's. Since the NHP is of great importance for the further possible WKB analysis, it is therefore critical to classify the different situations of $PBAS$ in advance, in order to gain a clearer understanding of the buckling problem, and also indicate the possible application of further WKB approximations. We have employed numerical simulations on the orthoradial stress with respect to η_1, λ. Figs. 4-3 to 4-5 include the most representative behaviours of the $PBAS$ with the background coloured as defined in Table 4.1. For the sake of notational convenience, we denote the $PBAS$ on the boundaries and interface as

$$I_a := \sigma_{\theta\theta}^{(0)I}(\eta_1), \quad I_b := \sigma_{\theta\theta}^{(0)I}(\eta_2), \tag{4.29a}$$

$$II_a := \sigma_{\theta\theta}^{(0)II}(\eta_2), \quad II_b := \sigma_{\theta\theta}^{(0)II}(1). \tag{4.29b}$$

There are seven possible cases when we consider the $PBAS$ with respect to the location of
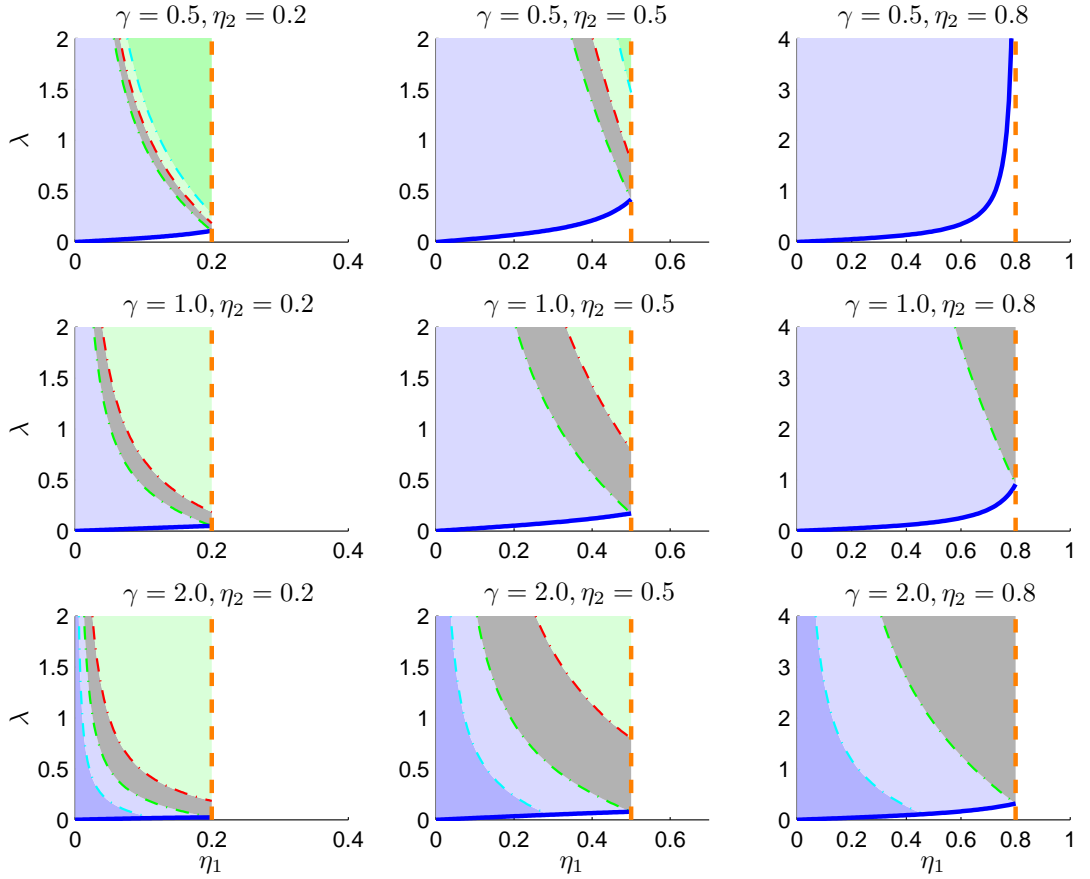
Figure 4-3: The coloured background in each subplot show different types of pre-buckling azimuthal stress $(PBAS)$ $\mathring{\sigma}_{\theta\theta}(\rho)$ corresponding to the notation defined in Table 4.1. The parameters are taken as $\nu_1 = 0.1, \nu_2 = 0.3$; γ, η_2 take the values as in the title of each subplot. The thick lines (either blue or red in later plots) in each subplots are the curves for λ^{low}.

NHP as illustrated in Table 4.1. These seven possible cases can be classified mainly into two categories: *shift-down* type $(I_b > II_a)$ at the interface and *shift-up* type $(I_b < II_a)$.

Shift-down type In Table 4.1, the types $\mathcal{B}_1$ (light blue), $\mathcal{R}$ (red), $\mathcal{G}_1$ (light green) and $\mathcal{Y}$ (yellow) fall into the shift-down type. All the four sketches are of similar tendency except for the relative locations of the dash line $(\mathring{\sigma}_{\theta\theta}(\bar{\rho}) = 0)$ with respect to the points $I_{a,b}$ and $II_{a,b}$. More specifically, by moving the sketch curves (thick solid lines) in the type $\mathcal{R}$ (with two NHP's) up or down with respect to the dashed line, it will transits to the types $\mathcal{B}_1$ (with one NHP in Ω_I) and $\mathcal{G}_1$ (one NHP in Ω_{II}), respectively. The transition from $\mathcal{R}$ to $\mathcal{Y}$ (with one NHP) is a matter of moving up the left section (the $\mathring{\sigma}_{\theta\theta}(\rho)$ in Ω_I) of the curve until $\mathring{\sigma}_{\theta\theta}$ is positive over the whole region Ω_I. Such relations are also embodied in the $\mathring{\sigma}_{\theta\theta}(\eta_1; \lambda)$ plots. As we can see from the subplots in the first row of Fig. 4-4 and all those in Fig. 4-5 (when γ is relatively small or ν_1/ν_2 is relatively large), the $\mathcal{R}$ background regions always border the $\mathcal{B}_1, \mathcal{G}_1$ and $\mathcal{Y}$ regions. To put it another way, by changing the values of λ and η_1 within the $\lambda - \eta_1$ plane, the situations shown in one colour may switch to the situations indicated by its border background.

Shift-up type On the other hand, $\mathcal{B}_2$ (light blue), $\mathcal{K}$ (black) and $\mathcal{G}_2$ (light green) belong
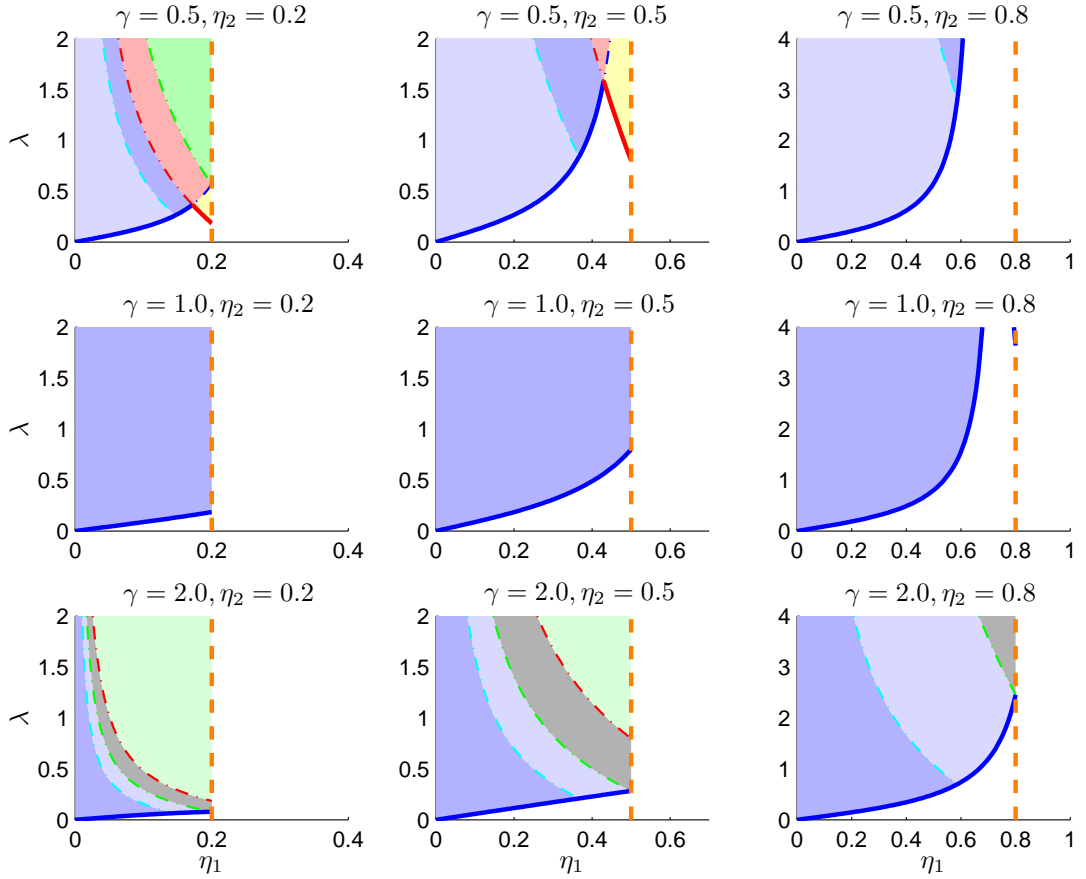
Figure 4-4: As per Fig. 4-3 except: $\nu_1 = 0.3, \nu_2 = 0.3$.

to the shift-up type. With the dash line $\mathring{\sigma}_{\theta\theta}(\bar{\rho}) = 0$ crossing different sections of the curve, there is one NHP in Ω_I for the $\mathcal{B}_2$ type, no NHP in $\mathcal{K}$, and one NHP located in Ω_{II} in the $\mathcal{G}_2$ type. If we refer to all the subplots in Fig. 4-3 and those in the last row of Fig. 4-4 (when γ is relatively large or $\nu_1 < \nu_2$), we may find that the $\mathcal{K}$ background region always share borders with $\mathcal{B}_2$ and $\mathcal{G}_2$ regions.

However, in Figs. 4-3 to 4-5, those background regions of different colours are separated by the boundaries between them. So we will keep our focus on the occurrences of those boundaries and their properties. Since the backgrounds are based on the $I_{a,b}$ and $II_{a,b}$, we would expect that the boundaries can be obtained by letting those values equal zero. Due to the large number of free parameters in this problem, the boundaries should also depend on some of the parameters, which motivates the following analytical investigations. We take $0 \leq \eta_1 \leq \eta_2 \leq 1$, $\gamma := E_1/E_2 > 0$ and $\nu_1, \nu_2 \in [0, 0.5]$ according to general physical sense, which will be used by default as the valid ranges for the parameters in the analysis on those boundaries hereafter.
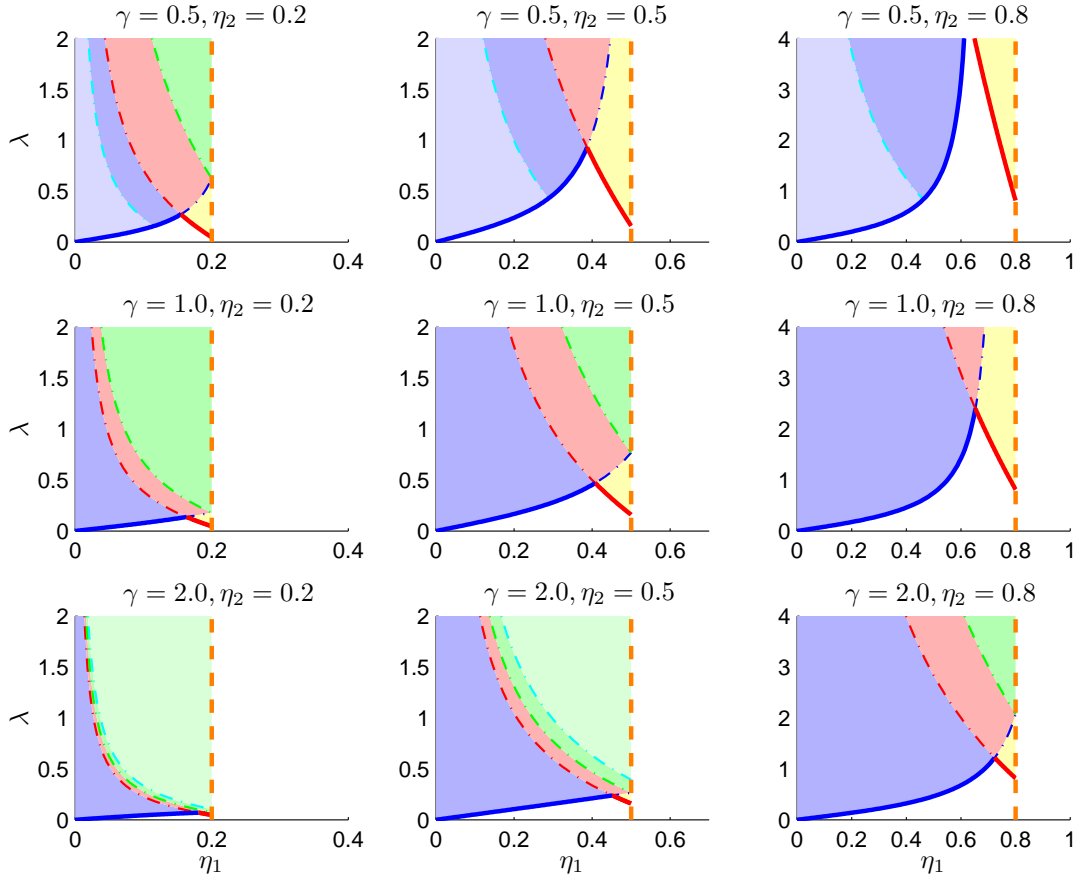
Figure 4-5: As per Fig. 4-3 except: $\nu_1 = 0.3, \nu_2 = 0.1$.

1° **Boundary $\mathbf{B}_1(I_a = 0)$**

If we let $I_a(\eta_1, \eta_2; \lambda) = 0$, then with fixed η_2, we obtain an expression

$$\lambda^{\mathrm{B}_1} = \frac{4\gamma\nu_1\eta_1\eta_2^2}{(1 - \nu_1^2)(1 - \nu_2^2)\left\{\kappa_1\left[\kappa_2 - \kappa_4 - (\kappa_2 + \kappa_3)\eta_2^2\right]\eta_1^2 + \kappa_2\left[\kappa_1 + \kappa_4 - (\kappa_1 - \kappa_3)\eta_2^2\right]\eta_2^2\right\}},$$

which apparently passes the origin $(0,0)$ in $\lambda - \eta_1$ plane and is monotonically increasing with η_1 for entire valid ranges of other parameters $(\eta_2, \nu_1, \nu_2, \gamma)$. However, the latter statement is not as straightforward as the former and requires some explanations as follows. For the sake of clarity, the λ^{B_1} can be expressed in the form

$$\lambda^{\mathrm{B}_1} = \frac{l_1\eta_1}{l_2\eta_1^2 + l_3\eta_2^2}, \tag{4.30}$$

by introducing

$$l_1 := \frac{4\gamma\nu_1\eta_2^2}{(1 - \nu_1^2)(1 - \nu_2^2)}, \quad l_2 := \kappa\left[\kappa_2(1 - \eta_2^2) - (\kappa_4 + \kappa_3\eta_2^2)\right],$$

$$l_3 := \kappa_2\left[\kappa_1(1 - \eta_2^2) + (\kappa_4 + \kappa_3\eta_2^2)\right].$$

The monotonicity of $\lambda^{B_1}(\eta_1)$ is predicted by the sign of its first derivative with respect to η_1

$$\frac{\partial \lambda^{B_1}}{\partial \eta_1} = \frac{l_1}{l_2 \eta_1^2 + l_3 \eta_2^2} - \frac{2 l_1 l_2 \eta_1^2}{(l_2 \eta_1^2 + l_3 \eta_2^2)^2} = \frac{l_1 (l_3 \eta_2^2 - l_2 \eta_1^2)}{(l_2 \eta_1^2 + l_3 \eta_2^2)^2} , \tag{4.31}$$

where l_1 and $(l_2 \eta_1^2 + l_3 \eta_2^2)^2$ are positive except at a singular point where the latter equals zero (referred to in subsequent discussions). If we agree to use the standard signum function 'sgn' in the following discussions, it follows immediately

$$\mathrm{sgn} \left(\frac{\partial \lambda^{B_1}}{\partial \eta_1} \right) = \mathrm{sgn}(l_3 \eta_2^2 - l_2 \eta_1^2) .$$

As $1 - \eta_2^2 > 0$, $\kappa_4 + \kappa_3 \eta_2^2 > 0$, and obviously $l_3 > 0$, so

$$\frac{l_2}{l_3} = \frac{\kappa_1 \left[\kappa_2 (1 - \eta_2^2) - (\kappa_4 + \kappa_3 \eta_2^2) \right]}{\kappa_2 \left[\kappa_1 (1 - \eta_2^2) + (\kappa_4 + \kappa_3 \eta_2^2) \right]} < \frac{\kappa_1}{\kappa_2} \cdot \frac{\kappa_2 (1 - \eta_2^2)}{\kappa_1 (1 - \eta_2^2)} = 1 < \left(\frac{\eta_2}{\eta_1} \right)^2 ,$$

therefore, we always have $l_3 \eta_2^2 - l_2 \eta_1^2 > 0$, which leads to $\partial \lambda^{B_1} / \partial \eta_1 > 0$. To put it another way, $\lambda^{B_1}(\eta_1)$ is an increasing function for any valid parameters ranges in our problem. As η_1 increases from zero, the denominator of λ^{B_1} in (4.30) is always positive (since $l_3 > 0$), before it possibly changes sign from positive to negative (provided $l_2 < 0$). More specifically, $\lambda^{B_1} \to \infty$ at

$$\eta_1 = \eta_2 \sqrt{\frac{(1 - \nu_2) \left[1 - \nu_1 + \gamma (1 + \nu_2) \right] + (1 + \nu_2) \left[1 - \nu_1 - \gamma (1 - \nu_2) \right] \eta_2^2}{(1 - \nu_2) \left[1 + \nu_1 - \gamma (1 + \nu_2) \right] + (1 + \nu_2) \left[1 + \nu_1 + \gamma (1 - \nu_2) \right] \eta_2^2}} .$$

The occurrence of such a singular point requires that the coefficient of η_2 falls between 0 and 1, which leads to the restriction

$$\eta_2 > \sqrt{\left(\frac{1 - \nu_2}{1 + \nu_2} \right) \cdot \frac{\gamma (1 + \nu_2) - \nu_1}{\gamma (1 + \nu_2) + \nu_1}} := \bar{\eta}_2 .$$

Actually, the expression for λ^{B_1} represents, in Fig. 4-3 to 4-5, the blue solid bounds between the bottom-side white region and the blue regions $\mathcal{B}_{1,2}$ in all sub-plots, also the blue dot-dash bounds between the red region $\mathcal{R}$ and the yellow region $\mathcal{Y}$ in the some of the sub-plots.

If the bi-annular problem degenerates into a simple-annular case described by $\rho \in [\eta, 1]$, $\theta \in [0, 2\pi)$, by letting $\eta_1 = \eta_2 = \eta, \gamma = 1.0, \nu_1 = \nu_2 = \nu$, in this case, the condition for such a singular point reads $\eta > \bar{\eta}_2 := \sqrt{(1 - \nu)/(1 + \nu)}$, which matches the previous work in [47].

$2°$ **Boundary $\mathbf{B}_2(II_a = 0)$**

Similarly, if we let $II_a(\eta_1, \eta_2; \lambda) = 0$, we have

$$\lambda^{B_2} = \left(\frac{1 - \nu_1^2}{1 - \nu_2^2} \right) \cdot \frac{(1 + \nu_1)(1 - \nu_1 + \gamma \nu_2) \eta_2^2 - (1 - \nu_1)(1 + \nu_1 - \gamma \nu_2) \eta_1^2}{\gamma \eta_1 \left[1 - \nu_2 - (1 + \nu_2) \eta_2^2 \right]} .$$

For the sake of notational convenience, we can rewrite the above expression as

$$\lambda^{B_2} = l_4 \left(l_5 \frac{\eta_2^2}{\eta_1} - l_6 \eta_1 \right), \tag{4.32}$$

where

$$l_4 := \left(\frac{1 - \nu_1^2}{1 - \nu_2^2} \right) \cdot \frac{1}{\gamma \left[1 - \nu_2 - (1 + \nu_2) \eta_2^2 \right]}, \quad l_5 := (1 + \nu_1)(1 - \nu_1 + \gamma \nu_2),$$

$$l_6 := (1 - \nu_1)(1 + \nu_1 - \gamma \nu_2).$$

It is easily shown that for all parameters within their valid ranges,

$$l_5 \frac{\eta_2^2}{\eta_1} - l_6 \eta_1 = \eta_1 \left(l_5 \frac{\eta_2^2}{\eta_1^2} - l_6 \right) > \eta_1 (l_5 - l_6) = 2 \gamma \nu_2 \eta_1 > 0,$$

then, the validity condition $\lambda^{B_2} > 0$ requires $l_4 > 0$, namely,

$$\eta_2 < \sqrt{\frac{1 - \nu_2}{1 + \nu_2}}.$$

Moreover, the monotonicity of the curves of $\lambda^{B_2}(\eta_1)$ can be indicated by

$$\mathrm{sgn} \left(\frac{\partial \lambda^{B_2}}{\partial \eta_1} \right) = \mathrm{sgn} \left(-l_5 \frac{\eta_2^2}{\eta_1^2} - l_6 \right). \tag{4.33}$$

Keeping in mind that $l_5 > 0$ and $\eta_2 / \eta_1 \leq 1$, then

$$-l_5 \frac{\eta_2^2}{\eta_1^2} - l_6 \leq -l_5 - l_6 = -2(1 - \nu_1^2) - 2\gamma \nu_1 \nu_2 < 0.$$

Consequently, we can conclude that $\lambda^{B_2}(\eta_1)$ is a monotonically decreasing function of η_1. Returning to the background plots for the $\mathring{\sigma}_{\theta\theta}(\eta_1; \lambda)$ in Fig. 4-3 to 4-5, the curves of $\lambda^{B_2}(\eta_1)$ are represented by the red lines (both solid and dot-dashed), which appear naturally between the red region $\mathcal{R}$ and the blue region $\mathcal{B}_1$, or between the yellow region $\mathcal{Y}$ and the white region below, such boundaries only occur under the condition $\eta_2 < \sqrt{(1 - \nu_2)/(1 + \nu_2)}$.

3° **Boundary $B_3(I_b = 0)$**

Following a similar strategy to 1° and 2°, another boundary B_3 can be found by assuming $I_b(\eta_1, \eta_2; \lambda) = 0$

$$\lambda^{B_3} = \frac{(\kappa_3 + \kappa_4)(-\kappa_2 \eta_1 + \kappa_1 \eta_2^2 / \eta_1)}{2 \kappa_1 \kappa_2 (1 - \eta_2^2) + (\kappa_4 + \kappa_3 \eta_2^2)(\kappa_2 - \kappa_1)},$$

which can be rewritten in the simpler form as

$$\lambda^{B_3} = l_7 \left(\kappa_1 \frac{\eta_2^2}{\eta_1} - \kappa_2 \eta_1 \right), \tag{4.34}$$

by introducing

$$l_7 := \frac{\kappa_3 + \kappa_4}{2\kappa_1\kappa_2(1 - \eta_2^2) + (\kappa_2 - \kappa_1)(\kappa_4 + \kappa_3\eta_2^2)}\,.$$

We notice that

$$\kappa_1\frac{\eta_2^2}{\eta_1} - \kappa_2\eta_1 = \eta_1\left(\kappa_1\frac{\eta_2^2}{\eta_1^2} - \kappa_2\right) > \eta_1(\kappa_1 - \kappa_2) = \frac{2\gamma\nu_1\eta_1}{1 - \nu_1^2} > 0\,,$$

therefore, the existence of such a boundary requires $l_7 > 0$, that is

$$\mathrm{sgn}(l_7) = \mathrm{sgn}\left(2\kappa_1\kappa_2(1 - \eta_2^2) + (\kappa_4 + \kappa_3\eta_2^2)(\kappa_2 - \kappa_1)\right) = \mathrm{sgn}\left(\gamma(1 - \eta_2^2) - \frac{\nu_1}{1 - \nu_2} - \frac{\nu_1\eta_2^2}{1 + \nu_2}\right) > 0\,.$$

After some direct analysis, the above statement leads to $\eta_2 < \bar{\eta}_2$ ($\bar{\eta}_2$ was introduced in 1° for the singularity point of $\mathbf{B}_1(\eta_1)$), provided that $\gamma > \nu_1/(1 + \nu_2)$. As for the monotonicity of the boundary λ^{B_3}, we have

$$\mathrm{sgn}\left(\frac{\partial \lambda^{\mathrm{B}_3}}{\partial \eta_1}\right) = \mathrm{sgn}\left(-\kappa_1\frac{\eta_2^2}{\eta_1^2} - \kappa_2\right)\,.$$

In fact,

$$-\kappa_1\frac{\eta_2^2}{\eta_1^2} - \kappa_2 \leq -\kappa_1 - \kappa_2 < 0\,,$$

which suggests that $\lambda^{\mathrm{B}_3}(\eta_1)$ is a monotonically decreasing function of η_1 once it exists. The curves $\lambda^{\mathrm{B}_3}(\eta_1)$ in Figs. 4-3 to 4-5 are shown by the green dot-dashed lines either between the black region $\mathcal{K}$ and the light blue region $\mathcal{B}_2$, or between the red region $\mathcal{R}$ and the green region $\mathcal{G}_1$. It is interesting to point out that the boundary $\lambda^{\mathrm{B}_1}(\eta_1)$ always intersects $\lambda^{\mathrm{B}_3}(\eta_1)$ at $\eta_1 = \eta_2$ when the former curve is not singular for the whole range of η_1 (η_2 is one root of the equation $\lambda^{\mathrm{B}_1} = \lambda^{\mathrm{B}_3}$). Of course, the conditions for the existence of such an intersecting point are $\gamma > \nu_1/(1 + \nu_2)$ and $\eta_2 < \bar{\eta}_2$.

4° **Boundary** $\mathrm{B}_4(I_b = II_a)$

If we let $I_b = II_a$, we have

$$\lambda^{\mathrm{B}_4} = \frac{\kappa_3(\kappa_2 - \kappa_4)\eta_1 + \kappa_4(\kappa_3 - \kappa_1)\eta_2^2/\eta_1}{\kappa_2(\kappa_1 - \kappa_3)\eta_2^2 + \kappa_1(\kappa_4 - \kappa_2)}\,,$$

Before dwelling on the analysis of its behaviours, we introduce some auxiliary notations

$$P^0 := \frac{\nu_1}{\nu_2}\,, \quad P^+ := \frac{\nu_1 + 1}{\nu_2 + 1}\,, \quad P^- := \frac{\nu_1 - 1}{\nu_2 - 1}\,,$$
$$Q^+ := \gamma - P^+\,, \quad Q^- := \gamma - P^-\,,$$

where P^0, P^+ and P^-, depending on ν_1 and ν_2, are obviously positive, whereas the relationship among these three terms is not immediately apparent, and whether the values of Q^- and Q^+

are positive or negative depend further on the relationship between γ, ν_1 and ν_2. Therefore,

$$\mathrm{sgn}(P^+ - P^0) = \mathrm{sgn}\left(\frac{\nu_2 - \nu_1}{\nu_2(1 + \nu_2)}\right) = \mathrm{sgn}(\nu_2 - \nu_1)\,,$$

$$\mathrm{sgn}(P^- - P^0) = \mathrm{sgn}\left(\frac{\nu_2 - \nu_1}{\nu_2(1 - \nu_2)}\right) = \mathrm{sgn}(\nu_2 - \nu_1)\,,$$

$$\mathrm{sgn}(P^- - P^+) = \mathrm{sgn}\left(\frac{\nu_2 - \nu_1}{1 - \nu_2^2}\right) = \mathrm{sgn}(\nu_2 - \nu_1)\,,$$

$$\mathrm{sgn}(1 - P^+) = \mathrm{sgn}\left(\frac{\nu_2 - \nu_1}{1 + \nu_2}\right) = \mathrm{sgn}(\nu_2 - \nu_1)\,,$$

$$\mathrm{sgn}(P^- - 1) = \mathrm{sgn}\left(\frac{\nu_2 - \nu_1}{1 - \nu_1}\right) = \mathrm{sgn}(\nu_2 - \nu_1)\,,$$

and for further reference, we record the results below

$$P^0 \leq P^+ \leq 1 \leq P^- \iff \nu_1 \leq \nu_2\,, \tag{4.35a}$$

$$P^- \leq 1 \leq P^+ \leq P^0 \iff \nu_1 \geq \nu_2\,, \tag{4.35b}$$

here ' $\iff$ ' stands for *if and only if*. After certain direct simplifications with the help of the previously introduced notation and results, we can rewrite λ^{B_4} as

$$\lambda^{\mathrm{B}_4} = \frac{-\eta_1 P^- Q^+ + \eta_2^2/\eta_1 P^+ Q^-}{\gamma(Q^+ - \eta_2^2 Q^-)} := \frac{Nume}{Deno}\,, \tag{4.36}$$

with $Nume$ and $Deno$ denoting the numerator and denominator of this fraction. If we take the first derivative of the above expression with respect to η_1, we have

$$\frac{\partial \lambda^{\mathrm{B}_4}}{\partial \eta_1} = -\frac{P^- Q^+ + \eta_1^2/\eta_1^2 P^+ Q^-}{\gamma(Q^+ - \eta_2^2 Q^-)}\,, \tag{4.37}$$

to be used for the discussion of the monotonicity of the boundary curve $\mathbf{B}_4$. The validity of its expression in Eq. (4.36) requires $\lambda^{\mathrm{B}_4}(\eta_1) > 0$. From (4.36), $\lambda^{\mathrm{B}_4}(\eta_1) > 0$ leads to two cases: the denominator $Deno > 0$ and the numerator $Nume \geq 0$ in the fraction therein; or $Deno < 0$ and $Nume \leq 0$. Moreover, after some direct analysis in terms of the values of Q^+ and Q^-, we have two situations below

$$Q^+, Q^- > 0 \iff \gamma > P^+, P^- \iff \gamma > \max(P^+, P^-)\,, \tag{4.38a}$$

$$Q^+, Q^- < 0 \iff \gamma < P^+, P^- \iff \gamma < \min(P^+, P^-)\,, \tag{4.38b}$$

while, other two situations $Q^+ > 0, Q^- < 0$ and $Q^+ < 0, Q^- > 0$, both yield $\lambda^{\mathrm{B}_4}(\eta_1) < 0$, are therefore dropped.

Case 1 $Deno > 0$ and $Nume \geq 0$

In this case, we have

$$Q^+ > \eta_2^2 Q^- > 0\,, \quad \text{and} \quad \eta_2^2/\eta_1 P^+ Q^- > \eta_1 P^- Q^+\,, \tag{4.39}$$

under such conditions, we shall consider the two sub-cases as listed in (4.38). Before doing so, we can rewrite the statement for the convenience of further analysis

$$\frac{Q^+}{Q^-} = \frac{\gamma - P^+}{\gamma - P^-} = 1 + \frac{P^- - P^+}{Q^-}\,, \tag{4.40a}$$

$$\frac{P^+ Q^-}{P^- Q^+} = \frac{P^+(\gamma - P^-)}{P^- Q^+} = 1 + \frac{\gamma(P^+ - P^-)}{P^- Q^+}\,, \tag{4.40b}$$

which holds irrespective of the value ranges of the parameters.

Case 1a If $Q^+ > 0, Q^- > 0$ as in (4.38a), then (4.39) gives

$$\eta_2 < \sqrt{Q^+/Q^-}\,, \tag{4.41a}$$

$$\frac{\eta_1^2}{\eta_2^2} \leq \frac{P^+ Q^-}{P^- Q^+}\,, \tag{4.41b}$$

There are still two situations regarding ν_1 and ν_2. When $\nu_1 \leq \nu_2$, we have $Q^+/Q^- \geq 1$ and $(P^+Q^-)/(P^-Q^+) \leq 1$. Hence, (4.41a) holds by default, while (4.41b), together with (4.38a) and $\eta_1 \leq \eta_2$, lead to

$$\eta_1 \leq \eta_2 \sqrt{\frac{P^+ Q^-}{P^- Q^+}} \leq \eta_2\,, \quad \gamma > \frac{1 - \nu_1}{1 - \nu_2} \geq 1\,, \quad \nu_1 \leq \nu_2\,. \tag{4.42}$$

On the other hand, if $\nu_1 \leq \nu_2$, then $Q^+/Q^- \leq 1$ and $P^+Q^-/P^-Q^+ \geq 1$, similarly, (4.41b) is satisfied automatically, and we can draw the conclusion

$$\eta_2 \leq \sqrt{\frac{Q^+}{Q^-}} \leq 1\,, \quad \gamma > \frac{1 + \nu_1}{1 + \nu_2} \geq 1\,, \quad \nu_1 \geq \nu_2\,. \tag{4.43}$$

It remains a routine exercise to verify in both situations (4.42) and (4.43), we always have $\partial\lambda^{B_4}/\partial\eta_1 < 0$.

Case 1b As in the case (4.38b), $Q^+ < 0, Q^- < 0$, when (4.39) results in

$$\eta_2 > \sqrt{Q^+/Q^-}\,, \tag{4.44a}$$

$$\frac{\eta_1^2}{\eta_2^2} \geq \frac{P^+ Q^-}{P^- Q^+}\,. \tag{4.44b}$$

It is manifest that in this case the assumption $\nu_1 \leq \nu_2$ will lead to the invalid conclusion $\eta_2 > \sqrt{Q^+/Q^-} \geq 1$, therefore this argument is not true. If we assume $\nu_1 \geq \nu_2$, from (4.44b) we will have $\eta_1^2/\eta_2^2 \geq 1$, which again conflicts with the valid parameter range of η_1. Thus, the

situation **Case** 1*b* does not exist.

Case 2 *Deno* < 0 and *Nume* ≤ 0

On this assumption, we get

$$Q^+ < \eta_2^2 Q^- \,, \quad \text{and} \quad P^+ Q^- \leq \frac{\eta_1^2}{\eta_2^2} P^- Q^+ \,, \tag{4.45}$$

which can be considered in two sub-cases just like **Case** 1.

Case 2*a* Assuming $Q^+ > 0, Q^- > 0$, (4.45) yields

$$\eta_2 > \sqrt{Q^+/Q^-} \,, \tag{4.46a}$$

$$\frac{\eta_1^2}{\eta_2^2} \geq \frac{P^+ Q^-}{P^- Q^+} \,. \tag{4.46b}$$

However, in both situations when $\nu_1 \leq \nu_2$ and $\nu_1 \geq \nu_2$, we arrive at the conclusions $\eta_1^2/\eta_2^2 \geq \sqrt{P^+ Q^-/P^- Q^+} \geq 1$ and $\eta_2 > \sqrt{Q^+/Q^-} \geq 1$, respectively, which both conflict with $0 \leq \eta_1 \leq \eta_2 \leq 1$, which means that the situation **Case** 2*a* is not valid.

Case 2*b* On the other hand, if take the assumption $Q^+ < 0, Q^- < 0$, then

$$\eta_2 < \sqrt{Q^+/Q^-} \,, \tag{4.47a}$$

$$\frac{\eta_1^2}{\eta_2^2} \leq \frac{P^+ Q^-}{P^- Q^+} \,. \tag{4.47b}$$

When $\nu_1 \leq \nu_2$, then $Q^+/Q^- \leq 1$ and $(P^+ Q^-)/(P^- Q^+) \geq 1$; hence (4.47b) is correct for all parameters in their valid ranges, while (4.47a), with the conditions in (4.38b), gives rise to the conclusion

$$\eta_2 < \sqrt{\frac{Q^+}{Q^-}} \leq 1 \,, \quad \gamma < \frac{1 + \nu_1}{1 + \nu_2} \leq 1 \,, \quad \nu_1 \leq \nu_2 \,. \tag{4.48}$$

However, once $\nu_1 \geq \nu_2$, we will have $Q^+/Q^- \geq 1$ and $P^+ Q^-/(P^- Q^+) \leq 1$, which makes the inequality (4.46b) to be always satisfied. In addition, we can have

$$\eta_1 < \eta_2 \sqrt{\frac{P^+ Q^-}{P^- Q^+}} \leq \eta_2 \,, \quad \gamma < \frac{1 - \nu_1}{1 - \nu_2} \leq 1 \,, \quad \nu_1 \geq \nu_2 \,, \tag{4.49}$$

In both cases of (4.48) and (4.49), we will always have $\partial \lambda^{\mathrm{B}_4}/\partial \eta_1 < 0$ according to (4.37).

To conclude, the existence conditions for the boundary $\mathbf{B}_4$ in the $\lambda - \eta_1$ plane are

$$\text{As } \nu_1 \leq \nu_2 \,, \quad \begin{cases} \gamma < P^+ \leq 1 \qquad \text{and } \eta_2 < \sqrt{\dfrac{Q^+}{Q^-}} \leq 1 \,, & (4.50a) \\[3ex] \gamma > P^- \geq 1 \qquad \text{and } \eta_1 \leq \eta_2 \sqrt{\dfrac{P^+ Q^-}{P^- Q^+}} \leq \eta_2 \,, & (4.50b) \end{cases}$$

or

$$\text{when } \nu_1 \geq \nu_2 \, , \quad \begin{cases} \gamma > P^+ \geq 1 \quad \text{and} \qquad \eta_2 < \sqrt{\dfrac{Q^+}{Q^-}} \leq 1 \; , & \text{(4.51a)} \\[4ex] \gamma < P^- \leq 1 \quad \text{and} \qquad \eta_1 \leq \eta_2 \sqrt{\dfrac{P^+ Q^-}{P^- Q^+}} \leq \eta_2 \; . & \text{(4.51b)} \end{cases}$$

Let us return to Figs. 4-3 to 4-5. The boundaries of $\mathbf{B}_4$ are represented by the cyan dot-line curves. Actually, this is the boundary which separates the shift-up and shift-down types. The conditions in (4.50a) apply for all the subplots in first row of both Figs. 4-3 and 4-4, where $\nu_1 \leq \nu_2, \gamma < P^+ \leq 1$; with the conditions (4.50b), $\mathbf{B}_4$ appears in the last row subplots in Figs. 4-3 and 4-4. While, (4.51a) and (4.51b) imply the existence of the cyan curves $\mathbf{B}_4$ in, respectively, the last row and the first row subplots in Figs. 4-4 and 4-5 when $\nu_1 \geq \nu_2$. All the curves of $\mathbf{B}_4$ appear to be monotonically decreasing with η_1 just as we obtained earlier $\partial \lambda^{\mathrm{B}_4} / \partial \eta_1 < 0$.

Lower bound of λ for the occurrence of compressive stresses

After discussing the boundaries of different backgrounds, we draw attention to the fact that, from the point of view of a pure membrane ($\mu = \infty$), it is their lower parts that are immediately relevant. In other words, as λ is progressively being increased from zero, the onset of compressive stresses coincides with the temporal quality when the value of this parameter first reaches the coloured background. We can think of the horizontal boundary separating the coloured background region from the white region as a mapping $\eta_1 \to \lambda^{\mathrm{low}}(\eta_1)$. With this convention in mind the observations just made above say that wrinkling occurs in the bi-annular membrane as soon as $\lambda = \lambda^{\mathrm{low}}$; for a plate, the counterpart of this statement is $\lambda \geq \lambda^{\mathrm{low}}$ i.e., we only have a lower bound in this case.

It can be seen from Fig. 4-3 to 4-5 that, there are two types of the lower bounds (shown in blue and red thick lines): one kind of lower bound is of 'rectangular-hyperbola' shape, which is actually the boundary $\mathbf{B}_1$ ($I_a = 0$, blue thick line) alone, and it coexists with the shift-up type sketches of $\mathring{\sigma}_{\theta\theta}(\rho)$, namely, those denoted by $\mathcal{B}_2, \mathcal{K}$ and $\mathcal{G}_2$; the other kind is of cusp shape, which is actually the lower intersecting parts of both boundaries $\mathbf{B}_1$ ($I_a = 0$, blue thick line) and $\mathbf{B}_2$ ($II_a = 0$, red thick line). This case always agrees with the concurrence of the aforementioned shift-down type $\mathring{\sigma}_{\theta\theta}(\rho)$ sketches, corresponding to the $\mathcal{B}_1, \mathcal{R}, \mathcal{G}_1$ and $\mathcal{Y}$ background subplots. The cusp (intersecting point of B_1 and B_2) can be understood mathematically as the point $I_a = II_a = 0$ in the first quadrant of the $\lambda - \eta_1$ plane. By solving $\lambda^{\mathrm{B}_1}(\eta_1) = \lambda^{\mathrm{B}_2}(\eta_1)$ and dropping the invalid roots of η_1, we are left with the root

$$\eta_1^{\mathrm{cusp}} = \eta_2 \sqrt{\frac{1 - \nu_1 + \gamma \nu_2}{1 + \nu_1 - \gamma \nu_2}}$$

thus, the possibility of the cusp is guaranteed by forcing the intersecting point η_1^{cusp} to be

within $(0, \eta_2)$, which requires $0 < \gamma < \nu_1/\nu_2$. On the contrary, once $\gamma > \nu_1/\nu_2$, the η_1^{cusp} falls outside $(0, \eta_2)$, $\lambda^{\mathrm{low}}(\eta_1)$ appears to be 'rectangular-hyperbola' shape. In conclusion,

$$
\begin{cases}
0 < \gamma < \nu_1/\nu_2\,, & \text{cusp-shape } \lambda^{\mathrm{low}}\,, \\[2mm]
\gamma > \nu_1/\nu_2\,, & \text{rectangular-hyperbola-shape } \lambda^{\mathrm{low}}\,.
\end{cases}
\tag{4.52}
$$

4.4 Remarks on the numerical solutions

In this section, we discuss various strategies for the numerical investigation of the bifurcation equations (4.21) to (4.28) derived in the previous section. The differential equations can be written in linear system form,

$$
\frac{d\boldsymbol{y}^{(j)}}{d\rho} = \boldsymbol{A}^{I}(\rho)\boldsymbol{y}^{(j)}\,, \qquad \rho \in \Lambda_{(j)}\,,
\tag{4.53}
$$

in which the vectors $\boldsymbol{y}^{(j)}$ are defined by

$$
\boldsymbol{y}^{(j)} := \left[W^{(j)},\, \frac{\mathrm{d}W^{(j)}}{\mathrm{d}\rho},\, \frac{\mathrm{d}^2 W^{(j)}}{\mathrm{d}\rho^2},\, \frac{\mathrm{d}^3 W^{(j)}}{\mathrm{d}\rho^3} \right]^{T}\,,
$$

and the matrices $\mathbf{A}^{(j)}(\rho)$ are represented by

$$
\boldsymbol{A}^{(j)}(\rho) := \begin{bmatrix}
0 & 1 & 0 & 0 \\
0 & 0 & 1 & 0 \\
0 & 0 & 0 & 1 \\
-\mathcal{C}_0^{(j)}(\rho) & -\mathcal{C}_1^{(j)}(\rho) & -\mathcal{C}_2^{(j)}(\rho) & -\mathcal{C}_3^{(j)}(\rho)
\end{bmatrix}\,.
$$

The boundary conditions on the inner and outer rims, (4.22), can be cast in vector form,

$$
\boldsymbol{B}^{I}\boldsymbol{y}^{I}(\eta_1) = \boldsymbol{0} \quad \text{and} \quad \boldsymbol{B}^{II}\boldsymbol{y}^{II}(1) = \boldsymbol{0}\,,
\tag{4.54}
$$

where

$$
\boldsymbol{B}^{(j)} := \begin{bmatrix}
1 & 0 & 0 & 0 \\
0 & 1 & 0 & 0
\end{bmatrix}\,.
$$

In addition the continuity conditions (4.28) are also amenable to a similar transformation,

$$
\boldsymbol{G}\boldsymbol{y}^{I}(\eta_2) - \boldsymbol{H}\boldsymbol{y}^{II}(\eta_2) = \boldsymbol{0}\,.
\tag{4.55}
$$

The non-zero elements of the matrices $\boldsymbol{G}$ and $\boldsymbol{H}$ are

$$
G_{11} = G_{22} = 1\,, \quad H_{11} = H_{22} = 1\,,
$$

$$G_{31} = -\beta_1 \frac{n^2 \nu_1}{\eta_2^2}, \quad G_{32} = \beta_1 \frac{\nu_1}{\eta_2}, \quad G_{33} = \beta_1,$$

$$H_{31} = -\beta_2 \frac{n^2 \nu_2}{\eta_2^2}, \quad H_{32} = \beta_2 \frac{\nu_2}{\eta_2}, \quad H_{33} = \beta_2,$$

$$G_{41} = \frac{\beta_1}{\eta_2^3}(3 - \nu_1)n^2, \quad G_{42} = -\frac{\beta_1}{\eta_2^2}\left[1 + (2 - \nu_1)n^2\right], \quad G_{43} = \frac{\beta_1}{\eta_2}, \quad G_{44} = \beta_1,$$

$$H_{41} = \frac{\beta_2}{\eta_2^3}(3 - \nu_2)n^2, \quad H_{42} = -\frac{\beta_2}{\eta_2^2}\left[1 + (2 - \nu_2)n^2\right], \quad H_{43} = \frac{\beta_2}{\eta_2}, \quad H_{44} = \beta_2,$$

The numerical solution of the eigensystem formed with (4.53) to (4.55) can be pursued by using several different strategies. One of the non-trivial features in this problem is the presence of the interface requiring the solutions of (4.53) to be matched via the equations (4.55). In standard terminology, we are dealing with a three-point boundary-value problem. The `MATLAB` software provides built-in functions that allow us to deal with such problems very easily, without the need to do any preliminary work (e.g., see the comprehensive overview given in [110] for the '`bvp4c`' solver). Both the eigenvalues and the corresponding eigenmodes are available by using this software.

Other alternatives are the boundary-value solver '`sbvp`' (see [9, 10, 11]) and a version of the compound matrix method described by Lindsay in [80]. The disadvantage of the latter consists in the fact that only the eigenvalues are available by following that route; to get the eigenmodes one must turn to standard boundary-value solvers like the ones mentioned above. We have used all three approaches to check the accuracy of our results. A further check was done by letting $\gamma = 1.0, \nu_1 = \nu_2$ with various choices for η_1, η_2, and then comparing the results with those obtained in the case of a simple annular plate with uniform material in [47].

4.4.1 Observations regarding the collocation solver '`sbvp`'

Here, for the sake of completeness, we review a few preliminary steps that are needed for using the `MATLAB`-based collocation boundary-value solver '`sbvp`' [9, 11]. This is particularly effective in dealing with problems involving singularities, nonlinearities or any other complicated situations; in certain respects this software copes better than '`bvp4c`' with unexpected difficulties that are usually encountered in problems with large numbers of parameters (where a vast range of solution behaviours is possible). Basically, we have to reformulate our governing equations as a two-point boundary-value problem – this is a standard technique whose pros and cons are reviewed in detail in [7].

By using the change of variables

$$x := \frac{\rho - \eta_1}{\eta_2 - \eta_1} \quad \text{or} \quad \rho = \eta_1 + (\eta_2 - \eta_1)x, \qquad 0 \leq x \leq 1, \tag{4.56}$$

the differential equations (4.21 when $j = I$) are written over the fixed range $\eta_1 \leq \rho \leq \eta_2$. To

accomplish this, let $W^I(\rho) = W^I(\eta_1 + x(\eta_2 - \eta_1)) =: U_1(x)$ and, similarly,

$$\frac{dW^I}{d\rho}(\eta_1 + x(\eta_2 - \eta_1)) =: U_2(x), \quad \frac{d^2W^I}{d\rho^2}(\eta_1 + x(\eta_2 - \eta_1)) =: U_3(x), \quad \frac{d^3W^I}{d\rho^3}(\eta_1 + x(\eta_2 - \eta_1)) =: U_4(x).$$

With these notations, the differential equation (4.21) within Ω_I becomes

$$\frac{d\overline{U}_1}{dx} = \overline{U}_2,$$

$$\frac{d\overline{U}_2}{dx} = \overline{U}_3,$$

$$\frac{d\overline{U}_3}{dx} = \overline{U}_4,$$

$$\frac{d\overline{U}_4}{dx} = -\delta_1^4 \overline{\mathcal{C}}_0^I \overline{U}_1 - \delta_1^3 \overline{\mathcal{C}}_1^I \overline{U}_2 - \delta_1^2 \overline{\mathcal{C}}_2^I \overline{U}_3 - \delta_1 \overline{\mathcal{C}}_3^I \overline{U}_4,$$

where $\delta_1 := \eta_2 - \eta_1$. The coefficients $\overline{\mathcal{C}}_i^I$, $i = 0, 1, 2, 3$ are obtained from the original bifurcation equations (4.21) by expressing ρ in terms of x via (4.56).

Equation (4.21) when $j = II$ is amenable to similar treatment by introducing the new dependent variables $\overline{U}_i$ $(i = 5, 6, 7, 8)$ and the change of variable

$$y := \frac{\rho - \eta_2}{1 - \eta_2} \quad \text{or} \quad \rho = \eta_2 + (1 - \eta_2)y, \qquad 0 \le y \le 1,$$

so that

$$\frac{d\overline{U}_5}{dy} = \overline{U}_6,$$

$$\frac{d\overline{U}_6}{dy} = \overline{U}_7,$$

$$\frac{d\overline{U}_7}{dy} = \overline{U}_8,$$

$$\frac{d\overline{U}_8}{dy} = -\delta_2^4 \overline{\mathcal{C}}_0^{II} \overline{U}_5 - \delta_2^3 \overline{\mathcal{C}}_1^{II} \overline{U}_6 - \delta_2^2 \overline{\mathcal{C}}_2^{II} \overline{U}_7 - \delta_2 \overline{\mathcal{C}}_3^{II} \overline{U}_8,$$

where $\delta_2 := 1 - \eta_2$. Also, with the help of the new variables introduced above, the boundary conditions (4.54) and continuity conditions (4.55) can be recast as

$$\overline{U}_1(0) = \overline{U}_2(0) = 0 \quad \text{and} \quad \overline{U}_5(1) = \overline{U}_6(1) = 0,$$

$$\overline{U}_1(1) = \overline{U}_5(0) \quad \text{and} \quad \overline{U}_2(1) = \overline{U}_6(0),$$

$$\sum_{i=1}^{3} \left[\overline{G}_{3i} \overline{U}_i(1) + \overline{H}_{3i} \overline{U}_{i+4}(0) \right] = 0,$$

$$\sum_{i=1}^{4}\left[\overline{G}_{4i}\,\overline{U}_i(1)+\overline{H}_{4i}\,\overline{U}_{i+4}(0)\right]=0\,,$$

where $\overline{G}_{ij}$ and $\overline{H}_{ij}$ are obtained from their counterparts G_{ij} and H_{ij}, and by taking into account the obvious rules

$$\frac{d}{d\rho}=(\eta_2-\eta_1)^{-1}\frac{d}{dx}\qquad\text{in}\quad\Omega_I\,,$$

$$\frac{d}{d\rho}=(1-\eta_2)^{-1}\frac{d}{dy}\qquad\text{in}\quad\Omega_{II}\,.$$

The upshot of re-writing the equations in this new form is the simplification from a three-point to a two-point boundary value problem. Although there is an increase in order of the new system that needs to be solved, this is a minor impediment since originally we had to solve two fourth-order equations, see equations (4.53). Any boundary-value solver can be used to tackle the new problem. Here, the previously introduced variables x and y are independent variables defined in Ω_I ($\overline{U}_{1\sim4}$) and Ω_{II} ($\overline{U}_{5\sim8}$) respectively. Yet, in this coupled eighth-order boundary value problem, both variables are of the same integral interval $[0,1]$. From a computational point of view, both can be replaced by a unique variable (say z) .

To determine the eigenvalue λ by using the eighth-order boundary-value problem with the help of 'sbvp', we should introduce two auxiliary functions, $\overline{U}_9(z):=\lambda$ and $\overline{U}_{10}(z)$ to be defined shortly. We regard λ as a function of z, so that

$$\overline{U}'_9(z)=\lambda'(z)=0\,.$$

Furthermore, we still need to choose a normalisation for the eigenfunction; here we adopt

$$\overline{U}_{10}(z):=\int_0^z\left|\overline{U}_1(t)\right|^2+\left|\overline{U}_5(t)\right|^2\mathrm{d}t\,.$$

By using the condition $\overline{U}_{10}(1)=1$, the uniqueness of the eigenmodes is ensured. Differentiation with respect to z of the above expression yields

$$\overline{U}_{10}{}'(z):=\left|\overline{U}_1(z)\right|^2+\left|\overline{U}_5(z)\right|^2\,,$$

which is then supplemented with two obvious boundary conditions

$$\overline{U}_{10}(0)=0\,,\quad\overline{U}_{10}(1)=1\,.$$

This completes the set-up process for using 'sbvp'; for further details, such as formulating the Jacobian matrices, we refer to [9, 10, 11].

4.4.2 Compound matrix method

The compound matrix method (CMM) is a natural candidate for finding eigenvalues of boundary-value problems that have turning points. Unlike the classical determinantal method, which fails in this situation because of the presence of turning point, CMM is very robust and requires solving only an initial-value problem for an auxiliary system of differential equations (e.g., [66, 81]); in a certain sense CMM is just a variation of the classical shooting technique, and thus its numerical implementation is fairly straightforward.

With the exception of [80], most applications of this method to *Solid Mechanics* have been centred around two-point boundary-value problems. As already pointed out in §4.4.1, the presence of the interface introduces non-trivial complications; trying to tackle these directly, by using the eighth-order system formulated above leads to no sensible progress since the associated CMM system will contain 70 differential equations. A different strategy, proposed by Lindsay in [80], eliminates the need to go through the reformulation of the previous section and handle the interface directly (without any unwanted increase in dimension). The precise details of how this is accomplished for the present problem have been relegated to *Appendix* B to preserve the flow of the chapter.

4.5 Numerical study of the wrinkling problem

Using the numerical strategies recorded in last section, we can solve the eigenvalue problem formulated in (4.53) to (4.55). Then, the eigenvalue λ can be treated as a function of parameters indicating the geometrical and mechanical properties as defined earlier in (4.11), (4.12) and (4.17), i.e.

$$\lambda = \lambda(\mu, n; \eta_1, \eta_2, \gamma, \nu_1, \nu_2), \qquad n \in \mathbb{N}, \tag{4.57}$$

that provide the vital information for understanding the neutral stability envelope of this problem. With the discussions in §4.3, we will explore the dependence on the parameters in (4.57) on the eigenvalue λ.

As in §4.3, η_1 is regarded as the main variable in this function, i.e., $\lambda(\eta_1)$, while keeping all the other parameters fixed. However, we have an additional parameter (mode number $n \in \mathbb{N}$), which was introduced to the problem through the separable-variable solution (4.20), so eventually we need to identify those values which lead to the smallest eigenvalue. It is for this reason that we need to plot the individual response curves for a whole range of mode numbers as in §4.5.1, and then move on to the smallest eigenvalues, namely, the neutral stability envelope (NSE) as introduced in §1.

4.5.1 Response curves

Recalling the annular plates (both single-annular and multi-annular) under compression (e.g., [55, 56, 85]), the buckling mode normally appears to be either axisymmetric $n = 0$ or asymmetric with $n = 1$. It is also pointed out by Yamaki [127] that under certain boundary conditions the axisymmetric mode does not have the lowest critical load, higher modes must be taken into consideration for compressed annular plates. However, when an annular plate is under tensile stretching (e.g., [28, 41, 47]), the wrinkling modes with $n = 0, 1$ are irrelevant because the original eigenproblem has no solutions, and localised instabilities normally develops fine buckling structures (wrinkling) with mode number $n \gg 1$.
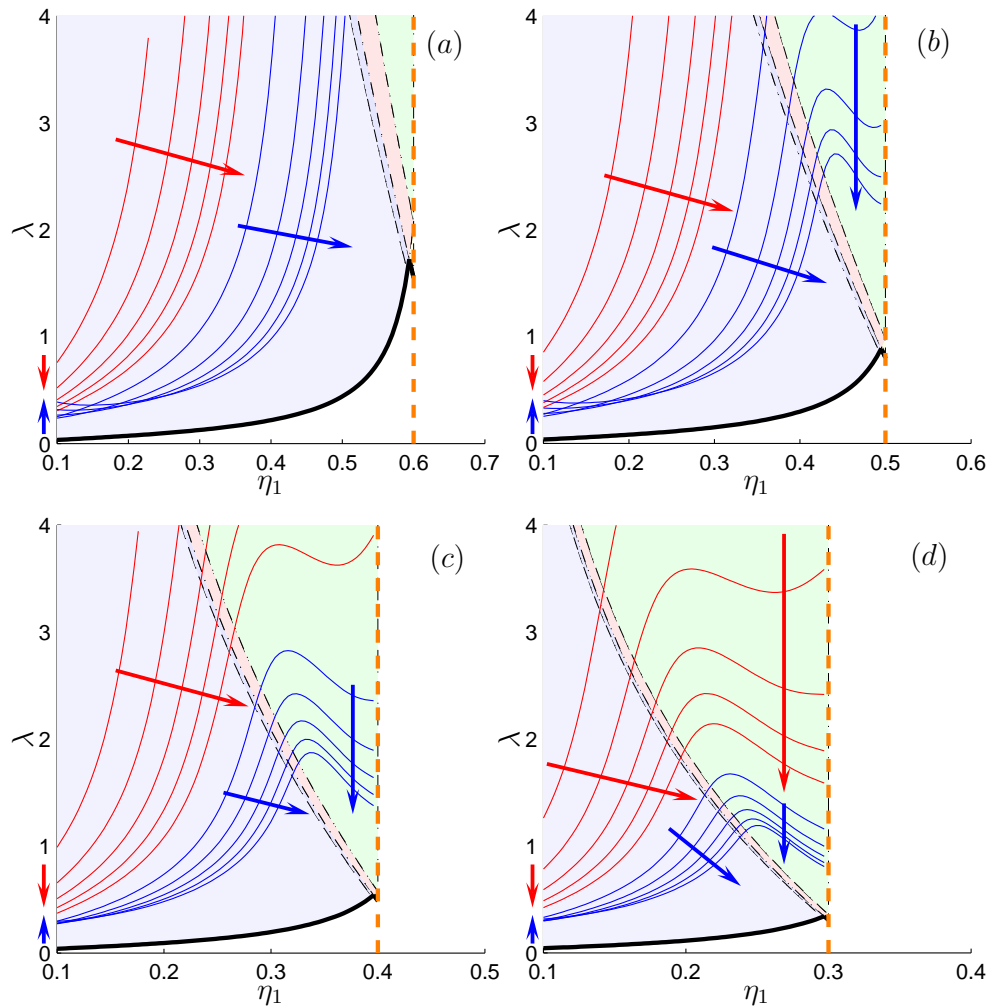
Figure 4-6: Dependence of the eigenvalue λ on the parameter η_1 for $\mu = 400.0, \nu_1 = 0.1, \nu_2 = 0.3, \gamma := E_1/E_2 = 0.3$. The locations of the interface (vertical dashed lines) in $(a) - (d)$ are $\eta_2 = 0.6, 0.5, 0.4, 0.3$, respectively. The values of the mode number for the *red curves* are $n = 6, 8, 10, 12, 14$ in all subplots; $n = 20, 30, 40, 50, 60, 70$ for the families of *blue curves* in (a) and (b), while, $n = 20, 25, 30, 35, 40, 45$ for those *blue curves* in (c) and (d). The red and blue arrows indicate the direction of increase for the mode number n. The coloured background show the prebuckling azimuthal stress types defined in §4.3, the thick black lines in the bottom indicate λ^{low} as for Fig. 4-3.

The relevant numerical results are recorded in Fig. 4-6 to 4-9. We follow the same structure as §4.3 in selecting the range of E_j and ν_j $(j = 0, 1)$ for the response curves, to cover all significant variations between the cases $\gamma \equiv E_1/E_2 < 1$, $\nu_1/\nu_2 < 1$ and their complements. For the purpose of understanding the effect of the interface location on eigenvalue λ, a range values of η_2 have been considered subject to the requirement that they are not too close to either the inner or the outer rims of the annular domain. Hence we chose $\eta_2 \in \{0.6, 0.5, 0.4, 0.3\}$ (shown in each figure as $(a), (b), (c)$ and (d)) and ensure that the starting value of η_1 is never below 0.1. Also, $\mu \gg 1$ will be tacitly assumed in all of our examples. In the response curves in Figs. 4-6 to 4-9, we adopt a moderately large value: $\mu = 400.0$.

The response curves will be denoted by $C^{(n)}$, where the dependence on $n \in \mathbb{N}$ is indicated explicitly. In each set of plots there are two families of curves $C^{(n)}$ shown in different colours. The red ones are obtained by using $n \ll \mu^{1/2}$, and they correspond (roughly) to the *membrane-like* regime identified by Coman and Haughton in [47]. This group of curves contributes nothing to the neutral stability envelope. Similarly with the response curves of a stretched single-annular plate as shown in Fig. 1-7, it is still true that $C^{(n)}$ is always above $C^{(n+1)}$ for the entire range of relevant values $0 < \eta_1 < \eta_2 < 1$ (as indicated by the red arrows showing the increasing direction of the mode number n), and that is why we use the same terminology. The other set of curves, shown in 'blue' and for which $\mu^{1/2} \leq n \ll \mu$, are basically the building blocks of the neutral stability envelope (NSE as mentioned in §1.3). In the language of [47] this will form the *plate-like* regime, in which, the response curves intersect each other, thus forming the NSE.

However, unlike the work in [47] (in Fig. 1-7), the dependence λ vs. η_1 is not always monotonically increasing in both red and blue sets of response curves. For a better understanding of the novel features and seeking clearer linkages between the prebuckling and the buckling state, in Figs. 4-6 to 4-9, the response curves are superimposed with the background indicating the NHP styles proposed in §4.3. Actually, the existence of these features can be indicated by the basic state. For a moderately large μ ($\mu = 400.0$), the response curves appear with a kink-like shape as soon as the lower bound λ^{low} is cusp type, and are of monotonic shape when the λ^{low} is of rectangular-hyperbola type, which is in line with our earlier expectations. Now we will discuss this two types in detail.

$1°$ **kink-type response curves**

In Figs. 4-6 $(b) - (d)$ and 4-7 $(a) - (d)$, the response curves appear to be 'kinked', the value of λ increases when η_1 is far away from η_2, then arrives at a peak at a larger value of η_1 before decreasing with η_1 as η_1 approaches η_2. (Notice that here we use the terminology 'kink' to represent the non-monotonic feature in the response curves and later the neutral stability envelopes, in order to distinguish with the previously introduced 'cusp' in the analysis of the lower bound λ^{low} in $PBAS$ plots.) The sharpness of the kink is dependent on several factors including the mechanical parameters γ, ν_1 and ν_2, the value of large parameter μ and the mode
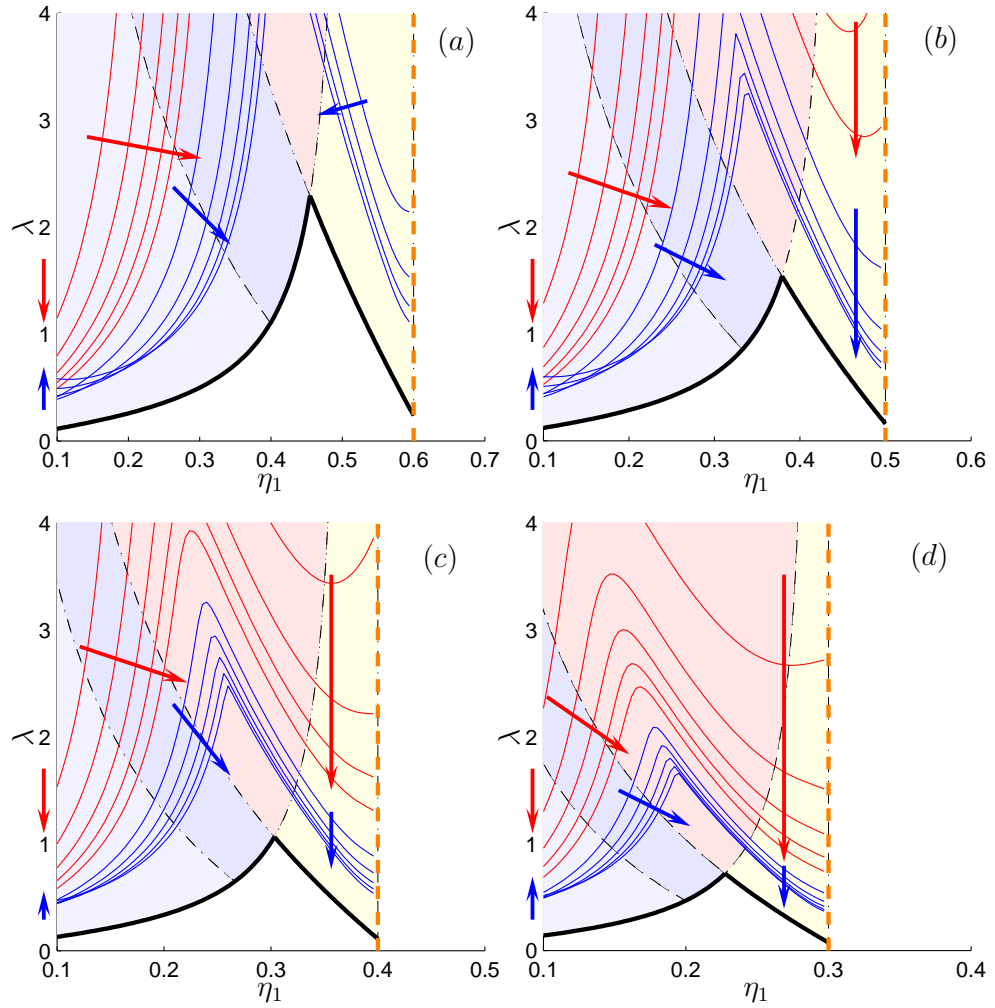
Figure 4-7: Similar to Fig. 4-6, the parameters are taken as: $\mu = 400.0, \nu_1 = 0.3, \nu_2 = 0.1, \gamma := E_1/E_2 = 0.3$. The values of the mode numbers n and the interface locations η_2 in $(a) - (d)$ are the same as the corresponding subplots Fig. 4-6.

number n.

From Figs. 4-6 and 4-7, the smaller the ratio between $\gamma : (\nu_1/\nu_2)$ (which means that $\gamma \ll \nu_1/\nu_2$), the more pronounced will be the 'kink' in the response curves of the same mode number, for instance, comparing the 'kinked' feature in the subplots of Fig. 4-7 (as $\gamma : (\nu_1/\nu_2) = 0.1$) and Fig. 4-6 (when $\gamma : (\nu_1/\nu_2) = 0.9$);

Furthermore, in each set of response curves where a kink is present, the kink-like feature is sharper for larger mode number n than that with smaller n. Also, The 'kinks' become more pronounced as μ increases because $\lambda \to \lambda^{\text{low}}$ in the limit $\mu \to \infty$, which will be shown in NSE analysis in the coming sections.

As $\eta_1 \to \eta_2$, all the 'kinks' of the response curves occur within $\mathcal{R}$ or $\mathcal{G}_1$ background regions, after the response curves enter from $\mathcal{B}_1$ (with compressive stresses only in Ω_I) to $\mathcal{R}$ and $\mathcal{G}_1$ (there are compressive hoop stresses in both Ω_I and Ω_{II}). That is, from a physical point of view, as $\eta_1 \to \eta_2$, the resistance of the wrinkling of a bi-annular plate deteriorates after both
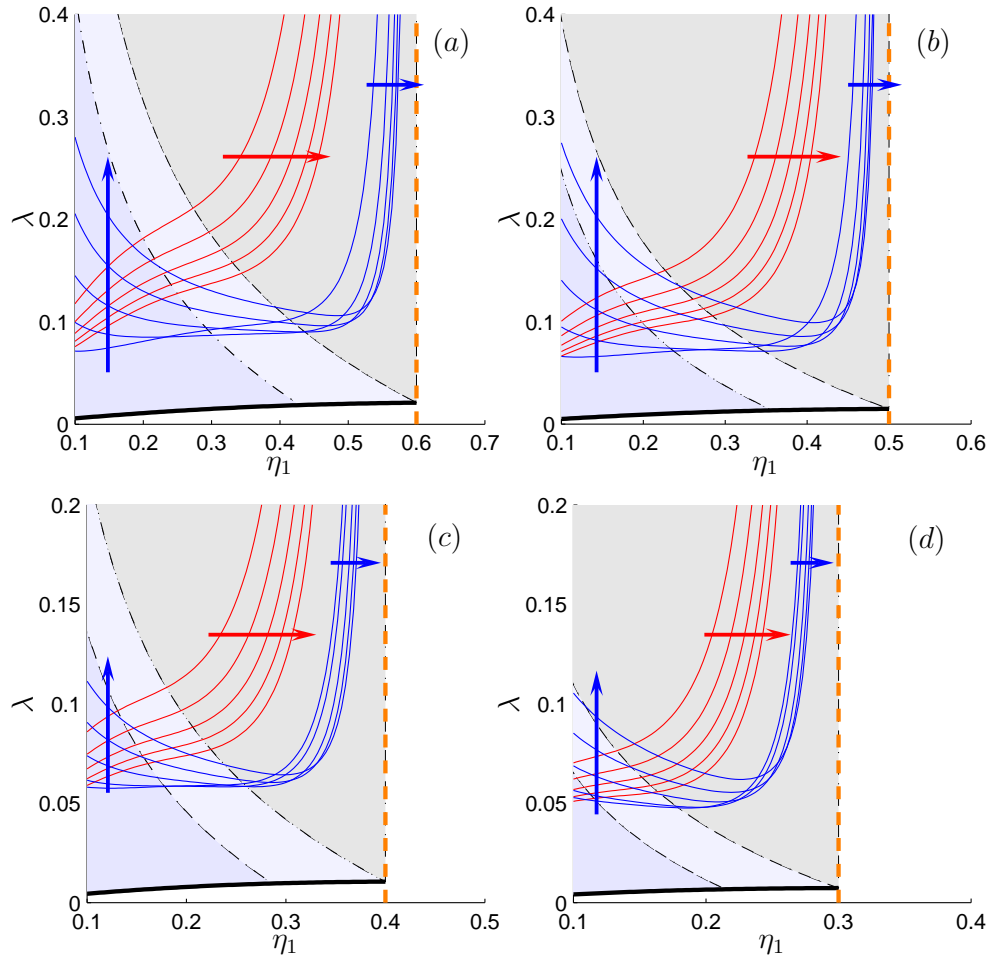
Figure 4-8: Similar to Fig. 4-6; here, the parameters are $\mu = 400.0, \gamma := E_1/E_2 = 10.0, \nu_1 = 0.1, \nu_2 = 0.3$. The *red curves* correspond to the mode numbers $n = 5, 6, 7, 8, 9, 10$, while those in *blue* are obtained for $n = 20, 30, 40, 50, 60, 70$. The location of the interface is $\eta_2 = 0.6$ in (a), $\eta_2 = 0.5$ in (b), while, $\eta_2 = 0.4$ in (c), and $\eta_2 = 0.3$ in (d).

regions experience compressive hoop stresses. The latter statement is a necessary condition for reducing the anti-wrinkling capability of the bi-annular structure. We can also notice that for smaller η_2 (i.e. (d) in Figs. 4-6 and 4-7), the kinks of the response curves occur for a smaller η_1.

$2°$ monotonic response curves

When $\gamma > (\nu_1/\nu_2)$, the response curves corresponding to the rectangular-hyperbola λ^{low} as in Figs. 4-8 and 4-9 also present different characteristics compared with the singular-annular case. It can be observed from these two figures that the response curves are not always convex but can be composed of both convex and concave sections (e.g., see the red curves therein). Even thought the envelope formed by the family of blue curves is monotonically increasing with η_1, it just increase modestly first, then experiences a blow-up like trend when η_1 approaches η_2.

Both the above novel features will be discussed more thoroughly in the context of Neutral Stability Envelop (NSE) in next section.
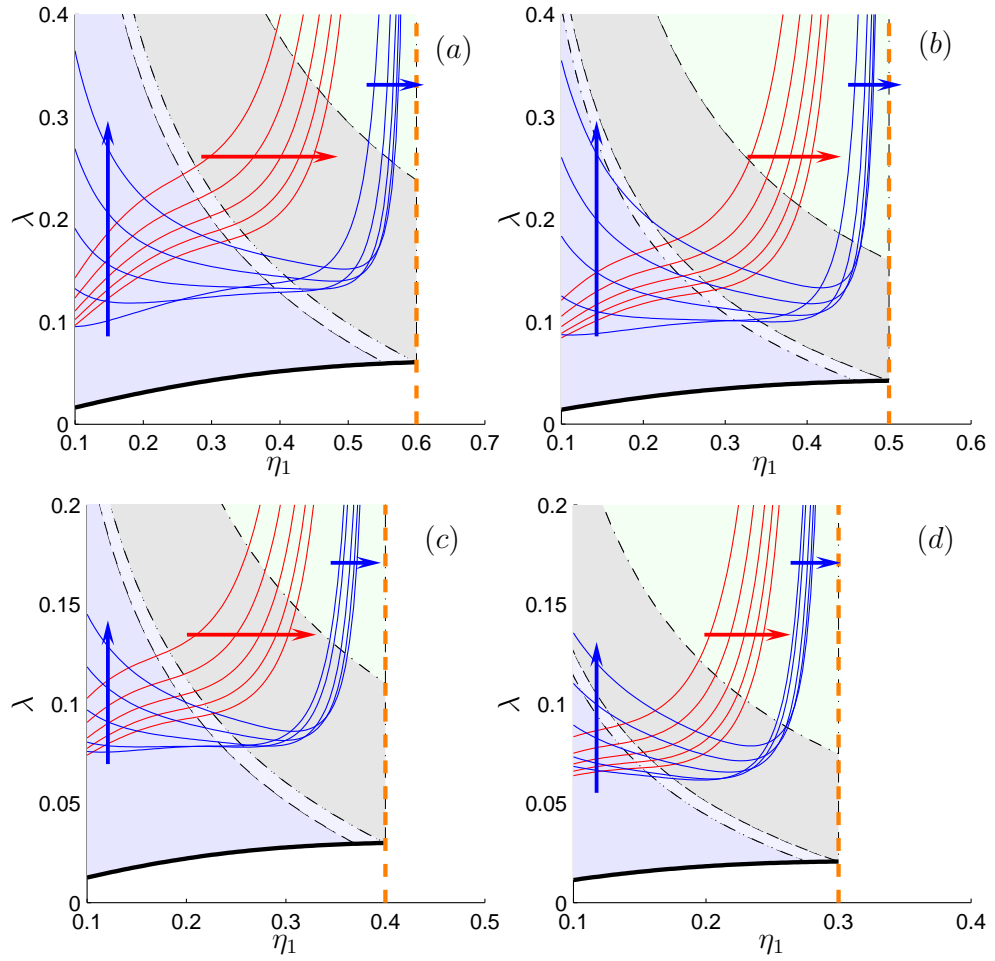
Figure 4-9: Similar to Fig. 4-6; the parameters used are: $\mu = 400.0$, $\gamma := E_1/E_2 = 10.0$, $\nu_1 = 0.3$, $\nu_2 = 0.1$. The *red curves* for all subplots correspond to the mode numbers $n = 5, 6, 7, 8, 9, 10$, while the *blue* ones in (a) and (b) are obtained for $n = 20, 30, 40, 50, 60, 70$, and $n = 18, 20, 25, 30, 35, 40, 45$ for the mode number of *blue curves* in (c) and (d). The interface locations are the same as per Fig. 4-6.

4.5.2 Neutral stability envelope

Now we are in position to investigate the role played by the mechanical parameters γ, ν_1 and ν_2 on the neutral stability (characterised by λ_C, n_C) of the stretched annular plate. In light of the response curves reported in last section, it is these sets of blue curves forming the NSE, like the stretched single-annular case, $\lambda = \lambda(n)$ for our current problem is also a U-shape curve with a global minimum. Hence, the so-called NSE can be cast as $\lambda_C(\eta_1) = \min_{n \in \mathbb{N}} \lambda(n; \eta_1)$, corresponding to the critical wrinkling mode number n_C. So for certain values of η_1, we can solve the eigenproblem numerically [7, 9, 10, 11, 80] by using an optimal strategy with respect to the mode number n.

Firstly, we found that higher elasticity modulus ratio $\gamma := E_1/E_2$ will decrease the wrinkling resistant capability (in terms of the rescaled stretching parameter $\lambda := U_1/U_2$) of a stretched bi-annular plate. We have conducted numerical simulations on the neutral stability curves for
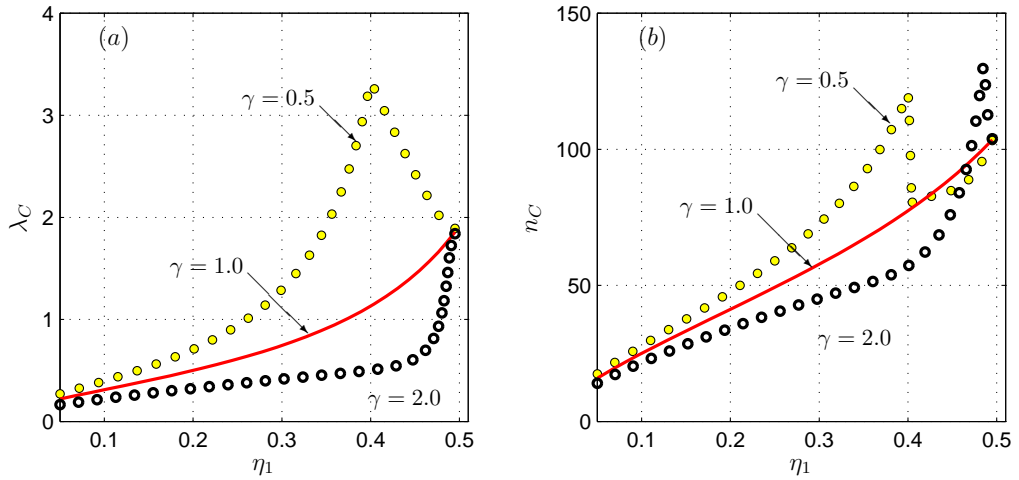
Figure 4-10: Dependence of the neutral stability envelope λ_C and the corresponding critical mode number n_C on the ratio of Young's modulus of inner and outer annuli $\gamma := E_1/E_2$, other parameters are: $\mu = 400.0, \nu_1 = \nu_2 = 0.3$ and $\eta_2 = 0.5$.

a range values of γ when other parameters are fixed. For clarity, Fig. 4-10 only includes three values: $\gamma = 0.5, 1.0$ and 2.0 (other values of γ indicate similar tendency) all with fixed Poisson ratio $\mu = 400.0, \nu_1 = \nu_2 = 0.3$ and $\eta_2 = 0.5$. It is easily seen that the three curves range in a diminishing sequence with increase of γ for all range of η_1. It means that with Poisson ratios fixed, λ_C is inversely proportional to γ, which is true for the entire range of $\eta_1 \in (0, \eta_2)$ (this is also to be shown in § 4.6.3, e.g., in Fig. 4-23); as $\eta_1 \to \eta_2$, whatever the value of γ is, all the curves of λ_C coincide to a limit point (the same happens for those of n_C). At this point, the inner annulus disappears as the bi-annular shrinks to a single annulus with inner radius η_2 and Poisson ratio ν_2, where the two curves of bi-annular plates with $\gamma = 0.5$ and 2 match the results of the single-annular case in [41, 47] (shown in red continuous line). We have also conducted numerical simulations systematically for other fixed Poisson ratio contrasts of these two annuli, the results are consistent with the above conclusions.

Secondly, once γ is fixed, ν_1 plays a dominant role on the the occurrence of wrinkling when η_1 is far away from η_2; whereas, as $\eta_1 \to \eta_2$, ν_2 becomes to be of controlling effect on λ_C and n_C. Fig. 4-11 shows the effect of Poisson ratios of the two annuli on the tensile instability of bi-annular plate with other parameters given in the caption. It is interesting to notice that in Fig. 4-11(a), the yellow dots ($\nu_1 = 0.3, \nu_2 = 0.1$) closely follows the red continuous line ($\nu_1 = \nu_2 = 0.3$) when $\eta_1 < 0.4$ or so. Similarly, the curves of black circles ($\nu_1 = 0.1, \nu_2 = 0.3$) and its counterpart blue continuous line ($\nu_1 = \nu_2 = 0.1$) approach each other for the same regime of η_1. This feature also applies for the associated curves of n_C in Fig. 4-11(b). Moreover, we found that with fixed γ, both the curves of λ_C and n_C approach limit points at $\eta_1 = \eta_2$ if the value of ν_2 is unique (the red continuous line and black circles, the blue continuous line and the yellow dots), which matches closely with the conclusions in last paragraph.

Interestingly enough, our extensive numerical simulations also suggest two representative
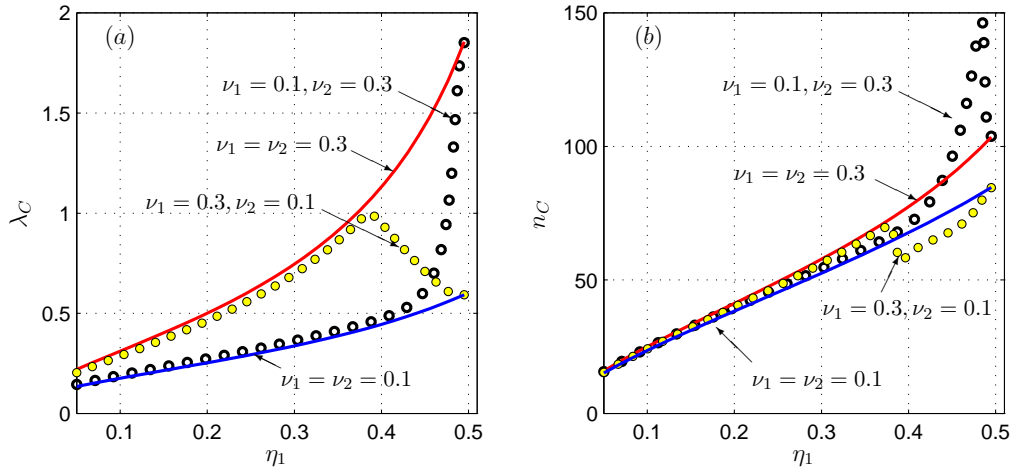
Figure 4-11: Dependence of the neutral stability envelope λ_C and the corresponding critical mode number n_C on the Poisson ratio of two annuli ν_1, ν_2; the other parameters are taken as $\mu = 400.0, \gamma := E_1/E_2 = 1.0$ and $\eta_2 = 0.5$.

types of neutral stability envelopes (NSE) for λ_C, namely, the kink-type (yellow dots in Fig. 4-10(a) and 4-11(a)) and the monotonic-type (black circles therein), which are both different from the curves of the stretched single-annular plate (continuous lines). For the kink-type NSE, with increasing η_1, λ_C increases first up to the a kink, then descends monotonically until η_1 approaches η_2. While, in the monotonic-type NSE, although the curves remain monotonically increasing for the whole range of η_1, λ_C increases modestly with η_1 when η_1 and η_2 are far apart, but increase rapidly as $\eta_1 \to \eta_2$.

4.6 Critical wrinkling modes and morphological changes

In §4.3 and §4.5.2, we discussed thoroughly the prebuckling azimuthal stresses (indicated by $PBAS$ analysis) and the neutral stability envelope (NSE) on the discontinuities that are present in the two-layer structures. Nevertheless, it is important to have a preliminary assessment of how the information in §4.3 and §4.5.2 is reflected in the possible behaviours of the critical eigenfunctions generated by solving the boundary-value problem (4.21) to (4.28). For this we consider a number of representative critical eigenmodes together with their corresponding pre-buckling azimuthal stress-distributions, followed by the morphological changes in the wrinkling modes for the novel kink-type and monotonic-type NSE.

4.6.1 Examples of critical eigenmodes

The results of critical eigenmodes and the related $PBAS$ distribution are summarised in Figs. 4-12 and 4-13 with the parameters recorded in Table 4.2. We shall denote by λ_C and n_C the critical values of the eigenvalue and the mode number, respectively. For each case the eigenmodes are represented by a continuous black line, while the azimuthal stresses appear in green.

Table 4.2: The parameters used in Fig. 4-12.

subplot	γ	ν_1	ν_2	η_1	η_2	n_C	λ_C
$\mathcal{B}_1$-①	0.5	0.3	0.3	0.350	0.500	76.06	2.201548
$\mathcal{B}_2$-①	1.0	0.1	0.3	0.200	0.400	32.78	0.318883
$\mathcal{R}$-①	0.3	0.3	0.1	0.264	0.400	69.20	2.322499
$\mathcal{R}$-②	0.5	0.3	0.1	0.332	0.400	46.15	1.030182
$\mathcal{R}$-③a	0.5	0.3	0.1	0.280	0.400	45.11	1.575215
$\mathcal{R}$-③b	0.5	0.3	0.3	0.400	0.500	101.25	3.937109
$\mathcal{K}$-①	2.0	0.1	0.3	0.400	0.500	56.16	0.265950
$\mathcal{G}_1$-①	2.0	0.3	0.1	0.425	0.500	54.31	0.474511
$\mathcal{G}_1$-②	0.5	0.1	0.3	0.490	0.500	102.54	1.869891
$\mathcal{G}_2$-①	0.5	0.1	0.3	0.470	0.500	129.61	1.639835
$\mathcal{G}_2$-②	2.0	0.3	0.1	0.475	0.500	75.63	0.520341
$\mathcal{G}_2$-④	2.0	0.1	0.3	0.490	0.500	162.45	1.482214
$\mathcal{Y}$-②	0.3	0.3	0.1	0.340	0.400	47.35	1.252496

The orange vertical dashed lines mark the positions of the interface ($\rho = \eta_2$). One of the selecting criteria for picking up these particular eigenmodes was to cover all possible distinct cases when solving the original eigenproblem with respect to the seven types of $PBAS$ as classified in Table 4.1, in order to establish the connections between the $PBAS$ analysis and the wrinkling problem. From an extensive set of numerical simulations we chose only the ones that were the most representative. Loosely speaking, depending on μ, one encounters three general classes of eigenmodes. For $\mu = \mathcal{O}(1)$ the solutions are not necessarily localised, so there is a wide range of behaviours; these were not seriously taken into account because we are interested in the situation $\mu \gg 1$. If this parameter falls (roughly) within the range $200.0 \sim 700.0$ then μ can be regarded as moderately large, and we noticed that the solutions experienced pronounced localised effects. This is the situation that we illustrate in our plots. A third class of eigenmodes would be that corresponding to extremely large values of μ (much greater than 700.0). This is the true asymptotic range in which the critical eigenmodes will reveal significantly less diverse behaviours. The reason for this is that λ_C gets smaller and smaller as μ grows; in the limit $\mu \to \infty$, the neutral stability curve will be almost indistinguishable from the boundary between the white region and the coloured markers in the lower part of the plots included in Figs. 4-3 to 4-5, the curve that was identified as $\lambda^{\text{low}} = \lambda^{\text{low}}(\eta_1)$ in §4.3. Unfortunately, for such large values of μ obtaining the eigenvalues for a whole range of mode numbers becomes problematic because of the singular-perturbation character of the problem and the large number of arbitrary parameters. Nonetheless, it will be seen later in this chapter that our asymptotic predictions compare well with direct numerical simulations even for modest values of the asymptotic parameter μ. The wrinkling mode of a stretched annular plate can be loosely classified into four types: ①-④. Types ① represents the wrinkling mode localised within the inner annulus next to the inner rim; ② stands for the case when wrinkles are located in the outer annulus; there is another interesting wrinkling mode ③, where wrinkling is localised in both sub-regions near the interface; and type ④ describes the wrinkling mode located at the interface.
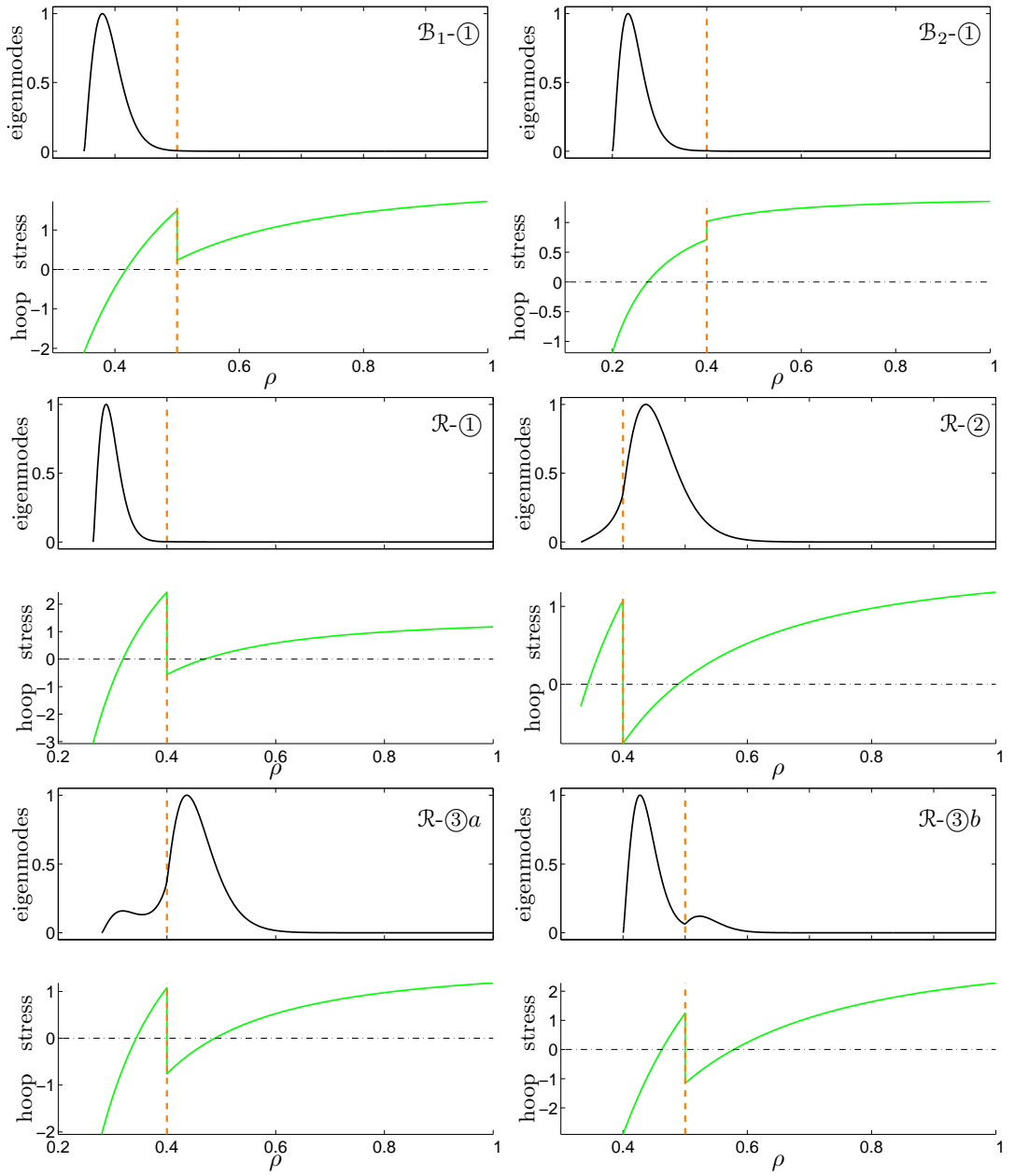
Figure 4-12: Examples of critical eigenmodes for the classifications (a) to (n) in Fig. 4.1 (the examples for $(a), (d), (i)$ are not included here since the corresponding eigenmodes are observed only when the interval $[\eta_1, \eta_2]$ is extremely small). Each example consists of two subplots, namely, the eigenmodes $W(\rho)$ and the corresponding hoop stresses $\mathring{\sigma}_{\theta\theta}(\rho)$. The vertical dashed lines indicate the interface separating the radial direction of Ω in the two regions, $[\eta_1, \eta_2]$ (for Ω_I) and $[\eta_2, 1]$ (for Ω_{II}). The horizontal dot-dashed lines identify the neutral hoop stress $\mathring{\sigma}_{\theta\theta}(\rho) \equiv 0$. All the eigenmodes are appropriately normalised such that their maximum amplitude is equal to one, and the parameters adopted in each sub-plot are shown in Table 4.2.
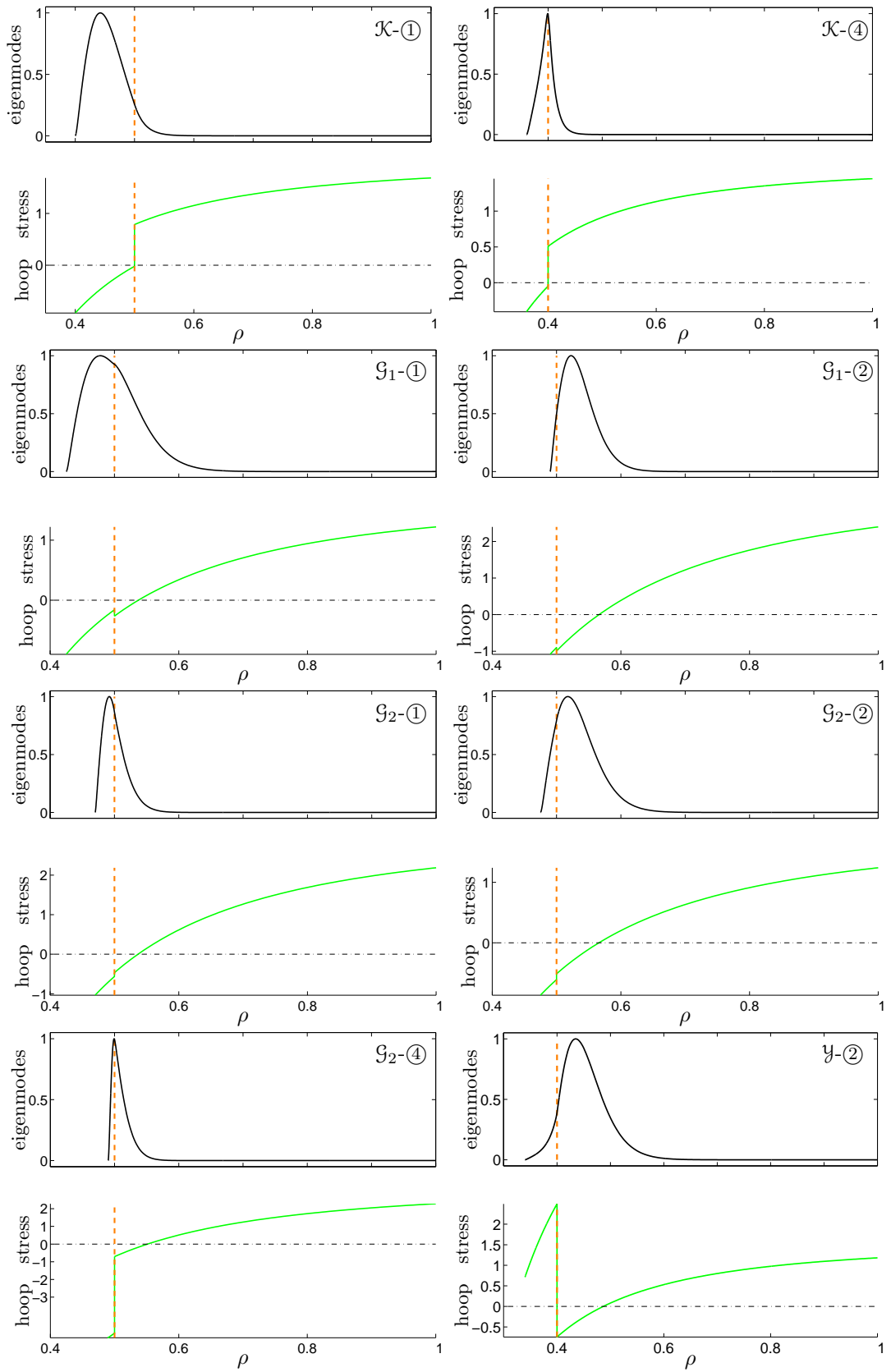
Figure 4-13: Continued from Fig. 4-12.

The most prevalent situations are characterised by eigenmodes localised within the region Ω_I, which resemble closely those seen in the stretched simple annulus (e.g., [47]), and we denote as type ①. For example, see the subplots with the notation containing '-①' in in Figs. 4-12 and 4-13. This type of wrinkling mode is generally encountered for the cases in which there is just one NHP in Ω_I (when η_1 and η_2 are far apart), like $\mathcal{B}_1 - $① and $\mathcal{B}_2 - $① in Fig. 4-12, and there are disjoint regions in the inner annulus in which the hoop stresses have opposite signs in Ω_I; the outer annulus is fully under tensile stresses. Extensive numerical experiments show that for all the cases of $\mathcal{B}_1$ and $\mathcal{B}_2$, the associated critical wrinkling mode is certainly of type ①. It might be tempting to say that only this class of $PBAS$ will lead to type ①. However, this would be wrong: since $\mu \to \infty$ is not true for our problem, the occurrence of the type ① does not exclude other classes of $PBAS$ such as $\mathcal{R}$ and $\mathcal{K}$.

We also have wrinkling mode localised in the Ω_{II} next to the interface, which are labelled type '②' in Figs. 4-12 and 4-13. It is again very straightforward to understand the situation $\mathcal{G}_1, \mathcal{G}_2$ and $\mathcal{Y}$, this situation is typically encountered when $|\eta_2 - \eta_1|$ is sufficiently small and $0 < \gamma < 1$. On the other hand, we can also have the wrinkling mode of type ② when the $PBAS$ background is of type $\mathcal{R}$. The reason is the same as those of type ①.

As we change the size of the inner annulus, namely the value of η_1, we would have expected that there should be intermediate wrinkling modes which are localised near the interface. Indeed, an interesting mode ③, as presented as $\mathcal{R}$-③a and $\mathcal{R}$-③b in Fig. 4-12, is localised in both Ω_I and Ω_{II}. However, this wrinkling mode is limited to the $PBAS$ case when we have NHPs in both annular subregions (within $\mathcal{R}$ background and $\gamma < \nu_1/\nu_2$). For $\mu \gg 1$ such a case is only noticeable for an extremely narrow window of $0 < \eta_1 < \eta_2 < 1$, so it represents an exception, and will be discussed again later on.

Yet another scarce occurrence, ④, is the wrinkling mode with a crest located in the vicinity of the interface, which also happens only for a small interval of η_1 within the $\mathcal{R}$ or $\mathcal{G}_2$ background. This type of wrinkle only happens for the shift-up $PBAS$ distribution with $\gamma > \nu_1/\nu_2$, when the azimuthal stresses are fully compressive in Ω_I, and those of the entire or part of Ω_{II} is under tensile hoop stresses. For instance, see $\mathcal{G}_2$-④ and $\mathcal{K}$-④ in Fig. 4-13. A quick glance at Figs. 4-10 and 4-11 suggests that this scenario is also unlikely in the asymptotic regime, a fact that was confirmed by our extensive numerical simulations.

4.6.2 Morphological changes on critical wrinkling modes

Having seen what the critical eigenmodes look like, the next task is to understand a bit better the novel kink- and monotonic-type NSE combined with the possible morphological changes of the wrinkling modes undergone by these eigenmodes as $\eta_1 \to \eta_2$. Both the monotonic and kinked features can be traced back to the $PBAS$ analysis in § 4.3, which is the case for $\mu \to \infty$. For the plate scenario ($0 < \mu < \infty$) that information is not immediately relevant, although for very large values of μ, we expect the latter situation to mirror closely the former. As we shall

see shortly in § 4.8, for $\mu \gg 1$ (but finite), the role of the NHP's is replaced by the *turning points* of certain second-order differential equations. Therefore, we will try to understand by means of the pre-buckling analysis and the corresponding critical eigenmodes.
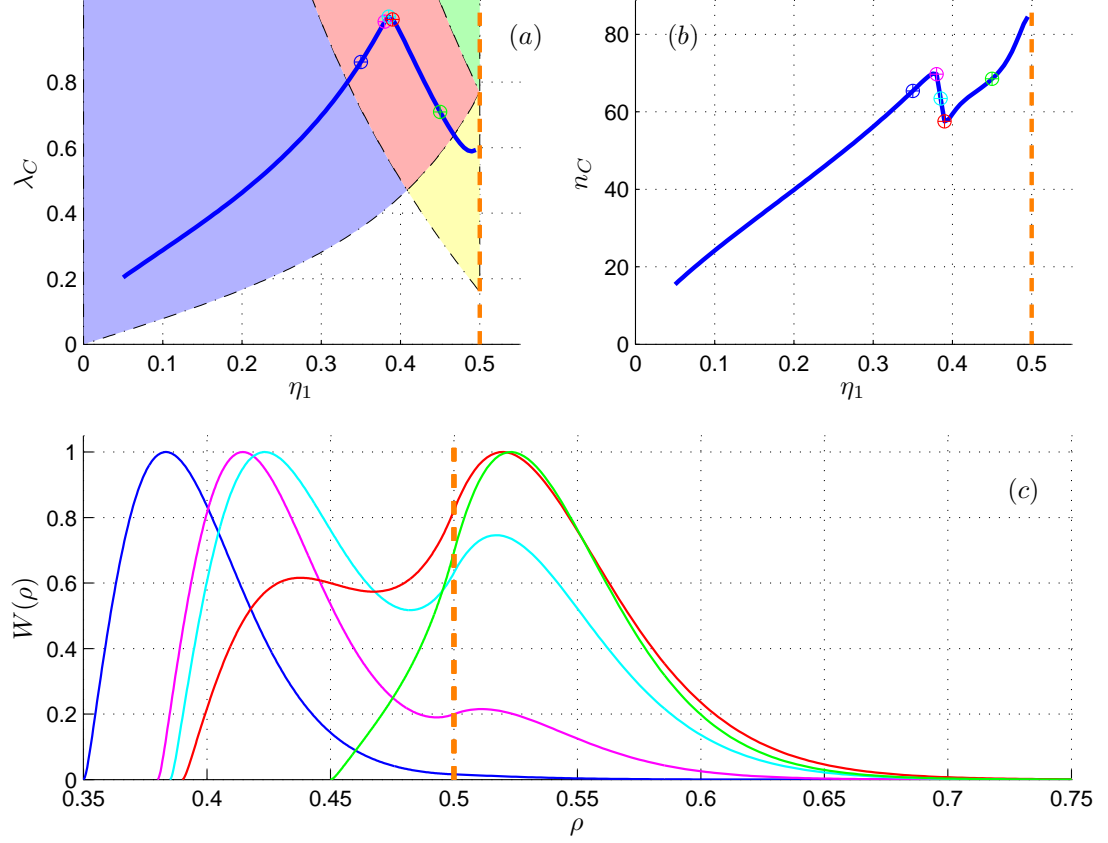
Figure 4-14:   Morphological changes of the critical eigenmodes as $\eta_1 \to \eta_2$ before and after the 'kink' for the kink-type neutral stability envelope. In both (a) and (b), we use different colours of '$\oplus$' to show the chosen critical values of λ_C and n_C near the kink of the kink-type NSE, namely, at $\eta_1 = 0.35, 0.38, 0.385, 0.39, 0.45$; while (c) includes the critical eigenmodes showing the morphological changes at those points labelled by the corresponding coloured '$\oplus$' as in (a) and (b). In (a), the coloured background indicates the classification of the prebuckling azimuthal stress $(PBAS)$ which was introduced in § 4.3. Here $\mu = 400.0$, $\gamma = 1.0$, $\nu_1 = 0.3$, $\nu_2 = 0.1$, $\eta_2 = 0.5$.

1° Kink-type neutral stability envelopes

Kink-type neutral stability envelopes (NSE) generally occur in the stretched bi-annular plates with flexible inner annulus (when $0 < \gamma < \nu_1/\nu_2$ as indicated in basic state analysis), which follows the features of the lower bound λ^{low} as shown in Fig. 4-14 (a).

In Fig. 4-14(a) and (b), we use colour '$\oplus$'s to label the values of λ_C, n_C for a sequence of η_1, while the corresponding critical eigenmodes are shown with the same colour, in which the largest amplitude is normalised to 1. On a closer look at the critical eigenmodes together with the related points on the kink-shape λ_C, it is clearly that, when η_1 is on the left but not close to the kink (the blue $\oplus$ in (a)), the critical eigenmodes localised within region Ω_I near its inner rim $\rho = \eta_1$, see the left-most (blue) wrinkling mode in Fig. 4-14(c), which is of type ①. While, on the right side of the kink, when $\eta_1 \to \eta_2$, the critical eigenmodes are localised within region

Ω_{II} next to the interface, such as the right-most (green) wrinkling mode in Fig. 4-14(c), and it is of type ②. However, there is an interesting transition between the aforementioned two types of eigenmodes ① and ② corresponding to the vicinity of the kink on the kink-shape λ_C curve, e.g., the intermediate modes between the blue (type ①) and green modes (type ②).

Just before η_1 approaches the kink (pink wrinkling mode), when λ_C is still increasing with η_1, the wrinkling mode n_C arrives at its maximum in (c) (pink $\oplus$ in (a) and (b)), which means that at this stage, the wrinkled bi-annular plate displays the maximum number of wrinkles. While the wrinkling mode is mainly localised in Ω_I, a little bump develops in Ω_{II} (pink curves in (c)) compared with the blue one in (c).

As η_1 approaches the kink for maximum λ_C (the cyan $\oplus$ in (a)), n_C passed its maximum (the cyan $\oplus$ in (b)). The localised part in Ω_I shrinks gradually, and meanwhile, the bump in Ω_{II} near the interface increases, the wrinkles in both subregions are of matching maximal amplitudes (see the cyan wrinkling mode in (c)). We can also say it is localised in both regions near the interface. This wrinkling mode was classed as type ③ in the last section. It is important to mention that this type of transition only occurs for the cases that have NHP's in both annular subregions (the $PBAS$ being $\mathcal{R}$ type).

After the kink point of λ_C, the NSE decreases and the corresponding n_C continues to decrease until it approaches it local minimum (red $\oplus$ in (a) and (b)), then it increases again (e.g., the green $\oplus$'s).

As indicated above, the peak of λ_C does not coincide with that of n_C. A more transparent version on the kink-transition will be shown later in Fig. 4-19(a), by superimposing the plots of both λ_C and n_C (Fig. 4-14(a), (b)) and zooming-in near the kink. The curve of n_C has a local maximum at $\eta_1 \simeq 0.3755$ and a local minimum at $\eta_1 \simeq 0.3780$. There is one global maximum point of λ_C located between the two η_1s, at $\eta_1 \simeq 0.3770$.

The turning points in the curves of λ_C and n_C are not very sharp when γ is just slightly smaller than ν_1/ν_2, and the local extremum of λ_C does not coincide with those of n_C, such as the case in Fig. 4-19(a) where $\gamma : (\nu_1/\nu_2) = 1 : 3$. Such a gentle-shift character is rooted in the shape of response curves and the way they intersect; see more details in Fig. 4-15(a). It is of geometrical sense that the family of round-shape curves will intersect to form a 'round' kink of the NSE. Also, the corresponding n_C appears to be round-shape in (b), the shift from the local maximum ($n = 70$) to the local minimum ($n = 57$) involves a sequence of integral mode numbers ($n = 69$ to 58). The turning points on the curves become sharper when $\gamma \ll \nu_1/\nu_2$. For example, when we change the γ in last case to $\gamma = 0.3$, the response curves are much sharper (Fig. 4-16) than the previous case in Fig. 4-15; therefore, the turning point on the curve NSE is extremely sharp, and the shift point of n_C curves just looks like a discontinuity. When we only consider the integral mode number n, the shift of n_C is just a discontinuity, reducing from $n = 111$ directly to $n = 74$ as demonstrated in Fig. 4-16(b). Also, in this case, the peak location (in terms of η_1) for λ_C seems to happen just at the peak of n_C.
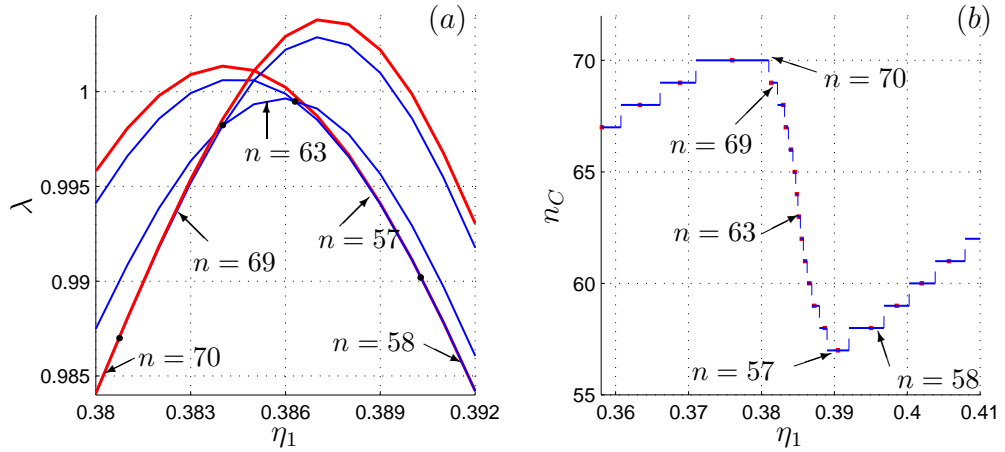
Figure 4-15: The intersected response curves of round-shape kink shown in (a) which form the non-sharp kink on neutral stability envelope NSE (we only include several curves of n for clarity, the black dots indicate the intersecting points), and the corresponding natural critical mode number n_C is given by the nearest integer function of the real results n_C designated by the staircase-like line in (b). Here, it is the identical case shown in Figs. 4-14 and 4-19(a), where the parameters are referred to, and $\gamma : (\nu_1/\nu_2) = 1 : 3$.
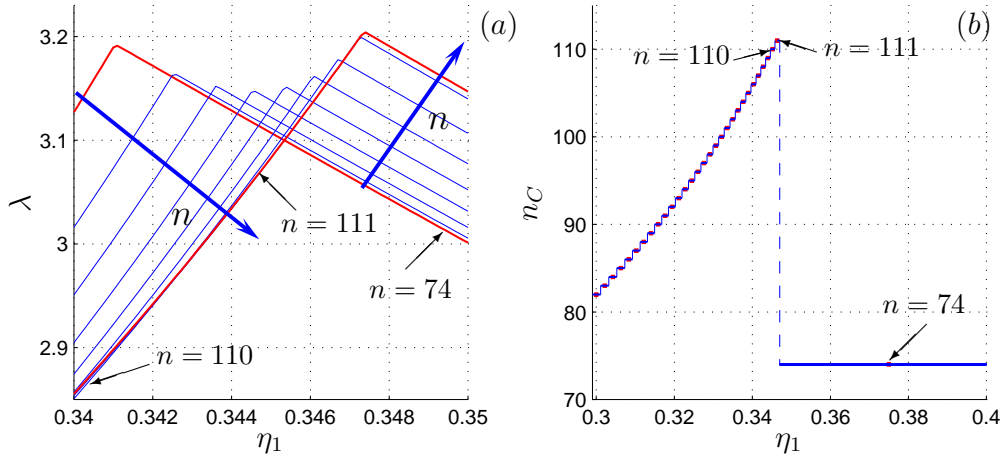
Figure 4-16: The counterpart case of Fig. 4-15, for sharp-shift curves of NSE and n_C. The intersected response curves of sharp kink shown in (a) form the sharp kink on neutral stability envelope NSE, when $\gamma : (\nu_1/\nu_2) = 0.3 : (0.1 : 0.3) = 1 : 10$ is extremely small. While the corresponding natural critical mode number n_C shown in (b) with the presence of a discontinuity. Other parameters are: $\mu = 400.0$ and $\eta_2 = 0.5$.

We mention in passing that the kink behaviour of λ_C (or the discontinuity feature of n_C) is more and more pronounced as μ increases, see Fig. 4-17. To put it another way, the turning points on the curves of both λ_C and n_C become sharper with increasing μ. This observation on neutral stability envelopes originates from similar behaviours of the response curves as discussed §4.5.1. Another piece of information can be collected from Fig. 4-17: as μ increases, the NSE always show a parallel pattern with the λ^{low}, and it approaches λ^{low} as $\mu \to \infty$. At the same time, the corresponding n_C increases with the value of μ.
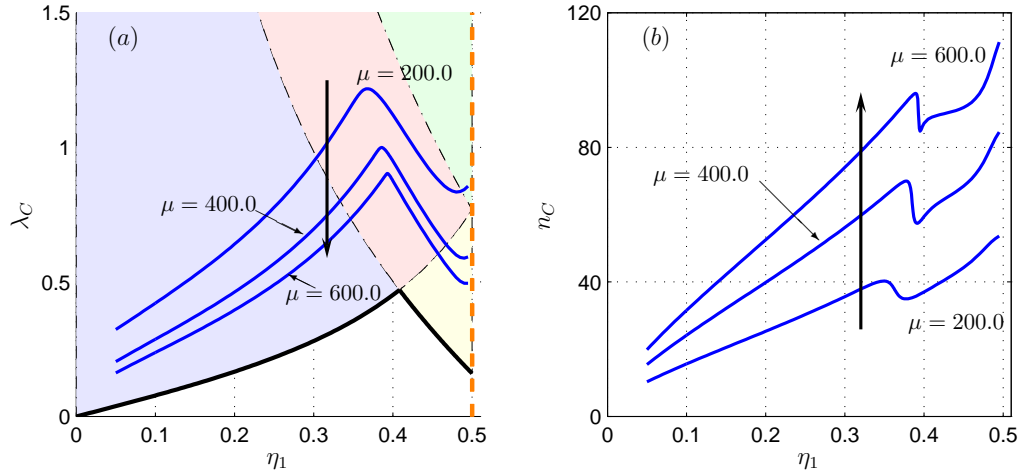
Figure 4-17: The critical eigenvalues λ_C and the corresponding critical mode number n_C with the rescaling parameter μ ranges $200.0, 400.0$ and 600.0. The other parameters are: $\gamma := E_1/E_2 = 1.0, \nu_1 = 0.3, \nu_2 = 0.1, \eta_2 = 0.5$. The black thick arrow indicates the direction of increasing μ.

$2°$ **Monotonic-type neutral stability envelopes**

In light of the pre-buckling azimuthal stress $PBAS$ analysis in § 4.3, a stretched bi-annular plate with flexible inner annulus $(\gamma := E_1/E_2 > \nu_1/\nu_2)$ tends to have 'monotonic' type neutral stability curves (NSE). Notice that even though this type is also monotonic just as the NSE of stretched single-annular plate, there are two differences. On the one hand, λ_C is very small when η_1 is far away from η_2 (see Fig. 4-18(a)), then increases steeply as η_1 approaches η_2, displaying a blow-up like trend before arriving at its limit as η_1 approaches η_2. On the other hand, the plots of n_C are not monotonically increasing with respect to η_1 (see Fig. 4-18(b)), but firstly increase gently with η_1 then reach a maximum (the red $\oplus$ in (b)) when η_1 is near η_2, then return to a limit value at $\eta_1 = \eta_2$.

These significant features can be understood further by looking at the critical eigenmodes in subplot (c) therein. The critical eigenmodes when η_1 and η_2 are apart from each other or when $\eta_1 \to \eta_2$ are localised in Ω_I (the blue $\oplus$'s in $(a), (b)$ and the blue eigenfunction in (c), which is of type ①) and Ω_{II} (the green $\oplus$'s in $(a), (b)$ and the green curve in (c), of type ②) respectively, just similar with the case in kink-type NSE. However, this monotonic-type λ_C has completely different features for the transition between the above two. On the process of η_1 going close to η_2, the localised wrinkles move towards the interface, until it starts to cross the interface as λ_C increase sharply. Then, when the wrinkle crest crosses the interface (see the red eigenmode in (c), of type ④), n_C reaches its first local maximum (red $\oplus$ in (b)). After that, the critical wrinkling mode shift to the mode localised in Ω_{II} (green curve in (c) of type ②) as soon as n_C drop rapidly to its limit point at η_2. It is to be emphasised that during the whole range of η_1 (①→④→②), there is only one bump for the critical mode, distinct from the special wrinkling mode of the kink-type NSE case.

The morphological change of the critical eigenmodes (from ① to ②) occurs when the critical
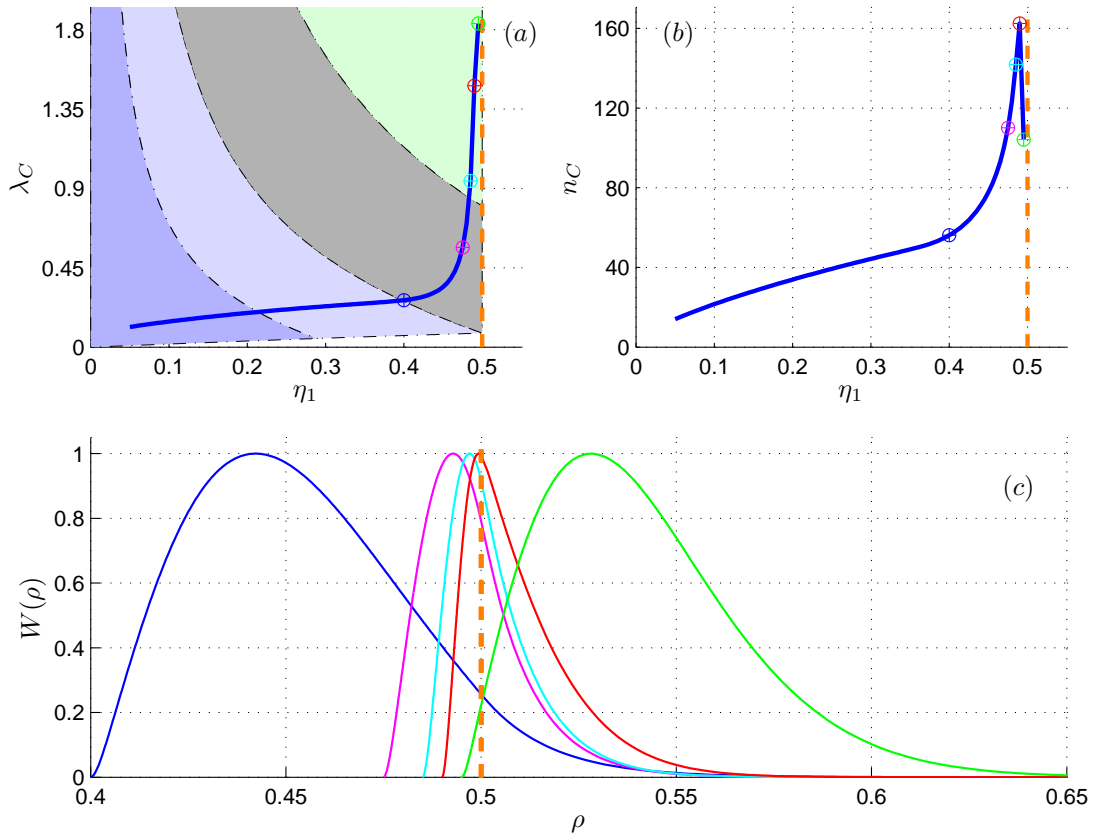
Figure 4-18: Morphological changes of the critical eigenmodes as $\eta_1 \rightarrow \eta_2$ for the "monotonic" type neutral stability envelopes (NSE). The subplots are similar with Fig. 4-14, but $\mu = 400.0$, $\gamma = 2.0$, $\nu_1 = 0.1$, $\nu_2 = 0.3$, $\eta_2 = 0.5$. The eigenfunctions from left to right correspond to $\eta_1 = 0.4, 0.475, 0.485, 0.49, 0.495$.

wrinkle number is in the vicinity of its maximum. That is to say, for this case, the maximum wrinkles number happens when the wrinkles are localised at the interface (of type ④). Finally, we shall discuss the influence of the physical discontinuity introduced by the interface on the novel behaviours of the λ_C, n_C and the critical eigenmodes. In order to see more clearly the new features, we superimpose the plots of λ_C and n_C both in Figs. 4-14 and 4-18 into the same plot as in Fig. 4-19. It is found that both types ③ (two-bump wrinkles) and ④ (wrinkle crest passes the interface) are the transition wrinkling modes between ① and ②, and they only occur for a very small window of η_1. Also, when the wrinkles are localised near the interface (either type ③ or types ④), the plate is likely to exhibit finer wrinkles (n_C is relatively larger). More specifically, when the localised wrinkle transits from the more flexible region to the stiffer region as η_1 varies, the curves of n_C will experience a steep increase to a local maximum at this transition point, then decrease. See Fig. 4-19, where it is shown that when we decrease η_1 in (a) (from right to left) or increase η_1 in (b) (from left to right), we will have an upward-shifting of n_C to a local minimum then a decrease.
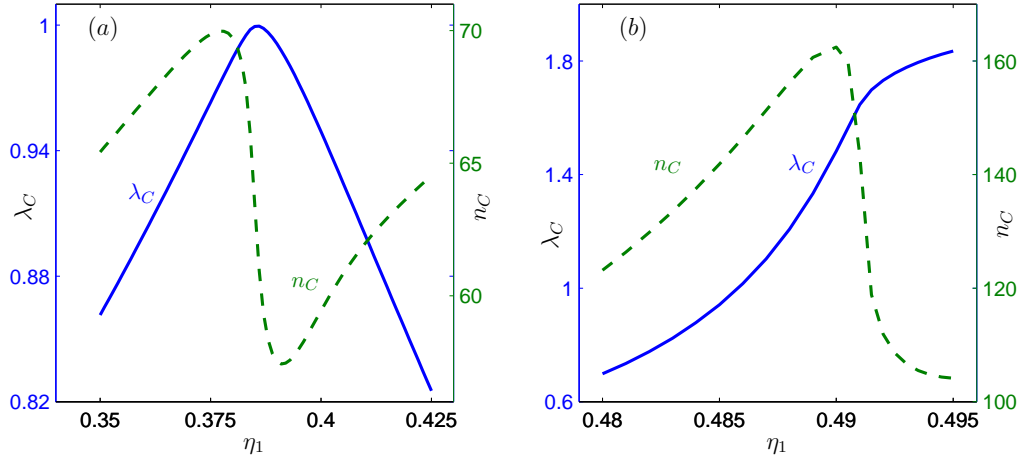
Figure 4-19: The close-up plots (a) and (b) include the two superimpositions of λ_C and the corresponding n_C in Fig. 4-14 and Fig. 4-18 respectively. In (a), we focus on the 'kink' of the kink-type NSE as in Fig. 4-14, while (b) emphasises the abnormal behaviour of n_C at $\eta_1 \to \eta_2$ for the case shown in Fig. 4-18. The blue continuous lines stand for the λ_C, and the green dashed curves denote the associated n_C.

4.6.3 The dependence of λ on $\gamma \equiv E_1/E_2$ and ν_1/ν_2

Given the large number of parameters in our boundary eigenvalue problem it seems desirable to get a more systematic understanding of the dependence of the eigenvalue on the ratios E_1/E_2 and ν_1/ν_2 for a range of different mode numbers. Here we include a sample of results that shed more light on these matters.
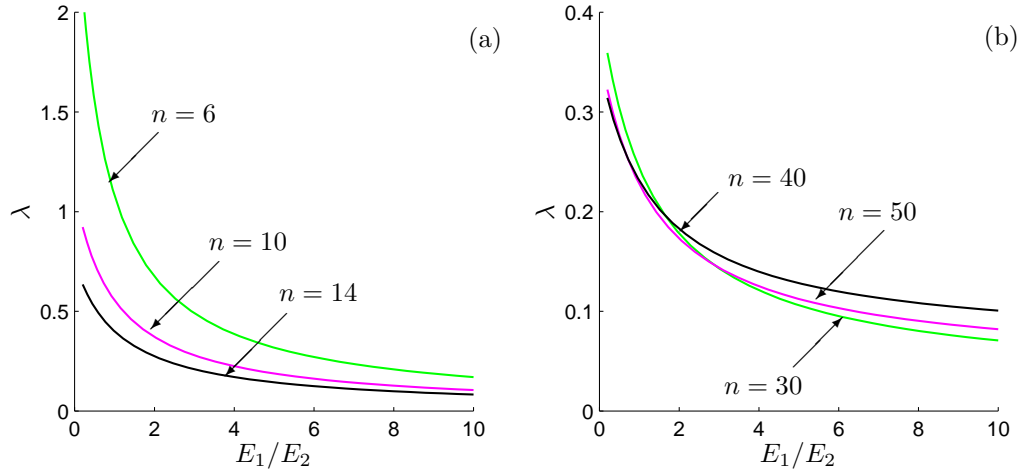
Figure 4-20: Dependence of the non-critical eigenvalues on the ratio E_1/E_2, where E_1 and E_2 are the Young's moduli for the two annular subregions. The values of the parameters are: $\mu = 500.0$, $\eta_1 = 0.3$, $\eta_2 = 0.6$, $\nu_1 = 0.1$, $\nu_2 = 0.3$ for both (a) and (b). The data shown here corresponds to $1 \ll n \ll \mathcal{O}(\mu^{1/2})$ $(n = 6, 10, 14)$ in (a), while for (b) $\mathcal{O}(\mu^{1/2}) \ll n \ll \mathcal{O}(\mu)$ $(n = 30, 40, 50)$.

Fig. 4-20 deals with the individual curves $\lambda = \lambda(\gamma)$ for a range of values of mode numbers that cover both the membrane- and plate-like regimes; here, $\mu = 500.0$ and all the other

parameters are fixed as indicated in the caption. In both cases the aforementioned dependence is monotonic decreasing. The difference between them consists in the fact that in the former case the curves do not intersect. The cross-over seen in the right window occurs around 1.6, and suggests that if $E_1/E_2 \gg 1.6$ (e.g., 8.0 or 10.0 in this problem) then high mode-number eigendeformations demand larger eigenvalues than their low mode-number counterparts. For $E_1/E_2 \ll R_E$ (e.g., 0.1 or 0.3) the situation is reversed. In light of this information it is not at all surprising that the $\mu^{1/2} \leq n \ll \mu$ response curves for $\gamma = 0.3$ and $\gamma = 10.0$ (shown in Fig. 4-7 and 4-9, for instance) are so radically different.
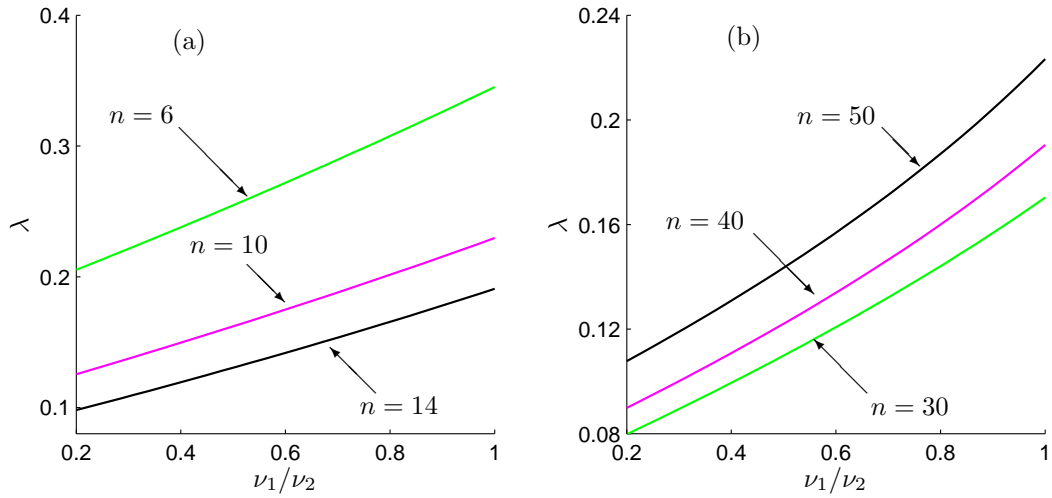
Figure 4-21: Dependence of the eigenvalues on the ratio ν_1/ν_2 of the Poisson's constants for the two annular subregions. Two cases are considered: in (a) $1 \ll n \ll \mathcal{O}(\mu^{1/2})$ ($n = 6, 10, 14$), while in (b) $\mathcal{O}(\mu^{1/2}) \ll n \ll \mathcal{O}(\mu)$ ($n = 30, 40, 50$). The values chosen for the other parameters are $\mu = 500.0$, $\eta_1 = 0.3$, $\eta_2 = 0.6$, $E_1/E_2 = 10$, $\nu_2 = 0.5$, with ν_1 ranging from 0.1 to 0.5.
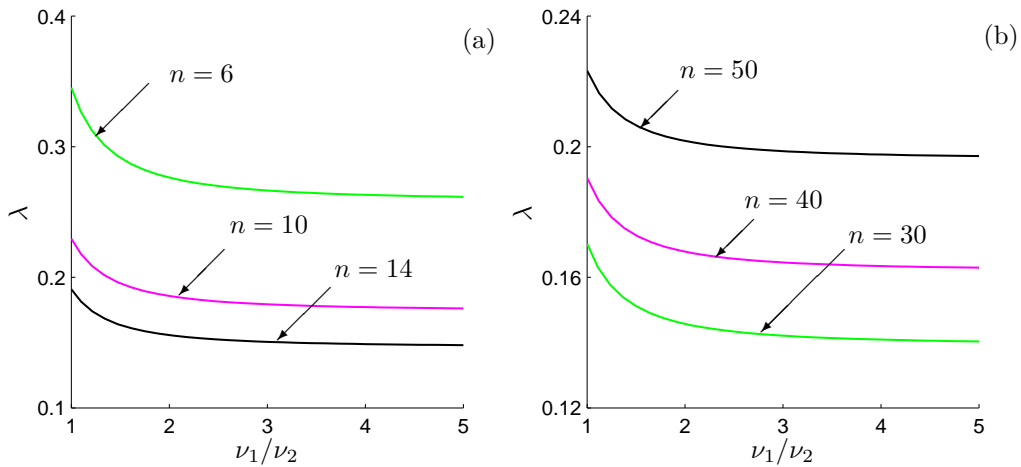
Figure 4-22: Similar to Fig. 4-21. Here, $\mu = 500.0$, $\eta_1 = 0.3$, $\eta_2 = 0.6$, $E_1/E_2 = 10$, $\nu_1 = 0.5$, and ν_2 ranges from 0.1 to 0.5.

In a similar fashion, the plots in Figs. 4-21 and 4-22 illustrate the dependence $\lambda = \lambda(\nu_1/\nu_2)$. For the sake of completeness we dealt with $\gamma > 1$ and $0 < \gamma < 1$ separately. Both sets of plots show that for each fixed mode number the corresponding eigenvalues increase monotonically with ν_1/ν_2. Note that in the left-hand windows n increases from top to bottom, while the plots on the right display opposite behaviour. Of course, the information gathered so far can be extrapolated to deduce the role of E_1/E_2 on λ_C (the critical value of the eigenvalue). This anticipation is indeed confirmed by the direct numerical simulations recorded in Fig. 4-23(a) for the dependence of the critical eigenvalue λ_C on the ratio of Young's Modulus $\gamma := E_1/E_2$ in two cases: one is when the inner rim $\eta_1 = 0.3$ is far away from the interface η_2; the other is when $\eta_1 = 0.45$ is near $\eta_2 = 0.5$. Here the results comprehensively verify the conclusions made from Fig. 4-10: when other parameters are fixed, λ_C decreases monotonically with γ. In Fig. 4-23(b) we also include the dependence of the mode number, n_C, on the quotient of the two Young's moduli. However, we notice n_C is not necessarily monotonically decreasing with γ, which also matches the findings from Fig. 4-10.
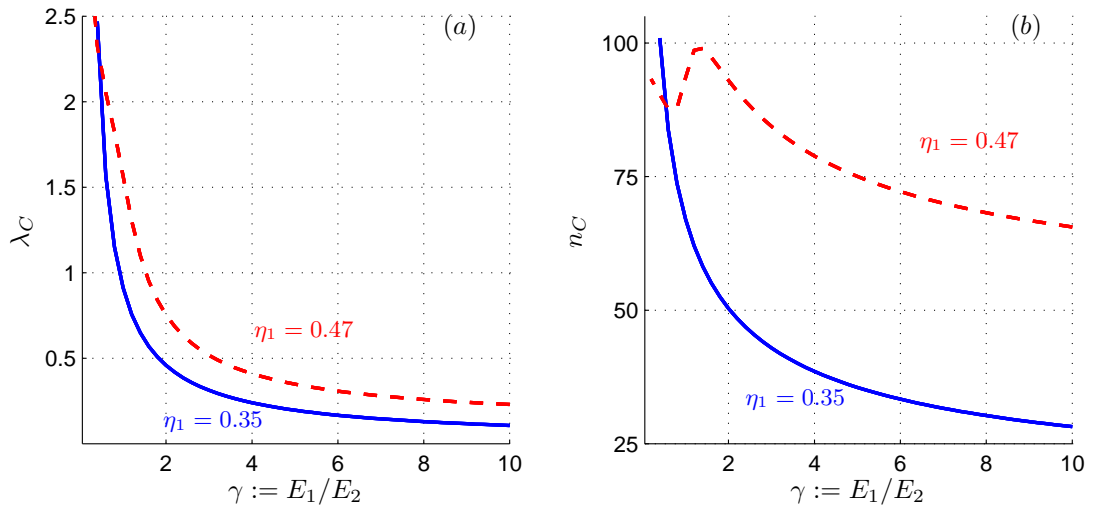
Figure 4-23: Dependence of the critical eigenvalue λ_C (shown in (a)) and the critical mode number n_C (shown in (b)) on $\gamma \equiv E_1/E_2$ for two cases: $\eta_1 = 0.35$ and $\eta_1 = 0.47$. In which, $\eta_1 = 0.35$ (*blue continuous lines*) corresponds to the case when η_1 is far away to $\eta_2 = 0.5$, while, the *red dashed lines* for $\eta_1 = 0.47$ represent the case when η_1 is close to $\eta_2 = 0.5$. The values adopted for other parameters are: $\mu = 400.0, \nu_1 = 0.3, \nu_2 = 0.1$ and $\eta_2 = 0.5$.

4.7 An alternative view of the response curves

A striking feature of the bi-annular plate is the rich behaviour displayed by the response curve $\lambda = \lambda(\eta_1; n)$ as η_1 is allowed to vary in $(0, \eta_2)$. In the previous section it has been seen that, despite this apparent complexity, one can still use the classification introduced by Coman and Haughton in [47], and which has been reviewed in detail in *Chapter 1*. It was pointed out at that point that the topology of the response curves is strongly influenced by the scalings adopted and that, in general, some choices are better than others. Since there is no method to

identify the best scaling *a priori*, the alternative is to examine at least two of them in order to ascertain how robust the global picture is. It turns out that for the bi-annular plate there is another natural rescaling of the problem, and we shall summarise some of its pros and cons in this section.

The starting point is the pre-buckling solution. Instead of using the original scalings, we notice that we can adopt

$$\eta_1 := \frac{R_1}{R_m} \qquad \text{and} \qquad \eta_2 := \frac{R_m}{R_2},\tag{4.58}$$

while keeping everything else the same as before. With this choice the rescaled annular sub-regions become

$$\Omega_I := \left\{ (\rho, \theta) \in \mathbb{R}^2 \mid \eta_1 \eta_2 \leq \rho \leq \eta_2, \quad 0 \leq \theta < 2\pi \right\},$$

$$\Omega_{II} := \left\{ (r, \theta) \in \mathbb{R}^2 \mid \eta_2 \leq \rho \leq 1, \quad 0 \leq \theta < 2\pi \right\},$$

so the inner rim is now given by $\rho = \eta_1 \eta_2$ and the interface by $\rho = \eta_2$. The eigenvalue problem can be rewritten using (4.58), which here is omitted in the interest of brevity, but the eigenvalue will remain the same $\lambda \equiv U_1/U_2$.
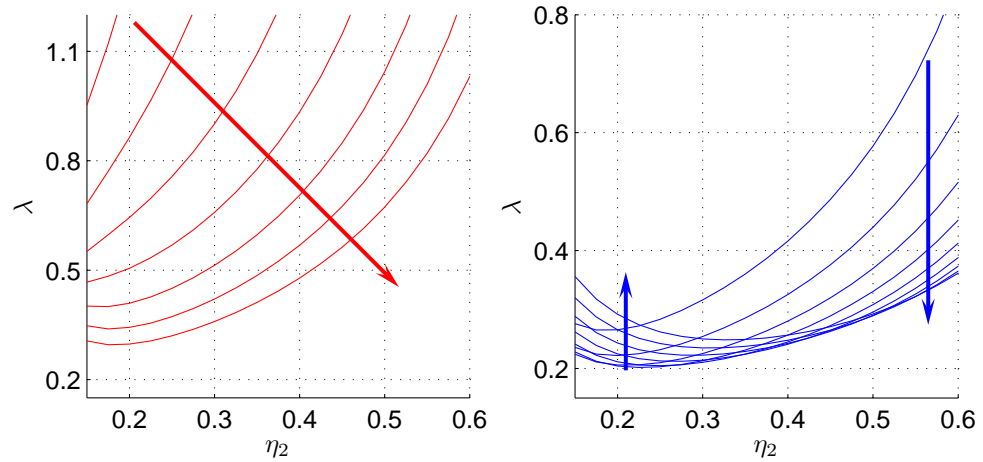
Figure 4-24: Dependence of the eigenvalues λ on the aspect ratio $\eta_2 = R_m/R_2$ for $\mu = 350.0$. Other parameters are given by $\gamma = 2.0$, $\nu_1 = 0.1$, $\nu_2 = 0.3$, $R_1/R_m \equiv 0.8$. The values of the mode number in the left-hand plots are $n = 4, 6, 8, 10, 12, 14, 16, 18$, while in the right plots, $n = 20, 25, 30, 35, 40, 45, 50, 55, 60$. The arrows indicate the direction in which n increases.

If we employ the same numerical and analytical analysis on *PBAS* as in §4.3 using this new scaling, we notice a notable feature in all of these plots: a smooth, monotonic boundary between the differently coloured regions identifying the distribution of *NHP*s according to the same classification as in Fig. 4.1. To a certain extent, this information seems to anticipate the more regular behaviour of the response curves $\lambda = \lambda(\eta_2; n)$, with η_1 fixed. For the sake of clarity, we only record here the response curves.
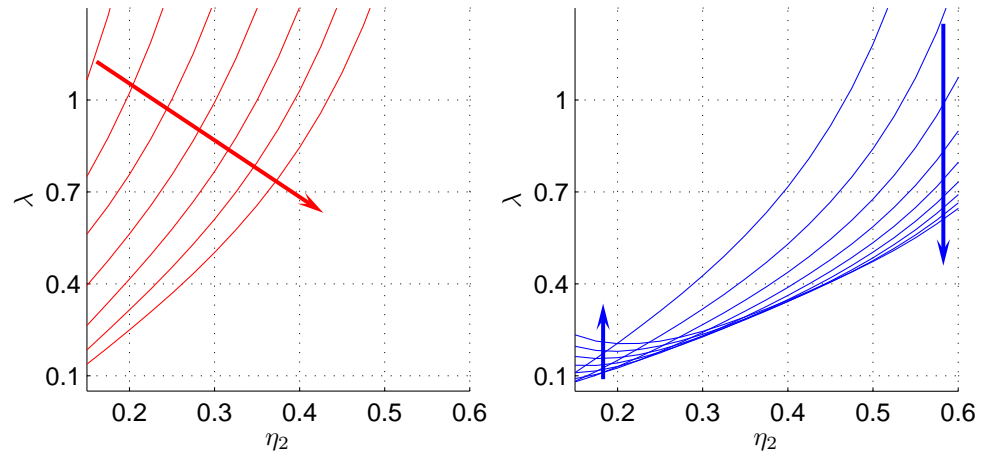
Figure 4-25:   Similar to Fig. 4-24, except for the following changes: $\gamma = 1.0$, $\nu_1 = 0.1$, $\nu_2 = 0.3$, $R_1/R_m \equiv 0.8$, and the values of the mode number in the left plots are $n = 4, 6, 8, 10, 12, 14, 16, 18, 20$, while in the right plots $n = 25, 30, 35, 40, 45, 50, 55, 60$.
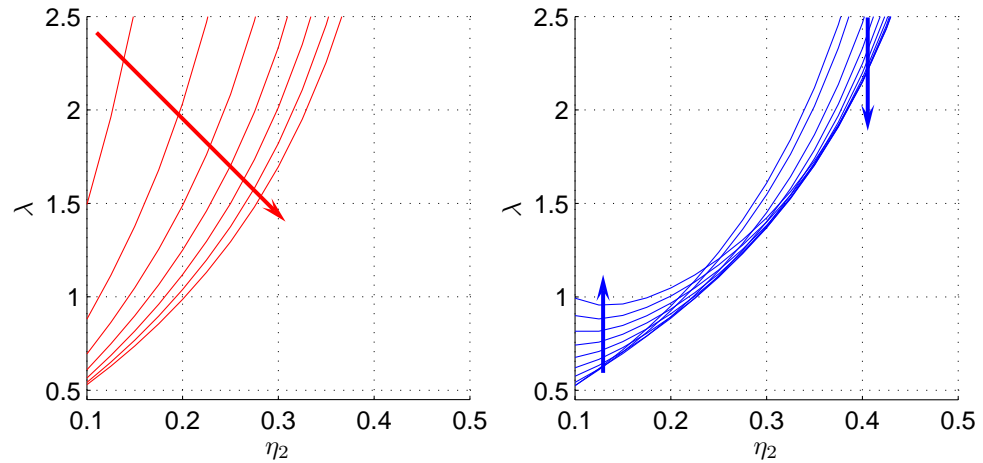
Figure 4-27:   Similar to Fig. 4-24, except for the following changes: $\gamma = 0.5$, $\nu_1 = \nu_2 = 0.3$, $R_1/R_m \equiv 0.8$, and the values of the mode number in the left plots are $n = 4, 6, 8, 10, 12, 14, 16$ while in the right plots, $n = 18, 20, 25, 30, 35, 40, 45, 50, 55, 60$.

Figs. 4-24 to 4-29 illustrate the new response curves and their behaviour for the two cases $1 \ll n \ll \mu^{1/2}$ and $\mu^{1/2} \leq n \ll \mu$ that were identified in [47] as the membrane- and plate-like regimes. It is very clear that the curves included in these plots are very similar to the ones shown in *Chapter 1*. We have not insisted on these scalings right from the outset because of the fact that the new response curves are somewhat misleading: when changing η_2 we are actually altering the inner rim as well. As a result the interesting features discovered in Figs. 4-6 to 4-7 for $\eta_1 \to \eta_2$ (e.g., the 'kink') are absent from this new scenario. Nevertheless, despite these shortcomings, this new scaling reconfirms the relevance of the WKB route taken in [47].
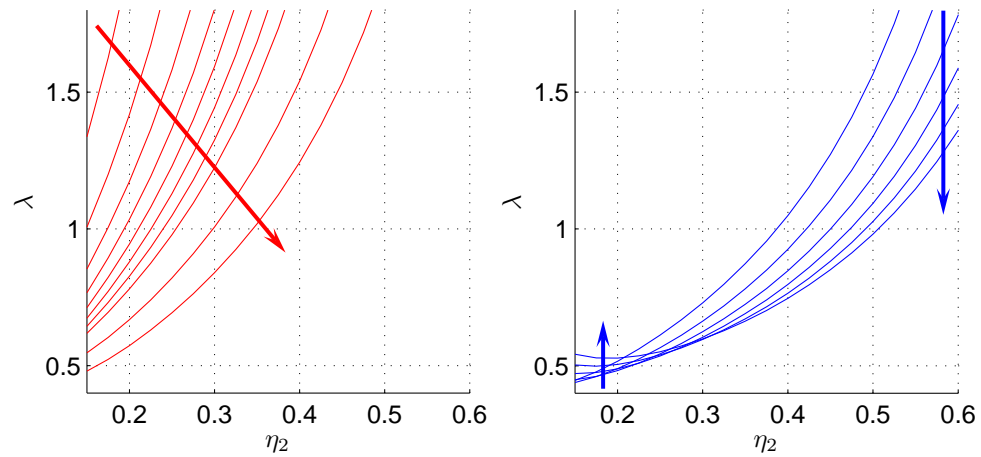
Figure 4-26: Similar to Fig. 4-24, except for the following changes: $\gamma = 0.5$, $\nu_1 = 0.1$, $\nu_2 = 0.3$, $R_1/R_m \equiv 0.8$, and the values of the mode number in the left plots are $n = 4, 6, 8, 10, 12, 14, 16, 18, 20, 25, 30, 35$, while in the right plots $n = 40, 45, 50, 55, 60$.
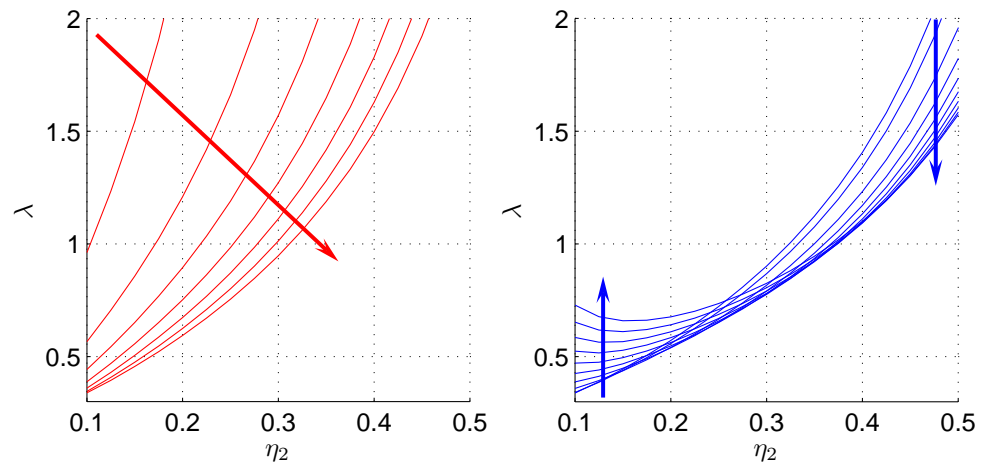
Figure 4-29: Similar to Fig. 4-24, except for the following changes: $\gamma = 0.5$, $\nu_1 = 0.3$, $\nu_2 = 0.1$, $R_1/R_m \equiv 0.8$, and the values of the mode number in the left plots are $n = 4, 6, 8, 10, 12, 14, 16$, while in the right plots $n = 18, 20, 25, 30, 35, 40, 45, 50, 55, 60$.

4.8 Asymptotic limits

As seen in the plots of the response curves discussed in §4.5.1, the situation encountered in the bi-annular plate problem shares several common features with the analogous situation of a simple annulus discussed in references [29, 47]. Here, we take advantage of this analogy and go one step further to derive a simplified three-point boundary-value problem that turns out to be capable of reproducing many of the qualitative behaviours of the original one. The next two sections represent a direct generalisation of the work in the references just mentioned but is much more involved.
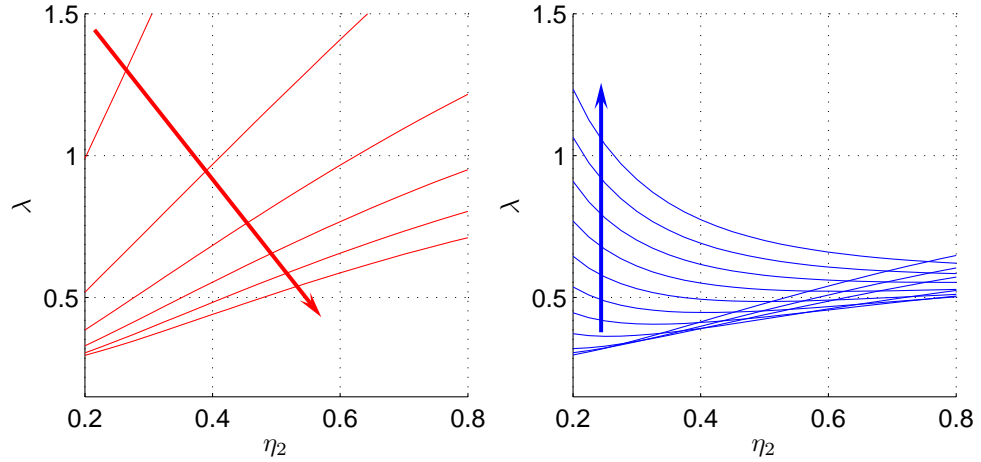
Figure 4-28: Similar to Fig. 4-24, except for the following changes: $\gamma = 0.5$, $\nu_1 = \nu_2 = 0.3$, $R_1/R_m \equiv 0.2$, and the values of the mode number in the left plots are $n = 4, 6, 8, 10, 12, 14$, while in the right plots $n = 16, 18, 20, 25, 30, 35, 40, 45, 50, 55, 60$.

4.8.1 The reduction of the bifurcation equations

When $1 \ll \mu$ and $1 \ll n$ (in this stage we left the question whether $n \ll \mu$ or $n \sim \mu$ to be open) the original equations (4.21) can be reduced to the compact form

$$\frac{d^2\overline{W}^{(j)}}{d\rho^2} + \frac{1}{\rho}\left[\frac{\mathring{\sigma}_{\theta\theta}^{(j)}(\rho)}{\mathring{\sigma}_{rr}^{(j)}(\rho)}\right]\frac{d\overline{W}^{(j)}}{d\rho} - \frac{n^2}{\rho^2}\left[\left(\frac{n}{\mu}\right)^2 \frac{1}{\rho^2\mathring{\sigma}_{rr}^{(j)}(\rho)} + \frac{\mathring{\sigma}_{\theta\theta}^{(j)}(\rho)}{\mathring{\sigma}_{rr}^{(j)}(\rho)}\right]\overline{W}^{(j)} = 0, \quad j \in \{I, II\}, \tag{4.59}$$

by using the arguments of reference [47], which will not be repeated here. The two equations in Ω_I or Ω_{II} are obtained by keeping either the label I or II, for all of the coefficients in (4.59). We shall also adopt an informal style of notation and do not insist on re-labelling W in these equation as was done in §1 in relation to (1.17).

Numerical evidence indicates that, augmented by appropriate boundary and interfacial conditions, these two equations can reproduce the plate-like behaviour of the stretched bi-annular plate. If $n \ll \mu^{1/2}$ then equation (4.59) reduces to

$$\frac{d^2\overline{W}}{d\rho^2} + \frac{1}{\rho}\left[\frac{\mathring{\sigma}_{\theta\theta}^{(j)}(\rho)}{\mathring{\sigma}_{rr}^{(j)}(\rho)}\right]\frac{d\overline{W}}{d\rho} - \left(\frac{n}{\rho}\right)^2 \frac{\mathring{\sigma}_{\theta\theta}^{(j)}(\rho)}{\mathring{\sigma}_{rr}^{(j)}(\rho)}\overline{W} = 0, \quad j \in \{I, II\}. \tag{4.60}$$

Again, when solved in conjunction with the boundary and interfacial conditions mentioned above, these two equations capture the membrane-like behaviour. Interestingly enough, we discovered that one can disregard (4.60) completely because equation (4.59) reproduces the membrane-like behaviour for $n \ll \mu^{1/2}$.

In obtaining (4.59) or (4.60) certain exponential solutions controlled by the size of the asymptotic parameter $\mu \gg 1$ were omitted. The reduction process is rather standard and is related to the (asymptotic) regular degeneracy of the original problem, a situation frequently

encountered in the hydrodynamic literature or in shell theory.

Since the order of our three-point boundary-value problem has decreased from 4 to 2, we are left with the task of identifying the reduced versions of the boundary constraints (4.22) and the interfacial conditions (4.27). Intuitively, it is the higher-order derivatives in both of them that will have to be ignored, and we notice that this will leave us with

$$W^I(\eta_1) = 0 \quad \text{and} \quad W^{II}(1) = 0 \,, \tag{4.61}$$

together with the continuity conditions,

$$W^I(\eta_2) = W^{II}(\eta_2) \quad \text{and} \quad \frac{dW^I}{d\rho}(\eta_2) = \frac{dW^{II}}{d\rho}(\eta_2) \,. \tag{4.62}$$

Incidentally, this is the right number of constraints required to solve either (4.59) or (4.60). However, this non-rigorous argument still needs to be placed on a firmer footing, and this is what we do next.

4.8.2 The reduction of the boundary and continuity conditions

Since the order of our three-point boundary-value problem has decreased from 4 to 2, we are left with the task of identifying the reductions of the boundary constraints (4.61) and the interfacial conditions (4.62). Because the differential equations in both Ω_I and Ω_{II} are of fourth-order, each can be represented as a linear combination of four linearly independent solutions, i.e.

$$W^{(j)}(\rho) = \sum_{i=1}^4 C_i^{(j)} W_i^{(j)}(\rho) \,, \quad j \in \{I, II\} \,, \tag{4.63}$$

where $C_i^{(j)} \in \mathbb{R}$ $(i = 1, ..., 4)$ are eight constants that are to be determined by the four boundary constraints (4.22) together with the the four continuity conditions (4.28). Following this strategy we end up with a homogeneous eighth-order linear algebraic system for $C_i^{(j)}$ whose non-trivial solvability requires that the determinant of the coefficient matrix, $\mathcal{D}(\lambda; \mu, \nu_1, \nu_2, \eta_1, \eta_2, n)$ (say), vanishes. More specifically,

$$\begin{vmatrix} W_1^I(\eta_1) & W_2^I(\eta_1) & \overline{W}_3^I(\eta_1) & \overline{W}_4^I(\eta_1) & 0 & 0 & 0 & 0 \\ W_1^{I'}(\eta_1) & W_2^{I'}(\eta_1) & \overline{W}_3^{I'}(\eta_1) & \overline{W}_4^{I'}(\eta_1) & 0 & 0 & 0 & 0 \\ \mathcal{D}_{31} & \mathcal{D}_{32} & \mathcal{D}_{33} & \mathcal{D}_{34} & \mathcal{D}_{35} & \mathcal{D}_{36} & \mathcal{D}_{37} & \mathcal{D}_{38} \\ \mathcal{D}_{41} & \mathcal{D}_{42} & \mathcal{D}_{43} & \mathcal{D}_{44} & \mathcal{D}_{45} & \mathcal{D}_{46} & \mathcal{D}_{47} & \mathcal{D}_{48} \\ \mathcal{D}_{51} & \mathcal{D}_{52} & \mathcal{D}_{53} & \mathcal{D}_{54} & \mathcal{D}_{55} & \mathcal{D}_{56} & \mathcal{D}_{57} & \mathcal{D}_{58} \\ \mathcal{D}_{61} & \mathcal{D}_{62} & \mathcal{D}_{63} & \mathcal{D}_{64} & \mathcal{D}_{65} & \mathcal{D}_{66} & \mathcal{D}_{67} & \mathcal{D}_{68} \\ 0 & 0 & 0 & 0 & W_1^{II}(1) & W_2^{II}(1) & \overline{W}_3^{II}(1) & \overline{W}_4^{II}(1) \\ 0 & 0 & 0 & 0 & W_1^{II'}(1) & W_2^{II'}(1) & \overline{W}_3^{II'}(1) & \overline{W}_4^{II'}(1) \end{vmatrix} = 0 \,, \tag{4.64}$$

where the following notation has been introduced,

$$\mathcal{D}_{3i} := W_i^I(\eta_2), i = 1, 2, 3, 4 \qquad \mathcal{D}_{3i} := -W_{i-4}^{II}(\eta_2), i = 5, 6, 7, 8.$$

$$\mathcal{D}_{4i} := W_i^{I'}(\eta_2), i = 1, 2, 3, 4 \qquad \mathcal{D}_{4i} := -W_{i-4}^{II}{}'(\eta_2), i = 5, 6, 7, 8,$$

$$\mathcal{D}_{5i} := \sum_{k=1}^{4} G_{3k} W_i^{I(k-1)}(\eta_2), i = 1, 2, 3, 4, \quad \mathcal{D}_{5i} := -\sum_{k=1}^{4} H_{3k} W_{i-4}^{II}{}^{(k-1)}(\eta_2), i = 5, 6, 7, 8,$$

$$\mathcal{D}_{6i} := \sum_{k=1}^{4} G_{4k} W_i^{I(k-1)}(\eta_2), i = 1, 2, 3, 4, \quad \mathcal{D}_{6i} := -\sum_{k=1}^{4} H_{4k} W_{i-4}^{II}{}^{(k-1)}(\eta_2), i = 5, 6, 7, 8,$$

where the notations $(\bullet)^{(k-1)}$ denotes the $(k-1)$th order derivative of $(\bullet)$ with respect to ρ.

The main idea is to take advantage of the presence of the large parameter $\mu \gg 1$ and simplify the above equation asymptotically. To this end, we need to use the WKB approximation in $\mu \gg 1$ and $n \gg 1$. In principle this is a routine task for small-dimensional problems, but it can become quite a tedious undertaking for the above 8×8 determinant. This will be accomplished by reviewing in some detail the WKB structure of the linearly independent solutions that feature in (4.63).

We start by making the observation that the differential equations in the annular subregions of Ω are the same except for the range of the independent variable and the coefficients $\mathring{\sigma}_{rr}^{(j)}, \mathring{\sigma}_{\theta\theta}^{(j)}$. In the interest of brevity, here we shall present the calculations for $W^I(\rho)$ only. The derivations for $W^{II}(\rho)$ are just a matter of changing the labels from I to II, and the corresponding range for the independent variable must be amended to $\eta_2 < \rho < 1$.

The differential equation (4.21) in $\Omega_{(j)} (j \in \{I, II\})$ are amenable to asymptotic integration by adopting the ansatz

$$W^{(j)}(\rho) := \left\{ a_0^{(j)}(\rho) + \frac{1}{\mu} a_1^{(j)}(\rho) + \dots \right\} \exp \left\{ \mu \int_{\bullet}^{\rho} H^{(j)}(\zeta) \, d\zeta \right\}, \qquad \rho \in \Lambda_{(j)}, \qquad (4.65)$$

where the intervals $\Lambda_{(j)}$ were defined in § 4.2 as $\Lambda_I := [\eta_1, \eta_2], \Lambda_{II} := [\eta_2, 1]$. If (4.65) is substituted into the bifurcation equation (4.16) applicable in $\Omega_{(j)}$, and like powers of μ are collected, at leading order we get the characteristic equation for $H^{(j)}$,

$$X^2 \left[X^2 - \mathring{\sigma}_{rr}^{(j)}(\rho) \right] = 0, \qquad \rho \in \Lambda_{(j)}. \qquad (4.66)$$

The coefficients $a_i^{(j)}(\rho)$ $(i = 1, 2, ...)$ are fixed by solving sequentially the so-called transport equations that result from setting to zero the coefficients of the other terms in the above expansion of (4.21). These will not be needed as all of our derivations rely only on leading-order approximations. Equation (4.66) has two distinct solutions corresponding to the linearly independent functions

$$W_i^{(j)}(\rho) \simeq P_i^{(j)}(\rho) E_i^{(j)}(\rho), \quad i \in \{1, 2\} \quad \text{(no sum over } i), \qquad (4.67)$$

in which

$$P_1^{(j)}(\rho) \equiv P_2^{(j)}(\rho) \equiv P^{(j)}(\rho) := \rho^{-1/2} \left[\mathring{\sigma}_{rr}^{(j)}(\rho) \right]^{-3/4},$$

$$E_{1,2}^{(j)}(\rho) := \exp \left\{ \pm\mu \int_{\eta_{(j)}}^{\rho} \sqrt{\mathring{\sigma}_{rr}^{(j)}(\zeta)} \, d\zeta \right\}, \quad \rho \in \Lambda_{(j)}.$$

If $\mu \gg 1$ then $W_1^I(\eta_2)$ and $W_1^{II}(1)$ are exponentially large, whereas $W_2^I(\eta_2)$ and $W_2^{II}(1)$ will be exponentially small (hence negligible). Next, we shall use the assumption $1 \ll n \ll \mu$ to identify the orders of $W_{1,2}^{(j)}$.

From equation (4.67) we deduce

$$W_{1,2}^I(\eta_1) \simeq P^I(\eta_1),$$

$$\frac{d^i W_{1,2}^I}{d\rho^i}(\eta_1) \simeq P^I(\eta_1) \left\{ \pm\mu \sqrt{\mathring{\sigma}_{rr}^I(\eta_1)} \right\}^i + \dots, \quad i = 1, 2, 3,$$

where the dots stand for lower-order contributions compared with the dominant terms. Similarly,

$$W_{1,2}^{II}(\eta_2) \simeq P^{II}(\eta_2), \quad \frac{d^i W_{1,2}^{II}}{d\rho^i}(\eta_2) \simeq P^{II}(\eta_2) \left\{ \mu \sqrt{\mathring{\sigma}_{rr}^{II}(\eta_2)} \right\}^i + \dots, \quad i = 1, 2, 3.$$

In conclusion,

$$W_{1,2}^I(\eta_1), \ W_{1,2}^{II}(\eta_2) \sim \mathcal{O}(1), \quad \frac{d^i W_{1,2}^I}{d\rho^i}(\eta_1), \ \frac{d^i W_{1,2}^{II}}{d\rho^i}(\eta_2) \sim \mathcal{O}(\mu^i), \quad i = 1, 2, 3. \tag{4.68}$$

We must also establish analogous order of magnitude estimates for the remaining values of $W_{1,2}^{I,II}$. To this end, let us introduce the auxiliary quantities

$$\mathcal{E}_\pm^I := \exp \left(\pm\mu \int_{\eta_1}^{\eta_2} \sqrt{\mathring{\sigma}_{rr}^I(\zeta)} \, d\zeta \right) \quad \text{and} \quad \mathcal{E}_\pm^{II} := \exp \left(\pm\mu \int_{\eta_2}^{1} \sqrt{\mathring{\sigma}_{rr}^{II}(\zeta)} \, d\zeta \right);$$

it should be clear that $\mathcal{E}_+^{I,II}$ are exponentially large, while $\mathcal{E}_-^{I,II}$ will be exponentially small. From (4.67) we then have

$$W_{1,2}^I(\eta_2) \simeq P^I(\eta_2) \mathcal{E}_\pm^I, \quad \frac{d^i W_{1,2}^I}{d\rho^i}(\eta_2) \simeq P^I(\eta_2) \left(\pm\mu \sqrt{\mathring{\sigma}_{rr}^I(\eta_2)} \right)^i \mathcal{E}_\pm^I + \dots, \quad i = 1, 2, 3,$$

and

$$W_{1,2}^{II}(1) \simeq P^{II}(1) \mathcal{E}_\pm^{II}, \quad \frac{d^i W_{1,2}^{II}}{d\rho^i}(1) \simeq P^{II}(1) \left(\pm\mu \sqrt{\mathring{\sigma}_{rr}^{II}(1)} \right)^i \mathcal{E}_\pm^{II} + \dots, \quad i = 1, 2, 3.$$

These results are summarised below for easy reference,

$$\frac{\mathrm{d}^i W_{1,2}^I}{\mathrm{d}\rho^i}(\eta_1) \sim \mathcal{O}(\mu^i)\,, \quad \frac{\mathrm{d}^i W_{1,2}^I}{\mathrm{d}\rho^i}(\eta_2) \sim \mathcal{O}(\mu^i \mathcal{E}_\pm^I)\,, \quad i = 0, 1, 2, 3\,, \tag{4.69a}$$

$$\frac{\mathrm{d}^i W_{1,2}^{II}}{\mathrm{d}\rho^i}(\eta_2) \sim \mathcal{O}(\mu^i)\,, \quad \frac{\mathrm{d}^i W_{1,2}^{II}}{\mathrm{d}\rho^i}(1) \sim \mathcal{O}(\mu^i \mathcal{E}_\pm^{II})\,, \quad i = 0, 1, 2, 3\,, \tag{4.69b}$$

where

$$\mathcal{E}_\pm^{(j)} := \exp\left\{ \pm\mu \int_{\Lambda_{(j)}} \sqrt{\mathring{\sigma}_{rr}^{(j)}(\zeta)}\mathrm{d}\zeta \right\}.$$

It remains to obtain information in a similar vein regarding $W_3^{(j)}$ and $W_4^{(j)}$. As in the related work [41], it turns out that the remaining functions $W_3^{(j)}$ and $W_4^{(j)}$ in (4.63) can be approximated by the solutions of the reduced equations (4.59); which can be indicated below, to distinguish between the two sets of functions we shall keep the same notations, but will use the 'overbar' for the approximations. Equation (4.59) can be recast in a more convenient form with the help of a standard Liouville–Green transformation

$$R^{(j)}(\rho) := \rho\,\mathring{\sigma}_{rr}^{(j)}(\rho)\,, \quad Y^{(j)}(\rho) := \sqrt{R^{(j)}(\rho)}\,\overline{W}^{(j)}(\rho)\,,$$

so that our original equation becomes

$$Y^{(j)''}(\rho) - n^2 Q^{(j)}(\rho)Y^{(j)}(\rho) = 0\,, \quad \rho \in \Lambda_{(j)}\,, \tag{4.70}$$

where the dash indicates differentiation with respect to ρ,

$$Q^{(j)}(\rho) := Q_1^{(j)}(\rho) + \frac{1}{n^2}Q_2^{(j)}(\rho)\,,$$

and

$$Q_1^{(j)} := \frac{1}{\rho R^{(j)}}\left(\frac{\delta^2}{\rho^2} + R^{(j)'}\right)\,, \quad Q_2^{(j)} := \frac{1}{4}\left\{ \left(\frac{R^{(j)'}}{R^{(j)}}\right)^2 + 2\frac{\mathrm{d}}{\mathrm{d}\rho}\left(\frac{R^{(j)'}}{R^{(j)}}\right) \right\}\,, \quad \delta := n/\mu \ll 1\,.$$

The general solution of (4.59) is a linear combination of $W_{3,4}^{(j)}$, which is generically written as

$$\overline{W}(\rho) = d_3 \overline{W}_3(\rho) + d_4 \overline{W}_4(\rho)\,, \qquad j \in \{I, II\}\,,$$

where d_3, $d_4 \in \mathbb{R}$ are arbitrary constants. At this stage, we aim to identify the leading-order behaviour of $\overline{W}_{3,4}$ as $\rho = \rho_B$, where ρ_B denotes one of the values in the set $\{\eta_1, \eta_2, 1\}$.

If $Q^{(j)}(\rho_B) < 0$ then

$$\overline{W}_3^{(j)}(\rho) \simeq \left[R^{(j)^2}(\rho)\,|Q^{(j)}(\rho)| \right]^{-1/4} \sin(n\chi^{(j)}(\rho))\,,$$

$$\overline{W}_4^{(j)}(\rho) \simeq \left[R^{(j)^2}(\rho) \, |Q^{(j)}(\rho)| \right]^{-1/4} \cos(n\chi^{(j)}(\rho)) \,,$$

which are both $\mathcal{O}(1)$ quantities (with respect to $n \gg 1$); here, $\chi(\rho) := \int_\bullet^\rho \sqrt{|Q(\zeta)|} \, \mathrm{d}\zeta$. By taking into consideration that the derivatives of $R(\rho)$ and $Q(\rho)$ are $\mathcal{O}(1)$, this WKB result (valid for $1 \ll n \ll \mu$) produces

$$\overline{W}_{3,4}^{(j)}(\rho_B) \sim \mathcal{O}(1) \quad \text{and} \quad \frac{\mathrm{d}^i \overline{W}_{3,4}^{(j)}}{\mathrm{d}\rho^i}(\rho_B) \sim \mathcal{O}(n^i) \,, \quad i = 1, 2, 3 \qquad (4.71)$$

On the other hand, if now $Q^{(j)}(\rho_B) > 0$ then

$$\overline{W}_3^{(j)}(\rho) \simeq \left[R^{(j)^2}(\rho) |Q^{(j)}(\rho)| \right]^{-1/4} \exp(n\chi^{(j)}(\rho)) \,, \qquad (4.72\text{a})$$

$$\overline{W}_4^{(j)}(\rho) \simeq \left[R^{(j)^2}(\rho) |Q^{(j)}(\rho)| \right]^{-1/4} \exp(-n\chi^{(j)}(\rho)) \,. \qquad (4.72\text{b})$$

Thus, we have the following simple estimates that follow directly from (4.71) and (4.72)

$$\frac{\mathrm{d}^i \overline{W}_3^{(j)}}{\mathrm{d}\rho^i}(\rho) \sim \mathcal{O}(n^i \mathcal{F}_+) \,, \quad \frac{\mathrm{d}^i \overline{W}_4^{(j)}}{\mathrm{d}\rho^i}(\rho) \sim \mathcal{O}(n^i \mathcal{F}_-) \,, \quad i = 0, 1, 2, 3 \,. \qquad (4.73)$$

In relation to this last approximation, let us introduce some further notation,

$$\mathcal{F}_\pm := \begin{cases} \mathcal{O}(1) \,, & \text{when} \quad Q(\rho_B) < 0 \,, \\[2mm] \exp(\pm n\chi(\rho_B)) & \text{when} \quad Q(\rho_B) > 0 \,. \end{cases}$$

It is clear, irrespective of whether $Q(\rho_B) < 0$ or $Q(\rho_B) > 0$, we get $\mathcal{E}_+^{(j)} \ll \mathcal{F}_+^{(j)}$ and $\mathcal{E}_-^{(j)} \gg \mathcal{F}_-^{(j)}$ once $1 \ll n \ll \mu$ is assumed to hold.

At last, we are in position to expand the 8×8 determinant in (4.64) by using the Laplace expansion theorem. This can be done in a number of different ways, but here we choose to carry out this procedure by using the first and the last two rows. Thus,

$$\mathcal{D}(\lambda; \mu, \nu_1, \nu_2, \eta_1, \eta_2, n)$$

$$= \sum_{\substack{1 \leq p_1 < p_2 < p_3 < p_4 \leq 8 \\ 1 \leq q_1 < q_2 < q_3 < q_4 \leq 8}} (-1)^{18 + p_1 + p_2 + p_3 + p_4} D(1, 2, 7, 8 | p_1, p_2, p_3, p_4) \, D(3, 4, 5, 6 | q_1, q_2, q_3, q_4) \,,$$

$$\qquad (4.74)$$

where $p_i \neq q_j$ for any $i, j \in \{1, 2, 3, 4\}$, and $D(i_1, i_2, i_3, i_4 \,|\, j_1, j_2, j_3, j_4)$ represents the minor formed with the elements situated at the intersections between the rows i_1, i_2, i_3, i_4 and the columns j_1, j_2, j_3, j_4. If we keep only the exponentially large terms in $\mathcal{E}_+^{(j)}$ and neglect all the terms containing $\mathcal{E}_-^{(j)}$, there should be one 5 and no 1, 2 among $p_1 \sim p_4$, and one 1 and no 2, 5 among $q_1 \sim q_4$. Eventually, only four leading terms are left, namely,

$$\mathcal{D}(\lambda; \mu, \nu_1, \nu_2, \eta_1, \eta_2, n) = -\phi_1 + \phi_2 + \phi_3 - \phi_4 + \cdots = 0 \,, \tag{4.75}$$

where

$$\phi_1 := D(1,2,7,8|2,3,5,7)\, D(2,3,4,5|1,4,6,8) \,, \quad \phi_2 := D(1,2,7,8|2,4,5,7)\, D(2,3,4,5|1,3,6,8) \,,$$

$$\phi_3 := D(1,2,7,8|2,3,5,8)\, D(2,3,4,5|1,4,6,7) \,, \quad \phi_4 := D(1,2,7,8|2,4,5,8)\, D(2,3,4,5|1,3,6,7) \,.$$

and the dots stand for lower-order terms that we suspect will play a secondary role.

The following results are immediately obvious and require no further justification,

$$\mathcal{D}_{3i} = W_i^I(\eta_2), \ \ i = 1,2,3,4 \,, \quad \mathcal{D}_{3i} = -W_{i-4}^{II}(\eta_2), \ \ i = 5,6,7,8 \,,$$

$$\mathcal{D}_{4i} = W_i^{I\,'}(\eta_2), \ \ i = 1,2,3,4 \,, \quad \mathcal{D}_{4i} = -W_{i-4}^{II\,'}(\eta_2), \ \ i = 5,6,7,8 \,.$$

However, the simplifications for $\mathcal{D}_{5i}, \mathcal{D}_{6i}$ $(i = 1,...,8)$ are more complex, and we will pay closer attention to them. According to the notation introduced immediately after (4.64),

$$\mathcal{D}_{51} = G_{31} W_1^I(\eta_2) + G_{32} W_1^{I\,'}(\eta_2) + G_{33} W_1^{I\,''}(\eta_2) \,, \tag{4.76}$$

and the definitions of the G_{kl} in (4.55) indicate that

$$G_{31} \sim \mathcal{O}(n^2) \quad \text{and} \quad G_{32}, G_{33} \sim \mathcal{O}(1) \,.$$

Taken together with (4.69), these results yield

$$G_{31} W_1^I(\eta_2) \sim \mathcal{O}(n^2 \mathcal{E}_+^I) \,,$$

$$G_{32} W_1^{I\,'}(\eta_2) \sim \mathcal{O}(\mu \mathcal{E}_+^I) \,,$$

$$G_{33} W_1^{I\,''}(\eta_2) \sim \mathcal{O}(\mu^2 \mathcal{E}_+^I) \,.$$

If we recall the initial assumption $1 \ll n \ll \mu$ then

$$\mathcal{D}_{51} \simeq \beta_1 W_1^{I\,''}(\eta_2) \sim \mathcal{O}(\mu^2 \mathcal{E}_+^I) \,,$$

being the leading-order term on the right-hand side of (4.76). The same procedure can be applied to $\mathcal{D}_{53} = G_{31} \overline{W}_3^I(\eta_2) + G_{32} \overline{W}_3^{I\,'}(\eta_2) + G_{33} \overline{W}_3^{I\,''}(\eta_2)$, taking account of (4.73), resulting in

$$G_{31} \overline{W}_3^I(\eta_2) \sim \mathcal{O}(n^2 \mathcal{F}_+^I) \,,$$

$$G_{32}\overline{W}_3^{I'}(\eta_2) \sim \mathcal{O}(n\mathcal{F}_+^I)\,,$$

$$G_{33}\overline{W}_3^{I''}(\eta_2) \sim \mathcal{O}(n^2\mathcal{F}_+^I)\,.$$

Hence the leading-order contribution coming from these three terms is the first and last one,

$$\mathcal{D}_{53} \simeq \beta_1\left[-\frac{n^2\nu_1}{\eta_2^2}\overline{W}_3^{I}(\eta_2) + \overline{W}_3^{I''}(\eta_2)\right] \sim \mathcal{O}(n^2\mathcal{F}_+^I)\,.$$

From (4.55) we have

$$G_{41},\, G_{42} \sim \mathcal{O}(n^2) \quad\text{and}\quad G_{43},\, G_{44} \sim \mathcal{O}(1)\,,$$

and the components of $\mathcal{D}_{61}$ are

$$G_{41}W_1^I(\eta_2) \sim \mathcal{O}(n^2\mathcal{E}_+)\,,$$

$$G_{42}W_1^{I'}(\eta_2) \sim \mathcal{O}(n^2\mu\mathcal{E}_+)\,,$$

$$G_{43}W_1^{I''}(\eta_2) \sim \mathcal{O}(\mu^2\mathcal{E}_+)\,,$$

$$G_{44}W_1^{I'''}(\eta_2) \sim \mathcal{O}(\mu^3\mathcal{E}_+)\,,$$

so that

$$\mathcal{D}_{61} \simeq \beta_1 W_1^{I'''}(\eta_2) \sim \mathcal{O}(\mu^3\mathcal{E}_+^I)$$

represents the leading-order term.

Similarly, a number of other estimates are derived below with the assumption $1 \ll n \ll \mu$, in preparation for the simplification of the ϕ_i $(i = 1, 2, 3, 4)$ in equation (4.75).

$$\mathcal{D}_{51} \simeq \beta_1 W_1^{I''}(\eta_2) \sim \mathcal{O}(\mu^2\mathcal{E}_+^I)\,, \quad \mathcal{D}_{52} \simeq \beta_1 W_2^{I''}(\eta_2) \sim \mathcal{O}(\mu^2\mathcal{E}_-^I)\,, \tag{4.77a}$$

$$\mathcal{D}_{53} \simeq \beta_1\left[-\frac{n^2\nu_1}{\eta_2^2}\overline{W}_3^{I}(\eta_2) + \overline{W}_3^{I''}(\eta_2)\right] \sim \mathcal{O}(n^2\mathcal{F}_+^I)\,, \tag{4.77b}$$

$$\mathcal{D}_{54} \simeq \beta_1\left[-\frac{n^2\nu_1}{\eta_2^2}\overline{W}_4^{I}(\eta_2) + \overline{W}_4^{I''}(\eta_2)\right] \sim \mathcal{O}(n^2\mathcal{F}_-^I)\,, \tag{4.77c}$$

$$\mathcal{D}_{55} \simeq -\beta_2 W_1^{II''}(\eta_2) \sim \mathcal{O}(\mu^2\mathcal{E}_+^{II})\,, \quad \mathcal{D}_{56} \simeq -\beta_2 W_2^{II''}(\eta_2) \sim \mathcal{O}(\mu^2\mathcal{E}_-^{II})\,, \tag{4.77d}$$

$$\mathcal{D}_{57} \simeq -\beta_2\left[-\frac{n^2\nu_2}{\eta_2^2}\overline{W}_3^{II}(\eta_2) + \overline{W}_3^{II''}(\eta_2)\right] \sim \mathcal{O}(n^2\mathcal{F}_+^{II})\,, \tag{4.77e}$$

$$\mathcal{D}_{58} \simeq -\beta_2\left[-\frac{n^2\nu_2}{\eta_2^2}\overline{W}_4^{II}(\eta_2) + \overline{W}_4^{II''}(\eta_2)\right] \sim \mathcal{O}(n^2\mathcal{F}_-^{II})\,, \tag{4.77f}$$

$$\mathcal{D}_{61} \simeq \beta_1 W_1^{I'''}(\eta_2) \sim \mathcal{O}(\mu^3\mathcal{E}_+^I)\,, \quad \mathcal{D}_{62} \simeq \beta_1 W_2^{I'''}(\eta_2) \sim \mathcal{O}(\mu^3\mathcal{E}_-^I)\,, \tag{4.77g}$$

$$\mathcal{D}_{63} \simeq \beta_1\left[-\frac{1 + n^2(2 - \nu_1)}{\eta_2^2}\overline{W}_3^{I'}(\eta_2) + \overline{W}_3^{I'''}(\eta_2)\right] \sim \mathcal{O}(n^3\mathcal{F}_+^I)\,, \tag{4.77h}$$

$$\mathcal{D}_{64} \simeq \beta_1\left[-\frac{1 + n^2(2 - \nu_1)}{\eta_2^2}\overline{W}_4^{I'}(\eta_2) + \overline{W}_4^{I'''}(\eta_2)\right] \sim \mathcal{O}(n^3\mathcal{F}_-^I)\,, \tag{4.77i}$$

$$\mathcal{D}_{65} \simeq -\beta_2 W_1^{II'''}(\eta_2) \sim \mathcal{O}(\mu^3\mathcal{E}_+^{II})\,, \quad \mathcal{D}_{66} \simeq -\beta_2 W_2^{II'''}(\eta_2) \sim \mathcal{O}(\mu^3\mathcal{E}_-^{II})\,, \tag{4.77j}$$

$$\mathcal{D}_{67} \simeq -\beta_2 \left[\frac{1 + n^2(2 - \nu_2)}{\eta_2^2} \overline{W}_3^{II'}(\eta_2) + \overline{W}_3^{II'''}(\eta_2) \right] \sim \mathcal{O}(n^3 \mathcal{F}_+^{II}), \tag{4.77k}$$

$$\mathcal{D}_{68} \simeq -\beta_2 \left[\frac{1 + n^2(2 - \nu_2)}{\eta_2^2} \overline{W}_4^{II'}(\eta_2) + \overline{W}_4^{II'''}(\eta_2) \right] \sim \mathcal{O}(n^3 \mathcal{F}_-^{II}), \tag{4.77l}$$

It now remains to use the information derived up to this point in order to evaluate $\phi_1 \sim \phi_4$; this will be done by another application of the Laplace expansion theorem for determinants. Taking ϕ_1 as an example,

$$\phi_1 = D(1,2,7,8|2,3,5,7) \cdot D(2,3,4,5|1,4,6,8)$$

$$= \begin{vmatrix} W_2^I(\eta_1) & \overline{W}_3^I(\eta_1) & 0 & 0 \\ W_2^{I'}(\eta_1) & \overline{W}_3^{I'}(\eta_1) & 0 & 0 \\ 0 & 0 & W_1^{II}(1) & \overline{W}_3^{II}(1) \\ 0 & 0 & W_1^{II'}(1) & \overline{W}_3^{II'}(1) \end{vmatrix} \cdot \begin{vmatrix} \mathcal{D}_{31} & \mathcal{D}_{34} & \mathcal{D}_{36} & \mathcal{D}_{38} \\ \mathcal{D}_{41} & \mathcal{D}_{44} & \mathcal{D}_{46} & \mathcal{D}_{48} \\ \mathcal{D}_{51} & \mathcal{D}_{54} & \mathcal{D}_{56} & \mathcal{D}_{58} \\ \mathcal{D}_{61} & \mathcal{D}_{64} & \mathcal{D}_{66} & \mathcal{D}_{68} \end{vmatrix} = \Gamma_{11} \cdot \Gamma_{12} \cdot \Gamma_{13}, \tag{4.78}$$

where,

$$\Gamma_{11} := \begin{vmatrix} W_2^I(\eta_1) & \overline{W}_3^I(\eta_1) \\ W_2^{I'}(\eta_1) & \overline{W}_3^{I'}(\eta_1) \end{vmatrix} = \begin{vmatrix} \mathcal{O}(1) & \mathcal{O}(\mathcal{F}_+^I) \\ \mathcal{O}(\mu) & \mathcal{O}(n\mathcal{F}_+^I) \end{vmatrix} \simeq -W_2^{I'}(\eta_1) \cdot \overline{W}_3^I(\eta_1) + \cdots,$$

$$\Gamma_{12} := \begin{vmatrix} W_1^{II}(1) & \overline{W}_3^{II}(1) \\ W_1^{II'}(1) & \overline{W}_3^{II'}(1) \end{vmatrix} = \begin{vmatrix} \mathcal{O}(\mathcal{E}_+^{II}) & \mathcal{O}(\mathcal{F}_+^I) \\ \mathcal{O}(\mu\mathcal{E}_+^{II}) & \mathcal{O}(n\mathcal{F}_+^I) \end{vmatrix} \simeq -W_1^{II'}(1) \cdot \overline{W}_3^{II}(1) + \cdots,$$

by using the order analysis in (4.69) and (4.73), where the dots represent the lower order terms, and Γ_{13} denotes the second determinant of ϕ_1 in (4.78) with the order analysis as

$$\Gamma_{13} := \begin{vmatrix} \mathcal{O}(\mathcal{E}_+^I) & \mathcal{O}(\mathcal{F}_-^I) & \mathcal{O}(\mathcal{E}_-^{II}) & \mathcal{O}(\mathcal{F}_-^{II}) \\ \mathcal{O}(\mu\mathcal{E}_+^I) & \mathcal{O}(n\mathcal{F}_-^I) & \mathcal{O}(\mu\mathcal{E}_-^{II}) & \mathcal{O}(n\mathcal{F}_-^{II}) \\ \mathcal{O}(\mu^2\mathcal{E}_+^I) & \mathcal{O}(n^2\mathcal{F}_-^I) & \mathcal{O}(\mu^2\mathcal{E}_-^{II}) & \mathcal{O}(n^2\mathcal{F}_-^{II}) \\ \mathcal{O}(\mu^3\mathcal{E}_+^I) & \mathcal{O}(n^3\mathcal{F}_-^I) & \mathcal{O}(\mu^3\mathcal{E}_-^{II}) & \mathcal{O}(n^3\mathcal{F}_-^{II}) \end{vmatrix} = \mu^6 \mathcal{E}_+^I \mathcal{F}_-^I \mathcal{E}_-^{II} \mathcal{F}_-^{II} \begin{vmatrix} \mathcal{O}(1) & \mathcal{O}(1) & \mathcal{O}(1) & \mathcal{O}(1) \\ \mathcal{O}(1) & \mathcal{O}(\delta) & \mathcal{O}(1) & \mathcal{O}(\delta) \\ \mathcal{O}(1) & \mathcal{O}(\delta^2) & \mathcal{O}(1) & \mathcal{O}(\delta^2) \\ \mathcal{O}(1) & \mathcal{O}(\delta^3) & \mathcal{O}(1) & \mathcal{O}(\delta^3) \end{vmatrix}.$$

where $\delta := n/\mu \ll 1$ as $1 \ll n \ll \mu$. If we apply the Laplacian expansion for the 4×4 determinant of Γ_{13}, we have

$$\Gamma_{13} = D(3,4|1,2) \cdot D(1,2|3,4) - D(3,4|1,3) \cdot D(1,2|2,4) + D(3,4|1,4) \cdot D(1,2|2,3)$$

$$+ D(3,4|2,3) \cdot D(1,2|1,4) - D(3,4|2,4) \cdot D(1,2|1,3) + D(3,4|3,4) \cdot D(1,2|1,2).$$

the leading order term should be $D(3,4|1,3) \cdot D(1,2|2,4)$, irrespective of whether $Q^{(j)}(\eta_2)$ is greater or smaller than zero. Hence

$$
\Gamma_{13} \simeq - \begin{vmatrix} \mathcal{D}_{51} & \mathcal{D}_{56} \\ \mathcal{D}_{51} & \mathcal{D}_{56} \end{vmatrix} \cdot \begin{vmatrix} \mathcal{D}_{34} & \mathcal{D}_{38} \\ \mathcal{D}_{44} & \mathcal{D}_{48} \end{vmatrix} = -\beta_1 \beta_2 \begin{vmatrix} W_1^{I''}(\eta_2) & W_2^{II''}(\eta_2) \\ W_1^{I'''}(\eta_2) & W_2^{II'''}(\eta_2) \end{vmatrix} \cdot \begin{vmatrix} \overline{W}_4^{I}(\eta_2) & -\overline{W}_4^{II}(\eta_2) \\ \overline{W}_4^{I'}(\eta_2) & -\overline{W}_4^{II'}(\eta_2) \end{vmatrix} .
$$

Therefore,

$$
\phi_1 \simeq -\beta_1 \beta_2 W_2^{I'}(\eta_1) \cdot W_1^{II'}(1) \cdot \begin{vmatrix} W_1^{I''}(\eta_2) & W_2^{II''}(\eta_2) \\ W_1^{I'''}(\eta_2) & W_2^{II'''}(\eta_2) \end{vmatrix} \cdot \begin{vmatrix} \overline{W}_3^{I}(\eta_1) & 0 \\ 0 & \overline{W}_3^{II}(1) \end{vmatrix} \cdot \begin{vmatrix} \overline{W}_4^{I}(\eta_2) & -\overline{W}_4^{II}(\eta_2) \\ \overline{W}_4^{I'}(\eta_2) & -\overline{W}_4^{II'}(\eta_2) \end{vmatrix} .
$$

Similarly, we can expand ϕ_2 as

$$
\phi_2 = D(1,2,7,8|2,4,5,7) \cdot D(2,3,4,5|1,3,6,8)
$$

$$
= \begin{vmatrix} W_2^{I}(\eta_1) & \overline{W}_4^{I}(\eta_1) & 0 & 0 \\ W_2^{I'}(\eta_1) & \overline{W}_4^{I'}(\eta_1) & 0 & 0 \\ 0 & 0 & W_1^{II}(1) & \overline{W}_3^{II}(1) \\ 0 & 0 & W_1^{II'}(1) & \overline{W}_3^{II'}(1) \end{vmatrix} \cdot \begin{vmatrix} \mathcal{D}_{31} & \mathcal{D}_{33} & \mathcal{D}_{36} & \mathcal{D}_{38} \\ \mathcal{D}_{41} & \mathcal{D}_{43} & \mathcal{D}_{46} & \mathcal{D}_{48} \\ \mathcal{D}_{51} & \mathcal{D}_{53} & \mathcal{D}_{56} & \mathcal{D}_{58} \\ \mathcal{D}_{61} & \mathcal{D}_{63} & \mathcal{D}_{66} & \mathcal{D}_{68} \end{vmatrix} = \Gamma_{21} \cdot \Gamma_{22} \cdot \Gamma_{23} ,
$$

$$\tag{4.79}$$

where

$$
\Gamma_{21} := \begin{vmatrix} W_2^{I}(\eta_1) & \overline{W}_4^{I}(\eta_1) \\ W_2^{I'}(\eta_1) & \overline{W}_4^{I'}(\eta_1) \end{vmatrix} = \begin{vmatrix} \mathcal{O}(1) & \mathcal{O}(\mathcal{F}_-^{I}) \\ \mathcal{O}(\mu) & \mathcal{O}(n\mathcal{F}_-^{I}) \end{vmatrix} \simeq -W_2^{I'}(\eta_1) \cdot \overline{W}_4^{I}(\eta_1) + \cdots ,
$$

$$
\Gamma_{22} := \begin{vmatrix} W_1^{II}(1) & \overline{W}_3^{II}(1) \\ W_1^{II'}(1) & \overline{W}_3^{II'}(1) \end{vmatrix} = \begin{vmatrix} \mathcal{O}(\mathcal{E}_+^{II}) & \mathcal{O}(\mathcal{F}_+^{I}) \\ \mathcal{O}(\mu\mathcal{E}_+^{II}) & \mathcal{O}(n\mathcal{F}_+^{I}) \end{vmatrix} \simeq -W_1^{II'}(1) \cdot \overline{W}_3^{II}(1) + \cdots .
$$

$$
\Gamma_{23} := \begin{vmatrix} \mathcal{D}_{31} & \mathcal{D}_{33} & \mathcal{D}_{36} & \mathcal{D}_{38} \\ \mathcal{D}_{41} & \mathcal{D}_{43} & \mathcal{D}_{46} & \mathcal{D}_{48} \\ \mathcal{D}_{51} & \mathcal{D}_{53} & \mathcal{D}_{56} & \mathcal{D}_{58} \\ \mathcal{D}_{61} & \mathcal{D}_{63} & \mathcal{D}_{66} & \mathcal{D}_{68} \end{vmatrix} = \begin{vmatrix} \mathcal{O}(\mathcal{E}_+^{I}) & \mathcal{O}(\mathcal{F}_+^{I}) & \mathcal{O}(\mathcal{E}_-^{II}) & \mathcal{O}(\mathcal{F}_-^{II}) \\ \mathcal{O}(\mu\mathcal{E}_+^{I}) & \mathcal{O}(n\mathcal{F}_+^{I}) & \mathcal{O}(\mu\mathcal{E}_-^{II}) & \mathcal{O}(n\mathcal{F}_-^{II}) \\ \mathcal{O}(\mu^2\mathcal{E}_+^{I}) & \mathcal{O}(n^2\mathcal{F}_+^{I}) & \mathcal{O}(\mu^2\mathcal{E}_-^{II}) & \mathcal{O}(n^2\mathcal{F}_-^{II}) \\ \mathcal{O}(\mu^3\mathcal{E}_+^{I}) & \mathcal{O}(n^3\mathcal{F}_+^{I}) & \mathcal{O}(\mu^3\mathcal{E}_-^{II}) & \mathcal{O}(n^3\mathcal{F}_-^{II}) \end{vmatrix} .
$$

The leading order of Γ_{23} reads

$$
\Gamma_{23} \simeq - \begin{vmatrix} \mathcal{D}_{51} & \mathcal{D}_{56} \\ \mathcal{D}_{61} & \mathcal{D}_{66} \end{vmatrix} \cdot \begin{vmatrix} \mathcal{D}_{33} & \mathcal{D}_{38} \\ \mathcal{D}_{43} & \mathcal{D}_{48} \end{vmatrix} = -\beta_1 \beta_2 \begin{vmatrix} W_1^{I''}(\eta_2) & W_2^{II''}(\eta_2) \\ W_1^{I'''}(\eta_2) & W_2^{II'''}(\eta_2) \end{vmatrix} \cdot \begin{vmatrix} \overline{W}_4^{I}(\eta_2) & -\overline{W}_3^{II}(\eta_2) \\ \overline{W}_4^{I'}(\eta_2) & -\overline{W}_3^{II'}(\eta_2) \end{vmatrix} .
$$

Therefore,

$$
\phi_2 \simeq -\beta_1\beta_2 W_2^{I'}(\eta_1) \cdot W_1^{II'}(1) \cdot
\begin{vmatrix} W_1^{I''}(\eta_2) & W_2^{II''}(\eta_2) \\ W_1^{I'''}(\eta_2) & W_2^{II'''}(\eta_2) \end{vmatrix}
\cdot
\begin{vmatrix} \overline{W}_4^{I}(\eta_1) & 0 \\ 0 & \overline{W}_3^{II}(1) \end{vmatrix}
\cdot
\begin{vmatrix} \overline{W}_3^{I}(\eta_2) & -\overline{W}_4^{II}(\eta_2) \\ \overline{W}_3^{I'}(\eta_2) & -\overline{W}_4^{II'}(\eta_2) \end{vmatrix} .
$$

Following similar procedure, ϕ_3 leads to

$$
\phi_3 = D(1,2,7,8|2,3,5,8) \cdot D(2,3,4,5|1,4,6,7) = \Gamma_{31} \cdot \Gamma_{32} \cdot \Gamma_{33} , \tag{4.80}
$$

where

$$
\Gamma_{31} := \begin{vmatrix} W_2^{I}(\eta_1) & \overline{W}_3^{I}(\eta_1) \\ W_2^{I'}(\eta_1) & \overline{W}_3^{I'}(\eta_1) \end{vmatrix}
= \begin{vmatrix} \mathcal{O}(1) & \mathcal{O}(\mathcal{F}_+^I) \\ \mathcal{O}(\mu) & \mathcal{O}(n\mathcal{F}_+^I) \end{vmatrix}
= -W_2^{I'}(\eta_1) \cdot \overline{W}_3^{I}(\eta_1) + \cdots ,
$$

$$
\Gamma_{32} := \begin{vmatrix} W_1^{II}(1) & \overline{W}_4^{II}(1) \\ W_1^{II'}(1) & \overline{W}_4^{II'}(1) \end{vmatrix}
= \begin{vmatrix} \mathcal{O}(\mathcal{E}_+^{II}) & \mathcal{O}(\mathcal{F}_-^I) \\ \mathcal{O}(\mu\mathcal{E}_+^{II}) & \mathcal{O}(n\mathcal{F}_-^I) \end{vmatrix}
= -W_1^{II'}(1) \cdot \overline{W}_4^{II}(1) + \cdots .
$$

$$
\Gamma_{33} \simeq -\begin{vmatrix} \mathcal{D}_{51} & \mathcal{D}_{56} \\ \mathcal{D}_{61} & \mathcal{D}_{66} \end{vmatrix} \cdot
\begin{vmatrix} \mathcal{D}_{34} & \mathcal{D}_{37} \\ \mathcal{D}_{44} & \mathcal{D}_{47} \end{vmatrix}
= -\beta_1\beta_2
\begin{vmatrix} W_1^{I''}(\eta_2) & W_2^{II''}(\eta_2) \\ W_1^{I'''}(\eta_2) & W_2^{II'''}(\eta_2) \end{vmatrix}
\cdot
\begin{vmatrix} \overline{W}_4^{I}(\eta_2) & -\overline{W}_3^{II}(\eta_2) \\ \overline{W}_4^{I'}(\eta_2) & -\overline{W}_3^{II'}(\eta_2) \end{vmatrix} .
$$

Hence,

$$
\phi_3 \simeq -\beta_1\beta_2 W_2^{I'}(\eta_1) \cdot W_1^{II'}(1) \cdot
\begin{vmatrix} W_1^{I''}(\eta_2) & W_2^{II''}(\eta_2) \\ W_1^{I'''}(\eta_2) & W_2^{II'''}(\eta_2) \end{vmatrix}
\cdot
\begin{vmatrix} \overline{W}_3^{I}(\eta_1) & 0 \\ 0 & \overline{W}_4^{II}(1) \end{vmatrix}
\cdot
\begin{vmatrix} \overline{W}_4^{I}(\eta_2) & -\overline{W}_3^{II}(\eta_2) \\ \overline{W}_4^{I'}(\eta_2) & -\overline{W}_3^{II'}(\eta_2) \end{vmatrix} .
$$

ϕ_4 is followed by similar simplifications as before

$$
\phi_4 = D(1,2,7,8|2,4,5,8) \cdot D(2,3,4,5|1,3,6,7) = \Gamma_{41} \cdot \Gamma_{42} \cdot \Gamma_{43} , \tag{4.81}
$$

where

$$
\Gamma_{41} := \begin{vmatrix} W_2^{I}(\eta_1) & \overline{W}_4^{I}(\eta_1) \\ W_2^{I'}(\eta_1) & \overline{W}_4^{I'}(\eta_1) \end{vmatrix}
= \begin{vmatrix} \mathcal{O}(1) & \mathcal{O}(\mathcal{F}_-^I) \\ \mathcal{O}(\mu) & \mathcal{O}(n\mathcal{F}_-^I) \end{vmatrix}
\simeq -W_2^{I'}(\eta_1) \cdot \overline{W}_4^{I}(\eta_1) + \cdots ,
$$

$$
\Gamma_{42} := \begin{vmatrix} W_1^{II}(1) & \overline{W}_4^{II}(1) \\ W_1^{II'}(1) & \overline{W}_4^{II'}(1) \end{vmatrix}
= \begin{vmatrix} \mathcal{O}(\mathcal{E}_+^{II}) & \mathcal{O}(\mathcal{F}_-^I) \\ \mathcal{O}(\mu\mathcal{E}_+^{II}) & \mathcal{O}(n\mathcal{F}_-^I) \end{vmatrix}
\simeq -W_1^{II'}(1) \cdot \overline{W}_4^{II}(1) + \cdots .
$$

$$
\Gamma_{43} \simeq -\begin{vmatrix} \mathcal{D}_{51} & \mathcal{D}_{56} \\ \mathcal{D}_{61} & \mathcal{D}_{66} \end{vmatrix} \cdot
\begin{vmatrix} \mathcal{D}_{33} & \mathcal{D}_{37} \\ \mathcal{D}_{43} & \mathcal{D}_{47} \end{vmatrix}
= -\beta_1\beta_2
\begin{vmatrix} W_1^{I''}(\eta_2) & W_2^{II''}(\eta_2) \\ W_1^{I'''}(\eta_2) & W_2^{II'''}(\eta_2) \end{vmatrix}
\cdot
\begin{vmatrix} \overline{W}_3^{I}(\eta_2) & -\overline{W}_3^{II}(\eta_2) \\ \overline{W}_3^{I'}(\eta_2) & -\overline{W}_3^{II'}(\eta_2) \end{vmatrix} ,
$$

leading to

$$\phi_4 \simeq -\beta_1\beta_2 W_2^{I'}(\eta_1) \cdot W_1^{II'}(1) \cdot \begin{vmatrix} W_1^{I''}(\eta_2) & W_2^{II''}(\eta_2) \\ W_1^{I'''}(\eta_2) & W_2^{II'''}(\eta_2) \end{vmatrix} \cdot \begin{vmatrix} \overline{W}_4^I(\eta_1) & 0 \\ 0 & \overline{W}_4^{II}(1) \end{vmatrix} \cdot \begin{vmatrix} \overline{W}_3^I(\eta_2) & -\overline{W}_3^{II}(\eta_2) \\ \overline{W}_3^{I'}(\eta_2) & -\overline{W}_3^{II'}(\eta_2) \end{vmatrix}.$$

Finally, putting all the leading orders in $\phi_1 \sim \phi_4$ together, excluding out the common coefficients, (4.75) becomes

$$-\begin{vmatrix} \overline{W}_3^I(\eta_1) & 0 \\ 0 & \overline{W}_3^{II}(1) \end{vmatrix} \cdot \begin{vmatrix} \overline{W}_4^I(\eta_2) & -\overline{W}_4^{II}(\eta_2) \\ \overline{W}_4^{I'}(\eta_2) & -\overline{W}_4^{II'}(\eta_2) \end{vmatrix} + \begin{vmatrix} \overline{W}_3^I(\eta_1) & 0 \\ 0 & \overline{W}_4^{II}(1) \end{vmatrix} \cdot \begin{vmatrix} \overline{W}_4^I(\eta_2) & -\overline{W}_3^{II}(\eta_2) \\ \overline{W}_4^{I'}(\eta_2) & -\overline{W}_3^{II'}(\eta_2) \end{vmatrix}$$

$$+\begin{vmatrix} \overline{W}_4^I(\eta_1) & 0 \\ 0 & \overline{W}_3^{II}(1) \end{vmatrix} \cdot \begin{vmatrix} \overline{W}_3^I(\eta_2) & -\overline{W}_4^{II}(\eta_2) \\ \overline{W}_3^{I'}(\eta_2) & -\overline{W}_4^{II'}(\eta_2) \end{vmatrix} + \begin{vmatrix} \overline{W}_4^I(\eta_1) & 0 \\ 0 & \overline{W}_4^{II}(1) \end{vmatrix} \cdot \begin{vmatrix} \overline{W}_3^I(\eta_2) & -\overline{W}_3^{II}(\eta_2) \\ \overline{W}_3^{I'}(\eta_2) & -\overline{W}_3^{II'}(\eta_2) \end{vmatrix}$$

$$+\cdots = 0,$$

where the dots stand for the lower order therefore were neglected. A close inspection of the above equation reveals that, to leading order, the original determinantal condition (4.64) is equivalent to

$$\begin{vmatrix} \overline{W}_3^I(\eta_1) & \overline{W}_4^I(\eta_1) & 0 & 0 \\ \overline{W}_3^I(\eta_2) & \overline{W}_4^I(\eta_2) & -\overline{W}_3^{II}(\eta_2) & -\overline{W}_4^{II}(\eta_2) \\ \overline{W}_3^{I'}(\eta_2) & \overline{W}_4^{I'}(\eta_2) & -\overline{W}_3^{II'}(\eta_2) & -\overline{W}_4^{II'}(\eta_2) \\ 0 & 0 & \overline{W}_3^{II}(1) & \overline{W}_4^{II}(1) \end{vmatrix} = 0,$$

which is the same with the determinantal equation for (4.59) corresponding to the boundary constrains (4.62) together with the continuity conditions (4.62).

This completes the proof of the assertion made at the end of §4.8.1.

4.8.3 The reduced equations: comparisons with full numerical simulations

In this section the reduced problems of (4.59) to (4.62) are compared with direct numerical simulations of the original boundary-value problem (4.21), (4.22) and (4.28). We concentrate on individual response curves with $\mu \gg 1$ and a range of mode numbers n. Both small and large values of this latter parameter are considered in order to understand the range of applicability of our work.

We solved the reduced equations (4.59) in Ω_I and Ω_{II}, subject to the simplified boundary constraints (4.61) and the interfacial matching conditions (4.62). The interface is situated at $\eta_2 = 0.5$ and the large parameter is taken to be $\mu = 400.0$ in all of our examples – from
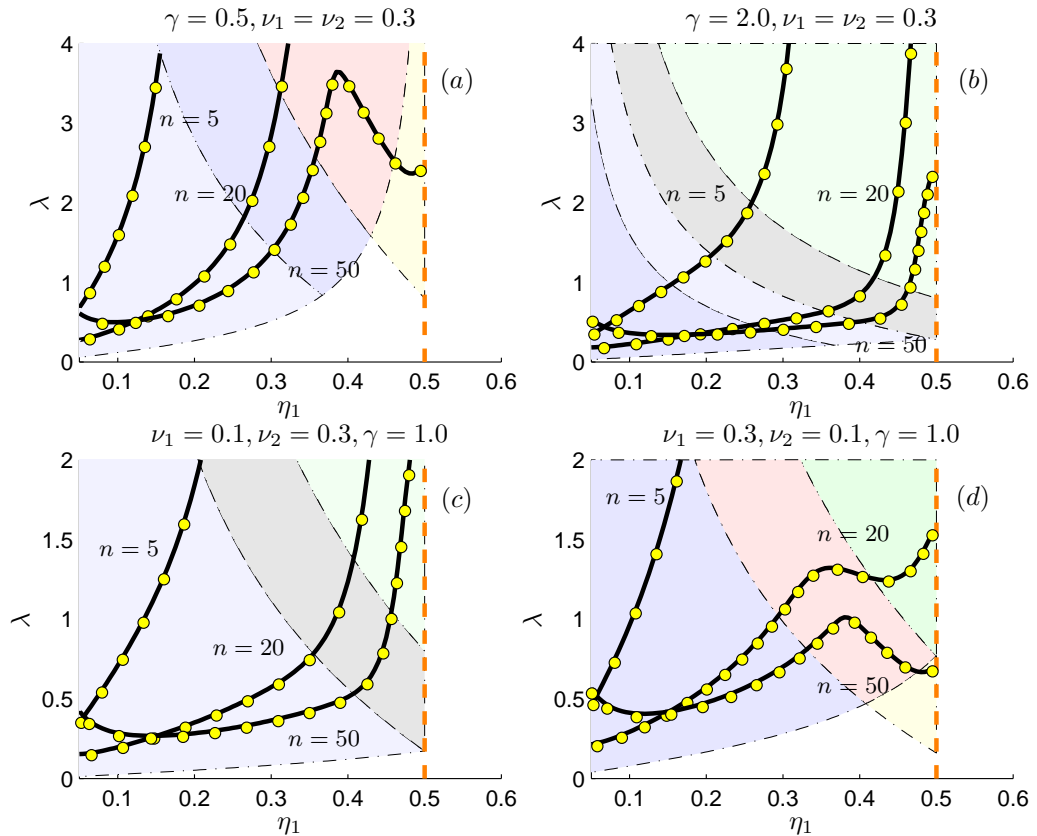
Figure 4-30: Comparison between the numerical solutions of the reduced problem (4.59) complemented by (4.62) (*yellow circles*), and the original problem (4.21) and (4.28) (*black continuous lines*). In these four windows: $\mu = 400.0$, $\eta_2 = 0.5$, three curves are for $n = 5, 20, 50$. More specifically, (a),(d) shows the 'kink' type solutions, while, (b),(c) illustrates the 'monotonic' solutions. The values of the parameters γ, ν_1, ν_2 are specified in the titles of the subplots. The colour background indicates the classification of the pre-bifurcation hoop stresses that was introduced in § 4.3.

an asymptotic point of view the latter value is only moderate. As our extensive numerical experiments (not included here for the sake of brevity) have indicated, larger μ's tend to lead to even more accurate results. The captions of the plots included above give full information about the values of the other parameters used in our comparisons.

In all four plots of Fig. 4-30, as η_1 increases from the initial value 0.1 towards the interface ($\eta_2 = 0.5$), all the four sets of curves are almost indistinguishable for all range of η_1 with different values of γ, ν_1, ν_2. More specifically, when $\mu = 400.0$, the WKB solution is in excellent agreement for both the "kink" and "monotonic" type response curves, and for any classifications of the pre-buckling hoop stress defined in Fig. 4.3. Noting that the continuity conditions Eq. (10) in [55] and Eq. (9) in [56] are problematic, these affect the final results slightly since the continuity conditions are not leading order conditions, and can be removed from the process of the order analysis in § 4.8. Here, we only included the comparison for $\eta_2 = 0.5$, but this approximation has proved to be very accurate for the individual response curves $\lambda = \lambda(\eta_1; n)$

for the whole range $0 < \eta_1 < \eta_2$, where $\eta_2 \in (0, 1)$. To summarise, the WKB approximation for moderately large μ and small n ($n = 5$) is of significance since it has been greatly reduced and much more easily being tackled but still provides accurate solutions.

4.9 Discussion and conclusions

The problem of tensile wrinkling for a radially stretched thin annular plate [47] has been extended to a system consisting of two (mechanically different) concentric annular plates perfectly bonded along a circular interface. The bi-layer structure can behave differently when considering the prebuckling stress distribution and the wrinkling compared with the case of homogeneous material.

The results obtained in this chapter are rather informative, here we try to conclude the findings from both engineering and mathematical aspects.

From the engineering point of view, this work is of guiding significance in designing with respect to buckling (wrinkling), as stated below. (Notice that the buckling resistance is discussed in terms of the stretching parameter $\lambda := U_1/U_2$.)

- We found that a bi-annular plate with stiffer inner annulus (larger $\gamma := E_1/E_2$) is prone to buckle under smaller stretching displacement on the inner rim, since a stiffer inner layer will intensify the stress concentration. On the other hand, a slender-inner-layer plate behaves in an opposite way, and can endure larger tensile displacement.

- The Poisson's ratio of either sub-annulus exerts a global effect on the buckling resisting capability of the bi-annular structure. Generally speaking, the smaller the Poisson's ratio, the lower the buckling resistance will be. Also, it is the Poisson's ratio of the wrinkled region that plays a dominant role on the critical stretching loading.

- The bifurcation mode exhibits a finer wrinkling structure (larger number of wrinkles) when the wrinkles are localised near the interface. This phenomenon is somewhat similar to the edge-buckling.

- When the inner rim is far from the interface (inner annulus is not very narrow), the wrinkles tend to locate within the inner annulus next to the inner rim; the wrinkling mode which is mainly localised in the outer annulus occurs when the inner annulus is very narrow. The wrinkles might also be localised in both annuli around the interface, or localised at the interface; however, the last two modes are rarely seen.

The above engineering conclusions were obtained from mathematical analysis on the corresponding eigenvalue problem, which itself is of great interest to us and could be summarised below.

- The wrinkling analysis was started by thorough investigations of the stress distributions in the basic state for a limit case $\mu \to \infty$, which suggests two types of lower bounds (λ^{low}) for such a limit case: the cusp type and the rectangular-hyperbola type. Some detailed numerical and analytical analysis reveals the succinct relations: the former type corresponds to the cases when $\gamma := E_1/E_2 < \nu_1/\nu_2$; while the latter type occurs when $\gamma > \nu_1/\nu_2$.

- Extensive numerical simulations have been carried out by using numerical strategies of an adapted version of compound matrix method, in conjunction with a collocation solver `sbvp`. The response curves and neutral stability curves are obtained with respect to different combinations of the mechanical parameters of the two annuli. The neutral stability envelopes (NSE) can be classified into two different types, the so called kink-type and monotonic-type, which asymptotically correspond to the two situations for the basic state, namely, the cusp type and the rectangular-hyperbola type prebuckling azimuthal stress distributions. More specifically, a bi-annular plate with a more flexible inner part $E_1/E_2 < \nu_1/\nu_2$ is typically seen as a kink-type NSE, and of higher resistance against wrinkling under stretching (defined by $\lambda = U_1/U_2$), while such a plate with a stiffer inner annulus tends to appear as a monotonic-type NSE with lower critical external stretching.

- By further investigation in the morphological changes of critical eigenmodes when we vary the location of the inner rim, we have gained a deeper understanding on the effects of the discontinuities of the interface on either the critical external stretching and the wrinkling mode. For example, the transition of the critical wrinkling modes is clearly related to the critical mode number, as the localised wrinkling shifts from a stiffer region to a more flexible region, the mode number n_C increases steeply to a local maximum then decreases.

The singular-perturbation nature of this problem enables conducting further asymptotic analysis. We have extended the earlier analysis of Coman *et al.* [47] into the bi-layer structure, which is also applicable for general multilayer regime. The asymptotic approximations are quite robust and accurate when the large parameter is moderately large (e.g., $\mu = 400.0$).

The above WKB reduction paves the way for the generalisation of the so-called double-WKB analysis put forth by Coman and Bassom in [41]. In such a double-WKB analysis, both asymptotic parameters μ and n are taken advantage of, and the reduced second-order eigenvalue problem obtained in this work can be further reduced and finally arrives at a transcendental equation. Then the value of $\lambda = \lambda(n)$ is obtained from this transcendental equation, without solving eigenvalue problems. This was done by Coman in [38] and is not included here.

Chapter 5

Tensile instability of a thick-walled tube based on Lamé solutions

5.1 Introduction

Elastic instabilities of bulky solids and thick-walled structural elements, such as plates and shells, have received considerable attention for the past several decades, starting with the works of Biot on incremental elasticity in the 1930's, which were later collected in [15]. A more modern treatment, together with many interesting examples, can be found in the classic text by Ogden [95] .

While for most part there is a close parallel between the bifurcations experienced by thin-walled bodies modelled with the help of classical plate and shell theories, on the one hand, and those of three-dimensional elastic bodies, on the other, a number of complementary issues arise in the latter situation. Largely speaking, these are related to the possible loss of ellipticity in the incremental bifurcation equations and the existence of surface instabilities [14, 67]; this last phenomenon is typical of compressed half-planes or half-spaces and has no counterpart in the classical theories of buckling. It is precisely these two aspects, and related phenomena, that we wish to revisit here within the scope of an approximate set of incremental bifurcation equations described by Novozhilov in his book [94]; this model can be traced back to some early incremental equations proposed by Biezeno and Hencky [13] as well as Biot ([15], pages 490-491). For convenience we shall refer to this model as the *simplified incremental deformation theory* (*SIDT* for short). To a certain extent, these incremental models are superior to the buckling equations used in structural mechanics, since in recent years they have been the object of several quantitative studies (e.g., [51, 72, 74, 96]). The mathematical structure of these equations in

the case of non-homogeneous stress fields appears to be little explored and, as seen in what follows, deserves much more consideration.

In some recent work Coman and Destrade [46] have investigated the asymptotic structure of the instability experienced by an incompressible neo-Hookean rubber block subjected to pure flexure (see [60] for some experimental considerations on the same problem). Based on the exact nonlinear pre-bifurcation solution obtained by Rivlin in [105] it was found that if the ratio of thickness to length was κ then for $0 < \kappa < \infty$ the bent block displayed an Euler-type instability with a well defined number of ripples on the compressed side, but in the limit $\kappa \to \infty$ this degenerated into a kinematic surface instability. In a later study [31] it was shown that the turning points found in the differential equation associated with the pure bending problem played only a passive role, in contrast to a deceivingly similar situation that crops up in relation to the wrinkling of stretched thin films [40, 41] – where turning points did play a crucial role.

The above instability scenario was associated with one of the traction-free circular surfaces of the bent block (the one that was in compression); the eversion of a cylindrical thick-walled tube represents an akin situation amenable to the same type of asymptotic treatment. A question that still remains is whether the asymptotic strategy developed in these studies can find any applicability to the case when the bifurcation is associated with a stressed rather than a free surface.

The problem we have in mind is that of a long hollow cylindrical body subjected to radial tensions on both boundaries. Invoking the standard plane-strain simplifications we can confine our attention to cross-sections situated sufficiently far away from the two ends of the cylinder. Thus, we are essentially dealing with a two-dimensional problem and a number of further simplifications can be called upon. For instance, if we assume that the pre-bifurcation state is sufficiently weak, so that linear elasticity is applicable, then the expressions of the stress and displacement fields are given by the Lamé solution for a radially loaded annulus (e.g., see [24]). It is a well-known fact that for tensile loads this solution predicts a typical stress concentration around the perimeter of the inner hole, so we expect the possible bifurcations to have a local character. However, it is not at all obvious *a priori* whether the inner rim will prefer a long-wave deformation mode, as seen in the left sketch in Figure 5-1, or whether it will have the tendency to accumulate many ripples (right sketch, same figure). Of course, a third possibility is material failure as heralded by loss of ellipticity prior to any changes in the radially symmetric pre-bifurcation state. All these questions will be addressed in the subsequent parts of this chapter.

As already hinted above, the *SIDT* has attracted interest in recent time, particularly in relation to buckling of thick circular cylindrical shells under hydrostatic pressure. Kardomateas and his associates have explored such aspects extensively (e.g., [72, 74] and the references therein). While not entirely as accurate as the incremental equations found in [15] or [95], they represent a versatile alternative whose status is perhaps somewhere between classical plate/shell

models and those found in the last two references just cited.
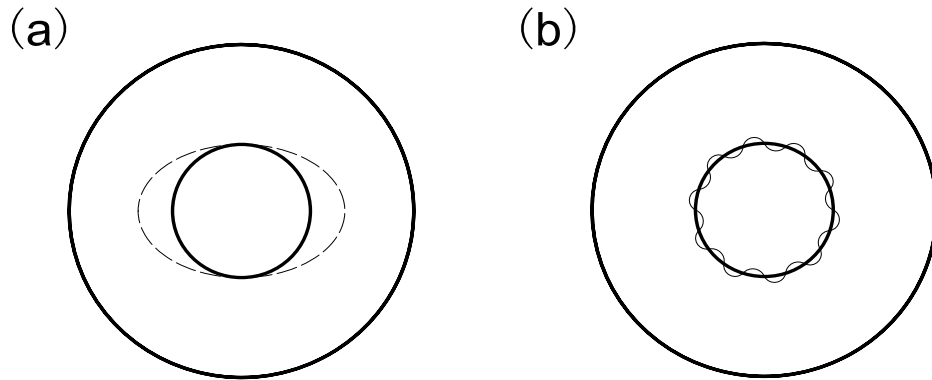
Figure 5-1: Long- and short-wavelength local deformations of the annulus

This chapter is laid out as follows. In §5.2 we review the *SIDT* by presenting an intrinsic-form derivation of the relevant equations; a brief glancing at the equivalent traditional-notation calculations ("á la Timoshenko") that appear in [72] indicates clearly the advantages of the route pursued here. By using the normal-mode approach, the bifurcation equations are reduced to an eigenvalue problem for two coupled second-order ordinary differential equations with variable coefficients. Direct numerical simulations are then employed in §5.3 to investigate the character of the possible linear bifurcations. This aspect turns out to be sensitive to the type of traction boundary conditions imposed on the curved boundaries of the annulus. Two complementary cases are discussed: (i) *dead loads* (i.e., the outward unit normal to the boundary remains unchanged in passing from the stressed configuration to the neutrally stable one), and (ii) *follower loads* (assumed to follow the direction of the normal to the boundary). As it happens, the outcome in both cases turns out to be somewhat similar, in the sense that the predominant instability mode is the short-wavelength deformation pattern seen on the right-hand side in Figure 5-1. Strictly speaking, the number of ripples along the inner rim is infinite and the 'bifurcation' is linked with the failure of the *Shapiro–Lopatinskij Condition* (*SLC*) in the corresponding incremental traction boundary-value problem – e.g., see [54] (pp. 106-108). The recent paper [93] contains a number of interesting discussions in the context of nonlinear elasticity problems and abstract bifurcation theory, as well as an extensive list of references. Motivated by our numerical findings, in §5.4 we indicate how some of the quantitative aspects of this material instability can be understood by a simple boundary-layer argument involving the mode number as the main asymptotic parameter.

5.2   Bifurcation equations

We consider a very long cylindrical body as seen on the righthand side in Fig. 5-2. By invoking the plane-strain approximation we shall confine our attention to a generic annular cross-section

of inner radius R_1 and outer radius R_2, situated far away from the ends of the cylinder. Our main interest in what follows is with the possible in-plane bifurcations experienced by such a cross-section when the two curved boundaries are subjected to purely radial tensile loads.
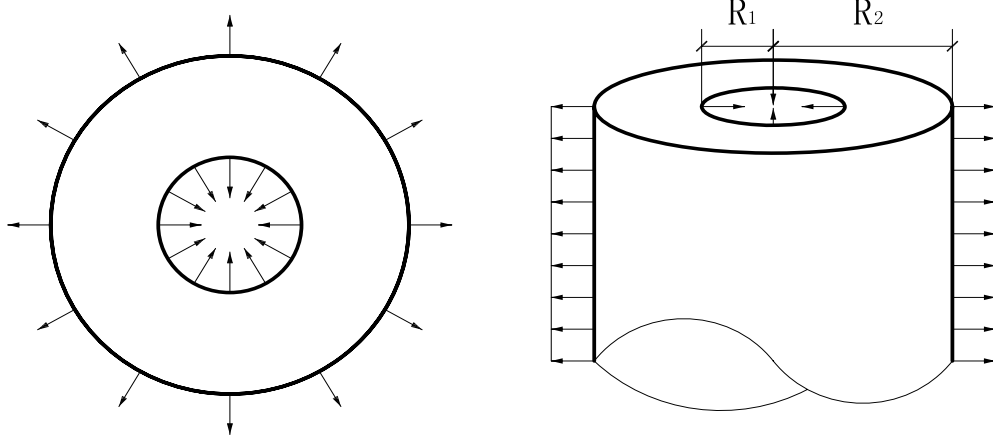
Figure 5-2: A thick cylindrical body under radial tensile loads

In this section, we will employ the Method of Adjacent Equilibrium (MAE) mentioned in §1.2 to derive the bifurcation equations, which amounts to writing the equilibrium equations on two neighbouring stressed configurations and taking their difference, followed by a geometrical linearisation of the kinematics.

Without losing generality, we assume a deformable continuous body $\mathcal{B}$ occupying a reference configuration $\mathcal{B}_r$ in three-dimensional Euclidean point space, in which an arbitrary particle is denoted by position vector $\boldsymbol{X}$. All pre-bifurcation fields will be indicated by using "$\circ$" and the relevant bifurcation equations are derived from the Method of Adjacent Equilibrium (MAE). For example, we denote the displacement field in the basic state as $\mathring{\boldsymbol{u}}$. To determine the bifurcation-point load of a structure $\mathcal{B}$, adjacent-equilibrium criterion can be applied. We give a small incremental displacement $\varepsilon \boldsymbol{u}_1$ (ε is a arbitrary small parameter) to the displacement vector $\mathring{\boldsymbol{u}}$ and examine the two adjacent configurations before and after increment. The perturbed position is denoted by

$$\boldsymbol{u} = \mathring{\boldsymbol{u}} + \varepsilon \boldsymbol{u}_1 \,, \tag{5.1}$$

Then the incremental fields between these two configurations caused by $\varepsilon \boldsymbol{u}_1$ will be labelled as " $(\bullet)_1$ ", by taking the difference between these two configurations and keeping the linear terms of ε.

Then, we take deformed configuration of the body as $\mathcal{B}_t$, $\boldsymbol{x}$ representing the position vector of the same particle in the deformed configuration. If we agree to use "$\boldsymbol{\nabla}$" to represent the gradient operator in the reference configuration, then the deformation gradient tensor $\boldsymbol{F}$ of the motion is defined by

$$\boldsymbol{F} = \boldsymbol{\nabla} \otimes \boldsymbol{x} = \boldsymbol{I} + \boldsymbol{H} = \boldsymbol{I} + \boldsymbol{u} \otimes \boldsymbol{\nabla}, \qquad (\forall)\boldsymbol{X} \in \mathcal{B}_r \,, \tag{5.2}$$

where $\boldsymbol{u}$ is the displacement vector and $\boldsymbol{I}$ is the identity tensor, $\boldsymbol{H}$ is the displacement gradient in referential configuration: $\boldsymbol{H} = \boldsymbol{u} \otimes \boldsymbol{\nabla}$. From mathematical point of view, $\boldsymbol{H}$ is a second-order tensor, and can be written as the sum of a symmetric and a skew-symmetric tensor, $\boldsymbol{H} = \boldsymbol{e} + \boldsymbol{\omega}$, with the first symmetric tensor describing changes in lengths (or linear strain tensor), while the second characterises the skew-symmetric tensor describing the rotation of material line elements (or linear rotation tensor). So, we have

$$\mathring{\boldsymbol{H}} = \mathring{\boldsymbol{u}} \otimes \boldsymbol{\nabla} = \mathring{\boldsymbol{e}} + \mathring{\boldsymbol{\omega}} \,, \tag{5.3a}$$

$$\boldsymbol{H}_1 = \boldsymbol{u}_1 \otimes \boldsymbol{\nabla} = \boldsymbol{e}_1 + \boldsymbol{\omega}_1 \,, \tag{5.3b}$$

which are applicable for pre-buckling state and neutral stability state respectively, and where

$$\mathring{\boldsymbol{e}} = \frac{1}{2} \left(\mathring{\boldsymbol{u}} \otimes \boldsymbol{\nabla} + \boldsymbol{\nabla} \otimes \mathring{\boldsymbol{u}} \right) \quad \text{and} \quad \mathring{\boldsymbol{\omega}} = \frac{1}{2} \left(\mathring{\boldsymbol{u}} \otimes \boldsymbol{\nabla} - \boldsymbol{\nabla} \otimes \mathring{\boldsymbol{u}} \right) \,, \tag{5.4a}$$

$$\boldsymbol{e}_1 = \frac{1}{2} \left(\boldsymbol{u}_1 \otimes \boldsymbol{\nabla} + \boldsymbol{\nabla} \otimes \boldsymbol{u}_1 \right) \quad \text{and} \quad \boldsymbol{\omega}_1 = \frac{1}{2} \left(\boldsymbol{u}_1 \otimes \boldsymbol{\nabla} - \boldsymbol{\nabla} \otimes \boldsymbol{u}_1 \right) \,. \tag{5.4b}$$

Substituting (5.1) into (5.2) yields

$$\mathring{\boldsymbol{F}} = \boldsymbol{I} + \mathring{\boldsymbol{H}} \,, \tag{5.5a}$$

$$\boldsymbol{F}_1 = \boldsymbol{H}_1 \,. \tag{5.5b}$$

Furthermore, the Green-Lagrange strain tensor is defined by

$$\boldsymbol{E} = \frac{1}{2} \left(\mathbf{C} - \boldsymbol{I} \right) = \frac{1}{2} \left(\boldsymbol{F}^T \cdot \boldsymbol{F} - \boldsymbol{I} \right) \,, \tag{5.6}$$

where $\mathbf{C}$ is the right Cauchy-Green tensor, $\mathbf{C} = \boldsymbol{F}^T \boldsymbol{F}$. If we assume small deformation such that $|\mathring{\boldsymbol{u}}| \ll 1$ and $|\boldsymbol{u}_1| \ll 1$. Then substituting (5.5) into (5.6), we have

$$\mathring{\boldsymbol{E}} = \frac{1}{2} \left(\mathring{\boldsymbol{F}}^T \cdot \mathring{\boldsymbol{F}} - \boldsymbol{I} \right) = \mathring{\boldsymbol{e}} + \frac{1}{2} \boldsymbol{\nabla} \otimes \boldsymbol{\nabla} (\mathring{\boldsymbol{u}} \cdot \mathring{\boldsymbol{u}}) \simeq \mathring{\boldsymbol{e}} \,, \tag{5.7a}$$

$$\boldsymbol{E}_1 = \frac{1}{2} (\boldsymbol{H}_1^T \cdot \mathring{\boldsymbol{F}} + \mathring{\boldsymbol{F}}^T \cdot \boldsymbol{H}_1) = \frac{1}{2} (\boldsymbol{H}_1 + \boldsymbol{H}_1^T + \mathring{\boldsymbol{H}}^T \cdot \boldsymbol{H}_1 + \boldsymbol{H}_1^T \cdot \mathring{\boldsymbol{H}})$$

$$= \boldsymbol{e}_1 + \boldsymbol{\nabla} \otimes \boldsymbol{\nabla} (\boldsymbol{u}_1 \cdot \mathring{\boldsymbol{u}}) \simeq \boldsymbol{e}_1 \,, \tag{5.7b}$$

where $\mathring{\boldsymbol{e}}$ and $\boldsymbol{e}_1$ are linear strain and the variation of linear strain respectively. Now we introduce the symmetric second Piola–Kirchhoff stress tensor $\boldsymbol{S}$, which is an objective Lagrangian tensor defined on $\mathcal{B}_r$ and unchanged under rigid-body deformation. The first Piola–Kirchhoff stress tensor (the nominal stress tensor) is $\boldsymbol{P} = \boldsymbol{S} \cdot \boldsymbol{F}^{\mathrm{T}}$, and the equilibrium equation $\boldsymbol{\nabla} \cdot \boldsymbol{P} = \boldsymbol{0}$ leads to

$$\boldsymbol{\nabla} \cdot \mathring{\boldsymbol{P}} = \boldsymbol{\nabla} \cdot \left[\mathring{\boldsymbol{S}} \cdot (\boldsymbol{I} + \mathring{\boldsymbol{H}}^{\mathrm{T}}) \right] = \boldsymbol{0} \,, \tag{5.8a}$$

$$\boldsymbol{\nabla} \cdot \boldsymbol{P} = \boldsymbol{\nabla} \cdot \left[\mathring{\boldsymbol{S}} \cdot \boldsymbol{H}^T + \boldsymbol{S} \cdot (\boldsymbol{I} + \mathring{\boldsymbol{H}}^{\mathrm{T}}) \right] = \boldsymbol{0} \,, \tag{5.8b}$$

where the subscript "$_1$" was dropped for notational convenience and hereafter we will keep this convention. Here, (5.8a) is the equilibrium equation for the basic state and (5.8b) is for the neutral stability configuration.

According to the principle of material frame-indifference, we can define a constitutive equation for hyperelastic solids as

$$\boldsymbol{S} = \frac{\partial \mathcal{W}}{\partial \boldsymbol{E}} \,, \tag{5.9}$$

in which $\mathcal{W}$, the strain energy is a function of the Green–Lagrange strain tensor. In particular, if we assume that the material follows Hooke's law, for general anisotropic linear materials, we have $\boldsymbol{S} = \mathbb{C} : \boldsymbol{E}$, where $\boldsymbol{S}$ and $\boldsymbol{E}$ are symmetric. The stiffness tensor $\mathbb{C}$ is a fourth-order tensor with 21 independent components. We take the assumption that the deformation is small as in (5.7), and we assume further that the material follows linear constitutive law in the form

$$\mathring{\boldsymbol{S}} = \mathbb{C} : \mathring{\boldsymbol{E}} \simeq \mathbb{C} : \mathring{\boldsymbol{e}} := \mathring{\boldsymbol{\sigma}} \,, \quad \text{and} \quad \boldsymbol{S} = \mathbb{C} : \boldsymbol{E} \simeq \mathbb{C} : \boldsymbol{e} := \boldsymbol{\sigma} \,, \tag{5.10}$$

where we have introduced the Cauchy Stress tensors in both pre-bifurcation state ($\mathring{\boldsymbol{\sigma}}$) and bifurcation state ($\boldsymbol{\sigma}$). In this work, we only use the linear Lamé solution for the pre-bifurcation state, and confine ourselves to the derivation of bifurcation equation (5.8b). Therefore, (5.8b) is reduced to

$$\boldsymbol{\nabla} \cdot [\boldsymbol{\sigma} \cdot (\boldsymbol{I} + \boldsymbol{\nabla} \otimes \mathring{\boldsymbol{u}}) + \mathring{\boldsymbol{\sigma}} \cdot (\boldsymbol{\nabla} \otimes \boldsymbol{u})] = \boldsymbol{0} \,. \tag{5.11}$$

Recalling the identity

$$\boldsymbol{\nabla} \cdot (\boldsymbol{A} \cdot \boldsymbol{B}) = (\boldsymbol{\nabla} \otimes \boldsymbol{A}) : \boldsymbol{B} + \boldsymbol{A} \cdot (\boldsymbol{\nabla} \cdot \boldsymbol{B}) \,,$$

which holds for any second-order tensors $\boldsymbol{A}, \boldsymbol{B}$, and considering the linear elasticity (5.10), we have

$$\mathbb{C} \vdots (\boldsymbol{\nabla} \otimes \boldsymbol{e}) + [\mathbb{C} : (\boldsymbol{\nabla} \otimes \boldsymbol{e})] : (\boldsymbol{\nabla} \otimes \mathring{\boldsymbol{u}}) + (\mathbb{C} : \boldsymbol{e}) \cdot (\nabla^2 \mathring{\boldsymbol{u}}) + (\boldsymbol{\nabla} \otimes \mathring{\boldsymbol{\sigma}}) : (\boldsymbol{\nabla} \otimes \boldsymbol{u}) + \mathring{\boldsymbol{\sigma}} \cdot (\nabla^2 \boldsymbol{u}) = \boldsymbol{0} \,. \tag{5.12}$$

Indeed, (5.11) can be rewritten as

$$\boldsymbol{\nabla} \cdot [\boldsymbol{\sigma} \cdot (\boldsymbol{I} + \mathring{\boldsymbol{e}} - \mathring{\boldsymbol{\omega}}) + \mathring{\boldsymbol{\sigma}} \cdot (\boldsymbol{e} - \boldsymbol{\omega})] = \boldsymbol{0} \,. \tag{5.13}$$

According to classical linear theory of elasticity, we have $\mathcal{O}(\boldsymbol{e}) \sim \mathcal{O}(\boldsymbol{\omega}^2)$ and $\mathcal{O}(\mathring{\boldsymbol{e}}) \sim \mathcal{O}(\mathring{\boldsymbol{\omega}}^2)$ (see [94], for example) under small deformation. Hence, we can take further assumptions

$$\|\mathring{\boldsymbol{e}}\| \ll \|\mathring{\boldsymbol{\omega}}\| \ll \|\boldsymbol{I}\| \quad \text{and} \quad \|\boldsymbol{e}\| \ll \|\boldsymbol{\omega}\| \,,$$

where '$\| \bullet \|$' is the norm of a second-order tensor, and is defined by $\|\boldsymbol{A}\| \equiv (\boldsymbol{A}{:}\boldsymbol{A})^{1/2}$. In this case, we have the following approximation

$$\boldsymbol{P} \simeq \boldsymbol{S} - \mathring{\boldsymbol{S}} \cdot \boldsymbol{\omega} \,. \tag{5.14}$$

Therefore, the bifurcation equation (5.13) is reduced to

$$\boldsymbol{\nabla} \cdot (\boldsymbol{\sigma} - \mathring{\boldsymbol{\sigma}} \cdot \boldsymbol{\omega}) = \boldsymbol{0} \,. \tag{5.15}$$

In particular, for isotropic elastic materials, the constitutive law in (5.10) takes the form

$$\boldsymbol{S} = \mathbb{C} : \boldsymbol{E} = \lambda \mathrm{tr}(\boldsymbol{E})\boldsymbol{I} + 2\mu\boldsymbol{E} \tag{5.16}$$

where, $\mathbb{C} = \lambda \boldsymbol{I} \otimes \boldsymbol{I} + 2\mu\mathbb{I}$.

$$\boldsymbol{S} = \mu \left[(\mathring{\boldsymbol{H}}^{\mathrm{T}} + \boldsymbol{I}) \cdot \boldsymbol{H} + \boldsymbol{H}^{\mathrm{T}} \cdot (\mathring{\boldsymbol{H}} + \boldsymbol{I}) \right] + \lambda \left(|\boldsymbol{H}| + |\mathring{\boldsymbol{H}}^{\mathrm{T}} \cdot \boldsymbol{H}| \right) \boldsymbol{I}$$

$$\simeq \boldsymbol{\sigma} = \mu(\boldsymbol{H} + \boldsymbol{H}^{\mathrm{T}}) + \lambda |\boldsymbol{H}| \, \boldsymbol{I} \,. \tag{5.17}$$

Use of (5.17) will then allow us to cast the bifurcation equation (5.15) in the following invariant form

$$\mu\nabla^2\boldsymbol{u} + (\lambda + \mu)\boldsymbol{\nabla}(\boldsymbol{\nabla} \cdot \boldsymbol{u}) - \mathring{\boldsymbol{\sigma}} : (\boldsymbol{\nabla} \otimes \boldsymbol{\omega}) = \boldsymbol{0} \,. \tag{5.18}$$

where we have taken $\boldsymbol{\nabla} \cdot \mathring{\boldsymbol{\sigma}} = \boldsymbol{0}$ for the pre-bifurcation state. It would be of interest to undertake a quantitative comparison between the two equations (5.18) and (5.12), and we hope to return to this problem in the near future.

The boundary conditions associated with this equation are briefly reviewed below. Let $\widehat{\boldsymbol{n}}$ be the outward unit normal to the cylindrical surface of the original unstressed body, and let $\mathring{\boldsymbol{n}}$ and $\boldsymbol{n}$ be the normals to the prestressed and, respectively, the neutrally stable adjacent configurations. Thus, the traction boundary conditions can be written as

$$\mathring{\boldsymbol{P}}^T \cdot \widehat{\boldsymbol{n}} = \boldsymbol{t}(\mathring{\boldsymbol{u}}) \qquad \text{and} \qquad (\mathring{\boldsymbol{P}} + \boldsymbol{P})^T \cdot \widehat{\boldsymbol{n}} = \boldsymbol{t}(\mathring{\boldsymbol{u}} + \boldsymbol{u}) \,, \tag{5.19}$$

where $\boldsymbol{t}$ represents the given traction vector – possibly depending on the displacement field in the case of follower loads. In this situation $\boldsymbol{t}(\boldsymbol{u}) = \sigma_j \boldsymbol{n}$, with $\sigma_j \in \mathbb{R}$ representing the magnitude of the applied radial stresses on $r = R_j$ ($j = 1, 2$): $\sigma_j < 0$ for compressive loads, while $\sigma_j > 0$ in the tensile case.

Since we are interested in the case of small pre-buckling deformations, we can introduce the approximation $\widehat{\boldsymbol{n}} \simeq \mathring{\boldsymbol{n}}$ and then, with the help of (5.14), the difference of the two relations in (5.19) leads to

$$(\boldsymbol{S} + \boldsymbol{\omega} \cdot \mathring{\boldsymbol{S}}) \cdot \mathring{\boldsymbol{n}} = \sigma_j(\boldsymbol{n} - \mathring{\boldsymbol{n}}) \,. \tag{5.20}$$

Eigenvalue problems & elastic instabilities

On the other hand, Nanson's formula with $J \equiv \det \boldsymbol{F} \simeq 1$ gives $\boldsymbol{n}\,\mathrm{d}a = \boldsymbol{F}^{-\mathrm{T}} \cdot \mathring{\boldsymbol{n}}\,\mathrm{d}\mathring{a}$, which on squaring out both sides produces

$$
\begin{aligned}
(\mathrm{d}a)^2 &= \mathring{\boldsymbol{n}} \cdot \boldsymbol{F}^{-1} \cdot \boldsymbol{F}^{-\mathrm{T}} \cdot \mathring{\boldsymbol{n}}(\mathrm{d}\mathring{a})^2 = \mathring{\boldsymbol{n}} \cdot \left[(\boldsymbol{I} + \boldsymbol{H})^{-1} \cdot (\boldsymbol{I} + \boldsymbol{H})^{-\mathrm{T}} \cdot \mathring{\boldsymbol{n}} \right] (\mathrm{d}\mathring{a})^2 \\
&\simeq (1 - 2\mathring{\boldsymbol{n}} \cdot (\boldsymbol{H} \cdot \mathring{\boldsymbol{n}}))(\mathrm{d}\mathring{a})^2 \,,
\end{aligned}
$$

and hence

$$
\boldsymbol{n} \simeq \boldsymbol{F}^{-\mathrm{T}} \cdot \mathring{\boldsymbol{n}}(1 + \mathring{\boldsymbol{n}} \cdot (\boldsymbol{H} \cdot \mathring{\boldsymbol{n}}))\,.
$$

When used in conjunction with (5.20) this last equation yields

$$
\sigma_j(\boldsymbol{n} - \mathring{\boldsymbol{n}}) \simeq -\sigma_j \boldsymbol{H}^{\mathrm{T}} \cdot \mathring{\boldsymbol{n}} \simeq \sigma_j \boldsymbol{\omega} \cdot \mathring{\boldsymbol{n}}\,,
$$

where in deriving the last result we have assumed that $\|\boldsymbol{e}\| \ll \|\boldsymbol{\omega}\|$. In conclusion, the constraints on the two curved boundaries of the annulus are

$$
(\boldsymbol{S} + \boldsymbol{\omega} \cdot \mathring{\boldsymbol{S}}) \cdot \mathring{\boldsymbol{n}} = \sigma_j \boldsymbol{\omega} \cdot \mathring{\boldsymbol{n}} \qquad \text{for} \quad r = R_j \qquad (j = 1, 2)\,. \tag{5.21}
$$

The term on the right-hand side of (5.21) has its origin in the changes of the applied forces with the current configuration, so this term will be absent in the case of dead loading.

Our next task will be to write the invariant-form equations (5.18) and (5.21) in component form in order to make them amenable to numerical calculations in the next sections. To this end, let $\{\boldsymbol{g}_1, \boldsymbol{g}_2, \boldsymbol{g}_3\}$ and $\{\boldsymbol{g}^1, \boldsymbol{g}^2, \boldsymbol{g}^3\}$ be a pair of reciprocal bases associated to the problem at hand; expressed in the latter base, the contravariant components of the identity tensor are $g^{ij} = \boldsymbol{g}^i \cdot \boldsymbol{g}^j$. A simple calculation then reveals that

$$
\begin{aligned}
\mathring{\boldsymbol{\sigma}} : (\boldsymbol{\nabla} \otimes \boldsymbol{\omega}) &= \frac{1}{2}\mathring{\boldsymbol{\sigma}} : \left[\boldsymbol{\nabla} \otimes (\boldsymbol{u} \otimes \boldsymbol{\nabla}) - \boldsymbol{\nabla} \otimes (\boldsymbol{\nabla} \otimes \boldsymbol{u}) \right] \\
&= \frac{1}{2}\mathring{\sigma}^{ij} \left(\nabla_i \nabla_j u_k - \nabla_i \nabla_k u_j \right) \boldsymbol{g}^k\,,
\end{aligned}
$$

where $\nabla_p u_q \equiv u_{q,p} - \Gamma_{pq}^r u_r$ denotes the covariant derivative of u_q with respect to the $\boldsymbol{g}_p$-coordinate and $\Gamma_{pq}^r \equiv \boldsymbol{g}^r \cdot \boldsymbol{g}_{p,q}$ are the well-known Christoffel symbols. Since in addition to this,

$$
\boldsymbol{\nabla}(\boldsymbol{\nabla} \cdot \boldsymbol{u}) = \left(g^{ij} \nabla_k \nabla_i u_j \right) \boldsymbol{g}^k \qquad \text{and} \qquad \nabla^2 \boldsymbol{u} = \left(g^{ij} \nabla_i \nabla_j u_k \right) \boldsymbol{g}^k\,,
$$

the desired component form of equation (5.18) assumes the expression

$$
\left(\mu g^{ij} + \frac{1}{2}\mathring{\sigma}^{ij} \right) \nabla_i \nabla_j u_k + (\lambda + \mu)g^{ij} \nabla_k \nabla_i u_j - \frac{1}{2}\mathring{\sigma}^{ij} \nabla_i \nabla_k u_j = 0\,. \tag{5.22}
$$

In cylindrical polar coordinates we find two coupled second-order partial differential equations

for the components of the in-plane displacement field $\boldsymbol{u}(r,\theta) = u_r(r,\theta)\boldsymbol{e}_r + u_\theta(r,\theta)\boldsymbol{e}_\theta$,

$$A_{11}\frac{\partial^2 u_r}{\partial r^2} + A_{12}\frac{\partial^2 u_\theta}{\partial \theta \partial r} + A_{13}\frac{\partial^2 u_r}{\partial \theta^2} + A_{14}\frac{\partial u_r}{\partial r} + A_{15}\frac{\partial u_\theta}{\partial \theta} + A_{16}u_r = 0\,, \tag{5.23a}$$

$$A_{21}\frac{\partial^2 u_\theta}{\partial r^2} + A_{22}\frac{\partial^2 u_r}{\partial \theta \partial r} + A_{23}\frac{\partial^2 u_\theta}{\partial \theta^2} + A_{24}\frac{\partial u_\theta}{\partial r} + A_{25}\frac{\partial u_r}{\partial \theta} + A_{26}u_\theta = 0\,, \tag{5.23b}$$

where

$$A_{11} := \lambda + 2\mu\,, \qquad\qquad A_{21} := \mu + \frac{1}{2}\mathring{\sigma}_{rr}\,,$$

$$A_{12} := \frac{1}{r}\left(\lambda + \mu - \frac{1}{2}\mathring{\sigma}_{\theta\theta}\right)\,, \qquad A_{22} := \frac{1}{r}\left(\lambda + \mu - \frac{1}{2}\mathring{\sigma}_{rr}\right)\,,$$

$$A_{13} := \frac{1}{r^2}\left(\mu + \frac{1}{2}\mathring{\sigma}_{\theta\theta}\right)\,, \qquad A_{23} := \frac{\lambda + 2\mu}{r^2}\,,$$

$$A_{14} := \frac{\lambda + 2\mu}{r}\,, \qquad\qquad A_{24} := \frac{1}{r}\left(\mu + \frac{1}{2}\mathring{\sigma}_{rr}\right)\,,$$

$$A_{15} := -\frac{1}{r^2}\left(\lambda + 3\mu + \frac{1}{2}\mathring{\sigma}_{\theta\theta}\right)\,, \qquad A_{25} := \frac{1}{r^2}\left(\lambda + 3\mu + \frac{1}{2}\mathring{\sigma}_{rr}\right)\,,$$

$$A_{16} := -\frac{\lambda + 2\mu}{r^2}\,, \qquad\qquad A_{26} := -\frac{1}{r^2}\left(\mu + \frac{1}{2}\mathring{\sigma}_{rr}\right)\,.$$

Note that due to plane-strain assumption the other equation obtained from (5.22) is automatically satisfied.

These equations are solved subject to the following boundary conditions at $r = R_j$ $(j = 1, 2)$,

$$B_{11}\frac{\partial u_r}{\partial r} + B_{12}\frac{\partial u_\theta}{\partial \theta} + B_{13}u_r = 0\,, \tag{5.24a}$$

$$B_{21}\frac{\partial u_r}{\partial \theta} + B_{22}\frac{\partial u_\theta}{\partial r} + B_{23}u_\theta = 0\,, \tag{5.24b}$$

where the coefficients that appear above are given by

$$B_{11} := \lambda + 2\mu\,, \qquad B_{21} := \frac{1}{2r}\left[2\mu - (\mathring{\sigma}_{rr} - \sigma_j)\right]\,,$$

$$B_{12} := \frac{\lambda}{r}\,, \qquad B_{22} := \frac{1}{2}\left[2\mu + (\mathring{\sigma}_{rr} - \sigma_j)\right]\,,$$

$$B_{13} := \frac{\lambda}{r}\,, \qquad B_{23} := \frac{1}{2r}\left[-2\mu + (\mathring{\sigma}_{rr} - \sigma_j)\right]\,.$$

The solution of the rather complicated system (5.23)–(5.24) is sought by using functions with

separable variables, i.e.

$$u_r(r, \theta) = U_1(r) \cos n\theta \qquad \text{and} \qquad u_\theta(r, \theta) = U_2(r) \sin n\theta \,, \tag{5.25}$$

where the arbitrary integer $n \geq 0$ will be determined from the usual minimisation strategy employed in similar contexts (see, for instance, [40, 41] for details on related problems). The amplitudes U_1 and U_2 turn out to satisfy two coupled second-order ordinary differential equations whose explicit expression we find next.

In the case of an elastic annulus loaded by radial tractions on both circular boundaries, the pre-buckling stress field has the well known expression (e.g., see [24])

$$\mathring{\sigma}_{rr} = \sigma_2 \left(A + \frac{B}{\rho^2} \right) \,, \qquad \mathring{\sigma}_{\theta\theta} = \sigma_2 \left(A - \frac{B}{\rho^2} \right) \,,$$

with

$$A := \frac{\eta^2 - \Lambda}{\eta^2 - 1} \,, \qquad B := \frac{\eta^2(\Lambda - 1)}{\eta^2 - 1} \,,$$

and

$$\rho := \frac{r}{R_1} \,, \qquad \eta := \frac{R_2}{R_1} \,, \qquad \Lambda := \frac{\sigma_1}{\sigma_2} \,.$$

It can be shown that the hoop stresses will vanish along the circumference of the circle $\rho = \overline{\rho}$,

$$\overline{\rho} := \left\{ \frac{\eta^2(\Lambda - 1)}{\eta^2 - \Lambda} \right\}^{1/2} \,;$$

furthermore, by letting

$$\Lambda_{\text{low}} = \frac{2\eta^2}{1 + \eta^2} \,, \qquad \Lambda_{\text{up}} = \frac{1}{2}(1 + \eta^2) \,,$$

we infer that if $\Lambda_{\text{low}} < \Lambda < \Lambda_{\text{up}}$ then the region $1 < \rho < \overline{\rho}$ experiences azimuthal compression, while the remaining part of the annulus, $\overline{\rho} < \rho < \eta$, is in tension. Thus, we expect the possible bifurcations present in this problem to have a local character and to be confined near the inner rim of the annulus. In this respect the situation appears to be entirely analogous to that involving the plane-stress problems discussed in [40, 41] but, as we shall see shortly, this is where the analogy stops.

After substituting the assumed form of solution (5.25) into the original equations (5.23)–(5.24), the resulting boundary-value problem for the U_j's ($j = 1, 2$) can be non-dimensionalised by introducing

$$\alpha := \frac{\sigma_2}{E} \,, \qquad \widehat{U}_1 := \frac{U_1}{R_2} \,, \qquad \widehat{U}_2 := \frac{U_2}{R_2} \,.$$

Dropping the "hats" for notational convenience and denoting by a dash differentiation with respect to ρ, we record below the final form of the bifurcation equations that hold for $1 < \rho < \eta$

$$\overline{A}_{11}U_1'' + \overline{A}_{12}U_2' + (\overline{A}_{13} + \overline{A}_{16})U_1 + \overline{A}_{14}U_1' + \overline{A}_{15}U_2 = 0\,, \tag{5.26a}$$

$$\overline{A}_{21}U_2'' + \overline{A}_{22}U_1' + (\overline{A}_{23} + \overline{A}_{26})U_2 + \overline{A}_{24}U_2' + \overline{A}_{25}U_1 = 0\,, \tag{5.26b}$$

where

$$\overline{A}_{11} := K_1\,, \qquad\qquad \overline{A}_{21} := \frac{1}{2}\left[K_3 + \alpha\left(A + \frac{B}{\rho^2}\right)\right]\,,$$

$$\overline{A}_{12} := \frac{n}{2\rho}\left[K_2 - \alpha\left(A - \frac{B}{\rho^2}\right)\right]\,, \qquad \overline{A}_{22} := -\frac{n}{2\rho}\left[K_2 - \alpha\left(A + \frac{B}{\rho^2}\right)\right]\,,$$

$$\overline{A}_{13} := -\frac{n^2}{2\rho^2}\left[K_3 + \alpha\left(A - \frac{B}{\rho^2}\right)\right]\,, \qquad \overline{A}_{23} := -\frac{n^2 K_1}{\rho^2}\,,$$

$$\overline{A}_{14} := \frac{K_1}{\rho}\,, \qquad\qquad \overline{A}_{24} := \frac{1}{2\rho}\left[K_3 + \alpha\left(A + \frac{B}{\rho^2}\right)\right]\,,$$

$$\overline{A}_{15} := -\frac{n}{2\rho^2}\left[K_4 + \alpha\left(A - \frac{B}{\rho^2}\right)\right]\,, \qquad \overline{A}_{25} := -\frac{n}{2\rho^2}\left[K_4 + \alpha\left(A + \frac{B}{\rho^2}\right)\right]\,,$$

$$\overline{A}_{16} := -\frac{K_1}{\rho^2}\,, \qquad\qquad \overline{A}_{26} := -\frac{1}{2\rho^2}\left[K_3 + \alpha\left(A + \frac{B}{\rho^2}\right)\right]\,,$$

and

$$K_1 = \frac{1-\nu}{(1+\nu)(1-2\nu)}\,, \qquad K_2 = \frac{1}{(1+\nu)(1-2\nu)}\,,$$

$$K_3 = \frac{1}{1+\nu}\,, \qquad K_4 = \frac{3-4\nu}{(1+\nu)(1-2\nu)}\,, \qquad K_5 = \nu K_2\,.$$

The relatively small parameter α that enters in these equations will be regarded as fixed in the numerical simulations of the next section.

The rescaled boundary conditions can be written in condensed form as

$$\overline{B}_{11}^{(j)}U_1' + \overline{B}_{12}^{(j)}U_2 + \overline{B}_{13}^{(j)}U_1 = 0\,, \tag{5.27a}$$

$$\overline{B}_{21}^{(j)}U_2' + \overline{B}_{22}^{(j)}U_2 + \overline{B}_{23}^{(j)}U_1 = 0\,, \qquad (j = 1, 2)\,, \tag{5.27b}$$

where the case $j = 1$ corresponds to the inner rim $(\rho = 1)$, and $j = 2$ applies to the outer boundary $(\rho = \eta)$. The expressions of the above coefficients take on different forms in the case of dead and follower loads, but can be written compactly as

$$B_{11}^{(1)} = K_1\,, \qquad B_{21}^{(1)} = \frac{1}{2}\left[K_3 + \alpha(A + B) - \underline{\underline{\alpha}}\right]\,,$$

$$B_{12}^{(1)} = nK_5\,, \qquad B_{22}^{(1)} = \frac{1}{2}\left[-K_3 + \alpha(A + B) - \underline{\underline{\alpha}}\right]\,,$$

$$B_{13}^{(1)} = K_5 \,, \qquad B_{23}^{(1)} = -\frac{n}{2} \left[K_3 - \alpha(A + B) + \underline{\alpha} \right] \,,$$

and

$$B_{11}^{(2)} = K_1 \,, \qquad B_{21}^{(2)} = \frac{1}{2} \left[K_3 + \alpha \left(A + \frac{B}{\eta^2} \right) - \underline{\underline{\alpha\lambda}} \right] \,,$$

$$B_{12}^{(2)} = \frac{nK_5}{\eta} \,, \qquad B_{22}^{(2)} = \frac{1}{2\eta} \left[-K_3 + \alpha \left(A + \frac{B}{\eta^2} \right) - \underline{\underline{\alpha\lambda}} \right] \,,$$

$$B_{13}^{(2)} = \frac{K_5}{\eta} \,, \qquad B_{23}^{(2)} = -\frac{n}{2\eta} \left[K_3 - \alpha \left(A + \frac{B}{\eta^2} \right) + \underline{\underline{\alpha\lambda}} \right] \,,$$

with the caveat that the underlined terms do not appear in the case of dead loading, whereas for follower loads all the $\alpha-$terms in the square brackets must be omitted (see also the remarks made after equation (5.21)). We mention in passing that the equations set up in this section are equivalent to the ones in [72] – cf. (27) and (28) featuring in that reference.

5.3 Numerical results

Direct numerical simulations of the boundary-value problem (5.26)-(5.27) were carried out in the usual fashion by first rewriting the equations as a first-order four-by-four linear system, which was then tackled with the help of the compound matrix method [40, 41]. In using the separable variable solutions (5.25) it was tacitly assumed that the equations (5.23) were elliptic. However, owing to the presence of variable coefficients, this statement need not be true everywhere in the annulus and, in fact, the equations do lose ellipticity for sufficiently large values of Λ. Also, since we are essentially concerned with a traction boundary-value problem, another subtle point is the verification of the Shapiro–Lopatinskij Condition (SLC, also named complementing or covering condition, see pp.107 in [54]). In order to understand the range of validity for the numerical integration of the ordinary differential equations, we first examine briefly under what conditions the loss of ellipticity becomes possible, and later we comment on the SLC.

To this end let us observe that (5.23) can be arranged in the form

$$\mathcal{L}_{rr}[u_r] + \mathcal{L}_{r\theta}[u_\theta] = 0 \,, \tag{5.28a}$$

$$\mathcal{L}_{\theta r}[u_r] + \mathcal{L}_{\theta\theta}[u_\theta] = 0 \,, \tag{5.28b}$$

where the differential operators that appear above have the following definitions,

$$\mathcal{L}_{rr} \equiv A_{11}\frac{\partial^2}{\partial r^2} + A_{13}\frac{\partial^2}{\partial \theta^2} + A_{14}\frac{\partial}{\partial r} + A_{16} \,,$$

$$\mathcal{L}_{r\theta} \equiv A_{12}\frac{\partial^2}{\partial r \partial \theta} + A_{15}\frac{\partial}{\partial \theta} \,,$$

$$\mathcal{L}_{\theta r} \equiv A_{22}\frac{\partial^2}{\partial r\partial\theta} + A_{25}\frac{\partial}{\partial\theta}\,,$$

$$\mathcal{L}_{\theta\theta} \equiv A_{21}\frac{\partial^2}{\partial r^2} + A_{23}\frac{\partial^2}{\partial\theta^2} + A_{24}\frac{\partial}{\partial r} + A_{26}\,.$$

The principal part of the symbol associated to the system (5.28) is defined by (see [54], for example)

$$\mathbf{L}^p(\boldsymbol{x}, \mathrm{i}\boldsymbol{\xi}) := - \begin{bmatrix} A_{11}(\boldsymbol{x})\xi_1^2 + A_{13}(\boldsymbol{x})\xi_2^2 & A_{12}(\boldsymbol{x})\xi_1\xi_2 \\ A_{22}(\boldsymbol{x})\xi_1\xi_2 & A_{21}(\boldsymbol{x})\xi_1^2 + A_{23}(\boldsymbol{x})\xi_2^2 \end{bmatrix}\,, \qquad (\mathrm{i} = \sqrt{-1})\,, \qquad (5.29)$$

where $\boldsymbol{\xi} \equiv (\xi_1, \xi_2) \in \mathbb{R}^2$ and we have indicated explicitly the dependence of the coefficients A_{ij} on the independent variable $\boldsymbol{x} \equiv (r, \theta)$. The type of the partial differential system (5.28) is classified according to the behaviour of $\mathbf{L}^p$, regarded as a quadratic form in ξ_1 and ξ_2. In particular, ellipticity requires that

$$\det \mathbf{L}^p(\boldsymbol{x}, \mathrm{i}\boldsymbol{\xi}) \neq 0\,, \qquad (\forall)\,\boldsymbol{\xi} \in \mathbb{R}^2\,,$$

which, after setting $t := \xi_2/\xi_1$ ($\xi_1 \neq 0$), can be reduced to the study of the signs of the roots for the bi-quadratic

$$Z_3 + Z_2 t^2 + Z_1 t^4 = 0\,, \tag{5.30}$$

where

$$Z_1 := A_{11}A_{21}\,,$$

$$Z_2 := A_{11}A_{23} + A_{13}A_{21} - A_{22}A_{12}\,,$$

$$Z_3 := A_{13}A_{23}\,.$$

This can be further transformed into a quadratic by making the obvious substitution $s = t^2$; if the equation in s has either negative or complex conjugate roots, then the problem is elliptic. Loss of ellipticity will occur when one of the roots passes through zero. Note also that due to the axial symmetry of the coefficients A_{ij} in (5.23), the boundary curve separating the elliptic regions of the material from the non-elliptic ones will have to be some circle $\rho = $const.

The discriminant of the quadratic in s is always positive as it turns out to be equal to

$$\left[\frac{1}{2r}(\lambda + 2\mu)(\mathring{\sigma}_{rr} - \mathring{\sigma}_{\theta\theta})\right]^2\,,$$

and the sum of the roots of the quadratic is just $2\mu - (\mathring{\sigma}_{rr} + \mathring{\sigma}_{\theta\theta})/2$. Since $3/2 < K_3 < 1$ and α is a relatively small parameter, it transpires that the sum of the roots is always negative. Thus, the condition for the loss of ellipticity will be given by $Z_3 = 0$ (since $Z_1 > 0$, after some

routine calculations), with the result that

$$\Lambda = \frac{\rho^2 \left[\eta^2 + (K_3/\alpha)(\eta^2 - 1)\right] + \eta^2}{\rho^2 + \eta^2} \, . \tag{5.31}$$

Regarded as a function of ρ, while all the other parameters are being kept fixed, $\Lambda = \Lambda(\rho)$ is an increasing function – as can be checked immediately by computing the derivative $\Lambda'(\rho)$. This means that loss of ellipticity will first occur for $\rho = 1$, i.e. at the inner rim. In conclusion, the curve that gives the loss of ellipticity in the $\lambda - \eta$ plane, say $\mathcal{C}$, has a simple analytical expression,

$$(\mathcal{C}): \qquad \Lambda_{\mathrm{ep}} = \frac{2\eta^2}{\eta^2 + 1} + \frac{K_3}{\alpha} \left(\frac{\eta^2 - 1}{\eta^2 + 1}\right) \, . \tag{5.32}$$

If $0 < \Lambda < \Lambda_{\mathrm{ep}}$ then the system (5.28) is elliptic and this is precisely the regime of interest here; note that the first term on the right-hand side of (5.32) is just Λ_{low} defined in the previous section.

It can be seen that the principal part of the symbol associated to the more complicated equation (5.12) does not coincide with (5.29) because the inhomogeneous character of the pre-bifurcation state of stress. This makes the analysis of that new equation even more relevant to understanding the nature of the simplifications that led to (5.18) and the potential loss of ellipticity. While for a homogeneous basic state both (5.18) and (5.12) are justly expected to produce very similar outcomes, it does not appear sensible to maintain these expectations in the case dealt with here.

The first set of numerical results appears recorded in Figure 5-3 and applies to the case of follower loads. We show the neutral stability curves corresponding to (5.26)-(5.27) for an increasing sequence of mode numbers ranging between 2 and 1000, when $\alpha = 0.05$ and $\nu = 0.33$. Changing these parameters does alter the *quantitative* features of the results, but the overall qualitative picture remains the same. Superimposed on these plots, the curve $\mathcal{C}$ is shown as the thick dashed line. It can be seen that the mode number $n = 2$ leads to the lowest eigenvalue for annular widths of up to $\eta \simeq 5.0$. Beyond that critical value, as n increases, the neutral stability curves move progressively into the elliptic region and seem to converge towards a limiting curve, which hereafter will be identified as $\mathcal{C}_\infty$. While not entirely obvious at this stage, the critical values of Λ associated with this curve identify a form of material rather than kinematic instability. In the next section we are going to show how an analytical approximation of $\mathcal{C}_\infty$ can be obtained by invoking some basic singular-perturbation arguments. In conclusion, when follower loads are considered the critical mode numbers are either $n = 2$ or $n = \infty$; the latter is essentially a material instability and is associated with the failure of the SLC – hence, the curve $\mathcal{C}_\infty$ provides the boundary in the $\Lambda - \eta$ plane across which this condition is violated.

When dead (or rigid) loading is considered we have included a typical scenario in Figure 5-4, which is laid out in the same fashion as the previous Figure. Note that the loss-of-ellipticity boundary $\mathcal{C}$ appears now as the envelope of the neutral stability curves as $n \to \infty$. For smallish
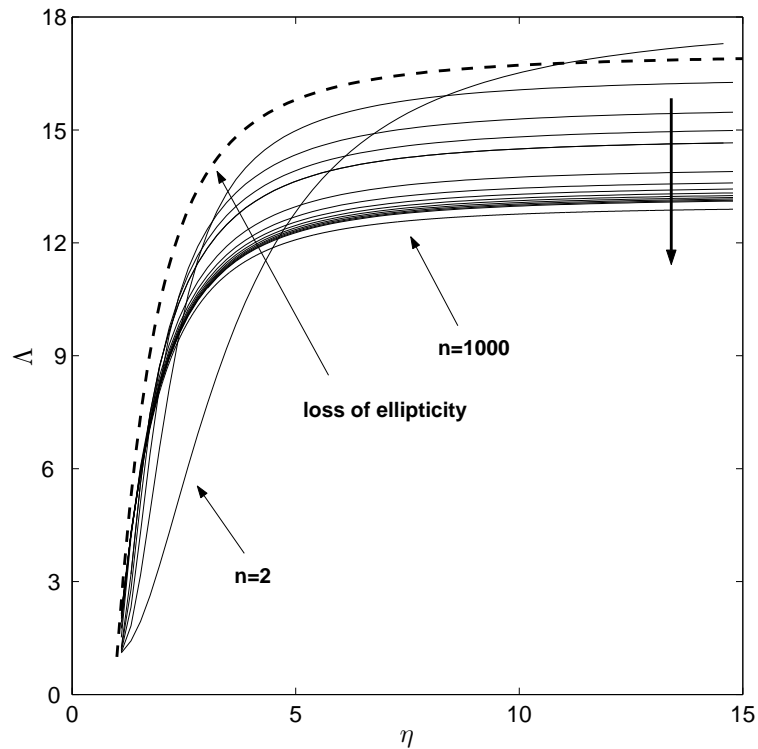
Figure 5-3: Dependence of the eigenvalues Λ on the aspect ratio $\eta > 1$ for different mode numbers: $n = 2, 4, \ldots, 8, 10, 20, \ldots, 80, 100, 1000$ in the case of *follower loads*. The thick arrow indicates the direction of increasing n and the dashed curve represents the loss of ellipticity boundary, as given by equation (5.32). Here $\alpha = 0.05$ and $\nu = 0.33$.

values of η (up to approximately 2.0), all response curves are inside the elliptic region and the lowest eigenvalue is rendered by $n = 2$, just as before. However, increasing the width of the annular domain, these curves are then found above the curve $\mathcal{C}$, which this time is attained in the limit of (infinitely) large mode numbers (i.e., $\mathcal{C} \simeq \mathcal{C}_\infty$, at least for largish η's). We recall here the well-known fact that the loss of ellipticity is a property of the differential equations themselves and it is independent of the type of boundary conditions employed. So in both Figures 5-3 and 5-4 the dashed line is the same, what changes is the position and the topology of the neutral stability curves. From this perspective the results obtained are to be expected, although the sharp transition between the two instability modes in Figure 5-3 cannot be anticipated right from the outset.

For the sake of completeness in Figure 5-5 we illustrate the eigenmodes for $n \to \infty$ in the case of follower loads. It is immediately clear that as n grows, i.e. the spatial oscillations in the azimuthal direction increase, the amplitude functions U_1 and U_2 defined in (5.25) get closer and closer to the inner rim of the annular domain. We mention in passing that these functions also display localisation if n is kept fixed and $\eta \to \infty$.
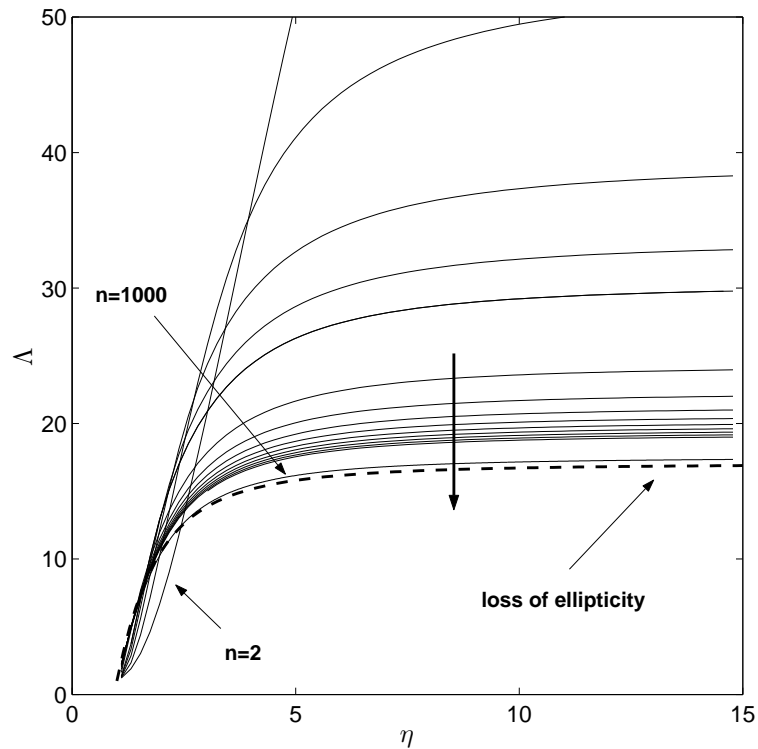
Figure 5-4: Response curves similar to Fig. 5-3, but in the case of *dead loading*; all values of the parameters are the same as before and the thick arrow shows again the direction of increasing mode numbers.

5.4 The limit $n \gg 1$

While in principle it would be possible to carry out an asymptotic analysis of (5.26) subject to either follower or dead loads, it is only the former case that is of some theoretical interest, and which therefore deserves a closer scrutiny. For the sake of completeness, we shall also make a few remarks regarding the asymptotic structure of the problem for dead loads. As it will become clear from our asymptotic calculations, the leading-order analysis presented here is in fact directly relevant to establishing the limits of validity for the SLC – although in keeping with the informal style of this section we shall not stress the technical side of that aspect. Section 5 of reference [93] contains some pertinent comments about similar situations and the ramifications for nonlinear bifurcation problems. The results in this section were obtained by the first author of [49], for the sake of self-consistence, they are reproduced here with permission.

The asymptotic structure in the two scenarios discussed in the previous section is different, although this is not immediately apparent. However, in both cases there is an $\mathcal{O}(n^{-1})$ boundary layer forming near the inner rim of the annular cross-section, and that is where we start.

To begin, in the limit $n \gg 1$ we introduce the stretched variable $X = \mathcal{O}(1)$ such that $\rho = 1 + X n^{-1}$, and look for solutions of (5.26) with

$$\boldsymbol{U} = \boldsymbol{U}_0(X) + \boldsymbol{U}_1(X)\frac{1}{n} + \dots , \tag{5.33a}$$
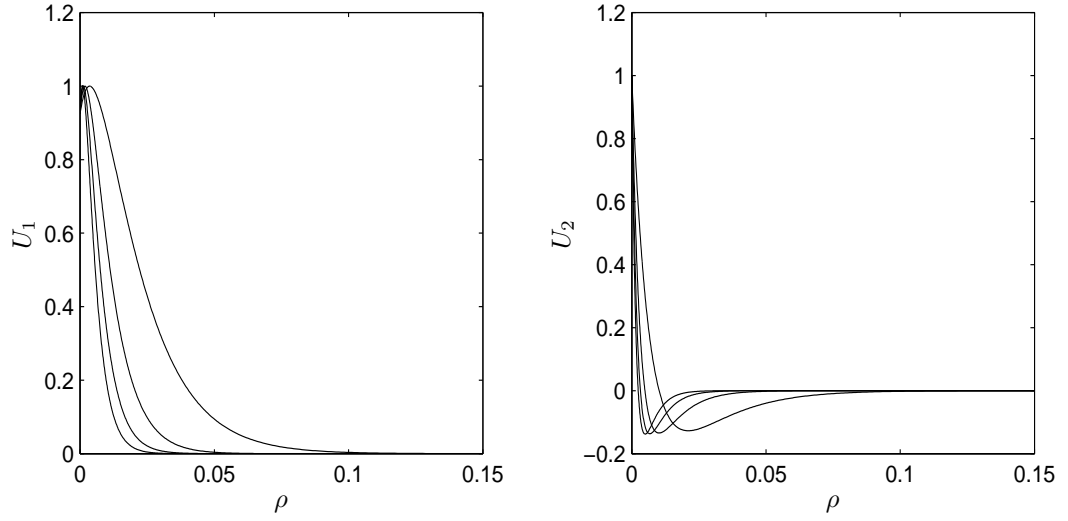
Figure 5-5: Normalised eigenmodes of (5.26) for follower loading when $\alpha = 0.05$, $\nu = 0.33$, and $\eta = 5.0$. Both U_1 and U_2 undergo localisation as the mode number n is progressively increased; here, $n = 50$, 100, 150, 200. The independent variable $1.0 \leq \rho \leq 5.0$ has been suitably adjusted to a smaller range in order to enhance the clarity of the localisation process.

$$\Lambda = \Lambda_0 + \frac{\Lambda_1}{n} + \dots , \tag{5.33b}$$

where

$$\boldsymbol{U} := \begin{bmatrix} U_1 \\ U_2 \end{bmatrix} , \qquad \boldsymbol{U}_j(X) := \begin{bmatrix} U_{1j}(X) \\ U_{2j}(X) \end{bmatrix} \qquad (j = 0, 1, \dots) .$$

The quantities that appear on the right-hand sides of (5.33) can be found systematically, although for our immediate purposes a leading-order analysis will suffice.

Routine algebraic manipulations indicate that if $\eta = \mathcal{O}(1)$ the boundary-layer behaviour is described by a hierarchy of equations governed by the differential operator

$$\mathcal{L}_{\mathrm{BL}} \equiv \boldsymbol{M}^{(2)} \frac{d^2}{dX^2} + \boldsymbol{M}^{(1)} \frac{d}{dX} + \boldsymbol{M}^{(0)} , \tag{5.34}$$

where the matrices $\boldsymbol{M}^{(j)} \in \mathcal{M}_{2 \times 2}(\mathbb{R})$ have the components recorded below

$$M_{11}^{(2)} := K_1 , \qquad\qquad M_{11}^{(1)} := 0 ,$$

$$M_{12}^{(2)} := 0 , \qquad\qquad M_{12}^{(1)} := \frac{\alpha}{2(\eta^2 - 1)} \left[\Lambda_0(\eta^2 + 1) - 2\eta^2 \right] + \frac{K_2}{2} ,$$

$$M_{21}^{(2)} := 0 , \qquad\qquad M_{21}^{(1)} := -\frac{1}{2}(K_2 - \alpha\Lambda_0) ,$$

$$M_{22}^{(2)} := \frac{1}{2}(K_3 + \alpha\Lambda_0) , \qquad M_{22}^{(1)} := 0 ,$$

$$M_{11}^{(0)} := \frac{\alpha}{2(\eta^2 - 1)} \left[\Lambda_0(\eta^2 + 1) - 2\eta^2 \right] - \frac{K_3}{2} \,,$$

$$M_{12}^{(0)} := 0 \,,$$

$$M_{21}^{(0)} := 0 \,,$$

$$M_{22}^{(0)} := -K_1 \,.$$

The leading-order terms in (5.33) satisfy

$$\mathcal{L}_{\mathrm{BL}}[\boldsymbol{U}_0] = \boldsymbol{0} \,; \tag{5.35}$$

when dead loads are considered, this equation must be solved subject to the homogeneous boundary conditions

$$\boldsymbol{H}_1 \frac{d\boldsymbol{U}_0}{dX} + \mathring{\boldsymbol{H}} \boldsymbol{U}_0 = \boldsymbol{0} \qquad \text{at} \quad X = 0 \,, \tag{5.36}$$

where

$$\boldsymbol{H}_1 := \begin{bmatrix} K_1 & 0 \\ 0 & \alpha\Lambda_0 + K_3 \end{bmatrix} \qquad \text{and} \qquad \mathring{\boldsymbol{H}} := \begin{bmatrix} 0 & K_5 \\ \alpha\Lambda_0 - K_3 & 0 \end{bmatrix} \,.$$

These constraints apply to follower loads as well, with the only modification that the parameter α in $\mathring{\boldsymbol{H}}$ and $\boldsymbol{H}_1$ must be set equal to zero. In both cases a second set of constraints must be enforced, as motivated by the numerical experiments of §3,

$$\frac{d^j \boldsymbol{U}_0}{dX^j} \to \boldsymbol{0} \qquad \text{as} \quad X \to \infty \,, \qquad (j = 0, 1) \,. \tag{5.37}$$

It will turn out that this naive set of conditions are not relevant to the dead loading situation but, nevertheless, it is instructive to carry on with both cases in parallel and see how the simple boundary-layer structure (5.33) fails in that situation.

Looking for a solution of (5.35) in the form $\boldsymbol{U}_0(X) = \boldsymbol{v} \exp(\zeta X)$, for some $\zeta \in \mathbb{C}$ and a column vector $\boldsymbol{v} \in \mathbb{R}^2$, it is found that the former must satisfy the characteristic equation

$$\det \left[\zeta^2 \boldsymbol{M}^{(2)} + \zeta \boldsymbol{M}^{(1)} + \boldsymbol{M}^{(0)} \right] = 0 \,,$$

with the roots

$$\zeta_{1,2} = \pm 1 \qquad \text{and} \qquad \zeta_{3,4} = \pm\beta(\Lambda_0, \eta) \,, \tag{5.38}$$

where

$$\beta(\Lambda_0, \eta) := \sqrt{\frac{K_3 - 2G}{K_3 + \alpha\Lambda_0}} \,, \qquad G := \frac{\alpha}{2(\eta^2 - 1)} \left[\Lambda_0(\eta^2 + 1) - 2\eta^2 \right] \,. \tag{5.39}$$

Guided by the fact that the requirement (5.37) must hold in the far-field, the boundary-layer

solution must be a linear combination of two exponentials involving the negative values from (5.38). Substituting this function in the two boundary conditions (5.36) results in the determinantal equation that supplies Λ_0. In the case of follower loads it is found that

$$H_3 \Lambda_0^3 + H_2 \Lambda_0^2 + H_1 \Lambda_0 + H_0 = 0 \,, \tag{5.40}$$

where

$$H_0 = -\frac{H_{04}\eta^4 + H_{02}\eta^2 + H_{00}}{(\eta^2 - 1)^2(\nu + 1)^3} \,, \qquad\qquad H_1 = -\frac{\alpha(H_{14}\eta^4 + H_{12}\eta^2 + H_{10})}{(\eta^2 - 1)^2(\nu + 1)^2} \,,$$

$$H_2 = \frac{\alpha^2 \left(H_{24}\eta^4 + H_{22}\eta^2 + H_{20}\right)}{(\eta^2 - 1)^2(\nu + 1)} \,, \qquad\qquad H_3 = -\frac{\alpha^3 \left(H_{34}\eta^4 + H_{32}\eta^2 + H_{30}\right)}{(\eta^2 - 1)^2} \,,$$

and

$$H_{04} := 4\alpha^2(1 - \nu^2)^2 - 2\alpha(1 + \nu) - 1 \,, \qquad H_{02} := 2\left[\alpha(\nu + 1) + 1\right] \,,$$

$$H_{14} := 4\alpha^2(1 - \nu^2)^2 - 4\alpha(\nu^3 + 1) + 1 - 2\nu \,, \qquad H_{12} := 4\left[\alpha(-\nu^3 + 2\nu^2 + 2\nu - 1) + \nu\right] \,,$$

$$H_{24} := 4\alpha(1 - \nu) - 2\alpha\nu^2(1 - 3\nu) - 1 \,, \qquad H_{22} := 2\left[\alpha\nu^2(\nu - 3) + 2\nu(1 - \nu) + 2\alpha(1 - \nu) - 1\right] \,,$$

$$H_{34} := 2\nu^2 - 2\nu + 1 \,, \qquad H_{32} := 2(\nu - 1)^2 \,,$$

$$H_{00} := -1 \,, \qquad H_{10} := -(1 + 2\nu) \,, \qquad H_{20} := 4\nu - 1 \,, \qquad H_{30} := 1 - 2\nu \,.$$

The results predicted by (5.40) are compared in Figure 5-6 with the direct numerical simulations of (5.26)-(5.27) for $n = 1000$ (which could serve as a good approximation for $\mathcal{C}_\infty$). For the sake of brevity we show only a representative sample of calculations corresponding to $\nu = 0.33$ and $\alpha = 0.05/0.005$, because no qualitative differences are observed when changing these parameters. It is evident that the agreement is excellent and the leading-order ansatz (5.33b) does capture all the features of the numerical solution.

If we try to approach the dead-loading problem with the same type of ansatz, then it quickly transpires that such a strategy would eventually be doomed for according to (5.39) as (Λ_0, η) gets close to the curve $\mathcal{C}$ defined in (5.32), $\beta(\Lambda_0, \eta) \to 0$. Hence there is now only one solution of (5.35) that falls off exponentially for $X \to \infty$. In this case the determinantal equation loses its relevance since it was obtained under the assumption that $\beta(\Lambda_0, \eta) = \mathcal{O}(1)$.

Figure 5-4 shows clearly that the neutral stability curves tend to accumulate on $\mathcal{C}$ (the dashed curve) in the limit $n \gg 1$. Interestingly enough, this feature is anticipated by the old expansion (5.33) although, as we have just remarked above, this leads to some spurious results as well. Following the same strategy that led to (5.40), its counterpart in the dead loading case is

$$(K_3 - 2G)(E_2 \Lambda_0^2 + E_1 \Lambda_0 + E_0) = 0 \,, \tag{5.41}$$
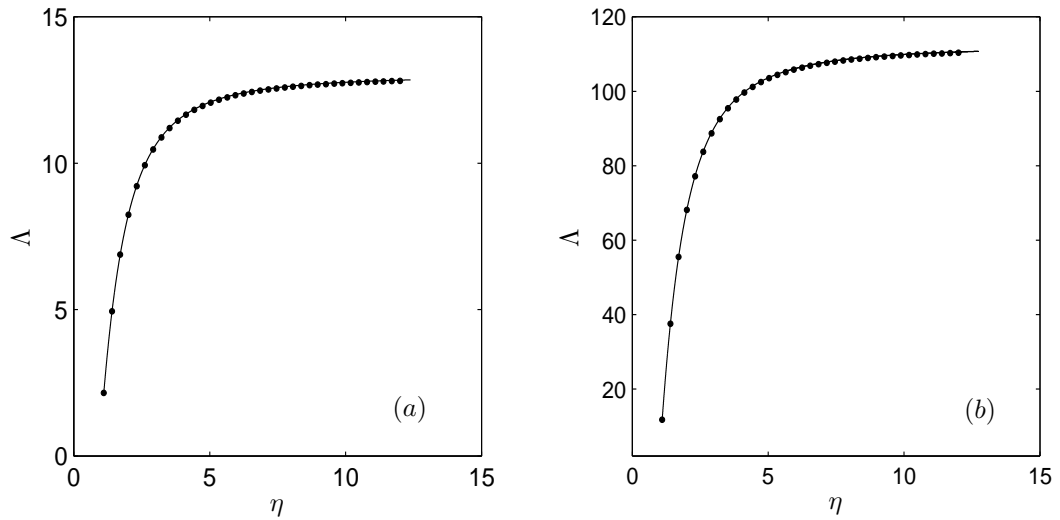
Figure 5-6: Follower loads: comparisons between the limiting curves $\Lambda \equiv \Lambda_0(\eta)$ predicted by the leading-order determinantal equations (*dotted lines*) and their counterparts obtained from direct numerical simulations of (5.26)-(5.27) in the large-n limit (*continuous curves, $n = 1000$*). In both windows $\nu = 0.33$, while $\alpha = 0.05$ in (*a*), and $\alpha = 0.005$ in (*b*).

with

$$E_2 := \frac{4\alpha^2(1-\nu)^2}{\eta^2 - 1} + \alpha^2(\eta^2 + 1),$$

$$E_1 := -2\alpha(\alpha\eta^2 - K_3) - \frac{8\alpha^2\eta^2(1-\nu)^2}{\eta^2 - 1},$$

$$E_0 := \frac{4\alpha^2\eta^4(1-\nu)^2}{\eta^2 - 1} - K_3^2(\eta^2 - 1) - 2K_3\alpha\eta^2.$$

Setting to zero the first bracket we get precisely the equation for the curve that marks the loss of ellipticity boundary in the $\Lambda - \eta$ plane. Alternatively, one can solve the quadratic in the second bracket that turns out to have a unique root $\Lambda_0 > 0$ slightly below that predicted by the previous equation. This apparent contradiction is a consequence of using the determinantal equation (5.41) beyond its intended range of validity. We have checked numerically for mode numbers up to $n = 5 \times 10^4$ that confirmed the accuracy of the scenario recorded in Figure 5-4 (and that the dashed curve is approached from above by the response curves).

To unravel the reason of the discrepancy generated by (5.41) we need to go back to the differential equations (5.26). When $K_3 - 2G = 0$ it is easily checked that $\overline{A}_{13}(\rho = 1) = 0$ and (5.26) admits an $\mathcal{O}(n^{-2/3})$ boundary layer governed by a rescaled Airy function, with the eigenvalue expanding now in powers of $n^{-2/3}$. The $\mathcal{O}(n^{-1})$-layer still survives and it is possible to carry out a relatively standard analysis involving the interaction of the two layers, very much in the spirit of [40, 41]. Since the non-elliptic regime is outwith the range of physical interest the details of that analysis are left out.

The boundary-value problem (5.26)-(5.27) contains a couple of additional parameters be-

sides the mode number. Several asymptotic regimes can be investigated in this respect, for instance $0 < \alpha \ll 1$ or $\eta \gg 1$ or assuming that the relative order of magnitude of these parameters are related to each other. However, none of these appears to be relevant to our immediate purposes, so we do not pursue matters further here.

The next-order problem is found to be described by the system of differential equations

$$\mathcal{L}_{\mathrm{BL}}[\boldsymbol{U}_1] = \boldsymbol{N}^{(00)}\boldsymbol{U}_0 + \boldsymbol{N}^{(10)}\frac{d\boldsymbol{U}_0}{dX} + \boldsymbol{N}^{(20)}\frac{d^2\boldsymbol{U}_0}{dX^2}\,, \tag{5.42}$$

where

$$N_{11}^{(00)} = -\frac{\Lambda_1\alpha}{2}\left(\frac{\eta^2+1}{\eta^2-1}\right) + X\left\{\frac{\alpha}{\eta^2-1}\left[\Lambda_0(1+2\eta^2) - 3\eta^2\right] - K_3\right\},$$

$$N_{12}^{(00)} = -\frac{\alpha}{2(\eta^2-1)}\left[\Lambda_0(1+\eta^2) - 2\eta^2\right] - \frac{K_4}{2},$$

$$N_{21}^{(00)} = \frac{1}{2}(K_4 + \alpha\lambda_0),$$

$$N_{22}^{(00)} = -2XK_1,$$

$$N_{11}^{(10)} = -K_1,$$

$$N_{12}^{(10)} = -\frac{\Lambda_1\alpha}{2}\left(\frac{\eta^2+1}{\eta^2-1}\right) + \frac{X}{2}\left\{\frac{\alpha}{\eta^2-1}\left[\Lambda_0(1+3\eta^2) - 4\eta^2\right] + K_2\right\},$$

$$N_{21}^{(10)} = -\frac{\Lambda_1\alpha}{2} - \frac{X}{2}\left\{\frac{\alpha}{\eta^2-1}\left[\Lambda_0(1-3\eta^2) + 2\eta^2\right] + K_2\right\},$$

$$N_{22}^{(10)} = 0,$$

$$N_{22}^{(20)} = -\frac{\Lambda_1\alpha}{2} + X\left[\frac{\alpha\eta^2(\Lambda_0-1)}{\eta^2-1}\right],$$

$$N_{12}^{(20)} = N_{21}^{(20)} = N_{11}^{(20)} = 0.$$

The relevant boundary conditions in this case are

$$\boldsymbol{H}_1\frac{d\boldsymbol{U}_1}{dX} + \mathring{\boldsymbol{H}}\boldsymbol{U}_1 = \boldsymbol{G}^{(10)}\frac{d\boldsymbol{U}^{(0)}}{dX} + \boldsymbol{G}^{(00)}\boldsymbol{U}_0\,, \tag{5.43}$$

where

$$\boldsymbol{G}^{(10)} := \begin{bmatrix} 0 & 0 \\ 0 & -\alpha\Lambda_1 \end{bmatrix} \quad \text{and} \quad \boldsymbol{G}^{(0)} := \begin{bmatrix} -K_5 & 0 \\ -\alpha\Lambda_1 & K_3 - \alpha\Lambda_0 \end{bmatrix}.$$

and again the decay conditions at infinity (5.37) must be enforced on $\boldsymbol{U}_1$. As before, the above formulae are also valid for follower loads by setting $\alpha = 0$ in (5.43).

5.5   Discussion and conclusions

We have considered the in-plane bifurcations of the classical plane-strain Lamé solutions for a St. Venant–Kirchhoff elastic solid. One of the main aims of this last chapter has been to explore the applicability of the asymptotic strategy proposed in [31, 46] to the case when the bifurcations are associated with a stressed rather than a free surface. Within the context of the simplified incremental deformation theory adopted here – $SIDT$ (e.g., [13, 15, 94]), it was shown that this is indeed possible, but the outcome is somewhat different from that of the earlier investigations. In the scenario for the pure bending of a neo-Hookean rubber block discussed in [46] the transition between small and large mode numbers was gradual and depended intimately on the ratio of thickness to length. More exactly, the larger the width of the block, the greater the number of ripples on the compressed side. In the limit of an infinitely large block the critical principal stretch became equal to that found in the compression of a half-plane [14]. The problem was strongly elliptic and the instabilities found had a kinematic character. Here, perhaps because of the fact that both boundaries of the annulus are stressed, the neutrally stable configuration has less freedom in accommodating the full spectrum of mode numbers. Our results indicated that in the case of follower loads, for a small range of annulus widths, $\eta \simeq 1$ to 2 when $\alpha = 0.05$ and $\nu = 0.33$ ($\eta \equiv R_2/R_1$), the predominant long-wave deformation mode corresponds to the inner rim becoming an ellipse. For larger widths a short-wavelength (material) instability is observed whereby the central hole of the cylinder experiences fine warping; this wrinkling-type instability is directly linked to the failure of the Shapiro–Lopatinskij Condition. In the case of dead loading loss of ellipticity dominates the global picture, although there is still a narrow window of annular widths for which the long-wave mode ($n = 2$) persists. (These findings were robust when changing the Poisson's ratio $0 < \nu < 0.5$ and the non-dimensional parameter $\alpha \equiv \sigma_2/E$).

   While from a practical point of view the immediate relevance of the specific type of loading adopted in this study is somewhat limited, the results reported here contribute towards a further rational understanding of the bifurcation phenomena experienced by elastic solids subjected to tensile loads. The analysis reported in this chapter also shows that one must tread with caution when dealing with incremental bifurcation equations involving non-homogeneous basic states because loss of ellipticity can severely restrict the scope of mathematical investigations. Last but not least, the work reported here reinforces the relevance of singular perturbation methods not only to thin-walled configurations, but also to incrementally linear elastic solids.

Chapter 6

Conclusions

6.1   Summary

The main contribution of this Thesis is the investigation of several bifurcation (eigenvalue) problems for the elastic instability in tension, which include the thin elastic plates, rectangular plates and thick cylindrical tubes subject to stretching loading. Then these mathematical models were discussed thoroughly by using a mixture of both numerical and asymptotic techniques.

As stated in the concluding sections in *Chapter 2* to *Chapter 5*, we summarise the main results here.

In *Chapter 2*, we first recorded a set of coordinate-free formulation for Föppl–von Kármán plate theory and the corresponding bifurcation equations by using *Calculus of Variations*. This is first started by assuming the Love–Kirchhoff displacement field, then we apply the minimum energy principle to the potential energy by using the *Calculus of Variations*. We showed the derivation of these equations in both weak form and strong form (together with the boundary conditions). This set of equations is applicable for any plate geometries made of general anisotropic elastic material. We also showed the reduction from the above general case to the isotropic elastic plate subject to only in-plane loading. The related weak form was then used in *Chapter 3*, and the strong form together with the boundary conditions were then applied to *Chapter 4*.

In *Chapter 3*, a hybrid energy method was proposed aiming to improve the existing asymptotic approximations in tensile edge-buckling (such as [41, 44]), and extend those results (valid for large asymptotic parameter $\mu \gtrsim 350.0$) to the regime when μ is small ($\mu \simeq 10.0$). This was achieved by adding extra unknowns (freedom) to the leading order asymptotic ansatzes, plugging them into the weak form of the bifurcation equation and the critical mode number condition to form a multi-variable optimisation problem. Then the results for smaller-μ regime ($\mu \lesssim 2.0$) are complemented by asymptotic analysis when μ is asymptotically small. This new approach provides approximations for both the neutral stability envelope (NSE) and the

corresponding critical number of wrinkles with minimum effort. The method is shown to be robust irrespective of the geometries as we have applied it to both rectangular and annular geometries. The accuracy achieved is fairly good despite the simplicity of the leading order asymptotics (membrane boundary-layer) employed . Additionally, including the effects of the bending boundary layer leads to an even better agreement with the numerics.

In *Chapter 4*, we have investigated the localised instabilities of a stretched bi-annular thin plate, which is composed of two concentric annuli with different mechanical properties and fully attached. The bi-layer structure can behave differently in terms of both the prebuckling stress distribution and the bifurcation compared with the single-annular case with homogeneous material. Owing to the different properties of the materials (Young's modulus E and Poisson ratio ν) in the two annular regions, the stress distribution in the basic state was first investigated both analytically and numerically, which is a limit case when $\mu \to \infty$. It suggests two types of limiting curves analytically that depend on the ratios of mechanical properties (Young's moduli and Poisson ratios) of these two annuli: the cusp type and the rectangular-hyperbola type. The former type corresponds to the cases when $\gamma := E_1/E_2 < \nu_1/\nu_2$; while the latter type occurs when $\gamma > \nu_1/\nu_2$. Complete parametric studies (mechanical and geometrical) were conducted for the full bifurcation problem. The NSE can be classified into two different types as well, asymptotically corresponding to the previous basic state analysis. We also found that localised instabilities (edge-buckling) can be triggered by discontinuities, not only from the boundaries but also from interface, depending on mechanical and geometrical parameters. Then, both the pre-bifurcation and bifurcation analyses were considered together and a deeper understanding was gained on the effects of the discontinuities caused by the interface on both the critical external stretching and wrinkling modes. Further asymptotic analysis has been undertaken by extending the earlier analysis of Coman *et al.*(2006) into bi-layer structure. The asymptotic approximations are quite robust and accurate when the large parameter is moderately large. It paves the way for generalisation of the asymptotic analyses given by Coman *et al.* (2007). Both the numerical and asymptotic strategies in this problem can, in principle, be extended for the bifurcation of multi-layered structures.

In *Chapter 5*, the in-plane bifurcation of an infinite thick cylindrical tube made of St Venant–Kirchhoff elastic material was considered, subject to radial stretching on the two cylindrical surfaces. Firstly, a novel tensor derivation that clarifies the assumptions introduced was given based on a simplified theory of Biot, and a new tensorial equation was presented in which some of the simplifications have been ignored informed by Novozhilov's theory. However, the bifurcation of plane-strain problem is completely different from the corresponding plane-stress case. Numerical investigations of the relevant incremental problem reveal two main bifurcation modes for the tube: a long-wave local deformation (critical mode number $n = 2$) around the central hole of the domain; or a material wrinkling-type instability ($n = \infty$) along the same boundary. Strictly speaking, the latter scenario is related to the violation of the Shapiro–Lopatinskij con-

dition in an appropriate traction boundary-value problem. From the physical point of view, it might be because the strong constraints such as the the plane-strain deformation and both the boundaries are stressed, the neutral stability configuration has less freedom in accommodating the full spectrum of mode numbers. The results contribute towards a further rational understanding of the bifurcation phenomena experienced by elastic solids subject to tensile loads. The analysis also shows that one must tread with caution when dealing with incremental bifurcation equations involving non-homogeneous basic states because loss of ellipticity can severely restrict the scope of mathematical investigations.

6.2 Future work

The work in this Thesis also suggests a number of interesting extensions that could be explored in the future.

There are several direct extensions for the formulation in *Chapter 2*: we can pursue thick plate theories such as the first- and higher-order shear deformation theories by introducing a rotation vector term in the assumption for the displacement field; or we can consider dynamic plate theory by including a kinetic energy term, which is of great importance since in dynamic analysis, the nonlinearities in deformation and elasticity are customarily assumed to be absent.

In *Chapter 3*, the proposed hybrid energy method has been proven to be robust for a class of edge-buckling problem in tension. It would be interesting to explore this strategy to problems in which the asymptotics are governed by differential equations that are not solvable in closed form. A pertinent example is provided by the paper [99], in which the authors used finite element simulations to identify the optimal choice of such an ansatz. The alternative asymptotic description given by Coman in [34] for the same problem hinged upon a boundary-layer analysis governed by a fourth-order differential equation with variable coefficients and which was not solvable in closed form. Extending the ideas discussed in this chapter to that situation would be an interesting exercise, and that could broaden the scope and relevance of the *Hybrid Energy Method* to new classes of eigenvalue problems.

Since we have investigated the localised instabilities of a stretched bi-annular plate in *Chapter 4*, there are a number of extensions for this problem. One direction would be extend it to a greater number of concentric annuli that make up a multi-annular plate. It would be of interest to see if there are further novel types of response curves and wrinkling modes, and more interesting findings are expected to appear in parametric analysis. In this direction, we can treat one annulus as stiffened, then it is of practical significance to study its stiffening effects on the buckling resistance under tension, in contrast to compressed buckling of stiffened annular plates as reported in [56]. Another aspect is focusing on how do the discontinuities (boundary and interfacial conditions) affect the localised wrinkling patterns. For example, in light of the localised instabilities of the initially stretched annular plate caused by the az-

imuthal shear stresses along the inner rim [40, 43], we expect the localised wrinkling mode and the NSE appear novel types for a multi-layer structure compared to a single-annular under the same geometries. Also, we can change the interfacial conditions from fully attached to be other contacting constraints (different discontinuities). By doing this, we investigate how those discontinuities affect the prebuckling stresses, and in that case, what is the influence of the mechanical and geometrical parameters on the wrinkling mode as well as the anti-wrinkling capability of that structure.

In *Chapter 5* we have discussed the plane-strain instability of a thick cylindrical tube. In this problem, linear Lamé solutions were used for the pre-buckling state, it would be interesting to see whether the findings of this work will persist when we treat the pre-buckling as nonlinear, such as the equations $\boldsymbol{\nabla} \cdot \boldsymbol{P} = \boldsymbol{0}$ before reduction, as stated in §5.2. Also, the linear bifurcation equations were obtained under a series of simplifications. However, for a compressed thick cylindrical shells, Kardomateas [73] pointed out that the effect of including the terms with pre-buckling normal strains and stresses ($\mathring{\boldsymbol{\sigma}} \cdot \boldsymbol{e}$ and $\boldsymbol{\sigma} \cdot \mathring{\boldsymbol{e}}$, which were neglected in our problem) as coefficients will lead to about 14% decrease in the critical compressive load compressed orthotropic tubes when $R_2/R_1 = 1.4$. It would be of interest to compare the solutions with the un-simplified and the simplified bifurcation equations in our problem, followed by asymptotic analysis (if applicable). Another immediate extension of this work vis-á-vis the developments of §5.3 could be directed towards the role of the boundary loading imposed on the annulus. For instance, the stress concentration phenomenon persists if the domain undergoes azimuthal shearing along the inner boundary, with tensile tractions still being imposed on the outer perimeter. By analogy with the plane-stress calculations carried out in [40] we expect the asymptotic structure of the problem to be different due to the obvious rotational symmetry inherent in that problem. Finally, it is also of interest to understand whether the phenomena observed in this chapter are an immediate consequence of the approximate nature of the $SIDT$; in this respect a comparison of the present analysis with a more rigorous one based on Ogden's incremental elasticity formulation would be desirable.

Another interesting aspect would be extending the bifurcation problems discussed in *Chapter 4* and *Chapter 5*, where the structures are made of isotropic material, to the same geometries but made of anisotropic materials (such as polar orthotropic, transversely isotropic, etc.). The formulation are already recorded in §2.1, §2.2 (for elastic plate) and §5.2 (for elastic solids). Those work can be companied by the asymptotic analysis in light of [35].

Appendix A

Some useful identities for vectors and tensor fields

Here we collect a few less standard identities that were used in *Chapter 2* and *Chapter 5*. In this appendix, we let ϕ and ψ be scalar fields, $\boldsymbol{a}$, $\boldsymbol{b}$, $\boldsymbol{c}$, $\boldsymbol{d}$, $\boldsymbol{e}$, $\boldsymbol{f}$, $\boldsymbol{g}$ and $\boldsymbol{h}$ be vector fields, and $\boldsymbol{T}$ a second-order tensor field.

A.1 Identities related to stiffness tensor

At first we introduce some fourth-order identity tensors, then we record some identities used to perform the manipulations that specifies the general anisotropic linear elastic plate into the plates made of isotropic material. The *double contraction* for second-order tensors, the *triple contraction* for third-order tensors and the *quadruple contraction* for fourth-order tensors are defined respectively by

$$(\boldsymbol{a} \otimes \boldsymbol{b}) : (\boldsymbol{c} \otimes \boldsymbol{d}) := (\boldsymbol{a} \cdot \boldsymbol{c})(\boldsymbol{b} \cdot \boldsymbol{d}) \,,$$

$$(\boldsymbol{a} \otimes \boldsymbol{b} \otimes \boldsymbol{c}) \vdots (\boldsymbol{d} \otimes \boldsymbol{e} \otimes \boldsymbol{f}) := (\boldsymbol{a} \cdot \boldsymbol{d})(\boldsymbol{b} \cdot \boldsymbol{e})(\boldsymbol{c} \cdot \boldsymbol{f}) \,,$$

$$(\boldsymbol{a} \otimes \boldsymbol{b} \otimes \boldsymbol{c} \otimes \boldsymbol{d}) \vdots\vdots (\boldsymbol{e} \otimes \boldsymbol{f} \otimes \boldsymbol{g} \otimes \boldsymbol{h}) := (\boldsymbol{a} \cdot \boldsymbol{e})(\boldsymbol{b} \cdot \boldsymbol{f})(\boldsymbol{c} \cdot \boldsymbol{g})(\boldsymbol{d} \cdot \boldsymbol{h}) \,.$$

These operations are extended in an obvious way when one of the terms is a tensor of higher order. For example, for any fourth-order tensor $\mathbb{C}$, we have

$$(\boldsymbol{a} \otimes \boldsymbol{b}) : \mathbb{C} : (\boldsymbol{c} \otimes \boldsymbol{d}) = \mathbb{C} \vdots\vdots (\boldsymbol{a} \otimes \boldsymbol{b} \otimes \boldsymbol{c} \otimes \boldsymbol{d}) \,.$$

We now introduce two important fourth-order identity tensors appear in the stiffness tensors, followed by some useful identities. One is $\boldsymbol{I} \otimes \boldsymbol{I}$ ($\boldsymbol{I}$ is the second-order identity tensor), whose

component form reads

$$(\boldsymbol{I} \otimes \boldsymbol{I})_{\alpha\beta\gamma\delta} := g_{\alpha\beta}g_{\gamma\delta}\,.$$

Another important fourth-order tensor is *symmetric projection* tensor $\mathbb{I}$, with the entries

$$\mathbb{I}_{\alpha\beta\gamma\delta} := \frac{1}{2}(g_{\alpha\gamma}g_{\beta\delta} + g_{\alpha\delta}g_{\beta\gamma})\,.$$

In what follows we record some properties of these two tensors.

$$(\boldsymbol{I} \otimes \boldsymbol{I}) : \boldsymbol{T} = tr(\boldsymbol{T})\boldsymbol{I}\,, \quad \mathbb{I} : \boldsymbol{T} = \boldsymbol{T}^s\,,$$

where $\boldsymbol{T}^s$ denotes the symmetric parts of $\boldsymbol{T}$, and $tr(\boldsymbol{T})$ is the first principal invariant of $\boldsymbol{T}$. Therefore, we have

$$(\boldsymbol{I} \otimes \boldsymbol{I}) : (\boldsymbol{\nabla}\phi \otimes \boldsymbol{\nabla}\psi) = (\boldsymbol{\nabla}\phi \cdot \boldsymbol{\nabla}\psi)\boldsymbol{I}\,, \quad \mathbb{I} : [(\boldsymbol{\nabla}\phi) \otimes (\boldsymbol{\nabla}\psi)] = [(\boldsymbol{\nabla}\phi) \otimes (\boldsymbol{\nabla}\psi)]^s\,.$$

For an arbitrary vector field $\boldsymbol{a}$, we have

$$(\boldsymbol{I} \otimes \boldsymbol{I}) : (\boldsymbol{\nabla} \otimes \boldsymbol{a}) = (\boldsymbol{\nabla} \cdot \boldsymbol{a})\boldsymbol{I}\,, \qquad \mathbb{I} : (\boldsymbol{\nabla} \otimes \boldsymbol{a}) = (\boldsymbol{\nabla} \otimes \boldsymbol{a})^s\,, \tag{A.1a}$$

$$(\boldsymbol{I} \otimes \boldsymbol{I}) \vdots (\boldsymbol{\nabla} \otimes \boldsymbol{\nabla} \otimes \boldsymbol{a}) = \boldsymbol{\nabla}(\boldsymbol{\nabla} \cdot \boldsymbol{a})\,, \qquad \mathbb{I} \vdots (\boldsymbol{\nabla} \otimes \boldsymbol{\nabla} \otimes \boldsymbol{a}) = \boldsymbol{\nabla} \cdot (\boldsymbol{\nabla} \otimes \boldsymbol{a})^s\,, \tag{A.1b}$$

$$(\boldsymbol{I} \otimes \boldsymbol{I}) \vdots (\boldsymbol{\nabla} \otimes \boldsymbol{\nabla} \otimes \boldsymbol{\nabla} \otimes \boldsymbol{a}) = \nabla^2(\boldsymbol{\nabla} \cdot \boldsymbol{a})\,, \quad \mathbb{I} \vdots (\boldsymbol{\nabla} \otimes \boldsymbol{\nabla} \otimes \boldsymbol{\nabla} \otimes \boldsymbol{a}) = (\boldsymbol{\nabla} \otimes \boldsymbol{\nabla}) : (\boldsymbol{\nabla} \otimes \boldsymbol{a})^s\,. \tag{A.1c}$$

Note that in $(A.1b)_2$ and $(A.1c)_2$

$$\boldsymbol{\nabla} \cdot (\boldsymbol{\nabla} \otimes \boldsymbol{a})^s = \frac{1}{2}\left[\boldsymbol{\nabla}(\boldsymbol{\nabla} \cdot \boldsymbol{a}) + \boldsymbol{\nabla} \cdot (\boldsymbol{\nabla} \otimes \boldsymbol{a})\right]\,,$$

$$(\boldsymbol{\nabla} \otimes \boldsymbol{\nabla}) : (\boldsymbol{\nabla} \otimes \boldsymbol{a})^s = \boldsymbol{\nabla} \cdot \left[\boldsymbol{\nabla} \cdot (\boldsymbol{\nabla} \otimes \boldsymbol{a})^s\right]\,.$$

If we replace $\boldsymbol{a}$ in (A.1) by $\boldsymbol{\nabla}\phi$, we have the identities below

$$(\boldsymbol{I} \otimes \boldsymbol{I}) : (\boldsymbol{\nabla} \otimes \boldsymbol{\nabla}\phi) = (\nabla^2\phi)\boldsymbol{I}\,, \quad \mathbb{I} : (\boldsymbol{\nabla} \otimes \boldsymbol{\nabla}\phi) = \boldsymbol{\nabla} \otimes \boldsymbol{\nabla}\phi\,, \tag{A.2a}$$

$$(\boldsymbol{I} \otimes \boldsymbol{I}) \vdots (\boldsymbol{\nabla} \otimes \boldsymbol{\nabla} \otimes \boldsymbol{\nabla}\phi) = \mathbb{I} \vdots (\boldsymbol{\nabla} \otimes \boldsymbol{\nabla} \otimes \boldsymbol{\nabla}\phi) = \boldsymbol{\nabla}(\nabla^2\phi)\,, \tag{A.2b}$$

$$(\boldsymbol{I} \otimes \boldsymbol{I}) \vdots (\boldsymbol{\nabla} \otimes \boldsymbol{\nabla} \otimes \boldsymbol{\nabla} \otimes \boldsymbol{\nabla}\phi) = \mathbb{I} \vdots (\boldsymbol{\nabla} \otimes \boldsymbol{\nabla} \otimes \boldsymbol{\nabla} \otimes \boldsymbol{\nabla}\phi) = \nabla^2(\nabla^2\phi)\,, \tag{A.2c}$$

in which

$$\boldsymbol{\nabla}(\nabla^2\phi) = \nabla^2(\boldsymbol{\nabla}\phi) = \boldsymbol{\nabla} \cdot (\boldsymbol{\nabla} \otimes \boldsymbol{\nabla}\phi)\,, \tag{A.3a}$$

$$\nabla^2(\nabla^2\phi) = (\boldsymbol{\nabla} \otimes \boldsymbol{\nabla}) : (\boldsymbol{\nabla} \otimes \boldsymbol{\nabla}\phi) = \boldsymbol{\nabla} \cdot \left[\boldsymbol{\nabla} \cdot (\boldsymbol{\nabla} \otimes \boldsymbol{\nabla}\phi)\right]\,. \tag{A.3b}$$

Moreover, in two-dimensional problems, if we introduce two orthogonal unit vectors $\boldsymbol{n}$ and $\boldsymbol{s}$ ($\boldsymbol{n} \cdot \boldsymbol{s} = 0$), then the gradient can be decomposed as

$$\boldsymbol{\nabla} := \boldsymbol{n} \nabla_n + \boldsymbol{s} \nabla_s = \boldsymbol{n} \frac{\partial}{\partial n} + \boldsymbol{s} \frac{\partial}{\partial s} \,.$$

Therefore, we have the following conclusions

$$\boldsymbol{I} : (\boldsymbol{n} \otimes \boldsymbol{n}) = tr(\boldsymbol{n} \otimes \boldsymbol{n}) = 1 \,, \qquad \boldsymbol{I} : (\boldsymbol{n} \otimes \boldsymbol{s}) = tr(\boldsymbol{n} \otimes \boldsymbol{s}) = 0 \,,$$

$$(\boldsymbol{I} \otimes \boldsymbol{I}) : (\boldsymbol{n} \otimes \boldsymbol{n}) = \boldsymbol{I} \,, \qquad \mathbb{I} : (\boldsymbol{n} \otimes \boldsymbol{n}) = \boldsymbol{n} \otimes \boldsymbol{n} \,,$$

$$(\boldsymbol{I} \otimes \boldsymbol{I}) : (\boldsymbol{n} \otimes \boldsymbol{s}) = \boldsymbol{O} \,, \qquad \mathbb{I} : (\boldsymbol{n} \otimes \boldsymbol{s}) = (\boldsymbol{n} \otimes \boldsymbol{s})^s \,,$$

$$(\boldsymbol{\nabla} \otimes \boldsymbol{\nabla} \phi) : (\boldsymbol{n} \otimes \boldsymbol{n}) = \nabla_n^2 \phi \,, \qquad (\boldsymbol{\nabla} \otimes \boldsymbol{\nabla} \phi) : (\boldsymbol{n} \otimes \boldsymbol{s}) = \nabla_n \nabla_s \phi \,,$$

$$(\boldsymbol{\nabla} \phi \otimes \boldsymbol{\nabla} \psi) : (\boldsymbol{n} \otimes \boldsymbol{n}) = \nabla_n \phi \nabla_n \psi \,, \quad (\boldsymbol{\nabla} \phi \otimes \boldsymbol{\nabla} \psi) : (\boldsymbol{n} \otimes \boldsymbol{s}) = \nabla_n \phi \nabla_s \psi \,,$$

where $\boldsymbol{O}$ is the second-order zero tensor.

We use $\mathbb{C}$ to denote the constant stiffness tensor for a general linear material (anisotropic). Due to the symmetric of the stress tensor and strain tensor, a stiffness tensor $\mathbb{C}$ has the following three symmetric properties, namely, two *minor symmetries* (defined in $(A.4)_{1,2}$) and the *major symmetries* (as in $(A.4)_3$)

$$\mathbb{C}_{\alpha\beta\gamma\delta} = \mathbb{C}_{\beta\alpha\gamma\delta} \,, \quad \mathbb{C}_{\alpha\beta\gamma\delta} = \mathbb{C}_{\alpha\beta\delta\gamma} \,, \quad \mathbb{C}_{\alpha\beta\gamma\delta} = \mathbb{C}_{\gamma\delta\alpha\beta} \,. \tag{A.4}$$

In three-dimensional problems, the above symmetry properties can reduce the original 81 independent components in two-dimensional problem into only 21. For two-dimensional problems, the number of independent components is reduced from 16 to 6. Some inferences drawn from the symmetry properties of a constant stiffness tensor $\mathbb{C}$ read

$$\mathbb{C} : \boldsymbol{T} = \boldsymbol{T} : \mathbb{C} \,,$$

$$\boldsymbol{\nabla} \cdot (\mathbb{C} : \boldsymbol{T}) = \mathbb{C} \vdots (\boldsymbol{\nabla} \otimes \boldsymbol{T}) \,,$$

$$\boldsymbol{\nabla} \cdot [\boldsymbol{\nabla} \cdot (\mathbb{C} : \boldsymbol{T})] = \mathbb{C} \vdots (\boldsymbol{\nabla} \otimes \boldsymbol{\nabla} \otimes \boldsymbol{T}) \,.$$

A.2 Divergence Theorem and Green Identities

In this Thesis, *Divergence Theorem* was also applied to conduct some of the integration derivations. More specifically, for two-dimensional problems,

$$\int_\Omega \boldsymbol{\nabla} \cdot (\phi \boldsymbol{a}) \, \mathrm{d}A = \int_\Omega (\phi \boldsymbol{\nabla} \cdot \boldsymbol{a} + \boldsymbol{a} \cdot \boldsymbol{\nabla} \phi) \, \mathrm{d}A = \int_{\partial\Omega} (\boldsymbol{a} \cdot \boldsymbol{n}) \phi \, \mathrm{d}S \,, \tag{A.5}$$

where $\boldsymbol{n}$ is the unit normal vector (outward drawn) on the boundary $\partial\Omega$. By letting $\boldsymbol{a} \to \boldsymbol{\nabla}\psi$, we obtain the *Green's first identity*

$$\int_\Omega (\phi\nabla^2\psi + \boldsymbol{\nabla}\psi \cdot \boldsymbol{\nabla}\phi)\,\mathrm{d}A = \int_{\partial\Omega} (\boldsymbol{\nabla}\psi \cdot \boldsymbol{n})\phi\,\mathrm{d}S\,. \tag{A.6}$$

Moreover, if we permute ϕ and ψ in (A.6) and subtract, we can obtain the *Green's second identity* as following

$$\int_\Omega (\phi\nabla^2\psi - \psi\nabla^2\phi)\,\mathrm{d}A = \int_{\partial\Omega} (\phi\boldsymbol{\nabla}\psi - \psi\boldsymbol{\nabla}\phi) \cdot \boldsymbol{n}\,\mathrm{d}S\,. \tag{A.7}$$

Another corollary of the *Divergence Theorem* is

$$\oint_{\partial\Omega} \boldsymbol{a} \cdot \boldsymbol{\nabla}\phi\,\mathrm{d}S = \oint_{\partial\Omega} [(\boldsymbol{a} \cdot \boldsymbol{n})\nabla_n\phi + (\boldsymbol{a} \cdot \boldsymbol{s})\nabla_s\phi]\,\mathrm{d}S = \oint_{\partial\Omega} [\boldsymbol{a} \cdot \boldsymbol{n}\nabla_n\phi - \nabla_s(\boldsymbol{a} \cdot \boldsymbol{s})\phi]\,\mathrm{d}S\,, \tag{A.8}$$

where $\boldsymbol{n}$ and $\boldsymbol{s}$ are the *normal* and *shear* unit vector attached to the boundary $\partial\Omega$.

A.3 Other identities

For any symmetric second-order tensor $\boldsymbol{T}$, where $\boldsymbol{T} = \boldsymbol{T}^T$, it is obvious that

$$\boldsymbol{T} : (\boldsymbol{a} \otimes \boldsymbol{b})^s = \boldsymbol{T} : (\boldsymbol{a} \otimes \boldsymbol{b}) = \boldsymbol{T} : (\boldsymbol{b} \otimes \boldsymbol{a}) = (\boldsymbol{T} \cdot \boldsymbol{b}) \cdot \boldsymbol{a} = (\boldsymbol{T} \cdot \boldsymbol{a}) \cdot \boldsymbol{b}\,.$$

Furthermore, we have the identity,

$$\boldsymbol{I} : (\boldsymbol{\nabla} \otimes \boldsymbol{\nabla}\phi) = \boldsymbol{\nabla} \cdot (\boldsymbol{\nabla}\phi) = \nabla^2\phi \quad \text{and} \quad \nabla^2(\boldsymbol{\nabla} \otimes \boldsymbol{a}) = \boldsymbol{\nabla} \otimes (\nabla^2\boldsymbol{a})\,. \tag{A.9}$$

By letting $\boldsymbol{a} \to \boldsymbol{\nabla}\phi$ in (A.9)$_2$ we find that

$$\nabla^2(\boldsymbol{\nabla} \otimes \boldsymbol{\nabla}\phi) = \boldsymbol{\nabla} \otimes (\nabla^2(\boldsymbol{\nabla}\phi))\,.$$

Other identities used earlier in the Thesis include

$$\boldsymbol{\nabla} \cdot (\phi\boldsymbol{I}) = \boldsymbol{\nabla}\phi\,,$$

$$\boldsymbol{\nabla} \cdot (\phi\boldsymbol{a}) = (\boldsymbol{\nabla}\phi) \cdot \boldsymbol{a} + \phi(\boldsymbol{\nabla} \cdot \boldsymbol{a})\,,$$

$$\boldsymbol{\nabla} \cdot (\boldsymbol{T} \cdot \boldsymbol{a}) = (\boldsymbol{\nabla} \cdot \boldsymbol{T}) \cdot \boldsymbol{a} + \boldsymbol{T} : (\boldsymbol{\nabla} \otimes \boldsymbol{a})\,,$$

$$\boldsymbol{\nabla}(\phi\psi) = \psi(\boldsymbol{\nabla}\phi) + \phi(\boldsymbol{\nabla}\psi)\,,$$

$$\boldsymbol{\nabla}(\boldsymbol{a} \cdot \boldsymbol{b}) = (\boldsymbol{\nabla} \otimes \boldsymbol{a}) \cdot \boldsymbol{b} + (\boldsymbol{\nabla} \otimes \boldsymbol{b}) \cdot \boldsymbol{a}\,,$$

$$\boldsymbol{\nabla} \otimes (\phi\boldsymbol{a}) = (\boldsymbol{\nabla}\phi) \otimes \boldsymbol{a} + \phi(\boldsymbol{\nabla} \otimes \boldsymbol{a})\,,$$

$$\boldsymbol{\nabla} \otimes (\boldsymbol{T} \cdot \boldsymbol{a}) = (\boldsymbol{\nabla} \otimes \boldsymbol{T}) \cdot \boldsymbol{a} + (\boldsymbol{\nabla} \otimes \boldsymbol{a}) \cdot \boldsymbol{T}^T \,,$$

$$\nabla^2(\boldsymbol{a} \otimes \boldsymbol{b}) = (\nabla^2 \boldsymbol{a}) \otimes \boldsymbol{b} + \boldsymbol{a} \otimes (\nabla^2 \boldsymbol{b}) + 2(\boldsymbol{\nabla} \otimes \boldsymbol{a})^T \cdot (\boldsymbol{\nabla} \otimes \boldsymbol{b}) \,.$$

Appendix B

Application of the compound matrix method to the bi-annular eigenvalue problem

This appendix contains the relevant calculations for the compound matrix method (CMM) applied to the wrinkling of the bi-annular plate in *Chapter 4* – see equations (4.53)-(4.55) in § 4.4. Our presentation follows the detailed treatment given by Lindsay in [80] for several related examples.

For the sake of clarity, we are going to rewrite the fourth-order governing differential equations in Ω_I and Ω_{II} as

$$\frac{d\boldsymbol{y}}{d\rho} = \boldsymbol{A}^I \boldsymbol{y}\,, \qquad \rho \in [\eta_1, \eta_2]\,, \tag{B.1a}$$

$$\frac{d\boldsymbol{z}}{d\rho} = \boldsymbol{A}^{II} \boldsymbol{z}\,, \qquad \rho \in [\eta_2, 1]\,, \tag{B.1b}$$

where $\boldsymbol{y} = [y_1, y_2, y_3, y_4]^T$, $\boldsymbol{z} = [z_1, z_2, z_3, z_4]^T$, and the 4×4 matrices introduced above are defined by

$$\boldsymbol{A}^{I,II} := \begin{bmatrix} 0 & 1 & 0 & 0 \\ 0 & 0 & 1 & 0 \\ 0 & 0 & 0 & 1 \\ A_{41}^{I,II} & A_{42}^{I,II} & A_{43}^{I,II} & A_{44}^{I,II} \end{bmatrix}\,.$$

These two linear systems are complemented by the boundary conditions on the inner and outer rims of the annular domain $\Omega \equiv \Omega_I \cup \Omega_{II}$

$$\boldsymbol{B}^I \boldsymbol{y} = 0 \quad \text{at} \quad \rho = \eta_1\,, \tag{B.2a}$$

166

$$\boldsymbol{B}^{II}\boldsymbol{z} = 0 \quad \text{at} \quad \rho = 1\,, \tag{B.2b}$$

where

$$\boldsymbol{B}^{I} = \boldsymbol{B}^{II} := \begin{bmatrix} 1 & 0 & 0 & 0 \\ 0 & 1 & 0 & 0 \end{bmatrix}\,.$$

In addition to this, on the interface between Ω_I and Ω_{II} we have the continuity condition

$$\boldsymbol{G}\boldsymbol{y} - \boldsymbol{H}\boldsymbol{z} = 0 \quad \text{at} \quad \rho = \eta_2\,, \tag{B.3}$$

where

$$\boldsymbol{G} := \begin{bmatrix} 0 & 1 & 0 & 0 \\ 0 & 0 & 1 & 0 \\ G_{31} & G_{32} & G_{33} & 0 \\ G_{41} & G_{42} & G_{43} & G_{44} \end{bmatrix} \quad \text{and} \quad \boldsymbol{H} := \begin{bmatrix} 0 & 1 & 0 & 0 \\ 0 & 0 & 1 & 0 \\ H_{31} & H_{32} & H_{33} & 0 \\ H_{41} & H_{42} & H_{43} & H_{44} \end{bmatrix}\,.$$

We are now ready to outline the CMM without being burdened by the precise expressions of the matrices introduced above. For the bi-annular plate problem, we have two strategies. The first transforms the boundary conditions (B.2a) and (B.2b) on the inner and, respectively, the outer rim of Ω into some initial conditions for two auxiliary linear differential systems; the continuity conditions on the interface $\rho = \eta_2$ serves as a target condition for these auxiliary initial-value problems, and its role is to identify the actual eigenvalues.

Alternatively, one can use the boundary conditions on either boundary (e.g., $\rho = \eta_1$) as the initial conditions to integrate one of the auxiliary systems mentioned above over the range from η_1 to η_2. Then, by using a suitable reformulation of the continuity conditions (B.3), a new set of initial conditions is derived for the second auxiliary system. The boundary conditions on $\rho = 1$ are arranged into a target condition (different from the previous scenario) that the second system must satisfy in order to identify the eigenvalues of the original problem (B.1).

A caveat is in order at this point: the former strategy is only applicable for an annular plate that has exactly two annular sub-regions, whereas the latter one is more general and can be used for multi-annular plates. The difference between the two strategies consist only in the treatment of the continuity conditions at the interface, the other details remain unchanged. Thus, we shall start with a preliminary description on how the two auxiliary differential systems are set up that will be followed by the particular details of the two alternatives mentioned.

The general solutions of (B.1a) and (B.1b) can be expressed in the form

$$\boldsymbol{y} = \alpha_1 \boldsymbol{y}^{(1)} + \alpha_2 \boldsymbol{y}^{(2)}\,, \qquad \boldsymbol{z} = \alpha_3 \boldsymbol{z}^{(1)} + \alpha_4 \boldsymbol{z}^{(2)}\,.$$

where, $\alpha_i \in \mathbb{R}$ $(i = 1, 2, 3, 4)$ are arbitrary constants, and $\boldsymbol{y}^{(1)}, \boldsymbol{y}^{(2)}, \boldsymbol{z}^{(1)}, \boldsymbol{z}^{(2)}$ are two independent solutions with

$$\boldsymbol{y}^{(k)} = [y_1^{(k)}, y_2^{(k)}, y_3^{(k)}, y_4^{(k)}]^T, \qquad \boldsymbol{z}^{(k)} = [z_1^{(k)}, z_2^{(k)}, z_3^{(k)}, z_4^{(k)}]^T \qquad (k = 1, 2).$$

These solutions are the building block for the the compound variables that are set up by using the matrices $\boldsymbol{Y}$ and $\boldsymbol{Z}$,

$$\boldsymbol{Y} := \begin{bmatrix} y_1^{(1)} & y_1^{(2)} \\ y_2^{(1)} & y_2^{(2)} \\ y_3^{(1)} & y_3^{(2)} \\ y_4^{(1)} & y_4^{(2)} \end{bmatrix} = \begin{bmatrix} \boldsymbol{R}_1 \\ \boldsymbol{R}_2 \\ \boldsymbol{R}_3 \\ \boldsymbol{R}_4 \end{bmatrix} \quad \text{and} \quad \boldsymbol{Z} := \begin{bmatrix} z_1^{(1)} & z_1^{(2)} \\ z_2^{(1)} & z_2^{(2)} \\ z_3^{(1)} & z_3^{(2)} \\ z_4^{(1)} & z_4^{(2)} \end{bmatrix} = \begin{bmatrix} \boldsymbol{S}_1 \\ \boldsymbol{S}_2 \\ \boldsymbol{S}_3 \\ \boldsymbol{S}_4 \end{bmatrix}, \qquad \text{(B.4)}$$

where $\boldsymbol{R}_i$, $\boldsymbol{S}_i$ $(i = 1, 2, 3, 4)$ represent the row vectors of $\boldsymbol{Y}$ and $\boldsymbol{Z}$ introduced for further reference when we shall discuss the second CMM strategy mentioned earlier. Furthermore, we also introduce the CMM variables ψ_i and ϕ_i $(i = 1, ..., 6)$ constructed from the matrix $\boldsymbol{Y}$ and $\boldsymbol{Z}$ as indicated below,

$$\psi_1 := \begin{vmatrix} y_1^{(1)} & y_1^{(2)} \\ y_2^{(1)} & y_2^{(2)} \end{vmatrix} = (1, 2)^y, \qquad \psi_2 := \begin{vmatrix} y_1^{(1)} & y_1^{(2)} \\ y_3^{(1)} & y_3^{(2)} \end{vmatrix} = (1, 3)^y,$$

$$\phi_1 := \begin{vmatrix} z_1^{(1)} & z_1^{(2)} \\ z_2^{(1)} & z_2^{(2)} \end{vmatrix} = (1, 2)^z, \qquad \phi_2 := \begin{vmatrix} z_1^{(1)} & z_1^{(2)} \\ z_3^{(1)} & z_3^{(2)} \end{vmatrix} = (1, 3)^z.$$

The notation (i, j) stands for the minor obtained by considering rows i and j in either $\boldsymbol{Y}$ or $\boldsymbol{Z}$; the superscripts indicate which one of the two matrices is chosen.

Similarly, we have

$$\psi_3 := (1, 4)^y, \quad \psi_4 := (2, 3)^y, \quad \psi_5 := (2, 4)^y, \quad \psi_6 := (3, 4)^y,$$

$$\phi_3 := (1, 4)^z, \quad \phi_4 := (2, 3)^z, \quad \phi_5 := (2, 4)^z, \quad \phi_6 := (3, 4)^z.$$

If we differentiate ψ_j with respect to ρ, by using the formula for differentiation of a determinant we can express the result as a linear combinations of the components of ψ. For example,

$$\frac{d\psi_1}{d\rho} \equiv {\psi_1}' = \begin{vmatrix} {y_1^{(1)}}' & {y_1^{(2)}}' \\ y_2^{(1)} & y_2^{(2)} \end{vmatrix} + \begin{vmatrix} y_1^{(1)} & y_1^{(2)} \\ {y_2^{(1)}}' & {y_2^{(2)}}' \end{vmatrix} = \psi_2$$

and

$$\frac{d\psi_3}{d\rho} \equiv \psi_3' = \begin{vmatrix} y_1^{(1)'} & y_1^{(2)'} \\ y_4^{(1)} & y_4^{(2)} \end{vmatrix} + \begin{vmatrix} y_1^{(1)} & y_1^{(2)} \\ y_4^{(1)'} & y_4^{(2)'} \end{vmatrix}$$

$$= \begin{vmatrix} y_2^{(1)} & y_2^{(2)} \\ y_4^{(1)} & y_4^{(2)} \end{vmatrix} + \begin{vmatrix} y_1^{(1)} & y_1^{(2)} \\ \sum_{i=1}^{4} A_i^I y_i^{(1)} & \sum_{i=1}^{4} A_i^I y_i^{(2)} \end{vmatrix}$$

$$= \begin{vmatrix} y_2^{(1)} & y_2^{(2)} \\ y_4^{(1)} & y_4^{(2)} \end{vmatrix} + \sum_{i=1}^{4} A_i^I \begin{vmatrix} y_1^{(1)} & y_1^{(2)} \\ y_i^{(1)} & y_i^{(2)} \end{vmatrix}$$

Taking into account the earlier definitions of $\psi_i, i = 1, ..., 6$, this last result becomes

$$\psi_3' = A_2^I \psi_1 + A_3^I \psi_2 + A_4^I \psi_3 + \psi_5 \,.$$

Similarly, we have

$$\psi_2' = \psi_3 + \psi_4 \,,$$
$$\psi_4' = \psi_5 \,,$$
$$\psi_5' = -A_2^I \psi_1 + A_3^I \psi_4 + A_4^I \psi_5 + \psi_6 \,,$$
$$\psi_6' = A_1^I \psi_2 - A_2^I \psi_4 - A_4^I \psi_6 \,.$$

and

$$\phi_1' = \phi_2 \,,$$
$$\phi_2' = \phi_3 + \phi_4 \,,$$
$$\phi_3' = A_2^{II} \phi_1 + A_3^{II} \phi_2 + A_4^{II} \phi_3 + \phi_5 \,,$$
$$\phi_4' = \phi_5 \,,$$
$$\phi_5' = -A_2^{II} \phi_1 + A_3^{II} \phi_4 + A_4^{II} \phi_5 + \phi_6 \,,$$
$$\phi_6' = A_1^{II} \phi_2 - A_2^{II} \phi_4 - A_4^{II} \phi_6 \,.$$

Performing the same type of calculations in relation to (B.1b), the original fourth-order equations are transformed into a couple of linear sixth-order systems involving the compound matrix variables,

$$\frac{d\psi}{d\rho} = \mathbf{M}^I \psi \,, \qquad \rho \in [\eta_1, \eta_2] \,, \tag{B.5a}$$

$$\frac{d\phi}{d\rho} = \mathbf{M}^{II} \phi \,, \qquad \rho \in [\eta_2, 1] \,, \tag{B.5b}$$

where $\mathbf{M}^{I,II}$ are the 6×6 matrices

$$\mathbf{M}^{I,II} := \begin{bmatrix} 0 & 1 & 0 & 0 & 0 & 0 \\ 0 & 0 & 1 & 1 & 0 & 0 \\ A_2^{I,II} & A_3^{I,II} & A_4^{I,II} & 0 & 1 & 0 \\ 0 & 0 & 0 & 0 & 1 & 0 \\ -A_1^{I,II} & 0 & 0 & A_3^{I,II} & A_4^{I,II} & 1 \\ 0 & -A_1^{I,II} & 0 & -A_2^{I,II} & 0 & A_4^{I,II} \end{bmatrix}.$$

Even though the problem has experienced an increase in the number of equations, the real advantage comes from the fact that now we only need to solve some initial-value problems. The formulation of the required initial conditions and the handling of the continuity equations at the interface are explained in the next two sections.

B.1 The first strategy

Assuming that $\mathbf{y}^{(1)}, \mathbf{y}^{(2)}$ satisfy the boundary conditions on the inner rim $\rho = \eta_1$, i.e., $y_1^{(1)}(\eta_1) = y_1^{(2)}(\eta_1) = y_2^{(1)}(\eta_1) = y_2^{(2)}(\eta_1) = 0$, by taking into account the definitions of the CMM variables we discover that

$$\psi_1(\eta_1) = \psi_2(\eta_1) = \psi_3(\eta_1) = \psi_4(\eta_1) = \psi_5(\eta_1) = 0 \quad \text{and} \quad \psi_6(\eta_1) \neq 0.$$

Without loss of generality we can set $\psi_6(\eta_1) = 1$, and hence the boundary conditions (B.2a) on the inner rim of the original problem correspond to the following initial conditions for the new system (B.5a),

$$\psi = [0, 0, 0, 0, 0, 1]^T \quad \text{at} \quad \rho = \eta_1. \tag{B.6}$$

Similarly, assuming that the solutions $\mathbf{z}^{(1)}, \mathbf{z}^{(2)}$ satisfy the boundary conditions (B.2b) on the outer rim of Ω, we obtain the other set of initial conditions for (B.5b),

$$\phi = [0, 0, 0, 0, 0, 1]^T \quad \text{at} \quad \rho = 1. \tag{B.7}$$

With the original boundary conditions embedded in these two initial conditions for the new system, the next item on the agenda is to rewrite the continuity conditions (B.3) at the interface in terms of the components of ψ and ϕ. To this end, we notice that

$$\boldsymbol{P\alpha} = \mathbf{0}, \tag{B.8}$$

where

$$\boldsymbol{P} := [\boldsymbol{G}\mathbf{y}^{(1)}, \boldsymbol{G}\mathbf{y}^{(2)}, \boldsymbol{H}\mathbf{z}^{(1)}, \boldsymbol{H}\mathbf{z}^{(2)}] \qquad \text{and} \qquad \boldsymbol{\alpha} = [\alpha_1, \alpha_2, \alpha_3, \alpha_4]^T \,.$$

From the nontrivial solvability of the linear system (B.8) in which α_i $(i = 1, 2, 3, 4)$ are regarded as the unknowns, we deduce the so-called *target condition*

$$\det(\boldsymbol{P}) = 0 \,. \tag{B.9}$$

By applying the Laplace expansion theorem for determinants, we can express the target conditions in terms of the 2×2 minors of $\boldsymbol{P}$. Hence equation (B.8) becomes

$$P_{1214}P_{3432} - P_{1221}P_{3434} - P_{1223}P_{3441} - (P_{1223}P_{3413} - P_{1231}P_{3424} - P_{1243}P_{3421}) = 0 \,,$$

where

$$P_{ijkl} := \begin{vmatrix} P_{k,i} & P_{k,j} \\ P_{l,i} & P_{l,j} \end{vmatrix} \,.$$

The 2×2 determinants above can be further expressed in terms of the compound matrix variables ψ_i and ϕ_i $(i = 1, .., 6)$ in light of their definitions

$$\begin{aligned} \begin{vmatrix} P_{k,1} & P_{k,2} \\ P_{l,1} & P_{l,2} \end{vmatrix} = &(G_{k1}G_{l2} - G_{k2}G_{l1})\psi_1 + (G_{k1}G_{l3} - G_{k3}G_{l1})\psi_2 \\ &+ (G_{k1}G_{l4} - G_{k4}G_{l1})\psi_3 + (G_{k2}G_{l3} - G_{k3}G_{l2})\psi_4 \\ &+ (G_{k2}G_{l4} - G_{k4}G_{l2})\psi_5 + (G_{k3}G_{l4} - G_{k4}G_{l3})\psi_6 \,, \end{aligned}$$

and

$$\begin{aligned} \begin{vmatrix} P_{k,3} & P_{k,4} \\ P_{l,3} & P_{l,4} \end{vmatrix} = &(H_{k1}H_{l2} - H_{k2}H_{l1})\phi_1 + (H_{k1}H_{l3} - H_{k3}H_{l1})\phi_2 \\ &+ (H_{k1}H_{l4} - H_{k4}H_{l1})\phi_3 + (H_{k2}H_{l3} - H_{k3}H_{l2})\phi_4 \\ &+ (H_{k2}H_{l4} - H_{k4}H_{l2})\phi_5 + (H_{k3}H_{l4} - H_{k4}H_{l3})\phi_6 \,. \end{aligned}$$

To summarise, the compound matrix method has transformed the original eigenproblem into an initial value problem for a linear system of 6 first-order ordinary differential equations. The eigenvalue λ is identified by searching for the least positive value of this parameter for which the target condition (B.9) is satisfied.

B.2 The second strategy

This differs from the earlier one in the way the continuity conditions are handled. Basically, the change of tack consists in integrating the problem sequentially, starting from the inner rim to the interface, and then using the continuity conditions to formulate new initial conditions for the equations that are integrated in the outer annulus. Such an approach is more general than the one already outlined in the previous section, and can be easily extended to multi-annular problems with an arbitrary number of concentric annular sub-regions.

After forward integration of equation (B.5a) over $[\eta_1, \eta_2]$ with the initial condition (B.6), the values of ψ_i $(i = 1, ..., 6)$ are obtained at the interface. Equation (B.3) can be recast in the form

$$CY\widehat{\alpha}_1 = DZ\alpha_2, \tag{B.10a}$$

$$EY\widehat{\alpha}_1 = FZ\alpha_2, \tag{B.10b}$$

where

$$\widehat{\alpha}_1 := \begin{bmatrix} \alpha_1 \\ \alpha_2 \end{bmatrix}, \qquad \widehat{\alpha}_2 := \begin{bmatrix} \alpha_3 \\ \alpha_4 \end{bmatrix}, \qquad C = D := \begin{bmatrix} 1 & 0 & 0 & 0 \\ 0 & 1 & 0 & 0 \end{bmatrix},$$

$$E = \begin{bmatrix} G_{31} & G_{32} & G_{33} & 0 \\ G_{41} & G_{42} & G_{43} & G_{44} \end{bmatrix}, \qquad F = \begin{bmatrix} H_{31} & H_{32} & H_{33} & 0 \\ H_{41} & H_{42} & H_{43} & H_{44} \end{bmatrix}.$$

From (B.10a) it follows that $\det{(CY)}\widehat{\alpha}_1 = \mathrm{adj}\,{(CY)}DZ\widehat{\alpha}_2$, where adj$(CY)$ is the adjugate matrix of CY. Substituting this into (B.10b) yields

$$\big\{EY\,\mathrm{adj}\,{(CY)}D - \det{(CY)}F\big\}Z\widehat{\alpha}_2 = 0.$$

As explained by Lindsay in [80] this relation must be satisfied for all $\widehat{\alpha}_2 \equiv [\alpha_3, \, \alpha_4]^T$ since there are still two boundary conditions left to satisfy on the outer rim of Ω. Hence

$$\big\{EY\,\mathrm{adj}\,{(CY)}D - \det{(CY)}F\big\}Z = 0. \tag{B.11}$$

Note that

$$CY = \begin{bmatrix} y_1^{(1)} & y_1^{(2)} \\ y_2^{(1)} & y_2^{(2)} \end{bmatrix}, \qquad \mathrm{adj}\,{(CY)} = \begin{bmatrix} y_2^{(2)} & -y_1^{(2)} \\ -y_2^{(1)} & y_1^{(1)} \end{bmatrix},$$

and then using the definitions for ψ_i $(i = 1, ..., 6)$, after routine manipulations (B.11) can be

shown to become

$$
\left[\widehat{\boldsymbol{F}}_1 \mid \widehat{\boldsymbol{F}}_2 \right]
\begin{Bmatrix}
\mathbf{S}_1 \\
\mathbf{S}_2 \\
\mathbf{S}_3 \\
\mathbf{S}_4
\end{Bmatrix} = 0 \,,
\tag{B.12}
$$

where,

$$
\widehat{\boldsymbol{F}}_1 :=
\begin{bmatrix}
(G_{31} - H_{31})\psi_1 - G_{33}\psi_4 & (G_{32} - H_{32})\psi_1 + G_{33}\psi_2 \\
(G_{41} - H_{41})\psi_1 - G_{43}\psi_4 - G_{44}\psi_5 & (G_{42} - H_{42})\psi_1 + G_{43}\psi_2 + G_{44}\psi_3
\end{bmatrix} \,,
$$

$$
\widehat{\boldsymbol{F}}_2 :=
\begin{bmatrix}
-H_{33}\psi_1 & 0 \\
-H_{43}\psi_1 & -H_{44}\psi_1
\end{bmatrix} \,,
$$

and the $\boldsymbol{S}_j$ $(j = 1, 2, 3, 4)$ have already been defined in equation (B.4).

The above equation provides two relations for the four quantities $\boldsymbol{S}_i$ $(i = 1, 2, 3, 4)$, so we can represent any two of them in terms of the other two (by routine algebraic manipulations). We choose to write

$$
\boldsymbol{S}_3 = k_1 \boldsymbol{S}_1 + k_2 \boldsymbol{S}_2 \,, \qquad \boldsymbol{S}_4 = k_3 \boldsymbol{S}_1 + k_4 \boldsymbol{S}_2 \,,
$$

where k_i $(i = 1, 2, 3, 4)$ can be obtained from the (B.12), and have the expressions recorded below

$$
k_1 = \frac{(G_{31} - H_{31})\psi_1 - G_{33}\psi_4}{H_{33}\phi_1} \,,
$$

$$
k_2 = \frac{(G_{32} - H_{32})\psi_1 - G_{33}\psi_2}{H_{33}\phi_1} \,,
$$

$$
k_3 = \frac{[H_{43}(H_{31} - G_{31}) - H_{33}(H_{41} - G_{41})]\psi_1 - (H_{33}G_{43} - H_{43}G_{33})\psi_4 - H_{33}H_{44}\phi_5}{H_{33}H_{44}\phi_1} \,,
$$

$$
k_4 = \frac{[H_{33}(H_{42} - G_{42}) + H_{43}(H_{32} - G_{32})]\psi_1 - (H_{33}G_{44} - H_{33}G_{43})\psi_2 - H_{33}H_{44}\phi_3}{H_{33}H_{44}\phi_1} \,.
$$

This information permits us to relate the CMM variables on the interface since

$$
\phi_1 := \begin{vmatrix} \boldsymbol{S}_1 \\ \boldsymbol{S}_2 \end{vmatrix} = \phi_1 \,, \qquad\qquad
\phi_2 := \begin{vmatrix} \boldsymbol{S}_1 \\ k_1\boldsymbol{S}_1 + k_2\boldsymbol{S}_2 \end{vmatrix} = k_2\phi_1 \,,
$$

$$
\phi_3 := \begin{vmatrix} \boldsymbol{S}_1 \\ k_3\boldsymbol{S}_1 + k_4\boldsymbol{S}_2 \end{vmatrix} = k_4\phi_1 \,, \qquad\qquad
\phi_4 := \begin{vmatrix} \boldsymbol{S}_2 \\ k_1\boldsymbol{S}_1 + k_2\boldsymbol{S}_2 \end{vmatrix} = -k_1\phi_1 \,,
$$

$$
\phi_5 := \begin{vmatrix} \boldsymbol{S}_2 \\ k_3\boldsymbol{S}_1 + k_4\boldsymbol{S}_2 \end{vmatrix} = -k_3\phi_1 \,, \qquad\qquad
\phi_6 := \begin{vmatrix} k_1\boldsymbol{S}_1 + k_2\boldsymbol{S}_2 \\ k_3\boldsymbol{S}_1 + k_4\boldsymbol{S}_2 \end{vmatrix} = (k_1 k_4 - k_2 k_3)\phi_1 \,.
$$

The first of these equations is trivially satisfied, so without loss of generality we can set $\phi_1(\eta_2) = 1$. In conclusion, the initial conditions for ϕ at the interface read

$$\phi = [1, k_2, k_4, -k_1, -k_2, k_1 k_4 - k_2 k_3] \qquad \text{at} \quad \rho = \eta_2 \,.$$

Equations (B.5b) are integrated towards the outer boundary of Ω_{II} with these initial conditions, and the eigenvalue is found once the target condition (B.7) is satisfied.

Glossary of Abbreviations

CMM Compound Matrix Method

CV Calculus of Variations

FvK Föppl–von Kármán

HEM Hybrid Energy Method

HGT Hybrid Galerkin Technique

MAE Method of Adjacent Equilibrium

NHP Nodal Hoop Point

NSE Neutral Stability envelope

$PBAS$ Pre-Buckling Azimuthal Stresses

$SIDT$ Simplified Incremental Deformation Theory

SLC Shapiro-Lopatinskij Condition

TP Turning Point

Bibliography

[1] G.G. Adams. Elastic wrinkling of a tensioned circular plate using von Kármán plate theory. *ASME Journal of Applied Mechanics*, 60:520–525, 1993.

[2] J.R. Albright. Integrals of products of Airy functions. *J. Math. Phys. A*, 10:485–490, 1977.

[3] N.A. Alfutov. *Stability of Elastic Systems*. Springer Verlag, New York, 2000.

[4] C.M. Andersen and J.F. Geer. A hybrid perturbation Galerkin technique with applications to slender body theory. *SIAM J. Appl. Math.*, 49:344–361, 1989.

[5] C.M. Andersen and J.F. Geer. A hybrid perturbation-Galerkin technique that combines multiple expansions. *SIAM J. Appl. Math.*, 49:1474–1495, 1990.

[6] C.M. Andersen and J.F. Geer. Investigating a hybrid perturbation-Galerkin technique using computer algebra. *J. Symbolic Computation*, 12:695–714, 1991.

[7] U. Ascher and R. D. Russell. Reformulation of boundary value problems into "standard" form. *SIAM Review*, 23(2):238–254, 1981.

[8] B. Audoly and Y. Pomeau. *Elasticity and Geometry: From Hair Curls to the Non-linear Response of Shells*. Oxford University Press, Oxford, 2010.

[9] W. Auzinger, E. Karner, O. Koch, and E. Weinmüller. Collocation methods for the solution of eigenvalue problems for singular ordinary differential equations. *Opuscula Math.*, 26(2):pp. 229–241, 2006.

[10] W. Auzinger, G. Kneisl, O. Koch, and E. Weinmüller. SBVP 1.0 - A MATLAB solver for singular boundary value problems. Technical report, Institute for Applied Mathematics and Numerical Analysis, http://www.math.tuwien.ac.at/ ewa/, 2002.

[11] W. Auzinger, G. Kneisl, O. Koch, and E. Weinmüller. A collocation code for singular boundary value problems in ordinary differential equations. *Numerical Algorithms*, 33:27–39, 2003. 10.1023/A:1025531130904.

[12] V. Berdichevsky. *Variational Principles of Continuum Mechanics I Fundamentals*. Springer, London, 2009.

[13] C.B. Biezeno and H. Hencky. On the general theory of elastic stability. *Koninklijke Akademie van Wettenschappen te Amsterdam*, 31:569–592, 1928.

[14] M.A. Biot. Surface instability of rubber in compression. *Applied Science Research*, pages 168–182, 1963.

[15] M.A. Biot. *Mechanics of Incremental Deformation.* John Wiley & Sons, New York, 1965.

[16] G. Birkhoff and G.C. Rota. *Ordinary Differential Equations (3rd. edition).* John Wiley & Sons, New York, 1978.

[17] F. Bloom and D. Coffin. *Handbook of Thin Plate Buckling and Post-buckling.* Chapman & Hall/CRC Press, Boca Raton, 2001.

[18] R. Brighenti. Buckling of cracked thin-plates under tension or compression. *Thin-walled Struct.*, 43:209–224, 2004.

[19] D.O. Brush and Bo.O. Almroth. *Buckling of Bars, Plates and Shells.* McGraw-Hill, New York, 1975.

[20] P.S. Bulson. *The Stability of Flat Plates.* Chatto & Windus, London, 1970.

[21] K. Burton and D.L. Taylor. Traction forces of cytokinesis measured using optically modified elastic substrata. *Nature*, 385:450–454, 1997.

[22] E. Cerda and L. Mahadevan. Geometry and physics of wrinkling. *Physical Review Letters*, 90:1–4, 2003.

[23] E. Cerda, K. Ravi-Chandar, and L. Mahadevan. Wrinkling of stretched elastic sheets. *Nature*, 419:579–580, 2002.

[24] P.C. Chou and N.J. Pagano. *Elasticity: Tensor, Dyadic and Engineering Approaches.* D. Van Nostrand Company, Princeton, 1967.

[25] E. Chu and Yu Xu. An elastoplastic analysis of flange wrinkling in deep drawing processes. *International Journal of Mechanical Sciences*, 43:1421–1440, 2001.

[26] P.G. Ciarlet. A justification of the von Kármán plate theory. *Archive for Rational Mechanics and Analysis*, 73:349–389, 1980.

[27] L. Collatz. *Eigenwertprobleme und Ihre Numerische Behandlung.* Chelsea Publishing Company, New York, 1948.

[28] C. D. Coman and D. M. Haughton. On some approximate methods for the tensile instabilities of thin annular plates. *Journal of Engineering Mathematics*, 56:79–99, 2006.

[29] C.D. Coman. Edge-buckling in stretched thin films under in-plane bending. *Z. angew. Math. Phys.*, 58:510–525, 2007.

[30] C.D. Coman. On the applicability of tension field theory to a wrinkling instability problem. *Acta Mechanica*, 190:57–72, 2007.

[31] C.D. Coman. Elastic instabilities caused by stress concentration. *International Journal of Engineering Science*, 46:877–890, 2008.

[32] C.D. Coman. The asymptotic limit of an eigenvalue problem related to the buckling of a rolled elastic strip. *Mechanics Research Communications*, 36:826– 832, 2009.

[33] C.D. Coman. Remarks on elastic buckling for sectorial plates. *International Journal of Engineering Science*, 47:1002–1013, 2009.

[34] C.D. Coman. Edge-wave buckling of rolled elastic strips: asymptotic results. *Acta Mech.*, 211:101–113, 2010.

[35] C.D. Coman. Global asymptotic approximations for wrinkling of polar orthotropic annular plates in tension. *International Journal of Solids and Structures*, 47(11-12):1572–1579, June 2010.

[36] C.D. Coman. On interactive buckling in a sandwich structure. *Zeitschrift für angewandte Mathematick und Physik*, 61:565–577, 2010.

[37] C.D. Coman. Instabilities of highly anisotropic spinning disks. *Mathematics and Mechanics of Solids*, 16:3–17, 2011.

[38] C.D. Coman. Some applications of the WKB method to the wrinkling of bi-annular plates in tension. *Acta Mechanica*, 2012. *Published online.*

[39] C.D. Coman and A.P. Bassom. A singular perturbation approach to the wrinkling of stretched annular membranes under in-plane torsion. Preprint 2006.

[40] C.D. Coman and A.P. Bassom. Boundary layers and stress concentration in the circular shearing of annular thin films. *Proceedings of the Royal Society of London A*, 463:3037–3053, 2007.

[41] C.D. Coman and A.P. Bassom. On the wrinkling of a pre-stressed annular thin film in tension. *Journal of the Mechanics and Physics of Solids*, 55:1601–1617, 2007.

[42] C.D. Coman and A.P. Bassom. An asymptotic description of the elastic instability of twisted thin elastic plates. *Acta Mech.*, 200:59–68, 2008.

[43] C.D. Coman and A.P. Bassom. Wrinkling of pre-stressed annular thin films under azimuthal shearing. *Math. Mech. Solids*, 13:513–531, 2008.

[44] C.D. Coman and A.P. Bassom. Higher-order asymptotics for edge-buckling of pre-stressed thin plates under in-plane bending. *J. Engng. Math.*, 63:327–338, 2009.

[45] C.D. Coman and A.P. Bassom. Erratum: "on the wrinkling of a pre-stressed annular thin film in tension" [Journal of Mechanics and Physics of Solids 55 (2007) 1601]. *Journal of the Mechanics and Physics of Solids*, 60(6):1240, 2012.

[46] C.D. Coman and M. Destrade. Asymptotic results for bifurcations in pure bending of rubber blocks. *Quarterly Journal of Mechanics and Applied Mathematics*, 61:395–414, 2008.

[47] C.D. Coman and D.M. Haughton. Localised wrinkling instabilities in radially stretched annular thin films. *Acta Mech.*, 185:179–200, 2006.

[48] C.D. Coman and X. Liu. Buckling-resistant thin annular plates in tension. *International Journal of Solids and Structures*, 2012. (submitted for publications 2012).

[49] C.D. Coman and X. Liu. On the bifurcations of the Lamé solutions in plane-strain elasticity. *International Journal of Non-Linear Mechanics*, 47(2), 2012.

[50] C.D. Coman and X. Liu. Semi-analytical approximations for a class of multi-parameter eigenvalue problems related to tensile buckling. *Z. angew. Math. Phys.*, 2012. (Published online 2012).

[51] N.D. Cristescu, E.M. Craciun, and E. Soós. *Mechanics of Elastic Composites*. Chapman Hall/CRC Press, Boca Raton, 2004.

[52] R.C. Di Prima. Application of the Galerkin method to problems in hydrodynamic stability. *Quart. Appl. Math.*, 13:55–62, 1955.

[53] P. Drazin and W. Reid. *Hydrodynamic Stability*. Cambridge University Press, Cambridge, 1981.

[54] Yu.V. Egorov and M.A. Shubin. *Foundations of the Classical Theory of Partial Differential Equations*. Springer Verlag, New York, 1998.

[55] Y. Frostig and G.J. Simitses. Buckling of multi-annular plates. *Computers & Structures*, 24(3):443–454, 1986.

[56] Y. Frostig and G.J. Simitses. Buckling of ring-stiffened multi-annular plates. *Computers & Structures*, 29(3):519–526, 1988.

[57] Y.C. Fung. *Foundations of Solid Mechanics*. Prentice-Hall, Inc., Englewood Cliffs, New Jersey, 1965.

[58] Anthony F Gangi. Fourth-order elastic-moduli tensors by inspection. *Proceedings of 9th international workshop on seismic anisotropy*, pages 1–10, 2000.

[59] J.C. Géminard, R. Bernal, and F. Melo. Wrinkle formations in axis-symmetrically stretched membranes. *The European Physical Journal E*, 15:117–126, 2004.

[60] A.N. Gent and I.S. Cho. Surface instabilities in compressed or bent rubber blocks. *Rubber Chemistry and Technology*, 72:253–262, 1999.

[61] A. Gilabert, P. Sibillot, D. Sornette, C. Vanneste, D. Maugis, and F. Muttin. Buckling instability and patterns around holes or cracks in thin plates under a tensile load. *Eur. J. Mech. A/Solids*, 11(1):65–89, 1992.

[62] A.E. Green and W. Zerna. *Theoretical Elasticity.* Clarendon Press, Oxford, 1960.

[63] V.Z. Gristchak and Ye.M. Dmitrijeva. A hybrid WKB Galerkin method and its application. *Technische Mechanik*, 15:281–294, 1955.

[64] V.Z. Gristchak and O.A. Ganilova. A hybrid WKB-Galerkin method applied to a piezo-electric sandwich plate vibration problem considering shear force effects. *J. Sound Vibration*, 317:366–377, 2008.

[65] D.M. Haughton and R.W. Ogden. Bifurcation of inflated circular cylinders of elastic material under axial loading II. Exact theory for thick-walled tubes. *Journal of the Physics and Mechanics of Solids*, 27:489–512, 1979.

[66] D.M. Haughton and A. Orr. On the eversion of compressible elastic cylinders. *Int. J. Solids Struct.*, 34:1893–1914, 1997.

[67] R. Hill and J.W. Hutchinson. Bifurcation phenomena in the plane tension test. *Journal of the Mechanics and Physics of Solids*, 23:239–264, 1975.

[68] T. Iwasa, M. C. Natori, and K. Higuchi. Evaluation of tension field theory for wrinkling analysis with respect to the post-buckling study. *ASME Journal of Applied Mechanics*, 71:532–540, 2004.

[69] Y. Stavsky J.B. Greenberg. Axisymmetric vibrations of concentric dissimilar isotropic composite plates. *Composites Part B: Engineering*, 30(6):553–567, 1999.

[70] Y. Stavsky J.B. Greenberg. Axisymmetric vibrations of concentric dissimilar orthotropic composite plates. *Journal of Sound and Vibration*, 254(5):849–865, 2002.

[71] N. Jillella and J. Peddieson. Modelling of wrinkling of thin circular sheets. *International Journal of Non-Linear Mechanics*, 47(1):85–91, 2012.

[72] G.A. Kardomateas. Buckling of thick orthotropic cylindrical shells under external pressure. *ASME Journal of Applied Mechanics*, 60:195–202, 1993.

[73] G.A. Kardomateas. Effect of normal strains in buckling of thick orthotropic shells. *Journal of Aerospace Engineering*, 13(3), 2000.

[74] G.A. Kardomateas and J. Simitses. Buckling of long sandwich cylindrical shells under external pressure. *ASME Journal of Applied Mechanics*, 72:493–500, 2005.

[75] R.J. Knops and E.W. Wilkes. Theory of elastic stability. In C. Truesdell, editor, *Handbuch der Physik*, pages 125–302, Berlin, 1973. Springer-Verlag.

[76] H.L. Langhaar. *Energy methods in Applied Mechanics*. Wiley, 1962.

[77] P.L. Larsson. On buckling of orthotropic stretched plates with circular holes. *Composite Structures*, 11:121–134, 1989.

[78] D.C. Leigh. *Nonlinear Continuum Mechanics*. McGraw-Hill Book Company, New York, 1968.

[79] H. Leipholz. *Stability Theory (2nd edition)*. B.G. Teubner, Stuttgart, 1987.

[80] K.A. Lindsay. The application of compound matrices to convection problems in multi-layered continua. *Mathematical Models and Methods in Applied Sciences*, 2(2):121–141, 1992.

[81] K.A. Lindsay and C.E. Rooney. A note on compound matrices. *Journal of Computational Physics*, 133:472–477, 1992.

[82] X. Liu and C.D. Coman. The localised wrinkling of a stretched bi-annular thin plate. *Proceeding of World Academy of Science, Engineering and Technology*, 8(71):896–901, 2012.

[83] V.A. Lubarda. Radial stretching of a thin hollow membrane: biaxial tension, tension field and buckling domains. *Acta Mechanica*, 217:317–334, 2011.

[84] V.A. Lubarda and A. Marzani. Viscoelastic response of thin membranes with applications to red blood cells. *Acta Mechanica*, 202:1–16, 2009.

[85] E.H. Mansfield. On the buckling of an annular plate. *Quarterly Journal of Applied Mathematics*, 13(1):16–23, 1960.

[86] E.H. Mansfield. Gravity-induced wrinkle lines in vertical membranes. *Proceedings of the Royal Society of London*, A 375:307–325, 1981.

[87] D. Maugis. *Contact, Adhesion, and Rupture of Elastic Solids*. Springer, Berlin, 2000.

[88] M.M. Mikulas. Behaviour of a flat stretched membrane wrinkled by the rotation of an attached hub. Technical report, NASA-TN D-2456, 1964.

[89] R.D. Mindlin. Influence of rotatory inertia and shear on flexural motions of isotropic elastic plates. *J. Appl. Mech.*, 18(10):31–38, 1951.

[90] A.B. Movchan and A.N. Movchan. *Mathematical Modelling of Solids with Non-regular Boundaries*. CRC Press, Boca Raton, 1995.

[91] P.M. Naghdi. The theory of plates and shells. In S. Flügge, editor, *Handbuch der Physik*, pages 425–640, Berlin, 1972. Springer-Verlag.

[92] M.M. Najafizadeh and M.R. Eslami. Buckling analysis of circular plates of functionally graded materials under uniform radial compression. *International Journal of Mechanical Sciences*, 44(12):2479–2493, 2002.

[93] P.V. Negron-Marrero and E. Montes-Pizarro. The complementary condition and its role in a bifurcation theory applicable to nonlinear elasticity. *New York Journal of Mathematics*, 17a:1–21, 2011.

[94] V.V. Novozhilov. *Foundations of the Nonlinear Theory of Elasticity*. Dover Publications, New York, 1999.

[95] R.W. Ogden. *Non-linear Elastic Deformations*. Dover Publications, New York, 1997.

[96] G. Papadakis. Buckling of thick cylindrical shells under external pressure: a new analytical expression for the critical load and comparisons with elasticity solutions. *International Journal of Solids and Structures*, 45:5308–5321, 2008.

[97] A. C. Pipkin. The relaxed energy density for isotropic elastic membranes. *IMA Journal of Applied Mathematics*, 36:85–89, 1986.

[98] W.H. Press, B.P. Flannery, S.A. Teukolsky, and W.T. Vetterling. *Numerical Recipies in Fortran: the Art of Scientific Computing*. Cambridge University Press, Cambridge, 1992.

[99] F.G. Rammerstorfer, F.D. Fischer, and N. Friedl. Buckling of free infinite strips under residual stresses and global tension. *ASME J. Appl. Mech.*, 68:804–809, 2001.

[100] J.N. Reddy and N.D. Phan. Stability and vibration of isotropic, orthotropic and laminated plates according to a higher-order shear deformation theory. *Journal of Sound and Vibration*, 98(2):157–170, 1985.

[101] E. Reissner. On tension field theory. In *Proceedings of the 5th International Congress of Applied Mechanics*, pages 88–92, 1938.

[102] E. Reissner. On the theory of bending of elastic plates. *J. Math. Phys.*, 23(4):184–191, 1944.

[103] F.P.J. Rimrott and M. Cvercko. Wrinkling in thin plates due to in-plane body forces. In R. Feijóo L. Bevilacqua and R. Valid, editors, *Inelastic Behaviour of Plates and Shells*, pages 19–48, Berlin, 1986. Springer.

[104] R.S. Rivlin and G. Thomas. Large Elastic Deformations of Isotropic Materials. VIII. Strain Distribution around a Hole in a Sheet. *Philosophical Transactions of the Royal*

Society A: Mathematical, Physical and Engineering Sciences, 243(865):289–298, April 1951.

[105] R.S. Rivlin. Large elastic deformations of isotropic materials V: The problem of flexure. *Proceedings of the Royal Society of London A*, 195:463–473, 1949.

[106] S. Roccabianca, D. Bigoni, and M. Gei. Long-wavelength bifurcations and multiple neutral axes in elastic multilayers subject to finite bending. *Journal of the Mechanics of Materials and Structures*, 6(1-4):511–527, 2011.

[107] S. Roccabianca, M. Gei, and D. Bigoni. Plane strain bifurcations of elastic layered structures subject to finite bending: theory versus experiments. *IMA Journal of Applied Mathematics*, 75(4):525–548, 2010.

[108] G.N. Savin. *Stress concentration around holes*. Pergamon Press, Oxford, 1961.

[109] B.W. Senior. Flange wrinkling in deep-drawing operations. *Journal of the Mechanics and Physics of Solids*, 4:235–246, 1956.

[110] L.F. Shampine, J. Kierzenka, and M.W. Reichelt. Solving boundary value problems for ordinary differential equations in Matlab with `bvp4c`. Technical report, The MathWorks, ftp://ftp.mathworks.com/pub/doc/papers/bvp/., 2000.

[111] D. Shaw and Y.H. Huang. Buckling behavior of a central cracked thin plate under tension. *Engng. Fract. Mech.*, 35(6):1019–1027, 1990.

[112] G. Shi. A new simple third-order shear deformation theory of plates. *International Journal of Solids and Structures*, 44(13):4399–4417, 2007.

[113] S. Shimizu, S. Yoshida, and N. Enomoto. Buckling of plates with a hole under tension. *Thin-walled Struct.*, 12(1):35–49, 1991.

[114] G.J. Simitses. Effect of boundary conditions and rigidities on the buckling of annular plates. *Thin-Walled Structures*, 5, 1987.

[115] R.A.C. Slater. *Engineering Plasticity: Theory and Application to Metal Forming Processes*. McMillan Press Ltd., London, 1977.

[116] M. Stein and J.M. Hedgepeth. Analysis of partly wrinkled membranes. Technical report, NASA-TN D-813, 1961.

[117] S. Timoshenko. *Theory of Elasticity*. McGraw-Hill Book Company, Inc., New York, 1934.

[118] S.P. Timoshenko and J.M. Gere. *Theory of plates and shells*. McGraw Hill, New York, 1959.

[119] S.P. Timoshenko and J.M. Gere. *Theory of Elastic Stability*. McGraw Hill, New York, 1961.

[120] C. Truesdell and W. Noll. *The Non-Linear Field Theories of Mechanics (2nd edition)*. Springer-Verlag, Berlin Heidelberg, 1992.

[121] E. Ventsel and T. Krauthammer. *Thin Plates and Shells: Theory and Applications*. Marcel Dekker, New York, 2001.

[122] R. Vermorel, N. Vaundenberghe, and E. Villermaux. Impact on thin elastic sheets. *Proceedings of the Royal Society of London A*, 465:823–842, 2009.

[123] B.Z. Vulikh. *Introduction to Functional Analysis*. Pergamn Press, Oxford, 1963.

[124] M.K. Wadee, C.D. Coman, and A.P. Bassom. Numerical stability criteria for localised post-buckling solutions in a strut-on-foundation model. *ASME, J. Appl. Mech.*, 71:334–341, 2004.

[125] H. Wagner. Flat sheet metal girders with very thin metal web. *Zeitschrift für Flugtechnik Motorluftshiffahrt*, 20:200–207, 227–233, 256–262, 279–284, 1929.

[126] A.I.M. Whitting. A Galerkin procedure for localised buckling of a strut on a nonlinear elastic foundation. *Int. J. Solids Structures*, 34:727–739, 1977.

[127] N. Yamaki. Buckling of a thin annular plate under uniform compression. *J. Appl. Mech.*, 25:267–273, 1958.

[128] T.X. Yu and W. Johnson. The buckling of annular plates in relation to the deep-drawing process. *International Journal of Mechanical Sciences*, 24:175–188, 1982.

[129] T.X. Yu and L.C. Zhang. The elastic wrinkling of an annular plate under uniform tension on its inner edge. *Int. J. Mech. Sci.*, 28(11):729–737, 1986.

[130] L.C. Zhang and T.X. Yu. The plastic wrinkling of an annular plate under uniform tension on its inner edge. *International Journal of Solids and Structures*, 24(5):497–503, 1988.